Summer 8-11-2011

Optical Spectroscopy of Massive Binary Stars

Stephen J. Williams
Department of Physics and Astronomy

Recommended Citation

Williams, Stephen J., "Optical Spectroscopy of Massive Binary Stars." Dissertation, Georgia State University, 2011.
https://scholarworks.gsu.edu/phy_astr_diss/49

OPTICAL SPECTROSCOPY OF MASSIVE BINARY STARS

by

STEPHEN J. WILLIAMS

Under the Direction of Douglas R. Gies

ABSTRACT

This is a spectroscopic and photometric study of suspected close binary systems among the massive stars. The stars studied here include stars with temperatures ranging from 45,000 Kelvin (K) to 15,000 K, corresponding to spectral types ranging from O3 V to B5 III, masses between 47 Solar Masses ($M_\odot$) and 5 $M_\odot$, and absolute V magnitudes from -6.28 to -2.0. I categorize 30 targets according to my spectroscopic observations into groups with no radial velocity variability, single-lined, and double-lined variability. My analysis of the 18 constant velocity stars results in estimates of stellar effective temperature, $T_{\rm eff}$, gravity, log g, projected rotational velocity, $v \sin i$, and spectral classification. Analyzing single-lined systems, I find the same stellar parameters for five more systems, and also present the first orbits for these systems. I also explore the probable characteristics of the unseen companions in these systems. Three double-lined systems, two eclipsing and one with an ellipsoidal variation in the light curve, are fully analyzed, and I present important astrophysical parameters for each of these systems, including stellar masses, radii, ages, and distances to each system. The masses are accurate to 4.3% and 3.6% for the primary and secondary for LH 54−425, 2.1% and 1.6% for HI Mon, and 1.1% and 0.6% for HD 42401. Two more double-lined systems are studied, and preliminary results are presented. Photometric observations are analyzed for 56 targets from the All Sky Automated Survey in order to facilitate spectroscopic observations at key points in the binary orbit where spectral features of both components will be well separated. New spectroscopic observations of these eclipsing binaries with my computed ephemerides will allow us to obtain double-lined orbital elements and determine their masses, radii, ages, and distances. These computed parameters will then allow for comparison with theoretical stellar models, and a better understanding of the evolution of massive stars.

INDEX WORDS: Massive stars, Binary stars, Optical spectroscopy

OPTICAL SPECTROSCOPY OF MASSIVE BINARY STARS

by

STEPHEN J. WILLIAMS

A Dissertation Submitted in Partial Fulfillment of Requirements for the Degree of

Doctor of Philosophy

in the College of Arts and Sciences

Georgia State University

2011

OPTICAL SPECTROSCOPY OF MASSIVE BINARY STARS

by

STEPHEN J. WILLIAMS

Committee Chair: Douglas R. Gies

Committee: Todd J. Henry

Harold A. McAlister

Jerome A. Orosz

Murad Sarsour

Russel J. White

Electronic Version Approved:

Office of Graduate Studies

College of Arts & Sciences

Georgia State University

August 2011

TABLE OF CONTENTS

LIST OF TABLES

LIST OF FIGURES

– 1 –

Introduction

1.1 Background

Massive stars are the reality show celebrities of the universe! In general, massive stars, when compared to their less massive counterparts, are brighter and larger in size, evolve faster, and end their lives in more spectacular and noticeable ways. Perhaps the quality that most uniquely defines massive stars is their rarity. Despite this rarity, massive stars are responsible for many of the phenomena that give us insight into our universe. From studies of the nearby universe and Local Group, to understanding our own Galaxy's kinematics, chemical composition, and star formation processes and history, the investigation of the fundamental properties of massive stars has consequences both locally and cosmologically.

To put massive stars in context, let's refer to them in comparison to the most well studied star, the Sun. The vital statistics for the Sun are (Cox 2000): effective temperature, $T_{\rm eff} = 5777$ K (5.8 kK); mass, $M_\odot = 1.919 \times 10^{33}$ grams; radius, $R_\odot = 6.955 \times 10^{10}$ cm. The stars studied here are listed according to their most common values in Table 1.1. These values are for stars on the main sequence, fusing hydrogen into helium in their cores. The values listed for the O-stars are from the calibration of Martins et al. (2005) and the B-stars from the calibration of Harmanec (1988).

The term "massive stars" is relative. For the stars studied in this dissertation, I will define "massive star" to mean a star with main-sequence mass ≥ 8 solar masses ($M_\odot$) corresponding to early B-type stars in Table 1.1. An "intermediate mass" star will refer to a star with main-sequence mass $3 \leq M_*/M_\odot < 8$, roughly covering the

Table 1.1. Massive Star Properites

Spectral Classification	$T_{\rm eff}$ (kK)	M ($M_\odot$)	R ($R_\odot$)
O3 V	44.9	58.0	13.8
O4 V	42.9	46.9	12.4
O5 V	40.9	38.1	11.2
O5.5 V	39.9	34.4	10.6
O6 V	38.9	31.0	10.1
O6.5 V	37.9	28.0	9.6
O7 V	36.9	25.3	9.2
O7.5 V	35.9	22.9	8.7
O7 V	34.9	20.8	8.3
O8.5 V	33.9	18.8	7.9
O9 V	32.9	17.1	7.5
O9.5 V	31.9	15.6	7.2
B0 V	29.8	14.6	5.8
B0.5 V	28.5	13.2	5.5
B1 V	26.1	11.0	4.9
B2 V	23.1	8.6	4.3
B3 V	19.0	6.1	3.6
B4 V	17.2	5.1	3.3
B5 V	15.5	4.4	3.0
B6 V	14.1	3.8	2.8
B7 V	12.9	3.4	2.7
B8 V	11.5	2.9	2.4

rest of the B spectral types down to B8 V in Table 1.1. These definitions will serve to classify all stars discussed in this work.

Prior to outlining the goals of this spectroscopic study, I will briefly discuss some areas of modern research that serve to illustrate the importance and applicability of my work.

1.2 Current Massive and Intermediate Mass Stellar Research

1.2.1 Star Formation Processes

Recent observational and theoretical work has concluded that massive star formation is not a simple scaled-up version of low-mass star formation (Zinnecker & Yorke 2007). Observations of several OB associations show that both high-mass and low-mass stellar populations are the same age (Preibisch & Zinnecker 1999). One way to create such a scenario is to have a supernova shockwave trigger star formation as seen in one Scorpio-Centaurus OB association subgroup (de Geus 1992). This picture is far from clear, however. Lee & Chen (2007) studied the λ Ori region, Ori OB1, and Lac OB1 associations and found that Lyman continuum photons from O-stars were ultimately responsible for the formation of lower mass classical T Tauri stars and Herbig Ae/Be stars. Their observations appear to support the hypothesis that the radiation-driven implosion mechanism (Kessel-Deynet & Burkert 2003) initiated by massive stars is the only way to form lower-mass objects. In order to help clarify both high- and low-mass star formation scenarios, for my dissertation I observed massive stars in a variety of environments.

1.2.2 Supernovae

1.2.2.1 Type Ia Supernovae

Type Ia supernovae arise from binary star systems. Accretion of material from a companion onto a carbon-oxygen white dwarf causes the thermonuclear detonation of the white dwarf when its mass approaches the Chandrasekhar limit $M_{\rm Ch} \simeq 1.38\ M_\odot$ (Nomoto et al. 1984). The uniformity of Type Ia supernovae has been the primary reason for their use in determining the Hubble parameter, $H_{\rm o}$ (Freedman & Madore 2010), and inferring the existence of dark energy responsible for the acceleration of the expansion of the universe (Riess et al. 1998).

The recent study by Gilfanov & Bogdán (2010) indicates that a binary system composed of two carbon-oxygen white dwarfs is the likely progenitor of most Type

Ia supernovae. This means that the main sequence mass of the two members of such a binary system would be below $\sim 8\ M_\odot$ and be considered intermediate mass stars, such as the components of HD 42401 described later in this dissertation. By studying binary systems in this mass range, binary evolution tracks that lead to carbon-oxygen white dwarf pairs and ultimately Type Ia supernovae can be constrained.

1.2.2.2 Other Supernovae

Supernovae arising from massive stars, known as core collapse or Type IIP supernovae, account for $\sim 66\%$ of observed supernovae (Smartt et al. 2009). While more diverse in brightness than Type Ia supernovae, Type IIP supernovae show promise as useful distance indicators at higher redshifts than we expect to see Type Ia supernovae (Olivares et al. 2010). Some long-duration, soft-spectrum, gamma-ray bursts happen simultaneously with core collapse supernovae (see Woosley & Bloom 2006 and references therein). Rotation is a key part of gamma-ray burst models where the iron core of a massive star must have a minimum amount of rotation to create a gamma-ray burst. Less than this amount results in the formation of a pulsar (Ott et al. 2006). Links between multiplicity, rotation rate, and metallicity of younger massive stars and the conditions that may result in gamma-ray bursts are another reason to observe massive stars and obtain at least some of these values.

1.3 This Work

The specific goal of this study was to determine as many fundamental properties of stars as the data allow. Two methods are used in the attempt to determine fundamental properties: photometric and spectroscopic observations. Specifically, the focus of the work is on binary stars, the only stars from which we can obtain accurate mass measurements.

1.3.1 Spectroscopic Variability – Radial Velocities

The bulk of spectroscopic observations in this dissertation consists of O stars in an effort to assess the multiplicity fraction for objects that were reported with a binary designation of “U” (unknown) or “?” (uncertain) by Mason et al. (1998). To this end, the observations are analyzed and spectroscopic signatures are used to infer the status of the object’s multiplicity, primarily radial velocity.

The status of the spectroscopic natures of a sample of stars can be loosely broken down into three categories. The first is a constant velocity star, where there is no variation over the timescales of observation. The second is a single-lined spectroscopic binary (SB1), where the star shows periodic Doppler shifts of spectral features. The last type is a double-lined spectroscopic binary (SB2), in which two sets of spectral features are seen. Both SB1 and SB2 systems are manifestations of stars in orbit around detected (SB2) or typically undetected (SB1) companions.

So what can be determined about the star or stars in the three categories of spectroscopic variability? Velocity constant stars typically reveal the least about their specific natures. However, the effective temperature, $T_{\rm eff}$, gravity, parameterized by $\log g$, and projected rotational velocity, $v \sin i$, may be estimated by fitting theoretical stellar atmosphere models to features in the spectra. SB1 systems build on those three parameters because the existence of a companion is inferred from the orbital motion of the primary, or visible component. In the course of fitting a Keplerian orbit for the primary, several properties of that orbit are determined, such as the period of the orbit, P, the eccentricity of the orbit, e, and the velocity semiamplitude, K. With these values, properties of the orbit and the secondary may be constrained via the following relations

$$M_{1,2} \sin^3 i = 1.036149 \times 10^{-7}(1 - e^2)^{3/2}(K_1 + K_2)^2 K_{2,1} P$$

$$a \sin i = 1.976682 \times 10^{-2}(1 - e^2)^{1/2}(K_1 + K_2) P$$

where the masses M are in units of solar masses, orbital velocity semiamplitudes are in km s^{-1}, the orbital period, P is in days, the orbital semi-major axis, a, is in solar radii, and i is the inclination in degrees (Torres et al. 2010). Inclination is defined to be 90° when the plane of the orbit is in the line of sight of the observer (i.e. edge-on), and this will consequently result in minimum values for the mass and semi-major axis of the orbit in the formulae above. SB2 orbits build upon SB1 orbits by allowing fits of the orbit to give the mass ratio between the two components, typically given as $q = M_2/M_1 = K_1/K_2$. Without knowing the inclination of the orbit little more can be said about the individual stars. The inclination can be measured by combining spectroscopic analyses with either visual binary observations or from the light curves of eclipsing binary systems.

1.3.2 Photometric Variability

When two stars are in close orbit around each other and the geometry is such that the stars pass in front of each other from our line of sight, we observe what is known as an eclipsing binary system. Such systems are typically too far away to resolve the individual components in the sky, so the light variation of the system is the primary way these objects are identified.

Studies of the light curves (eclipsing or not) of binary systems reveals information about the relative sizes and shapes of the stars, the nature of the orbit, and the temperatures of the stars. Equations characterizing the orbit of a close binary have been well described (Kopal 1959; Lucy 1968). The use of these equations in modeling the light curve of a close binary system is best suited to computer analysis. Many programs that have been used to synthesize light curves can be found in the literature (e.g., Lucy 1967; Mochnacki & Doughty 1972) with by far the most successful and often used being the Wilson-Devinney (WD) code (Wilson & Devinney 1971). In the WD code, the specific intensity of radiation emitted by a star is approximated by the Planck function at a particular effective temperature for the star. This intensity will vary across the observed stellar surface based upon the angle at which radiation exits the photosphere. This effect, known as "limb darkening," is parameterized by one of several relations, either linear, quadratic, square root (Diaz-Cordoves & Gimenez 1992), or logarithmic (Klinglesmith & Sobieski 1970), with coefficients for these relations tabulated for stars of various temperatures, log g values, and chemical compositions (see Wade & Rucinski 1985; van Hamme 1993). The models also calculate the tidal deformation and resulting gravity darkening of the component stars. Gravity darkening occurs when a rapidly rotating star becomes distorted, with the equatorial radius becoming larger than the polar radii. This results in the poles of the star, when compared to the equatorial regions, having higher log g values resulting in higher temperatures and these regions giving off more flux. So, compared to a slowly rotating star, the poles will appear gravity brightened while the equator appears gravity darkened.

Models in general took a step forward when Orosz & Hauschildt (2000) introduced the Eclipsing Light Curve (ELC) program that made direct use of stellar model atmosphere specific intensities, thereby eliminating the need for a blackbody approximation and limb darkening laws. ELC uses a grid of photometric bandpass-integrated intensities (standard Johnson filter bandpass response curves as described in Bessell 1990; Bessell & Brett 1988) at various temperatures, log g's, and emergent angles ($\mu = \cos\theta$). More recent incarnations of the WD code have adopted this technique, and now use models of stellar atmospheres as inputs (van Hamme & Wilson 2003).

The most widely used stellar atmosphere models are those of Kurucz (1979). One feature of these models is the assumption of local thermodynamic equilibrium (LTE) in the computation process. As admitted by Kurucz, this assumption is inappropriate for very hot stars and low-gravity stars at cool temperatures. In these cases, use of stellar models including non-LTE effects is desirable. Specifically, non-LTE models provide significantly improved predictions of line profiles. Also, the ultraviolet spectrum of hot stars contains a huge number of metal lines, which may then significantly influence not only the emergent SED but also the atmospheric structure in general (Lanz & Hubeny 2003). Thus, the effects of line-blanketing need also be addressed. One such set of models are the OSTAR 2002 (Lanz & Hubeny 2003) and BSTAR 2006 (Lanz & Hubeny 2007) grids that incorporate non-LTE and line-blanketed considerations in their computations.

Even the most recent front-end program using the WD code, called PHOEBE (PHysics Of Eclipsing BinariEs; Prša & Zwitter 2005), still uses the LTE atmospheres from Kurucz (1979). One appealing aspect of ELC is the ease of changing the model atmosphere input, thus including the OSTAR 2002 and BSTAR 2006 grids for a variety of metallicities when modeling hot stars. In tests run by Orosz & Hauschildt (2000), light curves computed by WD and ELC agreed to better than 0.1% or better than 1 millimag. Based on these tests and the chance to include more accurate model stellar atmospheres, the choice was made to use ELC for combined light curve and radial velocity curve analysis.

1.3.3 Combined Photometric and Spectroscopic Variability

The combination of spectroscopic measurements of an SB2 system, and photometric measurements for an eclipsing system, allows for the determination of fundamental parameters of stars. Photometric analysis gives the inclination of the binary system, the key parameter otherwise unknown from SB2 analyses. These fundamental parameters, like mass and radius, in turn give clues to virtually all important defining characteristics of the stars in the system. Studies of stars in double-lined eclipsing systems are the only way to constrain the masses of stars, the most important stellar parameter. Systems of this type – double-lined eclipsing binary systems – are extremely important because the determination of accurate stellar parameters help constrain evolutionary models for stars both as single entities and as members of binary star systems.

The basic outline for determining the fundamental properties of stars starts with a stellar atmosphere model. Stellar atmosphere models are based on well-studied radiative transfer physics. These physics apply to only a very thin outer layer of the star, down to a few optical depths into the star's atmosphere. Obtaining a stellar atmosphere model or spectral template for a star then permits the analysis to measure the velocity of the star. In the best cases, these velocities lead to estimations of the parameters of the star that can then be compared to predictions from evolutionary models that address the complex problem of the interior physics of stars.

1.3.4 Goals and Motivation

Almost every O and B-type star is found in a binary or multiple system. Many single stars of these types are most likely former multiple system members that were ejected by a supernova explosion or a dynamical interaction (Sana & Evans 2010). Multiplicity is therefore a defining characteristic of massive stars.

The results of the recent review by Sana & Evans (2010) reveal a need for more spectroscopic surveys of massive stars. Spectroscopic observations are efficient at determining multiplicity for orbital periods of up to a couple of years. Velocity variations for systems longer than this become increasingly smaller and more difficult to detect. In the list compiled by Sana & Evans (2010), there is an overabundance of systems with orbital periods less than 10 days with only about 50% of binaries in the Galactic O-star sample having constraints on their orbital solutions. The main goal of the sample of stars studied in this dissertation is to address these deficiencies.

1.3.5 Sample Selection

The sample of massive stars studied in this dissertation comes from **?**. In that work, several objects were denoted as "U" meaning unknown spectroscopic variability, or "?" meaning variability is suspected, but no orbit exists. Further constraints on the sample included only southern hemisphere stars, owing to long observing runs available on the 1.5-meter telescope at the Cerro Tololo Interamerican Observatory in Chile. Furthermore, a rough magnitude limit of $V = 10$ was set. With these conditions, the sample is not any sort of complete sample. It is not an exhaustive magnitude-limited sample, nor a distance-limited sample. Due to these limitations, the analysis of this sample will mainly address the unknown category and attempt to fit orbits to "SB1?" and "SB2?" systems.

1.4 Outline

Chapter 2 describes the specifics of the spectroscopic observation, data reduction, and preliminary analysis gathered from several different telescopes. Chapter 3 starts the analysis portion of the dissertation by describing the work done on constant velocity stars. Following the sequence of velocity variability introduced above, Chapter 4 discusses the SB1 systems studied during the course of this work. Results on two of the systems mentioned in Chapter 4, HD 215227 (Williams et al. 2010a), and BD+36°4063 (Williams et al. 2009) have already been published. To round out the velocity variability discussion, Chapter 5 covers SB2 systems, including the very important double-lined eclipsing systems. The systems that have already been published from Chapter 5 are HD 42401 (Williams 2009), LH 54-425 (Williams et al. 2008), and

HI Mon (Williams et al. 2011). Chapter 6 looks to the future with an analysis of light curves of intermediate-to-massive binary eclipsing systems that are likely to be found to be SB2s with spectroscopic observations. Finally, Chapter 7 summarizes the results of this effort, and expands on some of the more amusing lessons learned along the way.

– 2 –

Observations and Data Reduction

2.1 Spectroscopy

Spectra from early-type stellar systems are characterized primarily by hydrogen and helium lines in the optical region of the electromagnetic spectrum. Most of these lines exist in the 4000 to 5000 Å range, and spectral ranges for all observations in this dissertation have been chosen accordingly.

2.2 Individual Observing Runs

The data used in this dissertation come from five different telescopes. Each telescope and spectrograph result in a different wavelength range and resolution. These are summarized in Table 2.1, and individual observing setups are discussed below. The observing runs themselves are described in Table 2.2. The list of stars observed, including those awaiting further analysis, is shown in Table 2.3.

Table 2.1. Spectroscopic Observation Parameters

Telescope Name	Resolving Power $R = \lambda/\Delta\lambda$	Wavelength Coverage	Comparison Lamp
CTIO 1.5 m	2,750	4058−4732 Å	Helium-Argon
KPNO Coudé Feed[a]	13,500	4315−4490 Å	Iron-Argon
KPNO Coudé Feed[b]	11,500	4250−4570 Å	Iron-Argon
KPNO 2.1 m	3,030	3942−5032 Å	Helium-Neon-Argon
CTIO 4 m	5,400	3932−4750 Å	Helium-Neon-Argon
HIA DAO 1.8 m	4,290	4260−4669 Å	Iron-Argon

[a] T1KB CCD chip setup

[b] F3KB CCD chip setup

Table 2.2. Observing Runs

Start Date (UT)	Observatory and Telescope	Observer(s)	Number of Nights
2003 March 16	CTIO 1.5-m	M. V. McSwain	4
2004 January 13	CTIO 1.5-m	T. Hillwig	16
2004 May 27	CTIO 1.5-m	T. Hillwig	12
2006 January 12	CTIO 1.5-m	Service Observers	[a]
2008 January 9	KPNO 0.9-m	S. J. Williams	10
2008 November 15	KPNO 2.1-m	W. Huang	7
2009 December 23	CTIO 4-m	S. Caballero, S. J. Williams	5
2010 July 28	HIA DAO 1.8-m	S. J. Williams	2

[a] Service observing was done on various nights between January 17th and July 29th.

Table 2.3: Stars Observed

Object Name	Observatory and Telescope	Measurements	Analyzed	Comments
BD+36°4063	KPNO 2.1-m	7	Y	Chapter 4
BD+60°261	KPNO 2.1-m	7	Y	Chapter 3
BD−16°4826	CTIO 1.5-m	12	Y	Chapter 4
CD−38°11748	CTIO 1.5-m	11	Y	Chapter 3
CPD−26°2716	KPNO 2.1-m	7	Y	Chapter 3
CPD−35°2209	CTIO 1.5-m	14	N	No phot variation, unknown period
CPD−40°2666	CTIO 1.5-m	18	N	SB1 eclipsing
CPD−59°2629	CTIO 1.5-m	20	Y	Chapter 3
HD 10125	KPNO 2.1-m	7	Y	Chapter 3
HD 42401	KPNO 0.9-m	29	Y	Chapter 5
HD 48419	KPNO 0.9-m	31	N	Early F-type, work halted
HD 51082	KPNO 0.9-m	13	N	Early A-type, need more data?
HD 56995	CTIO 1.5-m	22	N	Eclipsing, triple?
HD 60389	KPNO 0.9-m	12	N	Early A-type, need more data?
HD 60476	KPNO 0.9-m	21	N	Eclipsing, unseen companion
HD 64315	CTIO 1.5-m	46	N	Triple system
HD 64568	CTIO 1.5-m	14	Y	Chapter 3
HD 76556	CTIO 1.5-m	16	Y	Chapter 3
HD 81389	KPNO 0.9-m	21	N	Published in AAS poster, F-type system
HD 92024	CTIO 1.5-m	32	N	β Cep system, complex spectra
HD 93250	CTIO 1.5-m	21	Y	Chapter 3
HD 96715	CTIO 1.5-m	24	Y	Chapter 3
HD 101191	CTIO 1.5-m	15	Y	Chapter 3
HD 101205	CTIO 1.5-m	22	N	Eclipsing, triple?
HD 101413	CTIO 1.5-m	14	Y	Chapter 3

Continued on next page…

Table 2.3 – Continued

Object Name	Observatory and Telescope	Measurements	Analyzed	Comments
HD 101436	CTIO 1.5-m	15	Y	Chapter 3
HD 101545 A	CTIO 1.5-m	15	Y	Chapter 3
HD 103146	CTIO 1.5-m	52	Y	Chapter 5
HD 113659	CTIO 1.5-m	23	N	Eclipsing, triple?
HD 114026	CTIO 1.5-m	30	N	Eclipsing, triple?
HD 124979	CTIO 1.5-m	12	Y	Chapter 3
HD 150135	CTIO 1.5-m	7	N	P≃183 d in literature
HD 150136	CTIO 1.5-m	33	N	Triple system
HD 152147	CTIO 1.5-m	15	Y	Chapter 4
HD 152246	CTIO 1.5-m	26	N	SB2? Line asymmetries
HD 153426	CTIO 1.5-m	16	N	SB2? Line asymmetries
HD 155775	CTIO 1.5-m	28	Y	Chapter 5
HD 158186	CTIO 1.5-m	24	N	Eclipsing, unsen companion
HD 164536	CTIO 1.5-m	16	Y	Chapter 4
HD 164794	CTIO 1.5-m	16	Y	Chapter 3
HD 164816	CTIO 1.5-m	31	N	Blending issues
HD 165246	CTIO 1.5-m	24	N	Eclipsing, triple?
HD 166734	CTIO 1.5-m	14	N	P= 34 d LC, need more data
HD 167263	CTIO 1.5-m	13	N	Previous orbit no good?
HD 167971	CTIO 1.5-m	9	N	Eclipsing, no double lines
HD 215227	HIA DAO 1.8-m	2	Y	Chapter 4
HD 228841	KPNO 2.1-m	7	Y	Chapter 3
HD 229232	KPNO 2.1-m	7	Y	Chapter 4
HD 237211	KPNO 2.1-m	7	Y	Chapter 3
HD 308813	CTIO 1.5-m	33	Y	Chapter 4
HD 344784	KPNO 2.1-m	6	Y	Chapter 4
KL CMa	KPNO 0.9-m	15	N	Need more data?

Continued on next page…

Table 2.3 – Continued

Object Name	Observatory and Telescope	Measurements	Analyzed	Comments
LH 54-425	CTIO 1.5-m	49	Y	Chapter 5
LS 1874	CTIO 1.5-m	41	N	SB2? Line asymmetries
LS 3052	CTIO 1.5-m	24	N	Eclipsing, very faint companion
LT CMa	KPNO 0.9-m	10	N	Faint companion, need more data
MP CMA	KPNO 0.9-m	8	N	Need more data
NGC 6231 SBL 314	CTIO 1.5-m	14	N	SB2? Line asymmetries
NGC 6231 SBL 521	CTIO 1.5-m	17	N	SB2? Line asymmetries

2.2.1 CTIO 1.5-m

The CTIO 1.5-m telescope was used to observe the vast majority of stars analyzed in this dissertation. All observing runs used the same setup that later became known as SMARTS Consortium 47/IIb. This setup is with a Ritchey-Chretien (RC) spectrograph and grating number 47 (831 lines per mm yielding an 8000 Å blaze wavelength in the first order Littrow configuration) in second order together with a BG39 or $CuSO_4$ order blocking filter and a slit width of $2''$. This arrangement produced spectra covering the range 4058-4732 Å with a resolving power of $R = \lambda/\Delta\lambda \approx 2750$ or resolution of 1.6 Å. These observations were wavelength calibrated with Helium-Argon comparison spectra.

The dates of observation using this setup were 2003 March 16 to 20 UT, 2004 January 13 to 29 UT and May 27 to June 8 UT, and 2006 January 17 to February 2 UT.

2.2.2 KPNO Coudé Feed

During 2008 January 9 to January 18 UT, The Kitt Peak National Observatory (KPNO) 0.9-m coudé feed telescope was used to observe HD 42401 (see section 5.2). Those spectra were obtained with the long collimator and grating A (632 grooves mm^{-1} with a blaze wavelength of 6000 Å) in second order with order-sorting filter 4-96. The first set of observations were made with the T1KB detector, a 1024×1024 pixel array with 24×24 μm^2 pixels, resulting in a resolving power of $R = \lambda/\Delta\lambda \approx 13,500$ or resolution of 0.33 Å covering 4315 to 4490 Å. The second set used the F3KB detector, a 3072×1024 pixel array with 15×15 μm^2 pixels. The wavelength coverage in this setup was from 4250 to 4570 Å with a resolving power $R = \lambda/\Delta\lambda \approx 11,500$ or 0.38 Å. An Iron-Argon comparison lamp was used for wavelength calibration for both setups.

2.2.3 KPNO 2.1-m

Objects were observed at the 2.1-m telescope at KPNO during an observing run from 2008 November 15 to 21 UT. These observations made use of the Goldcam spectrograph with grating G47 (831 grooves mm^{-1}) in second order with a $CuSO_4$ order sorting filter. The detector was the T3KC CCD, a 3072×1024 pixel array with 15×15 μm^2 pixels with the slit width set to $1\farcs3$. The resulting wavelength coverage spans 3942 to 5032 Å with a resolving power of $R = \lambda/\Delta\lambda \approx 3030$ or resolution of 1.5 Å. A Helium-Neon-Argon comparison lamp was used for wavelength calibration.

2.2.4 CTIO 4-m

The CTIO Blanco 4-m telescope was used to observe HI Mon (section 5.4) on 2009 Dec 23 through 27 UT. The RC-spectrograph was used with the G380 (1200 grooves mm^{-1}) grating in second order and blue collimator giving wavelength coverage from 3932 to 4750 Å with resolution $R = \lambda/\Delta\lambda \approx 5400$ or 0.8 Å. The same type of Helium-Neon-Argon comparison lamp that was used at the KPNO 2.1-m telescope was also used in wavelength calibration for the Blanco data.

2.2.5 HIA DAO 1.8 m

Spectra of HD 215227 (section 4.3) were obtained with the Herzberg Institute of Astrophysics Dominion Astrophysical Observatory's (HIA DAO) 1.8-m Plaskett telescope on 2010 July 28 and 29. These observations were made with the Cassegrain spectrograph with grating 1200B (12 grooves mm^{-1}) in first order. The spectra cover 4260 - 4669 Å and have a resolving power of $R = \lambda/\Delta\lambda \approx 4290$ or resolution of 1.0 Å. The detector was the SITe-2 CCD, a 1752×532 pixel array with 15×15 μm^2 pixels. An Iron-Argon comparison lamp was used for wavelength calibration.

2.3 Technique Overview

All data were reduced using the Image Reduction and Analysis Facility, known as IRAF[1]. Beginning with the raw data, bias frames and flat field frames were median combined into master images via the "zerocombine" and "flatcombine" tasks in the "ccdred" package. Next, the "ccdproc" task was used to bias subtract, flat field, and trim the images.

At this point in the data reduction process, a few header keyword values were computed to aid in data reduction and analysis later. In the "kpnocoude" package, the tasks "setjd" and "setairmass" computed the airmass and Julian date based on the midpoint of the exposure time for the particular image. The task "rvcorrect" in the "astutil" package was then used to calculate the heliocentric velocity correction. This correction is put in the header for the image and the spectrum itself is transformed according to this value later in the reduction process.

Extraction of the spectrum was performed using the "doslit" task, once again in the "kpnocoude" package. Aperture extraction was followed by wavelength calibration of the spectra using comparison lamps of varying compositions (see descriptions

---

[1] IRAF is distributed by the National Optical Astronomy Observatory, which is operated by the Association of Universities for Research in Astronomy, Inc., under cooperative agreement with the National Science Foundation.

of individual telescopes or observing runs below for the particular elements used) bracketed around the object frame. No flux calibrations were made for any of the data used in this dissertation. The goal was to end up with normalized spectra for comparison with stellar models, so flux calibrations were not deemed necessary.

Spectra obtained at the Cerro Tololo Inter-American Observatory (CTIO) 1.5-m telescope were taken in a sequence of three consecutive frames. Initially, one plan was to median combine the spectra before extraction. This could possibly pose some problems and the median combination process was ultimately dropped. Specifically, the median process will simply go pixel-by-pixel and take the median value of the three frames for that pixel. This is good in that it would eliminate possible problems like spike counts from cosmic ray events. However, taking the example that perhaps two of the sequence of three frames were affected by clouds, this would cause two images to have lower counts, and the median value would not be the highest signal-to-noise (S/N) ratio spectrum. Also, for fainter objects such as LH 54-425 in the Large Magellanic Cloud, a higher S/N can be attained by adding the three images together after extraction, and removing bad pixels after this addition. This process was done for all spectra, and necessitated adjusting header values for the final images to reflect the time averaged values of such things as heliocentric velocity correction, exposure time, heliocentric Julian date, and airmass.

The spectra were then normalized via the “continuum” task in the “kpnocoude” package. Spectra for each star were gathered and the normalization process was performed on the entire set. Stellar continuum regions of the spectra were fit with a cubic spline function of the lowest order possible resulting in a good “by-eye” fit. The exact value of the order used varies due to differences in a particular CCD chip's response to different wavelengths of light. There were no telluric features in the observed parts of the spectrum to remove.

The normalized spectra were then put into a spectrum matrix in the Interactive Data Language (IDL). In the process of making the spectrum matrix or spectrum stack, the heliocentric velocity correction was applied and the spectrum's flux was reapportioned in a logarithmic wavelength grid for ease of use with analysis programs.

The end result of the basic data reduction is a spectrum stack for a particular object and CCD chip, in which all the spectra are normalized and placed on the same log-λ wavelength grid.

– 3 –

Spectroscopically Single Stars

3.1 Introduction

In any general survey for variability, there will be objects that just do not seem to vary at all. This may be due to a real lack of variability, an object actually having a longer-term variability not seen in the data set studied, or a level of variability not detectable with the particular observing setup. In the case of a spectroscopic survey, there is still valuable information in such spectra. This chapter reports on 18 Galactic O-type stars showing small radial velocity scatter (> 20 km s^{-1}) over time scales of one to two weeks. By fitting theoretical model spectra to observed spectra, estimates are made for effective temperature, log g, rotational velocity, and average radial velocity.

3.2 Observations

The first sets of spectroscopic data were obtained with the Cerro Tololo Inter-American Observatory (CTIO) 1.5-m telescope and RC spectrograph. Exposure times were several minutes in order to reach a signal-to-noise ratio (S/N) exceeding 100 pixel^{-1} in the continuum. See Chapter 2 for the specifics on this instrument and setup. The 12 stars observed with this setup and discussed in this chapter are: HD 64568, HD 76556, HD 93250, CPD$-$59°2629, HD 96715, HD 101191, HD 101413, HD 101436, HD 101545A, HD 124979, CD$-$38° 11748, and HD 164794.

BD+60°261, HD 10125, HD 237211, CPD$-$26°2716, HD 344784, and HD 228841 were observed with the Kitt Peak National Observatory (KPNO) 2.1-m telescope.

Exposures varied in duration according to the brightness of the target, with a goal of a S/N = 200 per pixel in the continuum. Again, see Chapter 2 for the details of the setup.

3.3 Stellar Parameters and Radial Velocities

Initial inspections showed no significant velocity variations for any stars in this sample. Thus, individual spectra of each object were co-added to improve the signal-to-noise ratio and create a master spectrum for subsequent analysis.

In order to estimate stellar parameters, this combined spectrum was fit for each star with a model template by interpolating in the OSTAR2002 grid of stellar models from Lanz & Hubeny (2003) for stars with $T_{\rm eff} > 30$ kK, and the BSTAR2006 grid of stellar models from Lanz & Hubeny (2007) for stars with $T_{\rm eff} \leq 30$ kK, all with solar metallicity. Initial guesses for the effective temperature and log g were made based on spectral types from the literature and the spectral type calibration for O stars from Martins et al. (2005). An initial guess for the rotational broadening was obtained by convolving the model template with the instrumental broadening (found from the FWHM of comparison lines: 109 km s^{-1} for data from CTIO and 99.0 km s^{-1} for the KPNO data) and with a projected rotational velocity $v \sin i$ to obtain a broadening function making a rough match of one prominent absorption line.

A least squares grid search routine was employed to obtain values of $T_{\rm eff}$ and log g from fits of several spectral features (listed in the discussion for each individual object in section 3.4). In the O-type stars, spectral features from helium and silicon, for example, give information about the effective temperature and log g. However, these lines give reasonable fits in a valley along the effective temperature and log g plane. A higher $T_{\rm eff}$ and log g may in some instances be very similar to a model with lower $T_{\rm eff}$ and lower log g for a particular spectral feature. In order to resolve this degeneracy, the sensitivity of the Balmer line wings to log g can be used to pin down a unique $T_{\rm eff}$ and log g for a particular star. By omitting the core regions and only fitting the wings of at least one Balmer line in the analysis of each object, better constraints for log g via linear Stark broadening may be made.

These estimates for effective temperature and log g were then used to refine the v sin i value by comparing of the FWHM measurements of the combined spectrum with FWHM measurements from the model broadened for a range of v sin i. This process ends up performing two iterations of computing values for $T_{\rm eff}$, log g, and v sin i. The resulting values are listed in Table 3.1. Values listed for $T_{\rm eff}$ and v sin i are means of the individual measurements on specific spectral features, while the uncertainties are the line-to-line standard deviation of those measurements. For log g, a weighted average was employed where Balmer line wing fits are weighted twice as much as other line fits. The same weighting was used in estimating the uncertainty, which is the standard deviation of the individual measurements. These uncertainties are listed along with the corresponding values in Table 3.1.

In practice, values for v sin i much less than the instrumental broadening of ~ 100 km s^{-1} cannot be measured. Therefore, the v sin i values in Table 3.1 less than 120 km s^{-1}, namely those for HD 237211, HD 64568, CPD$-59^\circ 2629$, CD$-38^\circ 11748$, and HD 344784, should be taken as upper limits, and are preceded by a less than or equal to symbol. Note that CD$-38^\circ 11748$ is the odd member of the sample. There are only two absorption lines present in the spectrum, He II λ4200 and He II λ4541. One of these, and possibly both, may have emission filling the absorption, resulting in values that are not representative of the true stellar parameters.

Another limitation is that both OSTAR2002 (Lanz & Hubeny 2003) and BSTAR2006 (Lanz & Hubeny 2007) are based on plane-parallel atmosphere approximations and solar helium abundances. These approximations may be less accurate for very high luminosity stars, such as those with lower log g values in column 4 of Table 3.1, which generally have extended atmospheres and significant winds. These lower values for log g indicate a star is evolved, and such stars may have enhanced helium abundances due to mixing and mass loss. Despite these limitations, the values match reasonably well with previously published values for stellar parameters. For example, a recent study of HD 93250 was reported by Repolust et al. (2004), and the values they list are $T_{\rm eff} = 46.0$ kK, log $g = 3.95$, and v sin $i = 130$ km s^{-1}. These values agree very well, within uncertainties, with the values listed in Table 3.1. In Figure 3.1 the co-added spectrum for HD 93250 is plotted versus the best fit model, for comparison. With the values derived here for $T_{\rm eff}$ and log g, the spectral classification of each object is estimated based on the observational parameters in Tables 4, 5, and 6 of Martins et al. (2005) and listed in column 6 of Table 3.1. Figures 3.2 through 3.5 show the spectra ordered by this classification as early O-stars on the main-sequence (Fig. 3.2), late O-stars on the main-sequence (Fig. 3.3), early O-type giants (Fig. 3.4), and late O-type giants with the only O-type supergiant (Fig. 3.5).

Table 3.1. Individual Stellar Parameters

Object Name (1)	Spectral Classification (2)	$T_{\rm eff}$ (kK) (3)	log g (cm s^{-2}) (4)	v sin i (km s^{-1}) (5)	Spectral Classification From ($T_{\rm eff}$, log g)[a] (6)	$\langle V_r \rangle$ (km s^{-1}) (7)	$\sigma_{\rm I}$ (km s^{-1}) (8)	$\sigma_{\rm E}$ (km s^{-1}) (9)	N (10)	$\sigma_{\rm EC}/\sigma_{\rm I}$ (11)	Previous Status (12)	Current Status (13)
BD+60° 261	O7.5 III(n)((f))	34.7±1.2	3.60±0.16	189±17	O7.5 III	–85.0	1.5	4.6	7	0.0	U	C
HD 10125	O9.7 II	28.9±1.1	3.36±0.21	149±22	[b]	–51.8	1.6	6.8	7	3.1	U	SB1?
HD 237211	O9.5 Ib:p	29.7±0.7	3.35±0.16	≤96±12	O9.5 III	–36.8	1.6	8.8	7	4.6	U	SB1?
CPD−26° 2716	O6.5 IIIf	37.7±1.6	3.67±0.14	174±16	O6.5 III	57.8	2.3	4.4	7	0.0	U	C
HD 64568	O3 ((f*))	44.9±1.7	3.91±0.08	≤117±13	O3 V	87.1	1.5	5.7	14	2.1	SB1?	C
HD 76556	O7	36.0±1.8	3.74±0.06	240± 5	O7 III	28.2	2.6	5.2	16	0.8	SB1?	C
HD 93250	O3.5 V((f+))	45.4±2.4	3.85±0.06	132± 2	O3 V	0.2	1.6	6.2	21	2.5	C	C
CPD−59° 2629	O8.5 V	32.7±0.7	4.10±0.13	≤85± 7	O9 V	–7.4	3.7	12.8	20	3.2	U	SB1?
HD 96715	O4 V((f))	40.4±1.8	3.84±0.11	≤114±21	O5 V	–27.9	1.5	5.5	24	1.9	U	C
HD 101191	O8 V((n))	35.2±1.1	4.02±0.11	177±26	O8 V	5.0	1.5	5.1	15	1.3	C	SB1?
HD 101413	O8 V	32.3±1.3	3.75±0.26	149±17	O9 III	1.7	2.0	4.6	14	0.0	SB1?	SB2?
HD 101436	O6.5	37.3±1.2	3.96±0.05	172±21	O7 V	5.1	1.7	7.3	14	3.3	SB2?	SB2?
HD 101545 A	O9.5 Ib-II	30.8±0.4	3.60±0.23	131±19	O9.5 III	2.7	1.4	3.5	15	0.0	U	C
HD 124979	O8 ((f))	35.5±2.1	3.96±0.18	264±28	O7.5 V	–79.9	2.2	6.8	12	2.2	SB2?	C
CD−38° 11748	O4 If	:32.8±1.1	:3.92±0.11	:≤107±11	[c]	–51.0	3.4	4.3	11	1.3	U	C
HD 164794	O4 ((f))	46.1±2.8	3.97±0.11	191±17	O3 V	5.0	1.0	7.8	16	3.9	SB2?	SB2?
HD 344784	O7 III((f))	35.4±2.1	3.74±0.18	≤119±10	O7.5 III	5.5	1.6	3.6	6	0.0	U	C
HD 228841	O6.5 Vn((f))	36.9±0.9	3.99±0.19	306±30	O7 V	–57.7	2.2	3.3	7	0.0	U	C

[a] Calibration of Martins et al. (2005)

[b] Unable to estimate, too cool for the calibration of Martins et al. (2005)

[c] Unable to estimate, stellar parameters not accurate, see text

Note. — Spectral classification references: CD−38°11748: Massey et al. (2001); CPD−59°2629: Massey & Johnson (1993); BD+60°261, HD 96715, HD 101191, HD 101413, HD 101436, HD 101545, HD 164794, HD 10125, HD 228841, HD237211: Walborn (1973); HD 124979, HD 76556: MacConnell & Bidelman (1976); HD 64568, HD 93250: Walborn et al. (2002); HD 344784: Conti & Leep (1974); CPD−26°2716: Garrison et al. (1977).

Velocities for each spectrum and for each star were measured using the cross-correlation technique with uncertainties estimated as outlined in Zucker (2003). The best fit model spectrum was cross-correlated with each spectrum of the particular star's spectrum stack. Prior to cross-correlation, object dependent emission features and interstellar features were removed, including the broad diffuse interstellar band (DIB) near λ4428 Å and the 4640 Å(N III complex) for most objects (see the discussion of individual objects below). The velocities are listed in Table 3.2 with targets ordered by right ascension. Table 3.2 gives the heliocentric Julian date of observation, radial velocity, and velocity uncertainty for each measurement. The unweighted average velocity for each object is listed in column 7 of Table 3.1. The only exception to this method of determining velocities was made with CD−38°11748. As mentioned above, using the best fit model spectrum proved insufficient. Instead, the two He II lines were fit with Gaussians using the IRAF "splot" routine. These values and uncertainties are listed for CD−38°11748 in Table 3.2.

Table 3.2: Radial Velocities of Spectroscopically Single Stars

Star Name	Date HJD−2,450,000	V_r (km s^{-1})	σ (km s^{-1})
BD+60°261	4785.740	–82.2	1.4
BD+60°261	4786.733	–87.5	1.4
BD+60°261	4787.720	–83.2	1.4
BD+60°261	4788.773	–76.8	1.4
BD+60°261	4789.698	–87.8	1.7
BD+60°261	4790.710	–86.7	1.5
BD+60°261	4791.705	–90.5	1.4

Continued on next page…

Table 3.2 – Continued

Star Name	Date HJD−2,450,000	V_r (km s^{-1})	σ (km s^{-1})
HD 10125	4785.746	–57.2	1.6
HD 10125	4786.738	–48.9	1.5
HD 10125	4787.724	–57.7	1.5
HD 10125	4788.779	–46.1	1.6
HD 10125	4789.704	–40.8	1.5
HD 10125	4790.714	–58.9	1.6
HD 10125	4791.709	–53.0	1.5
HD 237211	4785.847	–44.6	1.7
HD 237211	4786.851	–40.8	1.6
HD 237211	4787.839	–44.8	1.6
HD 237211	4788.868	–36.9	1.6
HD 237211	4789.838	–41.6	1.6
HD 237211	4790.847	–24.2	1.6
HD 237211	4791.829	–24.9	1.6
CPD−26°2716	4785.993	60.5	2.1
CPD−26°2716	4786.989	55.5	2.0
CPD−26°2716	4787.994	60.3	2.0
CPD−26°2716	4788.977	54.6	2.2
CPD−26°2716	4789.969	65.1	2.2
CPD−26°2716	4790.978	56.4	2.8
CPD−26°2716	4791.957	52.2	2.4
HD 64568	3017.638	96.1	1.0
HD 64568	3019.595	85.2	1.1
HD 64568	3020.581	93.9	2.2
HD 64568	3021.574	88.1	1.1
HD 64568	3022.573	92.9	1.1
HD 64568	3023.564	92.8	1.0
HD 64568	3027.575	86.3	1.1
HD 64568	3028.570	85.5	3.5
HD 64568	3029.569	89.8	2.1
HD 64568	3030.569	80.9	1.3
HD 64568	3031.665	76.9	1.4
HD 64568	3032.653	82.7	1.1
HD 64568	3032.800	88.0	1.1
HD 64568	3033.677	80.2	1.1
HD 76556	3018.639	28.3	2.6
HD 76556	3019.643	29.6	2.5
HD 76556	3020.623	14.5	2.7
HD 76556	3020.873	28.0	2.6
HD 76556	3021.620	29.0	2.4

Continued on next page. . .

Table 3.2 – Continued

Star Name	Date HJD−2,450,000	V_r (km s^{-1})	σ (km s^{-1})
HD 76556	3022.619	22.1	2.9
HD 76556	3023.611	32.2	2.5
HD 76556	3023.870	29.6	2.5
HD 76556	3027.621	38.3	2.6
HD 76556	3028.616	24.6	2.7
HD 76556	3029.646	25.6	2.9
HD 76556	3030.615	26.5	2.6
HD 76556	3030.807	28.2	2.5
HD 76556	3031.677	29.5	2.6
HD 76556	3032.665	33.6	3.0
HD 76556	3033.666	31.0	2.6
HD 93250	3017.687	1.4	1.4
HD 93250	3018.703	3.2	1.4
HD 93250	3018.805	9.1	1.5
HD 93250	3019.689	–7.1	2.2
HD 93250	3020.672	–10.9	1.4
HD 93250	3020.778	1.2	1.4
HD 93250	3021.667	1.5	1.4
HD 93250	3022.676	6.6	2.8
HD 93250	3022.772	10.3	1.4
HD 93250	3023.650	–4.4	1.4
HD 93250	3027.669	1.3	2.5
HD 93250	3027.778	7.2	1.5
HD 93250	3028.667	–0.4	1.3
HD 93250	3029.699	1.2	1.4
HD 93250	3029.779	2.7	1.4
HD 93250	3030.657	–2.3	1.4
HD 93250	3031.610	2.3	1.6
HD 93250	3031.757	1.0	1.6
HD 93250	3032.693	–12.7	1.5
HD 93250	3033.614	–9.9	1.5
HD 93250	3033.774	3.0	1.5
CPD−59°2629	3017.712	3.6	2.8
CPD−59°2629	3018.723	–6.9	2.8
CPD−59°2629	3019.705	12.2	11.2
CPD−59°2629	3019.820	8.9	9.4
CPD−59°2629	3020.688	–0.5	3.1
CPD−59°2629	3021.683	–20.5	3.0
CPD−59°2629	3021.800	–5.1	2.9
CPD−59°2629	3022.692	–6.7	2.8

Continued on next page. . .

Table 3.2 – Continued

Star Name	Date HJD−2,450,000	V_r (km s^{-1})	σ (km s^{-1})
CPD−59°2629	3023.672	–7.5	3.0
CPD−59°2629	3023.789	–9.1	3.0
CPD−59°2629	3027.696	–14.7	3.1
CPD−59°2629	3028.674	–26.0	3.0
CPD−59°2629	3028.771	–1.7	3.0
CPD−59°2629	3029.714	–3.2	2.9
CPD−59°2629	3030.664	–3.3	2.8
CPD−59°2629	3030.760	–2.3	2.7
CPD−59°2629	3031.696	–41.1	3.1
CPD−59°2629	3032.616	–9.3	2.8
CPD−59°2629	3032.766	–22.3	2.9
CPD−59°2629	3033.697	8.4	3.0
HD 96715	3152.485	–35.8	1.4
HD 96715	3152.651	–27.5	1.4
HD 96715	3153.487	–28.2	1.5
HD 96715	3153.679	–34.6	1.5
HD 96715	3154.501	–12.8	1.5
HD 96715	3154.668	–27.6	1.5
HD 96715	3155.492	–22.0	1.6
HD 96715	3156.476	–26.9	1.4
HD 96715	3156.659	–31.1	2.3
HD 96715	3158.507	–32.9	1.4
HD 96715	3159.519	–21.9	1.6
HD 96715	3160.598	–27.1	1.8
HD 96715	3161.557	–29.7	1.6
HD 96715	3162.548	–20.7	1.5
HD 96715	3163.455	–32.1	1.4
HD 96715	3164.498	–18.7	1.5
HD 96715	3752.757	–34.8	1.4
HD 96715	3758.826	–31.2	1.5
HD 96715	3759.829	–32.4	1.6
HD 96715	3762.674	–26.0	1.4
HD 96715	3763.765	–31.7	1.3
HD 96715	3765.774	–26.8	1.4
HD 96715	3767.811	–29.7	1.4
HD 96715	3768.817	–28.0	1.4
HD 101191	3152.494	5.4	1.4
HD 101191	3152.661	–8.4	1.5
HD 101191	3153.463	2.4	1.5
HD 101191	3154.510	5.8	1.4

Continued on next page. . .

Table 3.2 – Continued

Star Name	Date HJD−2,450,000	V_r (km s^{-1})	σ (km s^{-1})
HD 101191	3155.502	5.5	1.4
HD 101191	3156.512	8.7	1.4
HD 101191	3158.486	9.2	1.5
HD 101191	3159.458	3.3	1.4
HD 101191	3159.646	10.2	1.5
HD 101191	3160.633	8.8	1.4
HD 101191	3161.478	0.6	1.5
HD 101191	3161.640	9.3	1.6
HD 101191	3162.446	–0.8	1.5
HD 101191	3162.635	10.1	1.5
HD 101191	3164.519	5.8	1.4
HD 101413	3152.672	–3.3	2.6
HD 101413	3153.496	2.6	1.7
HD 101413	3154.490	–2.5	1.8
HD 101413	3154.650	0.1	1.9
HD 101413	3155.464	6.7	1.8
HD 101413	3156.466	4.2	1.7
HD 101413	3156.677	4.0	2.7
HD 101413	3158.497	3.0	1.7
HD 101413	3159.530	7.7	1.7
HD 101413	3160.643	0.6	2.5
HD 101413	3161.578	–5.5	1.8
HD 101413	3162.457	7.4	1.8
HD 101413	3162.645	–6.3	2.2
HD 101413	3164.554	5.1	1.7
HD 101436	3152.516	1.3	1.5
HD 101436	3152.682	–10.0	2.0
HD 101436	3153.507	19.2	1.5
HD 101436	3154.520	5.0	1.5
HD 101436	3155.516	9.2	1.6
HD 101436	3156.522	10.6	1.6
HD 101436	3158.449	3.9	1.5
HD 101436	3158.590	–3.0	1.6
HD 101436	3159.566	5.9	1.6
HD 101436	3160.653	–0.6	1.8
HD 101436	3161.489	10.6	1.7
HD 101436	3161.651	10.0	2.8
HD 101436	3162.585	9.7	1.6
HD 101436	3164.454	0.0	1.6
HD 101545 A	3152.526	3.6	1.4

Continued on next page. . .

Table 3.2 – Continued

Star Name	Date HJD−2,450,000	V_r (km s^{-1})	σ (km s^{-1})
HD 101545 A	3152.691	–3.9	1.4
HD 101545 A	3153.515	8.9	1.5
HD 101545 A	3154.529	1.0	1.3
HD 101545 A	3155.527	3.1	1.4
HD 101545 A	3156.531	1.4	1.4
HD 101545 A	3158.457	1.8	1.4
HD 101545 A	3158.599	–3.8	1.4
HD 101545 A	3159.667	5.4	1.7
HD 101545 A	3160.456	3.4	1.4
HD 101545 A	3160.661	7.0	1.5
HD 101545 A	3161.588	4.6	1.4
HD 101545 A	3162.594	0.9	1.4
HD 101545 A	3163.500	1.6	1.4
HD 101545 A	3164.508	5.4	1.4
HD 124979	3152.641	–80.8	2.0
HD 124979	3153.725	–79.4	2.1
HD 124979	3154.711	–80.9	1.9
HD 124979	3155.618	–86.0	2.0
HD 124979	3156.722	–64.0	3.6
HD 124979	3158.643	–75.7	2.1
HD 124979	3159.676	–74.0	2.1
HD 124979	3160.480	–89.1	2.2
HD 124979	3160.703	–88.8	2.1
HD 124979	3161.720	–80.0	2.1
HD 124979	3162.675	–80.7	2.1
HD 124979	3164.579	–79.7	2.0
CD−38°11748	3152.818	–44.1	3.1
CD−38°11748	3153.740	–43.0	4.8
CD−38°11748	3154.617	–44.7	3.1
CD−38°11748	3154.877	–53.0	3.9
CD−38°11748	3158.779	–49.0	3.2
CD−38°11748	3159.763	–49.2	2.7
CD−38°11748	3160.756	–51.5	4.2
CD−38°11748	3161.824	–51.4	3.6
CD−38°11748	3162.820	–55.9	3.5
CD−38°11748	3163.762	–52.8	3.0
CD−38°11748	3164.714	–65.7	2.7
HD 164794	3152.761	12.0	0.9
HD 164794	3152.944	–5.9	0.9
HD 164794	3153.785	–0.4	0.9

Continued on next page. . .

Table 3.2 – Continued

Star Name	Date HJD$-$2,450,000	V_r (km s^{-1})	σ (km s^{-1})
HD 164794	3154.788	–1.8	1.0
HD 164794	3155.728	13.6	1.0
HD 164794	3156.808	10.7	0.9
HD 164794	3157.817	14.8	0.9
HD 164794	3158.657	11.8	1.0
HD 164794	3158.884	–4.9	1.0
HD 164794	3159.780	0.4	0.9
HD 164794	3160.781	14.8	1.0
HD 164794	3161.849	10.9	0.9
HD 164794	3162.854	9.1	1.0
HD 164794	3163.786	–4.6	0.9
HD 164794	3164.759	–0.6	0.9
HD 164794	3164.877	–0.1	1.0
HD 344784	4786.566	1.4	1.7
HD 344784	4787.549	7.9	1.6
HD 344784	4788.548	5.4	1.6
HD 344784	4789.559	8.6	1.6
HD 344784	4790.546	8.7	1.5
HD 344784	4791.551	1.0	1.6
HD 228841	4785.643	–61.5	2.3
HD 228841	4786.587	–58.8	2.3
HD 228841	4787.570	–58.8	2.3
HD 228841	4788.570	–55.6	2.2
HD 228841	4789.577	–51.4	2.2
HD 228841	4790.565	–58.9	2.2
HD 228841	4791.569	–58.9	2.0

To demonstrate the lack of radial velocity variability during the span of observations, two statistics were calculated. The "internal" uncertainty, $\sigma_{\rm I}$ in Table 3.1, is the average of the uncertainties of individual measurements listed in Table 3.2. This gives an idea of the measurement errors from the data set as a whole. The "external" uncertainty, $\sigma_{\rm E}$ in Table 3.1, is the standard deviation of the velocity measurements. This value characterizes the spectrum-to-spectrum variations of the data set. Part of this variability is due to measurement uncertainty (mainly related to the wavelength

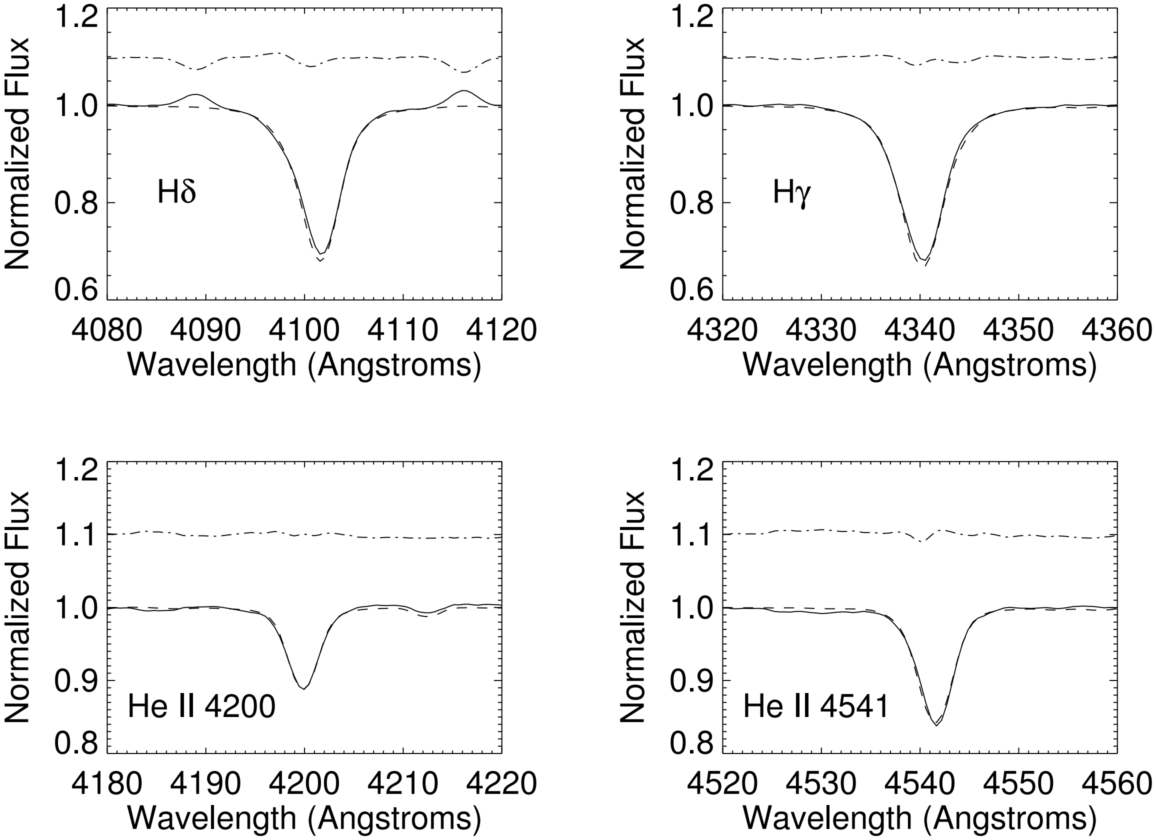

Figure 3.1 Comparison of the co-added spectrum of HD 93250 (solid line) against the derived best fit model (dotted line) given in Table 3.1 for four spectral features. Plotted above these is the residual (observed minus calculated) for each fit.

calibration and spectral resolving power) and part to any stellar variability. There are many cases of pairs of observations from a single night where the temporal variations due to any orbital motion are probably minimal, and these pairs were used to estimate that the basic measurement uncertainty from the wavelength calibration process is $\sigma_\lambda = 4.7$ km s^{-1} (for the 1.5-m CTIO spectra; this is also adopted for the similar resolution 2.1-m KPNO spectra). Then, the excess external scatter due to stellar variability may be estimated by $\sigma^2_{\rm EC} = \sigma^2_{\rm E} - \sigma^2_\lambda$, and the ratio $\sigma_{\rm EC}/\sigma_{\rm I}$ is listed in column 11 of Table 3.1. Only five of the stars in this sample have $\sigma_{\rm EC}/\sigma_{\rm I} > 3$ (HD

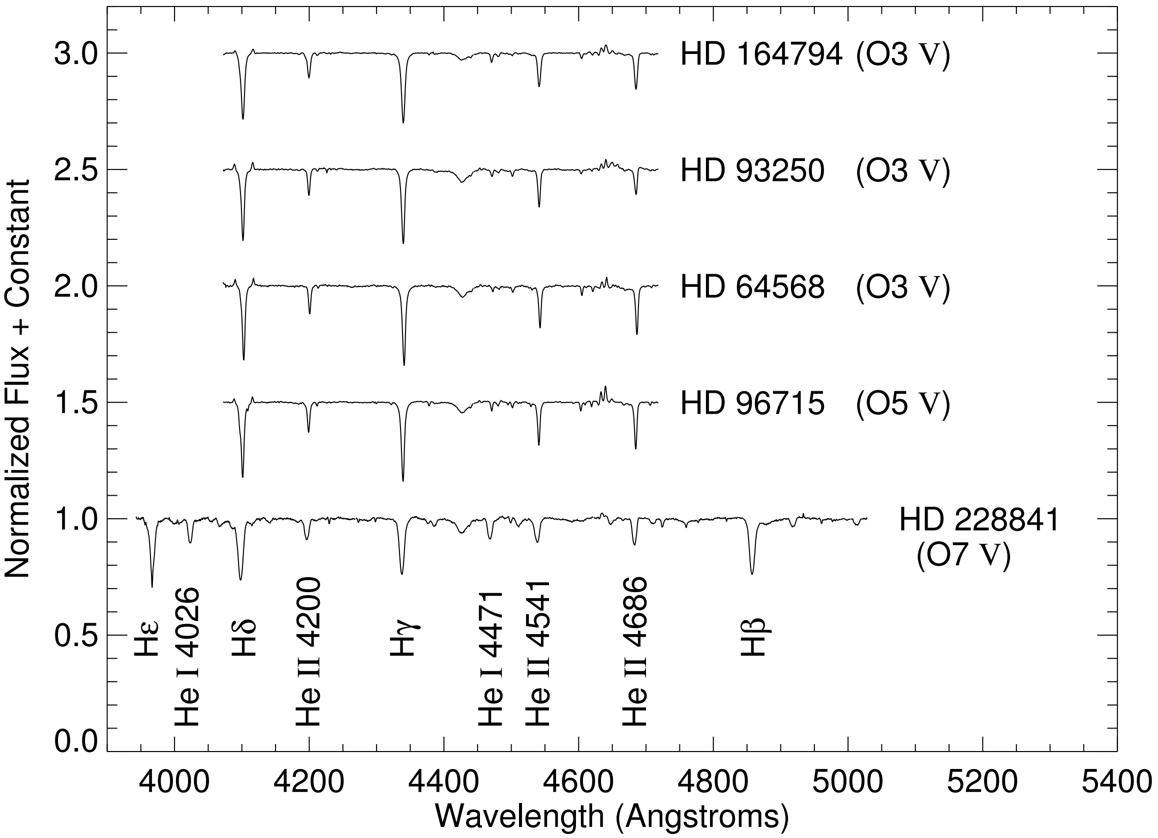

Figure 3.2 Spectra and prominent spectral features for the early O-type main sequence objects with constant velocity.

10125, HD 237211, CPD−59°2629, HD 101191, and HD 164794), and in these cases some stellar variability may be present.

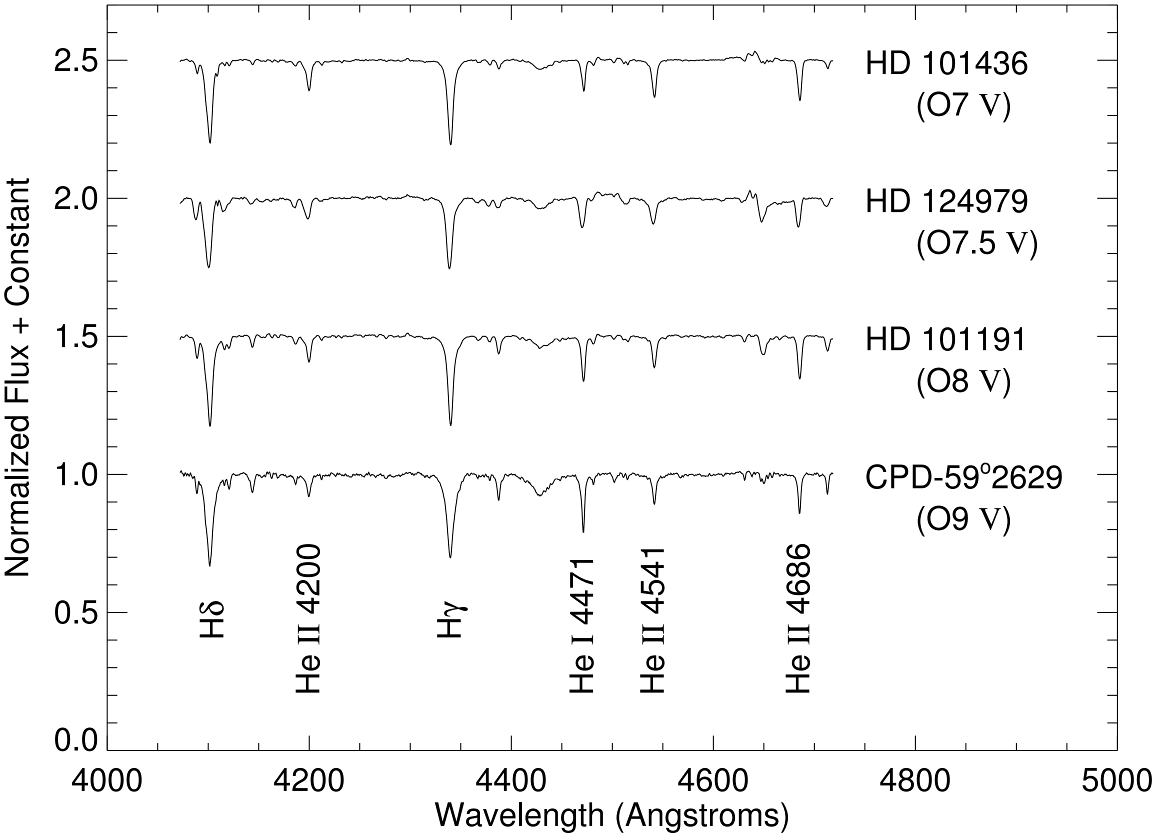

Figure 3.3 Spectra and prominent spectral features for the late O-type main sequence objects with constant velocity.

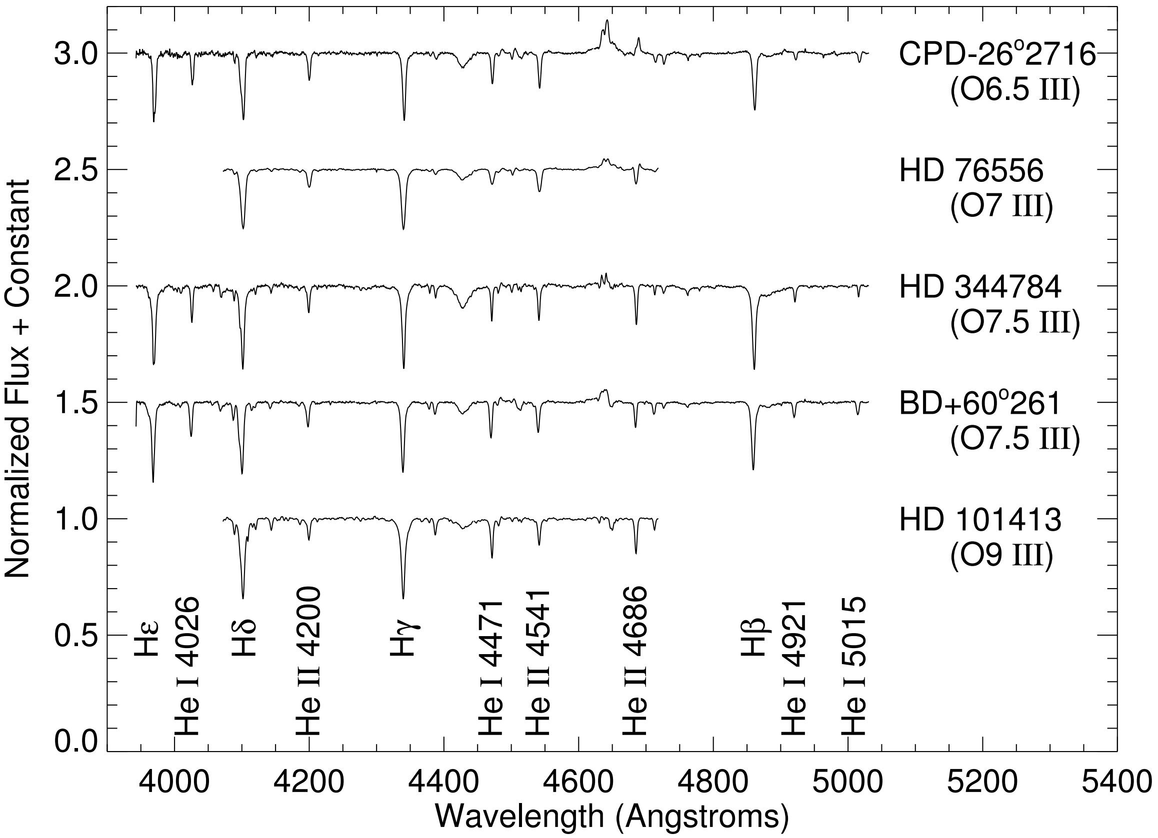

Figure 3.4 Spectra and prominent spectral features for the O-type giant objects with constant velocity.

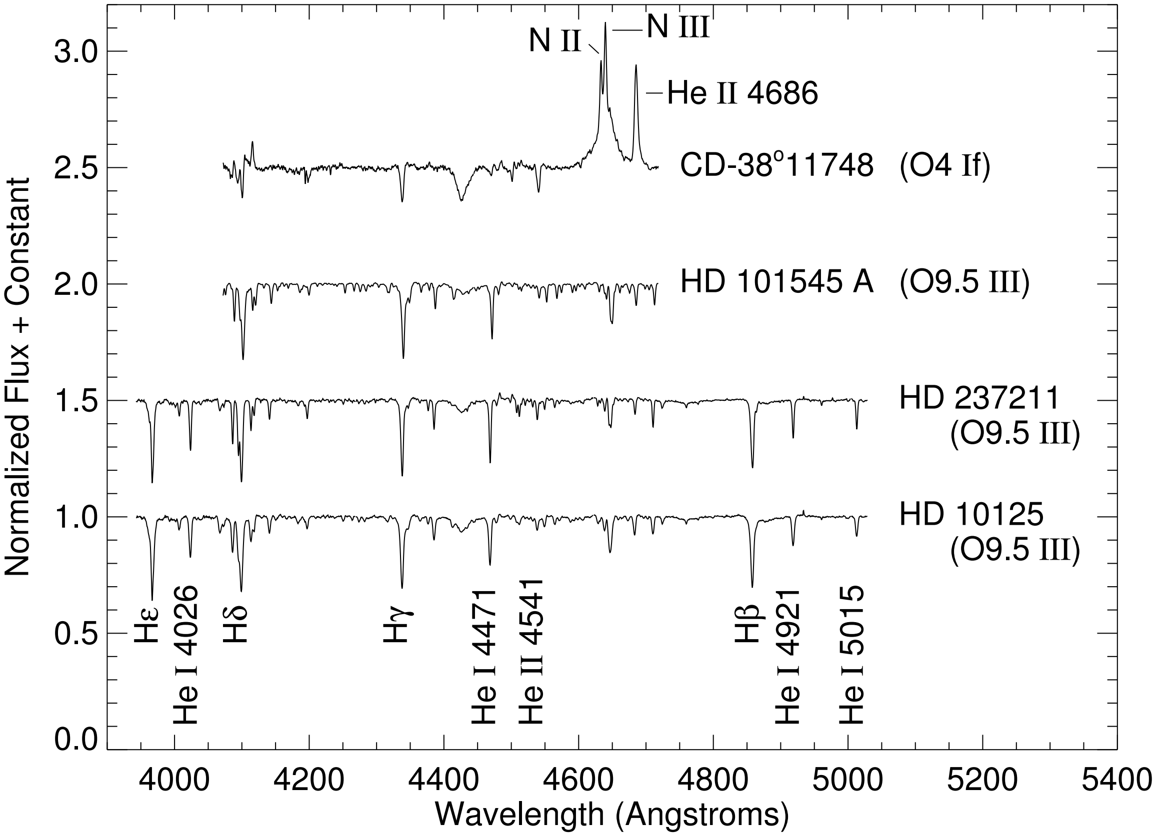

Figure 3.5 Spectra and prominent spectral features for the O-type supergiant CD−38°11748 and late O-type giants (log $g < 3.5$) with constant velocity.

3.4 Discussion of Individual Objects

3.4.1 BD+60°261 (ALS 6616)

The spectral classification of this star was originally done by Morgan et al. (1955) who found the star to be an O7. A more modern spectral classification is given by Walborn (1973), O7.5 III(n)((f)). To estimate $T_{\rm eff}$ and log g, He I λ4026, He II $\lambda\lambda4200, 4541$, and the wings of the Balmer lines Hγ λ4340 and Hϵ λ3970 were fit. The projected rotational velocity was computed using the helium lines, including He I λ4471. The literature value for $\langle V_r \rangle$ is –95 ± 10 km s^{-1} (McCuskey et al. 1974) and agrees within the uncertainties with the value computed here of –85.0 ± 4.6 km s^{-1}.

3.4.2 HD 10125

Lines used in the determination of effective temperature and log g were He I $\lambda\lambda4026, 4387, 4921$ and the wings of Hϵ λ3970 and Hγ λ4340. For the v sin i measurement, He I $\lambda\lambda4026, 4387, 4471, 4921, 5015$ and Si IV λ4088 were used. Three measures of the velocity of this star by Petrie & Pearce (1961) show $\langle V_r \rangle$ = –38 km s^{-1}. This is about 2σ different from the average reported here of –51.8±6.8 km s^{-1}. The value computed for $\sigma_{\rm EC}/\sigma_{\rm I}$, listed in column 11 of Table 3.1 is over 3, so the star is listed as a possible velocity variable candidate, "SB1?" in column 13 of Table 3.1. The velocity variations listed in Table 3.2 do not display any obvious periodicity. The star is evolved, so these velocity variations may be atmospheric in nature (Garmany et al. 1980), and not due to binary orbital motion.

3.4.3 HD 237211 (BD +56°873)

This star has had no previous velocity measurements. Temperature and log g were estimated by fits to the He I $\lambda\lambda4026, 4387, 4921$ lines and also the wings of Hϵ $\lambda3970$ and Hγ $\lambda4340$. The projected rotational velocity was estimated using He I $\lambda4026, 4387, 5015$ and Si IV $\lambda4088$. HD 237211 has the largest value of $\sigma_{\rm EC}/\sigma_{\rm I}$ (4.6) in column 11 of Table 3.1, so it may be a velocity variable. Of particular interest are the last two velocity measurements that may indicate periodic changes on timescales longer than that covered by these data. Therefore, the star is listed as a possible single-lined spectroscopic binary candidate "SB1?" in column 13 of Table 3.1.

3.4.4 CPD−26°2716 (LS 840)

This star has also been identified by Maíz-Apellániz et al. (2004) with its Tycho reference TYC 6561-960-1. The He II $\lambda\lambda4200, 4541$ lines and the wings of Hγ $\lambda4340$ were used to estimate the effective temperature and log g. The same He II lines and also He I $\lambda\lambda4026, 4471$ were used to derive the projected rotational velocity. No measurements for radial velocity appear in the literature for this object.

3.4.5 HD 64568

Estimates of the effective temperature and log g were made from fits to the He II $\lambda\lambda$4200, 4541 lines along with the Balmer Hδ $\lambda4101$ and Hγ $\lambda4340$ wings. The projected rotational velocity estimate comes from measures of the same He II lines with the addition of the He II $\lambda4686$ line. The emission complex around 4640 Å was again removed before the velocity analysis was performed. The value for $\langle V_r \rangle$ of 87.1

± 5.7 km s^{-1} agrees reasonably well with previous results from Crampton (1972) who found $\langle V_r \rangle = 77 \pm 4$ km s^{-1} from four measurements and from Solivella & Niemela (1986) who find a range between 50 and 100 km s^{-1}. All these measures do not match well with the single measurement from the Radial Velocity Experiment (RAVE) of 151.2 ± 33.7 km s^{-1} (Zwitter et al. 2008). This is not unexpected, as their technique for measuring both stellar parameters and velocities relies on metal lines near the Ca-triplet region, a region that is dominated by broad hydrogen lines for stars hotter than ∼9000 K. Zwitter et al. (2008) also use model atmospheres based on Kurucz models from Munari et al. (2005).

3.4.6 HD 76556

Lines used in the temperature and log g analysis were the Hδ and Hγ wings, He I λ4471, and the He II $\lambda\lambda$4200, 4541 lines. Only the He II lines were used to estimate the projected rotational velocity. Crampton (1972) reports on five velocity measurements that give $\langle V_r \rangle = 0 \pm 12$ km s^{-1} and claims that the star is variable. One observation from the data set is +34 km s^{-1}, close to the value average measured here of 28.2 ± 5.2 km s^{-1}. The observations are over four months, while those reported here are over 15 days. Unfortunately, there are no other observations over such a long time scale. The ratio of $\sigma_{\rm EC}/\sigma_{\rm I}$ is small, and thus velocity variation is not confirmed in this data set.

3.4.7 HD 93250

Si IV$\lambda\lambda 4088, 4116$ emission is prevalent in Figure 3.1. Model spectra were fit to the nearby Hδ wings as well as the Hγ wings, and the He II $\lambda\lambda 4200, 4541$ lines to estimate the temperature and log g. The same He II lines were used in the estimate of the projected rotational velocity. As was mentioned above, the values derived in this study for the stellar parameters (temperature, log g, and rotational velocity) match well with the recent work of Repolust et al. (2004). Thackeray et al. (1973) obtained five spectra of HD 93250 and found large internal scatter among their measurements. They attribute this scatter to the possibility that the star is a double-lined binary system. There is no evidence for double-lines in the 21 spectra over 16 days studied here, but there is modest internal scatter even on observations taken on the same night, as is evidenced in the large value (6.2 km s^{-1}) in Table 3.1 for the "external" scatter. Buscombe & Kennedy (1969) report on one velocity measurement in their table containing "stars with variable velocities or incomplete observations," but no further information is given. Levato et al. (1991) report on nine measurements that led them to conclude that the star has constant velocity within uncertainties. Their mean of –24.0±1.1 km s^{-1} is lower than that derived here (0.2±6.2 km s^{-1}), which may be due to differences in the line sample.

3.4.8 CPD–59°2629

This object is a member of the cluster Trumpler 16 and is identified as star number 22 by Carraro et al. (2004) and MJ 496 in Massey & Johnson (1993). The best-fitting model based on temperature and log g was derived using the wings of Hδ, the He I

$\lambda\lambda 4387, 4471$ lines and He II $\lambda\lambda 4541, 4686$ lines. The He I $\lambda 4471$ and He II $\lambda 4686$ lines were used to estimate the projected rotational velocity which is listed in column 5 of Table 3.1 is likely an upper limit. Several regions were omitted during velocity analysis, keeping only regions around Hγ, He I $\lambda\lambda 4387, 4471, 4713$ and He II $\lambda\lambda 4541, 4686$. Even omitting several regions, the "internal" and "external" uncertainties for this star are the highest of any object in this constant velocity star sample. In addition, the ratio of $\sigma_{\rm EC}/\sigma_{\rm I} = 3.2$ exceeds three, so this object is listed as "SB1?" in Table 3.1.

3.4.9 HD 96715

The wings of Hδ and Hγ, He I $\lambda 4471$, and He II $\lambda\lambda 4541, 4686$ were used to estimate temperature and log g. The projected rotational velocity was derived from fits to the two He II lines. The value listed in column 5 of Table 3.1 of 114 ± 21 km s^{-1} should be taken as an upper limit. Other measurements of the rotational velocity for HD 96715 are all from *International Ultraviolet Explorer* (*IUE*) spectra and are systematically lower. These measurements include values reported by Penny (1996), 88 km s^{-1}, Howarth et al. (1997), 76 km s^{-1}, Bouret et al. (2005), 80 km s^{-1}, and Penny & Gies (2009), 75 and 96 km s^{-1}. Bouret et al. (2005) estimate effective temperature and log g values from fits to UV spectral features with stellar model templates. Their values for effective temperature, 43.5 ± 2.2 kK, and log g, 4.0 ± 0.1, agree within uncertainties with values derived here of 40.4 ± 1.8 kK and 3.84 ± 0.11. No previous velocity measurements are found in the literature.

3.4.10 HD 101191

This star is a member of the association IC 2944 (Ardeberg & Maurice 1977). There is some confusion about this star in the literature. Balona (1992) claims that HD 101191 is an eclipsing binary with an orbital period of 1.042 d with a Strömgren b value of $\sim$ 6.56 mag out of eclipse. However, a later study by Kaltcheva & Georgiev (1994) gives $b = 8.618$. The photometric compilation of Hauck & Mermilliod (1998) reports $b = 6.586$ for the nearby variable star V871 Cen at 1.4 arcmin away. This appears to be just a simple mis-identification. Lines used in model fitting included the wings of Hδ and Hγ, He I $\lambda4471, 4713$ and He II $\lambda\lambda4541, 4686$. The lines He I $\lambda\lambda4387, 4471, 4713$ and He II $\lambda4686$ were used in deriving the value listed in Table 3.1 for projected rotational velocity. Thackeray & Wesselink (1965) measured three velocities between 1956 and 1958 that are consistent with the results from the 12-day time span of the data analyzed here. However, Sana et al. (2011) recently presented evidence that the system may display variations with a range of 30 km s^{-1} on a timescale of a few years. Therefore, HD 101191 is listed as a possible long-period binary.

3.4.11 HD 101413

The Hδ wings, He I $\lambda4471$, and He I $\lambda4541$ lines were used to derive temperature and log g. Thackeray & Wesselink (1965) concluded that the velocity was variable because their three measurements span the range from -81 to $+17$ km s^{-1}. Stickland & Lloyd (2001) added two more measurements from *IUE* spectra, 11.7 and -7.2 km s^{-1}, that are comparable to results presented here. On the other hand, Sana et al. (2011) obtained 10 high-dispersion spectra between 2005 and 2008 that appear to indicate a long-period variation of 3 to 6 months. Furthermore, they found evidence of a companion spectrum at the velocity extremum that suggests a B2-3 V classification. Therefore, although spectra here do not show evidence for variation, the star is listed as a possible variable. It is likely that the spectra in this dissertation simply lack the resolution to detect this variability. Only the He I $\lambda 4471$ and He II $\lambda 4686$ lines were used to derive the rotational velocity. Projected rotational velocity measurements from the literature have varied somewhat. Three efforts looking at archival *IUE* spectra were self consistent, with Penny (1996) deriving 102 km s^{-1}, while Howarth et al. (1997) give 98 km s^{-1} and Stickland & Lloyd (2001) list 98 km s^{-1}. Data from optical sources, namely the value derived here of 149 ± 17 km s^{-1}, the value from Conti & Ebbets (1977) of 140 km s^{-1}, and the reported value of 136 ± 17 km s^{-1} from Daflon et al. (2007) are systematically higher than the IUE data, but are consistent with each other.

3.4.12 HD 101436

The lines used to derive the temperature and log g were the wings of Hδ, He I $\lambda 4471$, He II $\lambda\lambda 4200, 4541, 4686$. Only the helium lines were used to estimate the projected rotational velocity. The value derived here of $\langle V_r \rangle = 5.1 \pm 7.3$ km s^{-1} agrees with the value of –3 km s^{-1} from five plates from Thackeray & Wesselink (1965). Rotational velocity measurements, like those for HD 101413, vary in the literature. The value derived here of 172 ± 21 km s^{-1} is about 1.7σ different than the *IUE* measurement in Penny (1996) of 138 km s^{-1} and is at odds with with the optical spectra presented in Conti & Ebbets (1977) giving a value of 270 km s^{-1}. The value given in Howarth et al. (1997) of 98 km s^{-1} is listed as being the mean value of two spectra. In a more recent study, Daflon et al. (2007) list a value of 76 km s^{-1} from their higher resolution spectra, noting that the line profiles are asymmetric. Penny (1996) mentions that the difference between the optical and IUE measurements may be the result of a binary system that is unresolved. The resolution of the spectra presented here would then also be insufficient to discern this possibility. For HD 101436, $\sigma_{\mathrm{EC}}/\sigma_{\mathrm{I}} = 3.3$, indicating possible velocity variability. This may be an indication of either an unresolved, low-amplitude short-period spectroscopic binary, or a long-period spectroscopic binary. The latter conclusion is supported by new observations from Sana et al. (2011), who argue that the system consists of two hot components in a 37-d period.

3.4.13 HD 101545A

Lines used to obtain the temperature and log g were He I $\lambda\lambda 4143, 4471$, Si IV $\lambda 4088$, and the wings of Hδ and Hγ. The $\langle V_r \rangle$ value from Thackeray & Wesselink (1965) of –5.3 km s^{-1} is 2.3σ different than this study's value of 2.7 ± 3.6 km s^{-1}. Sana et al. (2011) present seven new measurements and they also conclude that the star has a constant radial velocity. For the rotational velocity measurement the same lines were used excluding Si IV and adding He II $\lambda 4686$ and He I $\lambda 4387$. Previous measurements of rotational velocity are from *IUE* reported by Penny (1996), 71 km s^{-1}, and by Howarth et al. (1997), 78 km s^{-1}. These values marginally agree within 3σ with the value derived here of 131 ± 19 km s^{-1}, but the results may differ because of some amount of flux included from the nearby companion at a separation of $2\farcs54$ (Mason et al. 2009) and because of the instrumental broadening of the data analyzed here.

3.4.14 HD 124979

The lines used here for deriving the best fit model were He I $\lambda\lambda4471, 4713$, He II $\lambda\lambda4200, 4541$, and the wings of Hγ. For the velocity analysis, the emission complex just redward of Mg II $\lambda4481$ was removed, as was the emission complex around 4640 Å. Previous velocity measurements include four measurements made at the Radcliffe Observatory that give $\langle V_r \rangle$ = –68 km s^{-1} (Feast et al. 1957) and three measures resulting in $\langle V_r \rangle$ = –95 ± 10 km s^{-1} reported by Kilkenny & Hill (1975). The value measured here of $\langle V_r \rangle$ = –79.9 ± 6.8 km s^{-1} is intermediate to these two measurements. The rotational velocity was estimated from the helium lines used to estimate the temperature and log g. Two measurements of *IUE* spectra resulted in rotational velocity measurements of 232 km s^{-1} (Penny 1996) and 220 km s^{-1} (Howarth et al. 1997). These measurements agree within 1.6σ with this study's value of 264 ± 28 km s^{-1}.

3.4.15 CD–38°11748 (LSS 4067)

There is very strong emission of N III $\lambda\lambda4634, 4640$ as well as He II $\lambda4686$ as can be seen in Figure 3.5. Hydrogen Balmer lines also exhibit emission features, leaving only He II $\lambda4541$ and a very weak He II $\lambda4200$ available for measurement. The best match was found with a model template of $T_{\rm eff}$ = 32.8 kK and log g = 3.92. This model is too cool and has too high a log g according to the calibration of Martins et al. (2005) to match the lines of a star with a spectral classification of O4 If (Massey et al. 2001). Given the unusual nature of the spectrum, the stellar parameters and velocities should be viewed with caution. The velocities were measured by fitting

Gaussians to the two prominent absorption spectral features and averaging them, as mentioned above.

3.4.16 HD 164794 (9 Sgr)

Lines used to obtain the best fit model were the wings of Hδ and Hγ and the lines He II $\lambda\lambda 4200, 4541, 4686$. The rotational velocity was derived by fits to the He II lines listed above. There has been extensive radial velocity study in the literature. Perhaps the clearest picture of this system was shown by Rauw et al. (2005). They showed from high-resolution spectra obtained over several years, including one high-resolution spectrum from Fullerton (1990), that the system is likely a double-lined spectroscopic binary with an eight to nine year orbital period. Therefore, the measurements here and in the literature are made on a composite spectrum. Based on the evidence in the literature and the value derived here for $\sigma_{\mathrm{EC}}/\sigma_{\mathrm{I}} = 3.9$, Table 3.1 lists this system is an "SB2?", meaning there is no published orbit as of this work.

3.4.17 HD 344784 (BD+22°3782)

The following lines were used to estimate temperature and log g: He I $\lambda\lambda 4026, 4471$, He II $\lambda\lambda 4200, 4541, 4686$, and the wings of H$\gamma$ and Hδ. The rotational velocity was derived from measurements made on the He I $\lambda\lambda 4026, 4471$ lines and the He II $\lambda\lambda 4200, 4541$ lines. Daflon et al. (2007) measured the rotational velocity of BD+22 3782 using the equivalent widths of weak metal lines and He I $\lambda\lambda 4026, 4387, 4471$ and obtained 25 ± 2 km s^{-1} from the metal lines and 27 ± 5 km s^{-1} from the helium lines. As mentioned above, the value derived here of 119 ± 10 km s^{-1} is an upper limit, owing to the instrumental broadening of ∼100 km s^{-1}. If the star is a very sharp-lined object, as indicated by the Daflon et al. (2007) $v \sin i$ measurements, then the data analyzed here simply do not show that. For velocity analysis, the emission complex around 4640 and the red wing of Hβ were removed. Popper (1944) reports two velocity measurements yielding an average of 20 km s^{-1} and Conti et al. (1977) give one measurement of 10.2±2.1 km s^{-1}. These are a bit higher than the value of $\langle V_r \rangle$ of 5.5 ± 3.6 km s^{-1} derived here.

3.4.18 HD 228841

Lines used to derive the temperature and log g were He I $\lambda\lambda4026, 4471$, He II $\lambda\lambda4200, 4541, 4686$, and the wings of H$\gamma$ and Hδ. The same lines were used for the rotational velocity (excluding the Balmer lines) and a value of $v \sin i = 306 \pm 36$ km s^{-1} was derived. For the velocity analysis, both the emission complex around 4640 Å and the red wing of Hβ were removed. The velocities reported here appear to be the first published for this target.

3.5 Summary

Each star's previous status concerning spectroscopic variability is summarized in column 12 of Table 3.1. The same nomenclature is adopted as that of Table 4 of Mason et al. (2009), where "C" represents constant, "U" stands for an object with unknown spectroscopic variability, "SB1?" means single-lined spectroscopic variations, but no orbit, and "SB2?" means double-lined spectroscopic variations, but no orbit. The final analysis of each object's variability is given in column 13 of Table 3.1. It should be noted that not all of these stars are single, but they are velocity constant within the timescales and resolution of the data analyzed here. HD 101436 (Sana et al. 2011) and HD 164794 (Rauw et al. 2005) are seen to exhibit two sets of spectral features with higher resolution data. Other potential binaries that require more observations based on the $\sigma_{\rm EC}/\sigma_{\rm I}$ statisticare HD 101191 and HD 101413 (Sana et al. 2011), and HD 237211 (based upon these results).

This sample contains one previously identified runaway star, HD 124979, first listed by Massey & Hunter (1998). Another possible runaway is HD 228841 with a radial velocity of –57.7 km $\rm s^{-1}$. To estimate the peculiar space velocity of HD 228841, the procedure from Berger & Gies (2001) is followed. HD 228841 may be a member of the cluster Berkeley 86 (Massey et al. 1995) at a distance of 1.9 kpc. The proper motion components for HD 228841 listed in the *Tycho-2* catalog (Høg et al. 2000) are small, but more than three times their uncertainties. Combining the distance and proper motion measurements, the peculiar space velocity of HD 228841 is 87 km $\rm s^{-1}$, well above the runaway star threshold of 30 km $\rm s^{-1}$ adopted by Gies (1987). BD+60°261 is a third possible runaway candidate. To estimate a distance to BD+60°261, the absolute V magnitude for an O7.5 III star of -5.47 from Table 5 in Martins et al. (2005), the $(B-V)$ value listed in Simbad, and $(B-V)_0$ of -0.28 for a spectral classification of O7.5 III from Table 5 of Wegner (1994) can be used to compute a distance of 3.2 kpc. Following the same procedure as for HD 228841, the peculiar component of radial velocity is -50.8 km $\rm s^{-1}$. McCuskey et al. (1974) report an average velocity of -41 km $\rm s^{-1}$ for stars in this region. The average velocity for BD+60°261 derived here of -85.0 km $\rm s^{-1}$, which is -44 km $\rm s^{-1}$ different than other stars in the region, make a second case for BD+60°261 being a runaway. Blaauw

(1993) notes that runaway stars tend to have large rotational velocities, and it is interesting that HD 124979 and HD 228841 have the largest $v \sin i$ values in this sample, while BD+60°261 has a more intermediate rotational velocity.

– 4 –

Single-lined Spectroscopic Binaries

4.1 Introduction

For several systems, only one member of the binary was definitively seen. Multiplicity was concluded based on either the spectroscopic variation or the photometric variation, where spectra were insufficient in number to span an entire orbit.

This chapter is broken down by published works. The first section covers a sample of O-type stars observed at CTIO: HD 308813, HD 152147, HD 164536, BD$-16°$4826, while HD 229232 was observed at KPNO. The next two sections cover objects of particular interest that warranted their own individual study and publication, the gamma-ray binary HD 215227 and the W Serpentis like system BD+36°4063.

4.2 Single-lined Systems Observed at CTIO

4.2.1 Introduction

Results are presented here for five objects that were observed as part of a larger group of O-type stars with little prior observational work and that appear with a binary designation of “U” (unknown) or “?” (uncertain) in Mason et al. (1998). The current status of each of these systems is either unknown spectroscopic variability (HD 229232 and BD$-16°$4826) or known variability but with insufficient data to compute an orbit (HD 308813, HD152147, and HD 164536). With new data, radial velocities are measured, orbital elements determined, and stellar parameters for each system are computed, closely following the procedure used to analyze velocity non-variables in Chapter 3 of this dissertation. These first single-lined spectroscopic orbits and physical parameters for each system are discussed, as are the natures of the unseen companions.

4.2.2 Observations

Observations of HD 308813, HD 152147, BD−16°4826, and HD 164536 were obtained from the CTIO 1.5-m telescope ($R \approx 2750$), while HD 229232 was observed with the KPNO 2.1-m telescope ($R \approx 3030$). Exposure times were several minutes to reach at least a S/N of 100 per pixel in the continuum. The details of the instrumental setups and initial data reduction are discussed in Chapter 2.

4.2.3 Radial Velocities and Stellar Parameters

An approximate model template was used for initial measurements. A simple "by eye" fit to several prominent absorption features was made by interpolating in the OSTAR2002 grid (Lanz & Hubeny 2003) for stars with $T_{\rm eff} > 30$ kK and in the BSTAR2006 grid (Lanz & Hubeny 2007) for stars cooler than 30 kK.

Velocities for each spectrum for each object were then measured using the cross-correlation technique with uncertainties estimated as outlined by Zucker (2003). The model was cross-correlated with each spectrum in the particular object's spectrum stack. Prior to cross-correlation, object dependent emission features and interstellar features were removed, including the broad diffuse interstellar band (DIB) near $\lambda 4428$ Å (see the discussion of individual objects below). The radial velocities are listed in Table 4.1 with targets ordered by right ascension. Table 4.1 lists the object name, heliocentric Julian date of observation, orbital phase (see below), radial velocity, velocity uncertainty, and the observed minus calculated ($O - C$) value for each measurement.

Table 4.1: Radial Velocities for Single-lined Systems

Star Name	Date (HJD−2,450,000)	Orbital Phase	V_r (km s^{-1})	σ (km s^{-1})	$O - C$ (km s^{-1})
HD 308813	2714.805	0.699	–0.6	1.7	–2.2
HD 308813	2715.708	0.841	20.6	1.7	4.6
HD 308813	2715.840	0.862	31.2	1.8	8.2
HD 308813	2716.707	0.999	27.3	1.7	–3.3
HD 308813	2716.866	0.024	20.7	1.9	–9.7
HD 308813	2717.697	0.155	32.8	1.9	12.0
HD 308813	2717.801	0.171	16.3	1.8	–2.6
HD 308813	2718.699	0.313	4.5	1.8	4.7
HD 308813	3017.743	0.484	–13.6	2.0	0.0
HD 308813	3018.753	0.644	–1.6	1.8	3.6
HD 308813	3019.735	0.799	16.2	2.0	1.0
HD 308813	3019.836	0.815	26.0	1.9	8.8
HD 308813	3020.718	0.954	23.6	1.9	–6.1
HD 308813	3021.713	0.111	28.1	1.9	2.6
HD 308813	3021.816	0.127	29.6	1.9	5.7
HD 308813	3022.721	0.270	–3.7	1.9	–9.5
HD 308813	3022.865	0.292	–4.7	1.9	–7.4
HD 308813	3023.702	0.424	–18.5	2.0	–7.3
HD 308813	3023.806	0.441	–11.2	1.9	0.9
HD 308813	3027.727	0.059	24.9	2.0	–4.2
HD 308813	3028.704	0.213	16.4	2.0	3.0
HD 308813	3028.787	0.227	19.6	2.0	7.8
HD 308813	3029.744	0.377	–3.8	2.0	3.7
HD 308813	3030.694	0.527	–11.2	1.9	2.1
HD 308813	3030.776	0.540	–7.9	2.0	5.1
HD 308813	3031.712	0.688	–1.4	1.9	–1.5
HD 308813	3032.636	0.834	10.0	1.9	–9.6
HD 308813	3032.782	0.857	24.5	2.0	2.2
HD 308813	3033.713	0.004	34.9	1.9	4.3
HD 308813	3159.469	0.840	15.0	1.8	–5.4
HD 308813	3160.463	0.997	26.8	1.8	–3.8
HD 308813	3162.531	0.323	–1.9	1.8	–0.5
HD 308813	3163.532	0.481	–20.8	1.9	–7.3

Continued on next page…

Table 4.1 – Continued

Star Name	Date (HJD−2,450,000)	Orbital Phase	V_r (km s^{-1})	σ (km s^{-1})	$O-C$ (km s^{-1})
HD 152147	3152.593	0.668	–46.7	2.6	–0.2
HD 152147	3153.620	0.742	–33.6	2.5	7.2
HD 152147	3154.580	0.811	–43.7	2.5	–8.6
HD 152147	3154.811	0.828	–35.1	2.5	–1.2
HD 152147	3155.743	0.896	–32.0	2.7	–2.3
HD 152147	3156.775	0.970	–23.8	3.0	3.5
HD 152147	3157.764	0.042	–26.7	2.5	0.7
HD 152147	3157.874	0.050	–40.4	3.4	–12.7
HD 152147	3158.696	0.109	–29.2	2.5	0.8
HD 152147	3159.714	0.183	–35.0	2.4	–0.2
HD 152147	3160.721	0.256	–41.6	2.5	–1.0
HD 152147	3161.737	0.329	–39.2	2.5	7.1
HD 152147	3162.688	0.398	–60.2	2.6	–9.5
HD 152147	3163.709	0.472	–50.8	2.6	2.2
HD 152147	3164.599	0.536	–57.7	2.7	–4.8
HD 164536	3152.753	0.559	–26.6	2.0	2.7
HD 164536	3153.777	0.636	–27.4	1.9	–5.3
HD 164536	3153.916	0.646	–17.0	1.9	3.7
HD 164536	3154.781	0.711	–7.5	1.8	3.8
HD 164536	3155.720	0.782	2.1	1.9	1.9
HD 164536	3156.633	0.850	14.4	2.0	3.9
HD 164536	3156.910	0.871	4.8	2.0	–8.3
HD 164536	3157.881	0.943	15.1	2.0	–4.5
HD 164536	3158.803	0.012	20.4	1.9	–0.7
HD 164536	3159.750	0.083	21.0	1.9	3.2
HD 164536	3160.773	0.160	19.0	1.9	9.9
HD 164536	3161.842	0.240	–4.9	2.1	–1.5
HD 164536	3162.789	0.311	–26.5	2.0	–11.8
HD 164536	3163.779	0.385	–19.5	1.9	5.0
HD 164536	3164.751	0.458	–31.3	2.0	–1.1
HD 164536	3164.870	0.467	–30.8	2.0	–0.3
BD−16°4826	3152.899	0.391	–0.7	2.5	–0.5
BD−16°4826	3153.797	0.445	2.9	2.3	5.4
BD−16°4826	3153.929	0.453	1.6	2.5	4.3
BD−16°4826	3154.913	0.513	–6.1	2.3	–2.8
BD−16°4826	3156.646	0.617	3.9	2.4	3.5
BD−16°4826	3157.914	0.693	5.2	2.4	–0.7
BD−16°4826	3158.901	0.753	13.8	2.3	2.6
BD−16°4826	3159.902	0.813	13.4	2.5	–2.9
BD−16°4826	3161.900	0.934	26.6	2.7	2.9

Continued on next page…

Table 4.1 – Continued

Star Name	Date (HJD−2,450,000)	Orbital Phase	V_r (km s^{-1})	σ (km s^{-1})	$O-C$ (km s^{-1})
BD−16°4826	3162.901	0.994	22.3	2.4	–2.6
BD−16°4826	3164.888	0.114	20.2	2.4	–1.2
HD 229232	4785.649	0.198	–37.5	2.5	4.0
HD 229232	4786.594	0.351	–56.1	2.2	–0.2
HD 229232	4787.576	0.511	–69.7	2.1	–7.5
HD 229232	4788.576	0.673	–47.4	2.2	6.5
HD 229232	4789.583	0.836	–37.1	2.1	1.4
HD 229232	4790.572	0.997	–37.5	2.1	–6.5
HD 229232	4791.574	0.160	–36.9	2.1	1.3

For each object, fits of the radial velocity were made for eccentric orbits and for circular orbits using the nonlinear, least-squares fitting routine from Morbey & Brosterhus (1974). Note that no other period-search algorithm was employed because the data sets covered all of or significant fractions of each orbital period, so there was no ambiguity in the selection of an initial period estimate for the general orbital fitting scheme. Following Lucy & Sweeney (1971), a statistic is computed based on the rms of the fit for the eccentric and circular cases, $p = (rms_e/rms_c)^{\beta}$, where rms_e is the rms for the eccentric orbital fit, rms_c that for the circular orbital fit, and $\beta = (N - M)$, where N represents the number of observations, and M the number of parameters fit (6 for the eccentric case). Values of $p > 0.05$ (the 5% significance level) indicate that the eccentric orbit does not statistically improve the fit. For each of the orbits computed here, the eccentric fits provided no significant improvement in the residuals, so circular orbits were adopted. The circular orbital parameters of period, P, the time of maximum velocity, T_0, the systemic velocity for the system, γ, and the velocity semiamplitude, K_1, are listed in Table 4.2. Also listed are the

Table 4.2. Circular Orbital Elements

Parameter	HD 308813	HD 152147	HD 164536	BD$-16°$4826	HD 229232
$P(d)$	6.340±0.004	13.8194±0.0003	13.4±0.6	16.59±0.04	6.2±0.2
T_0(HJD $-$ 2,450,000.0)	3033.69±0.08	31212.0±0.2	3158.6±0.8	3162.0±35.1	4790.6±0.1
γ (km s^{-1})	8.5±1.1	–40.1±0.7	–4.9±1.1	10.52±0.04	–46.6±0.8
K_1 (km s^{-1})	22.2±1.5	13.1±1.0	26.2±1.5	14.23±0.05	15.6±1.2
$f(m)$ ($M_\odot$)	0.007±0.001	0.0032±0.0007	0.025±0.005	0.00496±0.00005	0.002±0.001
a_1 sin i ($R_\odot$)	2.8±0.2	3.6±0.3	6.9±0.5	4.7±0.2	1.9±0.2
rms (km s^{-1})	6.1	5.7	6.1	3.8	7.3
N	33	31	16	11	7

mass function, $f(m)$, the projected orbital semi-major axis, $a_1 \sin i$, the rms of the fit, and the number of observations. The radial velocities and orbits are plotted in Figures 4.1 through 4.5.

Using the final orbit fits, a shift-and-add algorithm was used on the spectrum stack in order to create a higher S/N master spectrum. These spectra are plotted in Figure 4.6.

Stellar parameters were estimated by fitting the master spectrum for each object with model templates. The process was identical to that used in section 3.3 for the velocity constant stars. The entire process of fitting stellar parameters was repeated once as a check.

The derived $T_{\rm eff}$, log g, and v sin i values are listed in Table 4.3, along with a spectral classification estimate made by comparing our computed values for $T_{\rm eff}$ and log g with Tables 4, 5, and 6 of Martins et al. (2005) for O-stars, and Table 2 from Böhm-Vitense (1981) for the two targets on the border between O- and B-type stars, HD 308813 and HD 152147. The final three columns in Table 4.3 list the parameters used to obtain a spectroscopic parallax estimate (see next section).

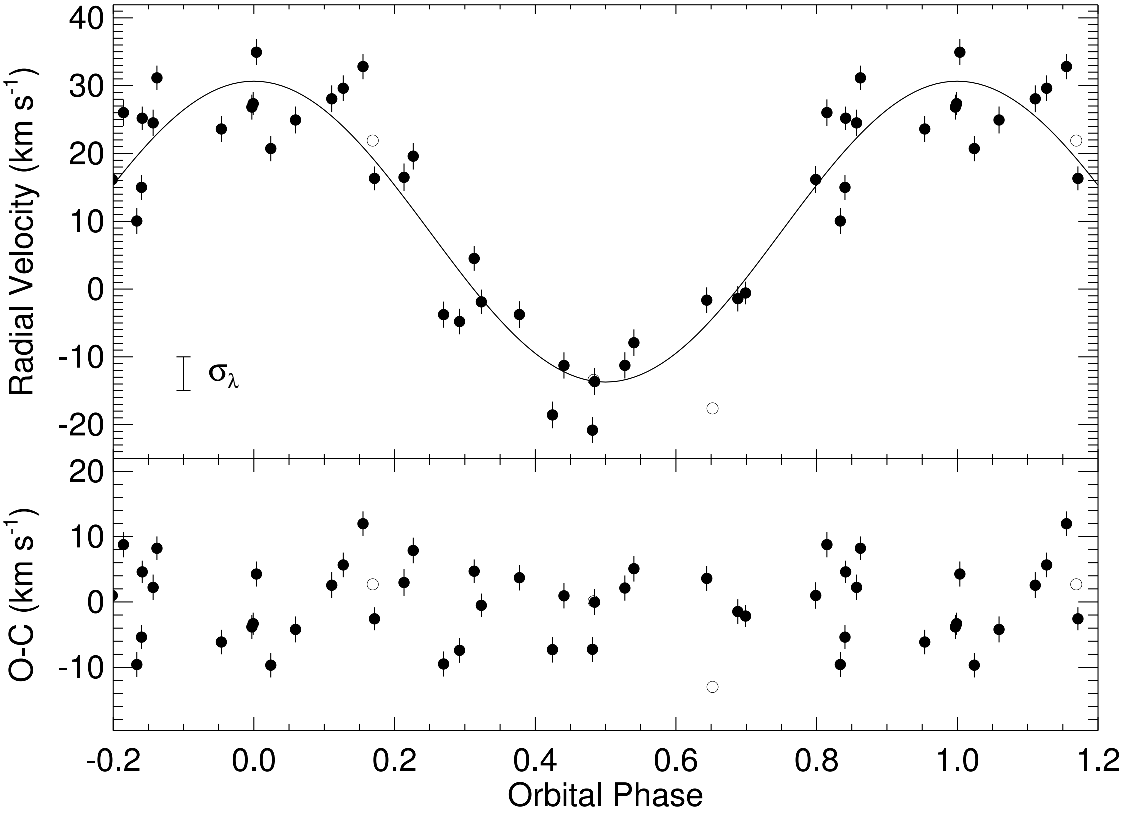

Figure 4.1 Radial velocities for HD 308813. Filled circles are data from this analysis with uncertainties shown by vertical lines, and open circles are data from Huang & Gies (2006). Plotted beneath the velocities are the observed minus calculated values based on the circular orbital fit. Also shown is the 5 km s^{-1} uncertainty from the wavelength calibration.

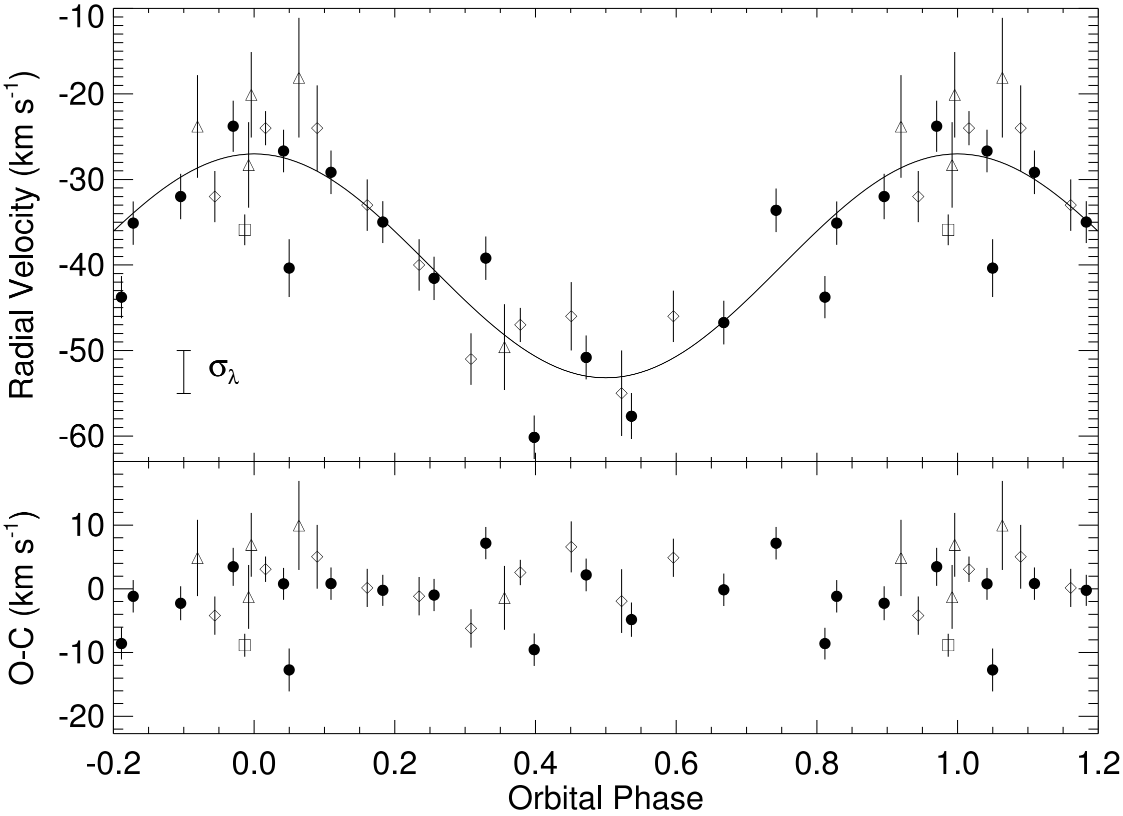

Figure 4.2 Radial velocities for HD 152147. Filled circles are data from this analysis, the open square is from Conti et al. (1977), open triangles are from Struve (1944), and open diamonds are from Levato et al. (1988), with uncertainties shown by vertical lines. Plotted beneath the velocities are the observed minus calculated values based on the circular orbital fit. Also shown is the 5 km s^{-1} uncertainty from the wavelength calibration.

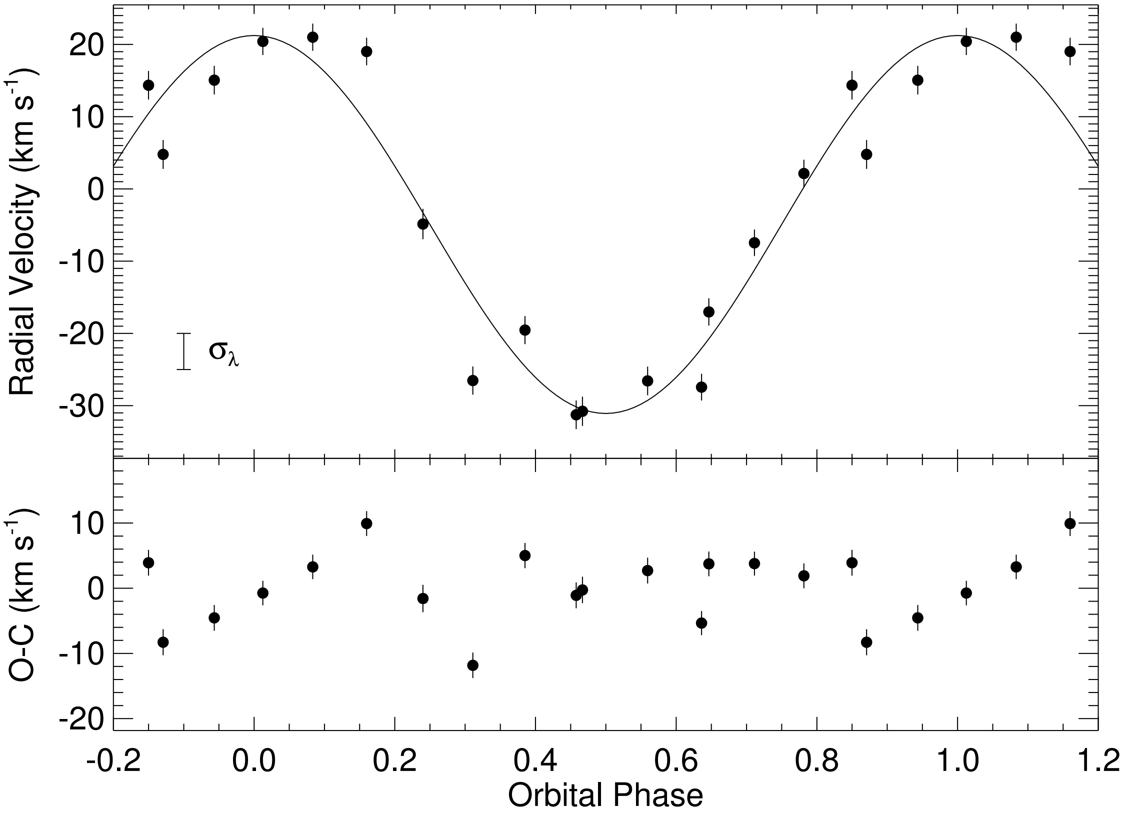

Figure 4.3 Radial velocities for HD 164536. Filled circles are data from this analysis, with uncertainties shown as vertical lines. Plotted beneath the velocities are the observed minus calculated values based on the circular orbital fit. Also shown is the 5 km s^{-1} uncertainty from the wavelength calibration.

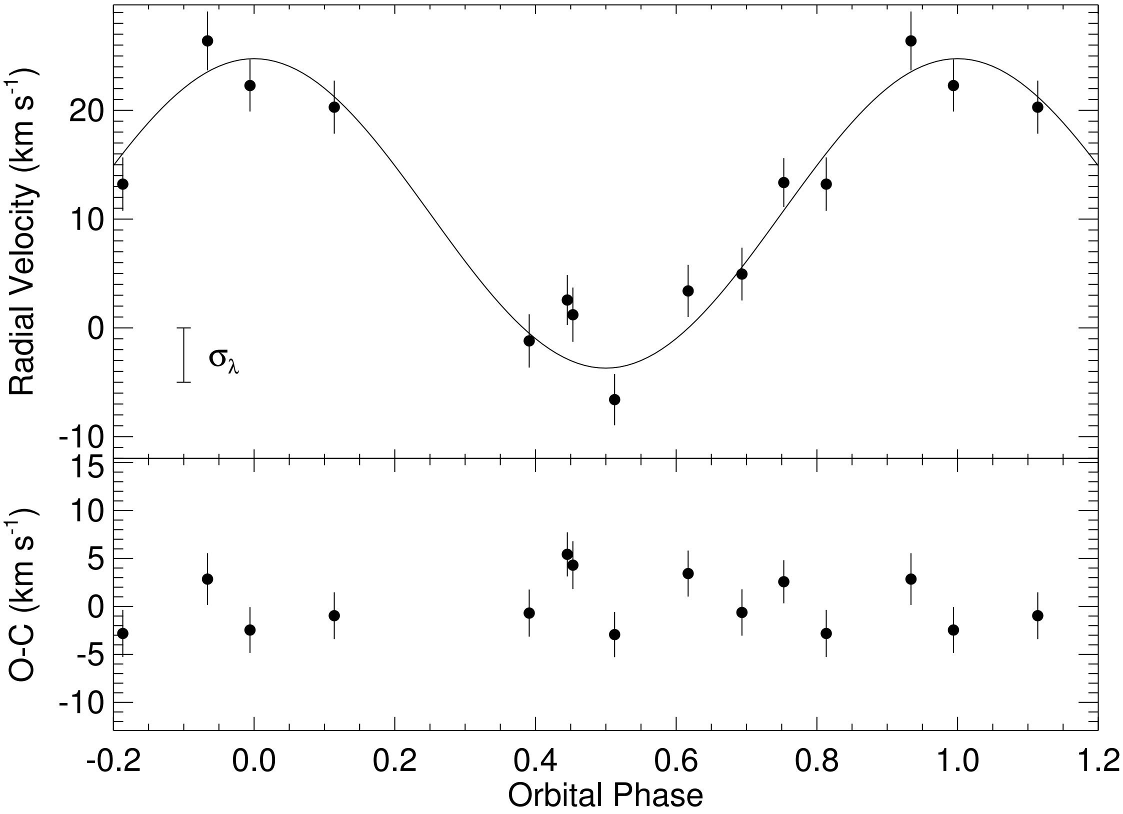

Figure 4.4 Radial velocities for BD−16°4826. Filled circles are data analyzed here, with uncertainties shown as vertical lines. Plotted beneath the velocities are the observed minus calculated values based on the circular orbital fit. Also shown is the 5 km s^{-1} uncertainty from the wavelength calibration.

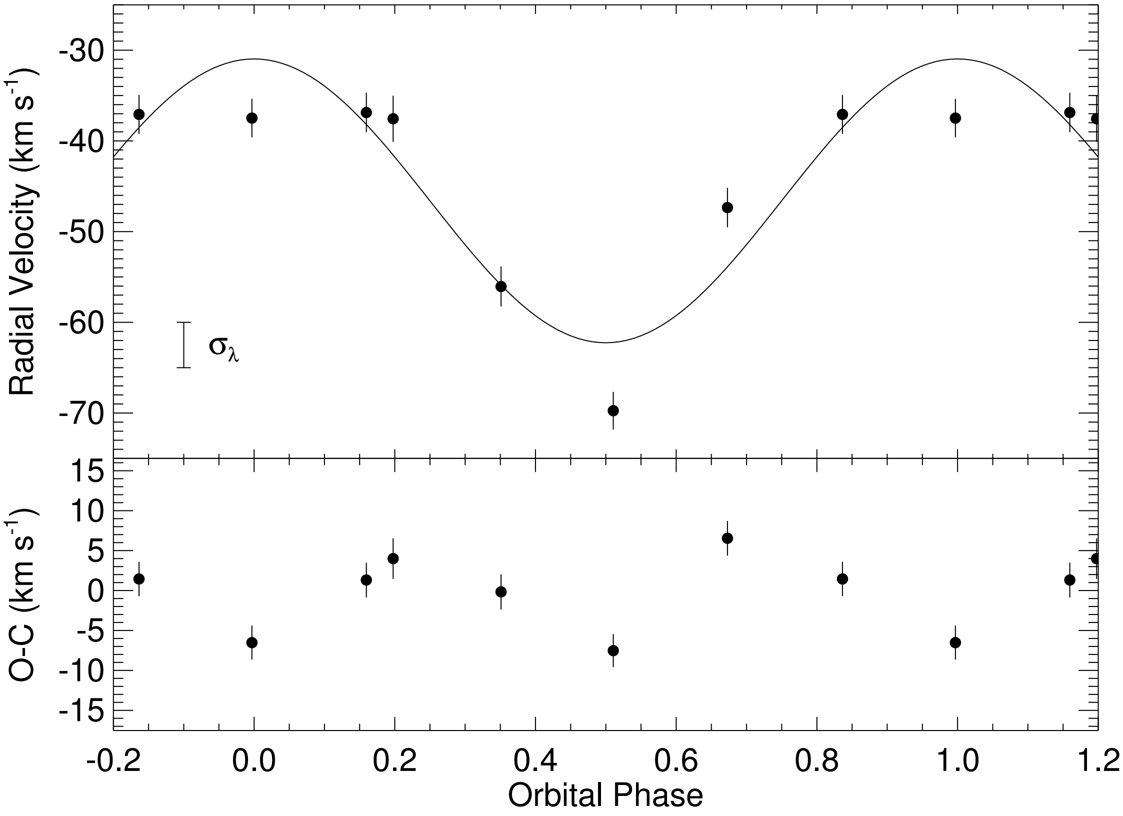

Figure 4.5 Radial velocities for HD 229232. Filled circles are data from this analysis, with uncertainties shown as vertical lines. Plotted beneath the velocities are the observed minus calculated values based on the circular orbital fit. Also shown is the 5 km s^{-1} uncertainty from the wavelength calibration.

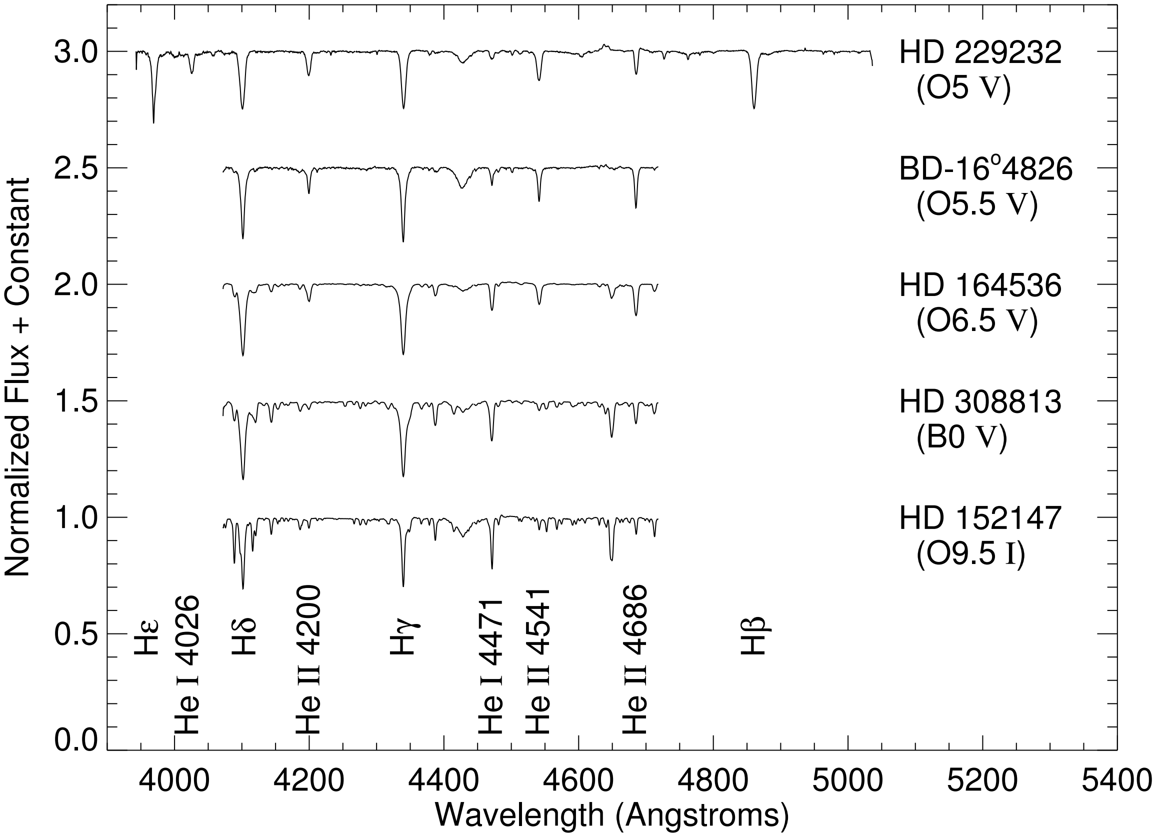

Figure 4.6 Spectra and prominent spectral features for objects discussed here. The hottest star is at top and targets are then plotted in order of decreasing effective temperature.

Table 4.3. Individual Stellar Parameters

Object Name (1)	Spectral Classification (2)	$T_{\rm eff}$ (kK) (3)	log g (cm s^{-2}) (4)	v sin i (km s^{-1}) (5)	Spectral Classification from ($T_{\rm eff}$,log g) (6)	M_V (mag) (7)	$E(B-V)$ (mag) (8)	Distance (kpc) (9)
HD 308813	O9.5 V	29.9±0.3	3.73±0.09	204±10	B0 V[a]	–3.90	0.28	2.95
HD 152147	O9.7 Ib	27.8±0.5	3.10±0.06	150±28	O9.5 I[a]	–6.28	0.55	2.37
HD 164536	O9 III	37.4±0.9	4.25±0.17	230±14	O6.5 V[b]	–4.77	0.22	1.78
BD−16°4826	O5	39.9±6.3	4.04±0.40	131±28	O5.5 V[b]	–5.07	1.24	1.60
HD 229232	O4 Vn((f))	41.7±1.3	4.05±0.14	273±19	O5 V[b]	–5.21	1.12	1.79

[a] Calibration of Böhm-Vitense (1981).

[b] Calibration of Martins et al. (2005).

Note. — Spectral classification references: HD 308813: Schild (1970); HD 152147: Walborn (1972); HD 164536: MacConnell & Bidelman (1976); BD−16°4826: Hiltner (1956); HD 229232: Walborn (1973).

4.2.4 Discussion of Individual Objects

4.2.4.1 HD 308813

The variable velocity of HD 308813 and its membership in cluster IC 2944 were first suggested by Thackeray & Wesselink (1965) based on three observations spaced two years apart. They suggested that HD 308813 may be an SB2 due to differences in velocities from He II compared to other lines seen on their last plate. Huang & Gies (2006) also measured three velocities, over a time span of 4 days, and suggested the system was a possible single-lined spectroscopic binary. Sana et al. (2011) gathered 11 velocities over time spans of days to years, and they were therefore unable to discern an orbital period or ephemeris for this system, although they did confirm the SB1 nature suggested by Huang & Gies (2006). The observations reported here have the benefit of being made over three separate epochs, the second one a 16-day span. The computed orbital period of 6.340 d (Table 4.2) is therefore covered twice in that time span. The radial velocity measurements from Thackeray & Wesselink (1965) (−12, 18, and −40 km s^{-1}), Ardeberg & Maurice (1977) (−10 km s^{-1}), and Huang & Gies (2006) (21.9,−13.4, and −17.6 km s^{-1}) all span the range of velocities presented here. The data from Huang & Gies (2006) are overplotted in Figure 4.1, but were not used in computing of the orbit.

Prior $v \sin i$ measurements are 186±11 km s^{-1} by Daflon et al. (2007) (using He I $\lambda\lambda 4026, 4387, 4471$), 196±9 km s^{-1} by Huang & Gies (2006) (who used the same lines plus Mg II $\lambda 4481$), and 197 km s^{-1} by Penny et al. (2004) (from UV lines in spectra obtained by the Hubble Space Telescope and Space Telescope Imaging Spectrograph).

All of these measurements agree to within 1σ of the computed value in this study of 204±10 km s^{-1} obtained by measuring He I $\lambda4143, 4387, 4471$. $T_{\rm eff}$ and log g were estimated using Hδ, Hγ, He I $\lambda\lambda4143, 4387$, and He II $\lambda4686$. The distance to HD 308813 was estimated via spectroscopic parallax. According to the values listed in Thackeray & Wesselink (1965), $(B-V) = 0.04$. Also adopted are $(B-V)_0 = -0.26$ for a B0 V star from Wegner (1994) and $M_V = -3.90$ for an O9.5 V star from Martins et al. (2005). Assuming the standard Galactic value for the total-to-selective extinction ratio ($R_{\rm V} = 3.1$) leads to a distance of 2.82 kpc, and this value is listed in Column 9 of Table 4.3. This distance puts HD 308813 a bit further than the distance for IC 2944 of 2.2 kpc from Tovmassian et al. (1998), but it may be a member of a more distant association (see their Table 5).

4.2.4.2 HD 152147

HD 152147 lies in the vicinity of the Galactic open cluster NGC 6231, but it is not likely to be a member. A number of velocities have been previously published; five by Struve (1944), one by Conti & Ebbets (1977), and 10 by Levato et al. (1988), who were also are the first to claim velocity variability. We fit an orbit to all these literature velocities, and the 15 new measurements reported here, using equal weights for all data to obtain the parameters listed in Table 4.2 (orbit shown in Figure 4.2).

Conti et al. (1977) measured v sin i = 80 km s^{-1} by comparing Hγ, He I $\lambda\lambda4387, 4471$, and He II $\lambda4541$ with calibrated standard stars. The rotational velocity from data presented here is 150±28 km s^{-1} from fits to Si IV $\lambda4088$, He I $\lambda\lambda4143, 4471, 4387$, and He II 4686. The Conti et al. (1977) spectra have higher resolution than the data used in this study, so our 150 km s^{-1} value should be taken as an upper limit. The estimates for $T_{\rm eff}$ and log g were made from fits to Hγ, He I $\lambda\lambda 4143, 4387$, and He II $\lambda 4686$. To estimate the spectroscopic parallax, the B and V values listed in Schild et al. (1969) were used to obtain $(B-V) = 0.37$. Wegner (1994) gives a value of $(B-V)_0 = -0.24$ for an O9.5 I star. Further assuming a standard value of $R_{\rm V} = 3.1$ and using the M_V listed in Martins et al. (2005) for an O9.5 I star, leads to a calculated distance to HD 152147 of 2.11 kpc. This value does not agree well with the recent distance estimate for HD 152147 of 1.64±0.24 kpc from Megier et al. (2009) that is based on Ca II interstellar line strength. Nor does the value derived here match with the distance estimate to NGC 6231 given by Sana et al. (2006) of 1.64 kpc. This may mean the estimate of $R_{\rm V}$ is inaccurate for the line of sight to HD 152147, but this also may be evidence suggesting HD 152147 is not a member of NGC 6231. For example, Humphreys (1978) places this star in the Sco OB1 association at a distance of 1.91 kpc, a distance similar to the estimate derived here.

4.2.4.3 HD 164536

The first radial velocity measurement published is by Hayford (1932) who reports a value of 6 km s^{-1} from 5 spectral lines on JD 2,425,371.99. Other radial velocities are averages from several, typically unspecified, nights. These include -11.1 ± 3.2 km s^{-1} from 5 plates reported by Neubauer (1943) and -10 km s^{-1} from three plates reported by Feast et al. (1955). None of these velocities were used in the derivation of the orbital parameters listed in Table 4.2.

HD 164536 is one of the brightest members of the cluster NGC 6530 (Walker 1957; Boggs & Bohm-Vitense 1989). A proper motion study was made of NGC 6530 by van Altena & Jones (1972), who claim that HD 164536 is not a member. However, its cluster membership was reestablished in a series of papers based on *IUE* spectra (Böhm-Vitense et al. 1984; Boggs & Bohm-Vitense 1989, 1990). Africano et al. (1975) claimed detection of a nearby companion during a lunar occultation observation at $\rho = 0\overset{''}{.}174 \pm 0\overset{''}{.}003$, $\theta = 203°$, and $\Delta m = 2.2 \pm 0.4$ mag. However, subsequent follow up observations that had the ability to see such a companion (Mason 1996; Turner et al. 2008) did not resolve this close companion. This star is the brightest of a trapezium (4 star) system listed in the Washington Double Star Catalog (WDS; Mason et al. 2001). Turner et al. (2008) resolve the closest component at $1\overset{''}{.}7$ distant, with other members outside their field of view. This close component is too faint ($V = 12.4$ according to the WDS) compared to HD 164536 ($V = 7.1$; Høg et al. 2000) to influence data in this study.

To derive the effective temperature and log g, Hδ, Hγ, He I $\lambda4471$, and He II $\lambda\lambda4541, 4686$ were used. The projected rotational velocity was computed from observations of the He II lines. Boggs & Bohm-Vitense (1989) arrive at an effective temperature of 32 kK and spectral type of O9 V from their analysis of *IUE* spectra. The value derived here of 37.4 ± 0.9 kK is $> 3\sigma$ higher, indicating an O6.5 V estimate of the spectral classification from Table 4 in Martins et al. (2005). The distance to HD 164536 is estimated by taking the Tycho B and V magnitudes (Høg et al. 2000) transformed to Johnson magnitudes, an $M_V = -4.77$ for an O6.5 V (Martins et al. 2005), $(B - V)_0 = -0.29$ (Wegner 1994), and $R_V = 3.1$. This results in a distance of 1.78 kpc, equal to the 1.78 kpc estimate given by van Altena & Jones (1972) and larger than the 1.33 kpc distance from Kharchenko et al. (2005). Using $R_V = 3.45$ for HD 164536, as reported in Wegner (2003), the distance drops to 1.71 kpc.

4.2.4.4 BD−16°4826

There appear to be no velocities in the literature, making the velocities and SB1 fit based on the 11 spectra presented here the first published.

BD−16°4826 is a member of the cluster NGC 6618, which is embedded in M 17. Estimates for effective temperature and log g were made from fits to Hδ, Hγ, He II $\lambda\lambda4200, 4541, 4686$ and He I $\lambda\lambda4387, 4471$. Only He I $\lambda\lambda4541, 4686$ were used to derive the v sin i value listed in Table 4.3. There was very large scatter in attempts to fit the spectrum of BD−16°4826, as evidenced by the highest uncertainties for stellar parameters in this work. Listed as an O5 in Hiltner (1956), the spectral classification of this object has varied from O3 V based on optical spectra (Garmany & Vacca 1991) to any of four spectral types ranging from O5 V to O9 III that were based upon IR data by Povich et al. (2009). The best estimators available for luminosity criteria are the wings of the Balmer lines. These definitively rule out the possibility of BD−16°4826 being evolved (see Fig. 4.6 and Table 4.3), and the spectral classification for BD−16°4826 is therefore estimated to be O5.5 V. The most recent optical photometry is reported by Ogura & Ishida (1976). They find, from two observations, $V = 9.85$ and $(B-V) = 0.94$. Using $M_V = -5.07$ (Martins et al. 2005), $(B-V)_0 = -0.30$ (Wegner 1994), and a standard value $R_V = 3.1$, the spectroscopic distance to BD−16°4826 is 1.60 kpc. The distance to NGC 6618 and M 17 is a topic of some debate. The recent IR study by Povich et al. (2009) lists two distances, 1.6 ± 0.3 kpc from Nielbock et al. (2001) and 2.1 ± 0.2 kpc from Hoffmeister et al. (2008). The value derived here agrees with the Nielbock et al. (2001) estimate. This computed value is within the uncertainty of the lower limit on the distance to M17 reported by Hanson et al. (1997) of $1.3^{+0.4}_{-0.2}$ kpc based on extinction corrected IR magnitudes of O-stars.

4.2.4.5 HD 229232

There is very little in the literature about HD 229232. As with BD$-16°$4826, the seven velocities reported in this work are the first published. However, with only seven data points, this orbit should be considered preliminary. The estimate that the star is an O5 V with a variable velocity indicates that this is a massive binary that deserves additional observational work.

To estimate effective temperature and log g, fits were made to the Hδ wings, He I $\lambda 4026$, and He II $\lambda\lambda 4200, 4541$. Only the helium lines were used to compute the v sin i. Using $V = 9.525$ and $(B - V) = 0.82$ from Hiltner (1956), $M_V = -5.21$ from Martins et al. (2005) and $(B - V)_o = -0.30$ (Wegner 1994) (both values for an O5 V star), and the standard $R_V = 3.1$, the distance to HD 229232 is 1.8 kpc. The galactic coordinates of HD 229232 are $\ell = 77\overset{\circ}{.}40$ and $b = 0\overset{\circ}{.}93$, looking down the Cygnus arm, a very complex situation (Uyanıker et al. 2001). It may be a member of the Cyg OB8 association that Humphreys (1978) places at a distance of 2.29 kpc.

4.2.5 Discussion

The five systems studied here have orbital periods ranging from 6 to 17 days, with velocity semiamplitues ranging from 13 to 26 km s−1. None of these systems show eclipses or photometric variation in either the All Sky Automated Survey (Pojmanski 2002) nor The Amateur Sky Survey (TASS[1]; Droege et al. 2006). The only object with published time series photometry is HD 152147, and Sterken et al. (1993) found no variability. BD−16°4826 is an X-ray source but with a flux typical of single O-stars (Nazé 2009).

For circular orbits, the orbital velocity semiamplitude is given by

$$K_1 = 289 \text{ km s}^{-1} (M_1/25M_\odot)^{1/3} (P/10 \text{ d})^{-1/3} \frac{q}{(1+q)^{2/3}} \sin i$$

where the mass ratio is $q = M_2/M_1$. Therefore, the low K_1 systems in this sample are those with low mass companions (small q) and/or low inclination (i). To estimate the most probable q, the statistical method of Mazeh & Goldberg (1992) is employed. This method requires assumptions about the mass ratio distribution of the sample and the mass of the primary, which is estimated from Martins et al. (2005). Based on observations of O-stars (Mason et al. 1998), the mass ratio distribution is assumed to be uniform. Column 2 in Table 4.4 lists the mass ratios derived from the spectroscopic orbits discussed previously, and column 3 lists the mass estimate based on the spectral classification in the calibration of Martins et al. (2005). The resulting mass ratios (q) from this distribution are listed in Table 4.4. Estimates for the spectral

---

[1] http://sallman.tass-survey.org/servlet/markiv/

classification of the secondary (column 6) are made by comparing the mass in column 5 to the values listed in Table B.1 of Gray (2005). These companions are all assumed to be main sequence stars, because all the primary stars are so young. Column 7 lists the difference in V magnitude between the primary and secondary, again as estimated from Gray (2005). These are all greater than 2.5 mag, and they lead to the monochromatic flux ratios given in column 8. The extremely small flux ratios are the first piece of evidence why companions are not seen in the data.

The true nature of the mass ratio distribution for O-type stars is unknown. To explore the range of possibilities besides the flat distribution used above, two extreme values were taken for a power law distribution $N(q) = N_0\, q^{\alpha}$. The first is the standard Salpeter distribution (Salpeter 1955) with an exponent of $\alpha = -1.35$. The second is from a radial velocity survey of the Cyg OB2 association by Kobulnicky & Kiminki (2011) who reported an exponent of $\alpha = 0.3$. With these mass ratio distributions, and estimates for the masses of the primary and secondary, the inclinations of the orbits may be computed based on the mass functions. The resulting ranges of mass ratio and inclination are listed in Table 4.5. These ranges are not large, and the estimates for orbital inclination are low ($i < 37°$). Such low inclinations are not surprising, given the low values for orbital velocity semiamplitude, K_1 (Table 4.2).

Taking the values for i and orbital periods from Table 4.4, combined with estimates of the stellar radii (Martins et al. 2005), the synchronous rotational velocities, $v \sin i$ (sync), are computed and listed in column 9 of Table 4.4. These numbers are all much smaller than the $v \sin i$ measurements listed in column 5 of Table 4.3, further supporting the premise that these systems are young because they are not yet synchronously rotating.

Do the companions influence the results for $v \sin i$ or K_1? To check the magnitude of the effect, the maximum separation of the spectral features of the individual components is considered. The ratio of maximum Doppler separation to projected rotational velocity is

$$\frac{K_1(1+1/q)}{(v \sin i)}.$$

By using the mass ratio as computed above, this separation is computed and listed in column 10 of Table 4.4. These values are all well below unity, and range from 0.45 to 0.67, meaning the lines of the components are always blended. The additional fact that the companions are extremely faint means that line blending problems related to measurements of $v \sin i$ and K_1 will be minimal. As an example, a model spectrum corresponding to a B4 V star, as estimated for the companion to BD−16°4826 (Column 6, Table 4.4), was added to the master spectrum at a shift of $K_1(1+1/q)$ and normalized according to the flux ratio. This object was chosen because it has the largest ratio of $K_1(1+1/q)/v \sin i$, so it should show the largest effect of blending problems. A $v \sin i$ for the companion of 20 km s^{-1} was chosen to match that predicted for the companion of BD−16°4826. Such very narrow lines would have more influence on the measured parameters of the primary than wider shallower lines. Measuring the velocity in the same way as described above, a maximum offset of 3.6 km s^{-1} is computed for velocity measurements, comparable to the measurement uncertainties on an individual spectrum. In addition, a secondary model spectrum was introduced at $\pm K_1(1+1/q)$ to each of the lines used to measure $v \sin i$, and a value 5.0 km s^{-1}

higher than that found previously is computed. Therefore, even for the narrowest lined star in the sample, the uncertainty in $v \sin i$ introduced by the companion is on the order of 5 km s^{-1}. Although the effects are small, the influence of a companion spectrum on the velocity measurements will be to pull the measurement back toward the rest wavelength of the line. This will make K_1 lower, the mass function lower, and thus the estimate of mass ratio and orbital inclination lower. Consequently, the values of q and i in Table 4.5 are probably lower limits.

Companions will also have an influence on $T_{\rm eff}$ and log g estimates. In the spectral range covered by the data, an O-star has several He II lines that a mid B-star does not. Therefore, the affect will be to make the O-star lines appear shallower, making the O-star appear cooler. He I lines are stronger in B-stars, and in combination with an O-star these lines will become deeper, again causing the O-star to appear cooler. Thus, our estimates for $T_{\rm eff}$ and log g are upper limits and are likely more indicative of the combined spectrum of the binary.

Results from this analysis suggest that all the objects in this sample are SB1. This is due to three main effects: low orbital inclination, broad spectral features of the primary stars, and faint companions. In the future, high resolution and high S/N spectra may be able to extract the companion spectrum in systems similar to those studied here through careful examination of subtle line asymmetries (Gies et al. 1994).

Table 4.4. Probable Unseen Companion Parameters

System (1)	$f(m)$ ($M_\odot$) (2)	M_1 ($M_\odot$) (3)	q (4)	M_2 ($M_\odot$) (5)	Secondary Spectral Classification (6)	ΔV (mag) (7)	Flux Ratio (f_2/f_1) (8)	$v \sin i$ (sync) (km s^{-1}) (9)	$\frac{K_1(1+1/q)}{v \sin i}$ (10)
HD 308813	0.007	14	0.26	3.4	B7 V	2.7	0.08	20	0.53
HD 152147	0.003	25	0.19	4.7	B4 V	4.8	0.01	23	0.55
HD 164536	0.025	28	0.30	8.3	B2 V	2.3	0.12	13	0.49
BD−16°4826	0.00496	34	0.19	6.6	B3 V	3.1	0.06	9	0.67
HD 229232	0.002	38	0.16	5.9	B3 V	3.2	0.05	29	0.45

Table 4.5. Mass Ratios and Inclinations for Various Mass Ratio Distributions

	q			$i(^\circ)$		
System	$\alpha = -1.35$	$\alpha = 0.0$	$\alpha = 0.3$	$\alpha = -1.35$	$\alpha = 0.0$	$\alpha = 0.3$
HD 308813	0.15	0.26	0.31	35.5	20.5	18.0
HD 152147	0.10	0.19	0.23	30.4	16.6	13.7
HD 164536	0.18	0.30	0.34	37.0	22.7	20.2
BD−16°4826	0.11	0.19	0.24	32.4	18.3	14.8
HD 229232	0.09	0.16	0.20	28.0	15.4	12.4

4.3 HD 215227

4.3.1 Introduction

Gamma-ray binaries are a class of high energy and very-high energy emitting sources that consist of a massive star and compact companion (Mirabel 2007; Dubus et al. 2010). As of the end of 2010, six such objects are known sources of TeV emission: LS 5039, Cygnus X-1, Cygnus X-3, LS I +61 303, PSR B1259−63, and HESS J0632+057. The massive star component is a luminous O-star in the first two, a probable WR star in the third, and a Be star in the last three cases. All these massive stars have winds, and the Be stars also eject mass into an outflowing circumstellar disk. The interaction of this mass loss with a degenerate companion can lead to gamma-ray emission in two ways (Paredes 2008). First, if the companion is a pulsar, then a high-speed wind from the mass donor can collide with the pulsar wind in a shock region, and inverse Compton scattering of stellar photons with relativistic electrons in the shock can create gamma-rays (Dubus et al. 2010). Second, if the companion is a black hole, then gas accretion can lead to the formation of relativistic jets, and gamma-ray emission may occur by inverse Compton scattering from jet electrons and/or by the decay of neutral pions that originate in inelastic proton - proton collisions (Romero et al. 2007).

Recently, Lucarelli et al. (2010) announced the detection with the AGILE satellite (Tavani et al. 2009) of gamma-ray emission above 100 MeV from a new unidentified source, AGL J2241+4454. The source has Galactic coordinates of $(l, b) = (100\overset{\circ}{.}0, -12\overset{\circ}{.}2)$ with an error circle radius of approximately $0\overset{\circ}{.}6$. The source has not yet been detected by the NASA Fermi Gamma-Ray Observatory[2]. The AGILE point sources found to date include pulsars, blazars, supernova remnants, and high-mass X-ray binaries (Pittori et al. 2009), but there are no cataloged examples of any of these in the region close to AGL J2241+4454 (Lucarelli et al. 2010). There are two possibilities that deserve further attention. First, Brinkmann et al. (1997) found an X-ray source and probable quasar in this region, RXJ2243.1 + 4441, that may be a possible source of gamma-ray flaring (Vercellone et al. 2008). However, there is no known optical counterpart (radio designation B3 2241 + 444), which would probably appear at $V \approx 16$ (based upon the observed X-ray flux and an assumed frequency power law with $\alpha = 1.3$). Further multiwavelength observations are required to say anything more about the candidacy of this object. Second, the area contains the Galactic Be star HD 215227 (BD +43°4279, HIP 112148, MWC 656), which is located at $(l, b) = (100\overset{\circ}{.}1755, -12\overset{\circ}{.}3985)$. This object was discovered as an emission-line star by Merrill & Burwell (1943) who estimated a spectral type of B0e, and the star was subsequently assigned types B5:ne (Harris 1955), B3neγ (Petrie & Lee 1965), and back to B0 (Hernández et al. 2005). The classification is difficult because the spectral lines are very broad and weak (the projected rotational velocity is $v \sin i = 262 \pm 26$

---

[2] Fermi LAT Report, 2010 July 30; http://fermisky.blogspot.com/

km s^{-1}; Yudin 2001) and often blended with emission features. The analysis here uses new blue spectra of the target to argue that HD 215227 is a potential optical counterpart of AGL J2241+4454 based upon its probable runaway and binary character.

4.3.2 Spectroscopic Observations and Analysis

Blue spectra of HD 215227 were obtained with the HIA Dominion Astrophysical Observatory 1.8-m telescope on 2010 July 28 and 29. Exposures were 300 s in duration, leading to spectra with a S/N = 100 per pixel in the continuum. See Chapter 2 for more details on the instrument and specifics of these particular data.

The two spectra are illustrated in Figure 4.7. There is clear evidence of double-peaked emission from the circumstellar disk that is seen in the core of $H\gamma$ and in numerous Fe II emission lines. The only clear photospheric lines are those of C II $\lambda4267$ and He I $\lambda\lambda4387, 4471$. A search through the Be star spectral survey of Grundstrom (2007) reveals the closest matching spectrum is that of HR 2142 = HD 41335, which is shown for comparison in the top section of Figure 4.7. HR 2142 is a well known Be binary system that shows deep, narrow, “shell” absorption features at certain phases in its 81-d orbit (Peters 1983). The most prominent shell feature appearing in Figure 4.7 is the sharp absorption core of $H\gamma$ $\lambda4340$. Such absorptions form in cooler, dense disk gas seen in projection against the stellar photosphere (Hanuschik 1995), and their strength may be modulated by azimuthal asymmetries in disk density that can occur in Be binaries (Oktariani & Okazaki 2009).

A number of stellar parameters for the star have been estimated by compar-

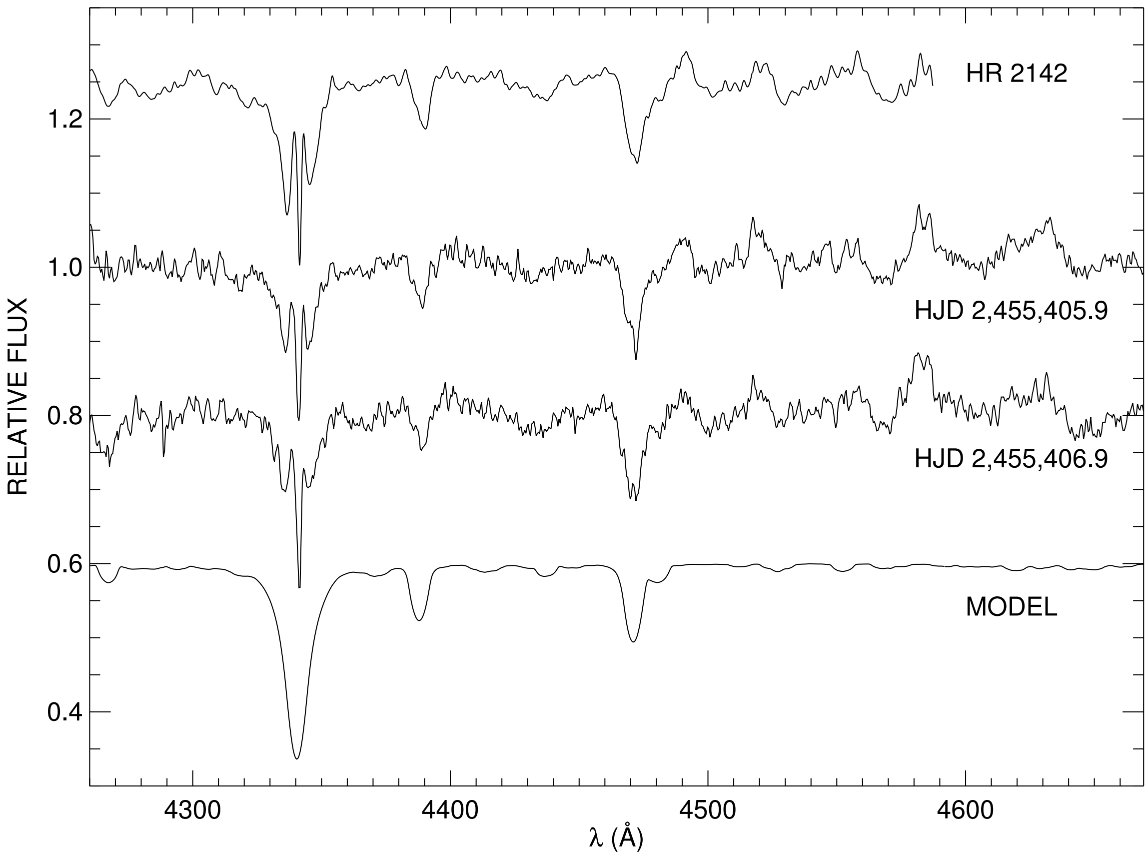

Figure 4.7 The continuum normalized spectrum of HD 215227 from the first and second nights (the latter is offset by −0.20 for clarity). Above is a similar spectrum of the Be binary HR 2142 (Grundstrom 2007) and below is a TLUSTY/SYNSPEC synthetic spectrum for the parameters listed in Table 1 (offset by +0.25 and −0.40, respectively).

ing the observed spectra with B-star model spectra from the TLUSTY/SYNSPEC grid of Lanz & Hubeny (2007). The best fit model parameters from an iterative visual match of the synthetic and two observed spectra are listed in Table 4.6. The uncertainties given in Table 4.6 are based on judgment of the boundary between reasonable and unsuitable solutions, and these are intentionally conservative given the incomplete understanding of emission contamination in the spectra. Focused on first are measurements based upon relative spectral intensity because clear evidence of a systematic line weakening due the presence of disk continuum flux was found. The projected rotational velocity $v \sin i$ was estimated from the shape of the He I $\lambda4471$ and Mg II $\lambda4481$ blend. The effective temperature $T_{\rm eff}$ derivation was based primarily on the He I $\lambda4471$ to Mg II $\lambda4481$ ratio. This ratio increases monotonically with increasing $T_{\rm eff}$, although the ratio is almost independent of $T_{\rm eff}$ near $T_{\rm eff} = 21$ kK, which corresponds to the peak of the He I strength. However, $T_{\rm eff}$ can be estimated even in this vicinity by the relative strength of the O II $\lambda4417$ blend, which is stronger at higher $T_{\rm eff}$. The gravity, $\log g$, was determined by fitting the emission-free parts of the Stark broadened, Hγ line wings. The model photospheric spectrum had line depths that were consistently deeper than the observed ones, and this is probably due to disk continuum flux in this spectral region. Consequently, the model spectrum was renormalized by adding a pure continuum component with a disk-to-star, monochromatic flux ratio $F_d/F_\star$. This renormalized model spectrum is shown as the lower plot in Figure 4.7. Finally, the radial velocity V_r for both spectra was estimated by cross-correlating the observed and model spectra over the wavelength range including the emission-free Hγ wings and He I $\lambda4387$. All of these measurements are summarized in Table 4.6.

The derived stellar parameters suggest a spectral classification of B3 IVne+sh, where the temperature – spectral type relation is taken from Böhm-Vitense (1981), the gravity – luminosity class relation for like stars is adopted from the results of Huang & Gies (2008), and “n” and “e” indicate broad lines and Balmer emission, respectively. The final suffix “sh” is often used to denote the presence of shell lines, which is indicated here by the sharp, central absorption in Hγ. Note that a simi-

Table 4.6. Stellar Properties for HD 215227

Parameter	Value
$T_{\rm eff}$ (kK)	19 ± 3
$\log g$ (cm s^{-2})	3.7 ± 0.2
$v \sin i$ (km s^{-1})	300 ± 50
V_r(HJD 2,455,405.9461) (km s^{-1})	0.2 ± 1.9
V_r(HJD 2,455,406.9124) (km s^{-1})	2.0 ± 2.4
$F_d/F_\star$	0.5 ± 0.3
$E(B-V)$ (mag)	0.02 ± 0.06
θ_{LD} (10^{-6} arcsec)	24 ± 5
$M_\star$ ($M_\odot$)	7.8 ± 2.0
$R_\star$ ($R_\odot$)	6.6 ± 1.9
d (kpc)	2.6 ± 1.0
z (kpc)	-0.56 ± 0.20
$V_{T\rm p}$ (km s^{-1})	19 ± 17
$V_{R\rm p}$ (km s^{-1})	21 ± 17
$V_{S\rm p}$ (km s^{-1})	28 ± 24

lar shell feature may be present in He I λ4471 in the spectrum from the first night. Wolff et al. (2007) determined a surprisingly low value of projected rotational velocity, $v \sin i = 30$ km s^{-1}, compared to our result. It is likely that their spectrum was obtained at a time when the shell lines dominated and that their measurement corresponds to the shell line width.

4.3.3 Discussion

The spectral properties of HD 215227 bear some resemblance to those of the gamma-ray binary LS I +61 303, which is a Be star in a 26.4960 d orbit (Aragona et al. 2009). The Hα profile in LS I +61 303 displays systematic variations in the ratio of the violet-to-red (V/R) peak emission around the time of periastron in this eccentric orbit ($e = 0.54$) binary (Grundstrom et al. 2007a; McSwain et al. 2010). The V/R ratio of the Hγ emission changed significantly in just one day (Figure 4.7), which is unusually fast for most Be stars (Grundstrom 2007). Such rapid variability might be associated with the changing tidal effects of a companion on the disk (especially strong near periastron).

If the disk in HD 215227 is modulated with a binary orbit, then the continuum flux from the disk may also show an orbital modulation. The disk contributes $\approx 33\%$ of the total flux in the optical, so one might expect to find some evidence of the orbital modulation in broad-band photometry. In fact, Koen & Eyer (2002) found evidence of a 61-d periodicity in the *Hipparcos* light curve (258 measurements). There are two other sets of photometric measurements from all sky survey experiments. The first set of 101 Cousins I_C measurements was made between 2003 and 2007 by The Amateur Sky Survey (TASS[3]; Droege et al. 2006). The second set of 52 points was made from 1999 to 2000 with the Northern Sky Variability Survey (NSVS[4]; Woźniak et al. 2004). Because these three sets were made with different broad-band filters, it is assumed that color variations are minimal and that the mean magnitude of each set was simply subtracted to form a combined photometric time series. These residual magnitudes are based upon differences from the average values of $< H_p >= 8.78$, $< I_C >= 8.52$, and $< m_{V,\mathrm{ROTSE}} >= 9.12$ for the *Hipparcos*, TASS, and NSVS photometry sets, respectively. A discrete Fourier transform period search revealed one significant signal with a period of 60.37 ± 0.04 d, an epoch of maximum brightness at HJD 2,453,243.3 ± 1.8, and a semiamplitude of 0.020 ± 0.002 mag. Based on this ephemeris, spectroscopic observations were made at phase 0.83, i.e., near maximum brightness. The

---

[3] http://sallman.tass-survey.org/servlet/markiv/

[4] http://skydot.lanl.gov/nsvs/nsvs.php

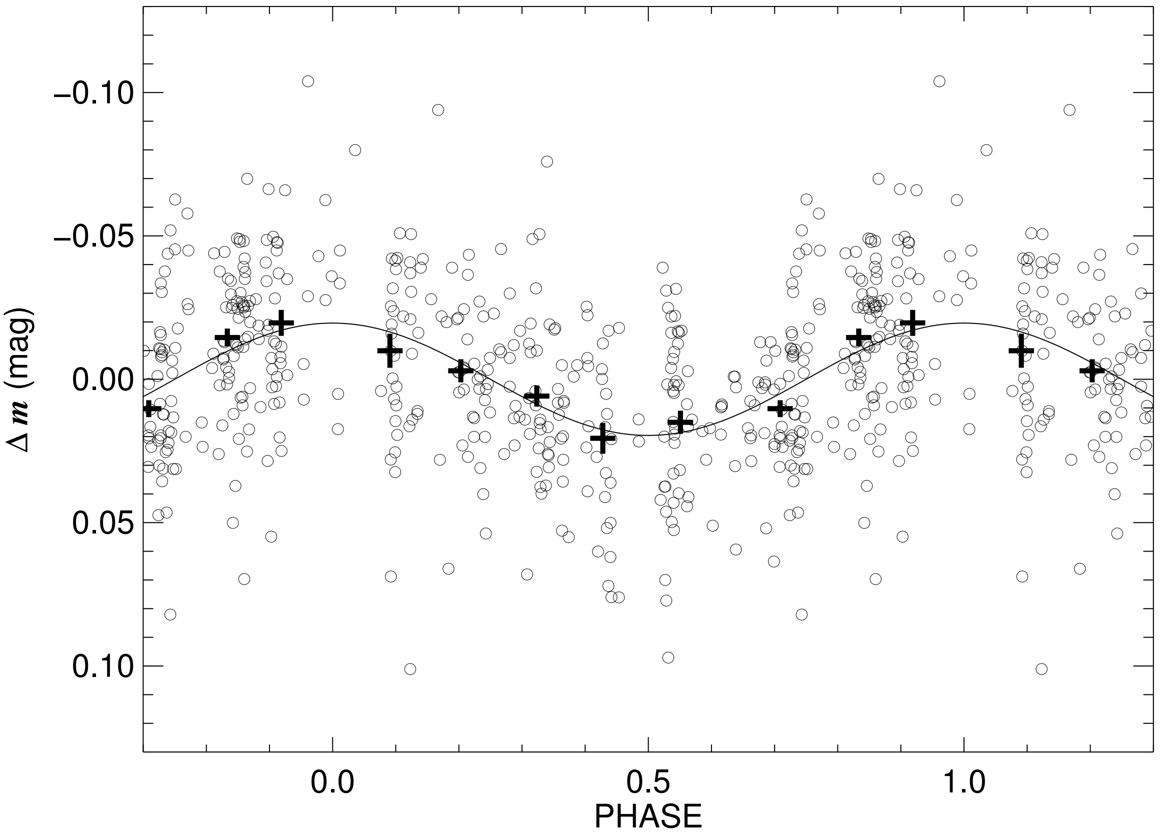

Figure 4.8 The combined, mean-subtracted, photometry of HD 215227 plotted as a function of cycle phase for a period of 60.37 d. Dark plus signs show the average ± one standard deviation of the mean in each of eight phase bins.

resulting light curve (Fig. 4.8) displays a low-amplitude, quasi-sinusoidal variation that probably corresponds to the binary orbital period. Note that the small radial velocity changes observed over a one-day interval are consistent with the small variations that are expected for an orbital period this long.

The Galactic latitude of HD 215227, $b = -12^\circ$, suggests that the star is quite far from the Galactic plane, and hence it may be a runaway star formed by a supernova (SN) explosion in a binary system (Gies & Bolton 1986a; Hoogerwerf et al. 2000). In this scenario, the SN explosion removes most of the mass of the progenitor star, and the stellar companion moves away from the explosion site with a speed comparable to its orbital speed at the time of the explosion. If the SN progenitor was the less massive component at the time of the explosion and if asymmetries in the SN outflow were modest, then the system remains bound as a runaway star with a degenerate companion. The runaway velocities may be large enough to move the system hundreds of parsecs away from the location of the SN over the lifetime of the stellar companion.

The distance to the star is quite uncertain, but an estimate may be made by comparing the expected stellar radius from evolutionary tracks with the angular diameter derived by fitting the spectral energy distribution (SED). Mass and radius estimates were derived from the $T_{\rm eff}$ and $\log g$ estimates in Table 4.6 by interpolating in the single star evolutionary tracks of Schaller et al. (1992). The SED was constructed using UV fluxes from the TD1 satellite (Thompson et al. 1978), Johnson magnitudes from Mermilliod (1991) transformed to flux using the calibration of Colina et al. (1996), 2MASS magnitudes (Skrutskie et al. 2006) transformed to flux according to the calibration of Cohen et al. (2003), and an AKARI 9 μm measurement (Ishihara et al. 2010). The SED (Fig. 4.9) indicates that there is a strong IR-excess from the Be star's disk that extends into the optical range. In order to fit the photosphere of the star alone, the range was restricted to the UV fluxes and B-band revised flux without the disk contribution (the lower point plotted at 4443 Å in Fig. 4.9). A theoretical flux spectrum was adopted from the models of R. L. Kurucz[5] for solar metallicity, $T_{\rm eff}$ and $\log g$ from Table 4.6, and a microturbulent velocity of 2 km s^{-1}.

---

[5] http://kurucz.harvard.edu/grids.html

This flux spectrum was fit to the restricted set of observations with two parameters: the limb-darkened, angular diameter θ_{LD} and the reddening $E(B-V)$ (assuming a ratio of total-to-selective extinction $R_V = 3.1$ and the reddening law from Fitzpatrick 1999). The observed and model emitted fluxes are related by

$$f_\lambda(\text{obs}) = \theta_{LD}^2 F_\lambda(\text{mod}) 10^{-0.4A_\lambda}$$

where A_λ is the wavelength dependent extinction (Fitzpatrick 1999). The first parameter θ_{LD} acts as a normalizing factor while $E(B-V)$ defines how the shape of the SED is altered by the extinction A_λ. The results for these two fitting parameters are given in Table 4.6, and the derived f_λ spectrum is plotted as a solid line in Figure 4.9. A very low reddening is found along this line of sight, $E(B-V) = 0.02$ mag. Earlier estimates consistently arrive at a higher reddening of $E(B-V) \approx 0.3$ mag (Snow et al. 1977; Neckel & Klare 1980; Hernández et al. 2005; Zhang et al. 2005), but all of these estimates are based upon the $B-V$ color and ignore the disk contribution in the optical that makes the star appear too red (Fig. 4.9).

Combining the SED-derived angular size θ_{LD} with the evolutionary radius $R_\star$ yields a large distance, $d = 2.6 \pm 1.0$ kpc, which places the star far beyond the nearby Lac OB1 association (Harris 1955). At this distance, HD 215227 resides well below the Galactic plane at $z = -0.56 \pm 0.20$ kpc. This is an extreme distance for a normal OB star. For example, in the Be star kinematical survey by Berger & Gies (2001), the mean distance is $<|z|>= 69$ pc and only one other star (HD 20340 at $z = -0.71$ kpc) out of a sample of 344 has a distance from the plane as large as

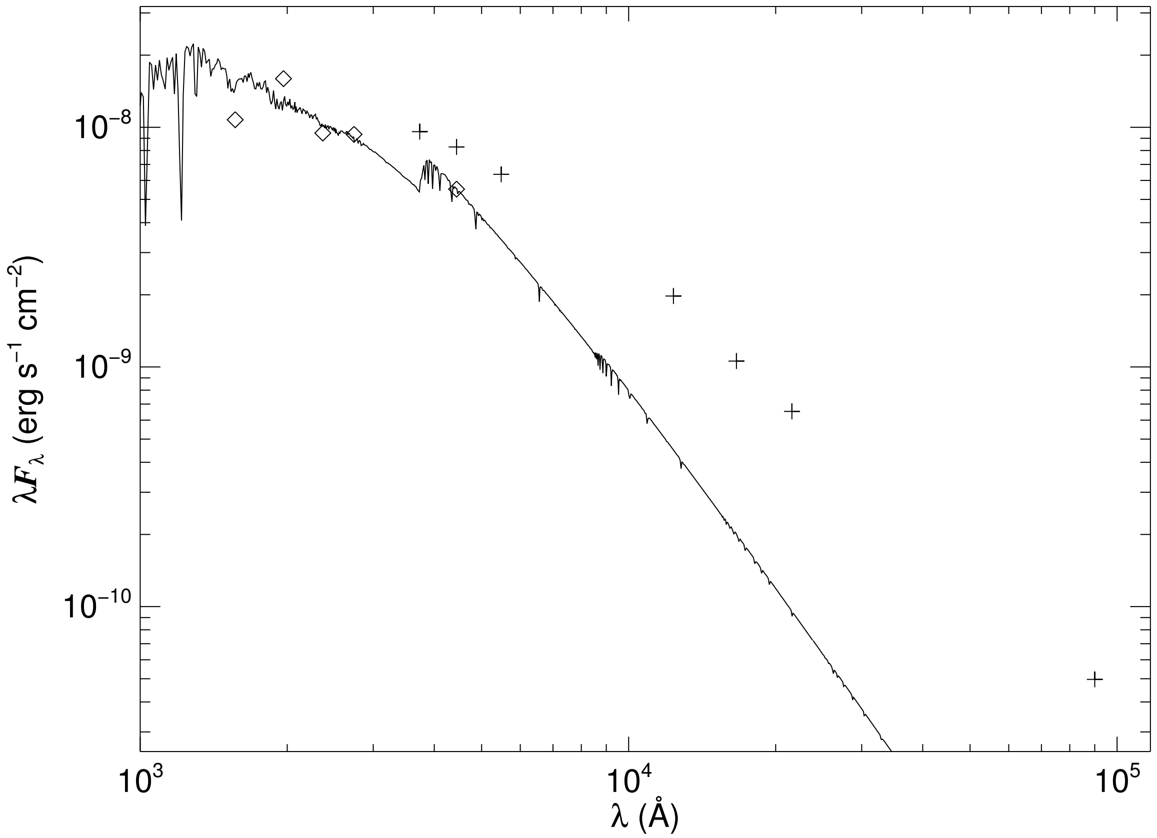

Figure 4.9 The spectral energy distribution of HD 215227. The diamonds indicate the observed fluxes used in the fit (UV fluxes and the B-band corrected flux) while the plus signs indicate those fluxes with a significant disk contribution that were omitted from the fit. The solid line shows the stellar model flux spectrum for the parameters given in Table 1.

that of HD 215227. This suggests that HD 215227 is a runaway star that probably obtained its initial high velocity and current position by a supernova explosion in a binary. The proper motions from van Leeuwen (2007) were adopted and the average radial velocity and distance from Table 4.6 were used to estimate the star's current peculiar values of tangential $V_{T\mathrm{p}}$, radial $V_{R\mathrm{p}}$, and space velocity $V_{S\mathrm{p}}$ via the method described by Berger & Gies (2001). These peculiar velocities are measured relative to the star's local standard of rest by accounting for the Sun's motion in the Galaxy and differential Galactic rotation. The estimates of the peculiar velocities (Table 4.6) are not unusually large, but the errors are significant and the star may have decelerated in the gravitational potential of the Galaxy.

The similarity of this Be binary to other gamma-ray binaries, its probable runaway status, and its close proximity to the gamma-ray source location all indicate that HD 215227 may be the optical counterpart of AGL J2241+4454. Additional spectroscopic observations are encouraged to search for orbital motion and to document the emission line variability around the orbit. New X-ray and radio observations with good angular resolution will be essential to secure the identification of the target (see the case of HESS J0632+057; Hinton et al. 2009; Skilton et al. 2009). Furthermore, a search for periodic gamma-ray brightening on the 60 d cycle would offer conclusive evidence of the connection with the Be star. If the orbital eccentricity is high, the gamma-ray emission may be restricted to a limited part of the orbit.

4.4 BD+36°4063

4.4.1 Introduction

Massive close binaries are destined to undergo extreme transformations once they begin to exchange mass and angular momentum (Langer et al. 2008). If mass transfer is conservative, then the system separation decreases as mass transfer progresses, and the orbit dimensions reach a minimum once a mass ratio of unity is reached. The system then experiences a critical phase in which the mass transfer rates may exceed $10^{-4} M_{\odot}$ y^{-1} (Wellstein et al. 2001). Subsequently, the orbit will widen after the mass donor becomes the lower-mass object, and a slower and more extended mass transfer stage will begin. The gainer accepts both mass and angular momentum, and it may quickly reach a state of critical rotation where gravitational and centripetal accelerations balance at the equator. This may limit further mass accretion and lead to the formation of a thick, opaque, and mass-losing disk surrounding the gainer star (Nazarenko & Glazunova 2006).

This stage of binary evolution is probably represented by the W Serpentis class of massive binaries (Plavec 1980; Tarasov 2000). These binaries contain a visible, low-gravity, donor star that fills its Roche lobe, while the higher-mass, gainer star is invisible in the composite spectrum because it is immersed in a thick disk. The first direct image of such a disk around a gainer star was recently made with the Center for High Angular Resolution Astronomy Array (CHARA Array; ten Brummelaar et al. 2005) for the best known member of the class β Lyrae (Zhao et al. 2008). The shortest period W Ser binary known is RY Scuti ($P = 11.1$ d). It consists of a $7M_{\odot}$, O9.7 Ibpe star and a $28M_{\odot}$ hidden companion (Grundstrom et al. 2007b), and the entire system is surrounded by a 2000-AU wide gas and dust torus (Smith et al. 2002). The known W Ser systems are probably experiencing the slow mass transfer stage after mass ratio reversal, and no W Ser system has yet been identified at the close, rapid mass transfer stage.

The missing link may be filled by BD+36°4063. The star (ON9.7 Iab; Walborn & Howarth 2000) is located in the Cyg OB1 association (Humphreys 1978). It was noted by Mathys (1989) as a key example of an ON star, showing spectral features indicating the N-enrichment and C-depletion characteristic of CNO-processed elements (Walborn & Howarth 2000). Many ON stars are members of binary systems

(Bolton & Rogers 1978) where mass transfer may remove the H envelope and reveal CNO-processed gas in the atmosphere. Thus, it is very pertinent that BD+36°4063 was discovered by Howarth (Walborn & Howarth 2000; Harries et al. 2002) to be a single-lined spectroscopic binary with a period of 4.8 d. In a recent meeting contribution[6], Howarth presents radial velocities and light curves confirming the 4.8-d orbital period, and he shows that although the companion is massive, its absorption features are completely absent from the observed spectrum.

The data collected and presented here confirm the binary motion detected by Howarth and preliminary orbital elements are presented. These data can be used to argue for the visible star filling its Roche lobe and that the high rate of mass transfer results in a dense disk that blocks a direct view of the massive companion.

4.4.2 Observations and Orbital Elements

Seven spectra of BD+36°4063 were obtained with the Kitt Peak National Observatory (KPNO) 2.1-m telescope from 2008 November 15 to 21. Exposures were usually 600 s in duration, leading to spectra with a S/N = 200 per pixel in the continuum. See Chapter 2 for more details on the instrument and specifics of these particular data.

Only one set of spectral lines was readily apparent in these spectra, so radial velocities were determined by cross-correlating each spectrum with a model spectrum from the TLUSTY/SYNSPEC BSTAR2006 grid (Lanz & Hubeny 2007). A model was selected for $T_{\rm eff} = 28$ kK, $\log g = 3.0$, and microturbulent velocity of 10 km $\rm s^{-1}$,

---

[6] http://www.lowell.edu/workshops/Contifest/talks/Howarth.pdf

Table 4.7. BD+36°4063 Radial Velocity Measurements

HJD ($-$2,400,000)	Orbital Phase	V_r (km s^{-1})	ΔV_r (km s^{-1})	$O-C$ (km s^{-1})
54785.624	0.660	126.7	2.4	5.1
54786.576	0.858	109.7	2.3	-0.8
54787.557	0.062	-61.9	1.9	16.7
54788.558	0.270	-180.0	2.2	-1.2
54789.567	0.480	-36.7	1.8	0.7
54790.556	0.685	132.1	2.1	-1.3
54791.559	0.894	77.9	2.1	-6.8

parameters that are typical for the star's classification (Ryans et al. 2002; Martins et al. 2005), although small variations in these stellar parameters do not significantly alter the resulting velocities. This model was also a N-enriched "CN" model to match the line spectrum better than Solar metallicity values. The model spectrum was transformed to the observed grid by interpolation and was then convolved with functions to account for rotational broadening (see section 4.4.3) and instrumental broadening. A number of spectral regions that contain ISM features or emission lines were omitted from the cross-correlation sample (all hydrogen lines, the diffuse interstellar band at λ4428, and He II λ4686). Table 4.7 lists the dates of observation, spectroscopic phases, radial velocities and uncertainties for the observations, and the observed minus calculated residual from the fit.

The seven day time span is much too short to derive an accurate orbital period, so the period was estimated from the light curve, which shows ellipsoidal variations in flux related to the tidal distortion of the star. Two sets of photometric measurements exist from all sky survey experiments. The first set of 111 Cousins I_C measurements was made between 2003 and 2007 by The Amateur Sky Survey (TASS[7]; Droege et al. 2006). The second set of 84 points was made in 1999 with the Northern Sky Variability Survey (NSVS[8]; Woźniak et al. 2004). Because the NSVS measurements record a broad spectral range (4500 – 10000 Å), a constant value of 1.099 mag was subtracted to bring their mean into coincidence with the mean of the I_C-band results. Despite differences in wavelength intervals, both the amplitude of variation and the ephemerides determined from each data set matched within uncertainties. A discrete Fourier transform of this combined time series immediately showed evidence of half the orbital period. A double-sinusoid light curve is exhibited in one orbit by tidally distorted stars, and for these data this yielded a period of $P = 4.8126 \pm 0.0004$ d and an epoch of ON star superior conjunction at $T_{\rm SC}$ = HJD 2,452,448.60 ± 0.08.

The remaining orbital elements were then determined using a fit of the velocities made with the non-linear, least-squares fitting program of Morbey & Brosterhus (1974). The weights were set to unity for most measurements (because they have comparable measurement errors), but the weight of the single datum in the negative branch was set to four (to balance the four measurements in the positive branch) and the weight of the two conjunction phase measurements was decreased to 0.5. The period was fixed at the photometrically derived value and then the orbit was fit for the circular orbital elements: systemic velocity $\gamma = -17 \pm 3$ km s^{-1}, velocity semi-amplitude $K = 163 \pm 3$ km s^{-1}, and epoch of superior conjunction of the ON star $T_{\rm SC}$ = HJD 2,454,787.26 ±0.03. Trial elliptical solutions did not improve the fit. The

---

[7] http://sallman.tass-survey.org/servlet/markiv/

[8] http://skydot.lanl.gov/nsvs/nsvs.php

rms of the fit, 6.6 km s^{-1}, is larger than the formal errors but comparable to those found in observations of other O-stars from this observing run. The spectroscopic epoch occurs (0.3 ± 0.2) d earlier than the prediction from the light curve ephemeris, which may indicate that the period is decreasing. The possibility of a measurable period change offers us an important diagnostic of the mass transfer rate that must be confirmed in future observations.

4.4.3 Binary Properties

The most surprising feature of the orbital solution is that the mass function is large, $f(m) = (2.18 \pm 0.12)M_\odot$, suggesting that the companion is a massive star. However, there is no clear evidence of absorption lines of the companion in the individual spectra. The expected radial velocities for any companion lines depend on the assumed mass ratio. An estimate of the mass ratio can be made by considering the projected rotational velocity $v \sin i$ of the ON star. If one assumes that the ON star fills its Roche lobe and rotates synchronously, then the ratio of $v \sin i$ to semiamplitude K is a monotonically increasing function of $Q = M_1/M_2$ (mass of the ON star divided by that of the hidden star; Gies & Bolton 1986b)

$$\frac{v \sin i}{K_1} = (Q+1)\Phi(Q)$$

where $\Phi(Q)$ is the fractional Roche radius of the ON star (Eggleton 1983). Thus, a measurement of $v \sin i$ may be used to determine the mass ratio. Measurements were made of the FWHM of the deep and relatively unblended line of Si IV $\lambda4088$, whose profile should be dominated by rotational broadening. The mean width of the line is FWHM $= 2.95 \pm 0.11$ Å, which is significantly larger than the instrumental broadening measured in comparison lines near this wavelength, FWHM $= 1.90 \pm 0.02$ Å. Synthetic spectra were then created for a grid of test values of $v \sin i$ by convolving the model spectrum with a rotational broadening function (Gray 2005) for a linear limb darkening coefficient of $\epsilon = 0.37$ (Wade & Rucinski 1985). It should be noted that varying the linear limb darkening coefficient even by a factor of two has no effect, within uncertainties, on $v \sin i$ measurements. These model profiles match the observed FWHM for $v \sin i = 126 \pm 15$ km s^{-1}. Although it is possible that some of the apparent line broadening is due to macroturbulence in the atmosphere, a test using a presumed macroturbulent broadening with $\xi = 50$ km s^{-1} (at the high end for similar supergiants; Ryans et al. 2002) resulted in the same $v \sin i$ because the instrumental broadening is so much larger than the expected macroturbulent broadening. The relation above then leads to a mass ratio $Q = 1.02 \pm 0.17$, i.e., the stars are about equal in mass.

No evidence is seen of absorption lines moving in anti-phase with a velocity comparable to that of the ON star. However, Figure 4.10 illustrates the orbital variations of the Hβ line in which an emission component does appear to share the orbital motion of the companion. A preliminary Doppler tomographic reconstruction of the two spectral components (Bagnuolo et al. 1994) was made assuming the mass ratio given above, and showed evidence of similar, anti-phase moving emission lines in Hγ, He I $\lambda\lambda 4387, 4471, 4713, 4921$, and He II $\lambda 4686$. These emission features probably form in a disk surrounding the gainer star. Significant emission lines also are observed at Hα

(see Howarth's conference poster) and in the near-IR at He II 2.058 μm and Brγ 2.166 μm (Hanson et al. 1996; Tamblyn et al. 1996). A comparison of the line depths in the reconstructed spectrum of the ON star with those in the model indicates that the continuum flux from the disk is faint, $F_2/F_1 \approx 0.1$. Note that the absorption part of Hβ appears deeper at conjunctions. The same deepening was observed in other lines that strengthen in slightly cooler atmospheres (Si III, O II). Similar changes are found in RY Scuti and are probably related to the tidal extension and gravity darkening of the donor star (Grundstrom et al. 2007b).

The example of RY Scuti shows that mass transfer to a thick disk can lead to systemic mass loss from the binary and the formation of circumbinary gas and dust structures (Smith et al. 2002). There is some indication that an infrared excess from such circumbinary material is present in the spectral energy distribution (SED) of BD+36°4063. Shown Figure 4.11 are the available flux measurements based upon Johnson UBV (Hiltner 1956; Colina et al. 1996), Strömgren (Crawford 1975; Gray 1998) TASS V, I_C, (Droege et al. 2006; Bessell et al. 1998), and 2MASS JHK_S magnitudes (Cohen et al. 2003; Skrutskie et al. 2006), plus mid-IR fluxes from the Spitzer/IRS post basic calibrated data archive[9] (Houck et al. 2004). These observed fluxes are fit with the BSTAR2006 flux model to determine the reddening (Fitzpatrick 1999) $E(B-V) = 1.28 \pm 0.06$ mag and ratio of total-to-selective extinction $R_V = 3.50 \pm 0.10$ (consistent with previous reddening estimates; Patriarchi et al. 2003). The limb darkened, angular diameter of the ON star is $\theta_{LD} = 97 \pm 8$ μas (after correction for a companion flux contribution of $F_2/F_1 = 0.1$). The resulting radius

---

[9] http://irsa.ipac.caltech.edu/applications/Spitzer/Spitzer/

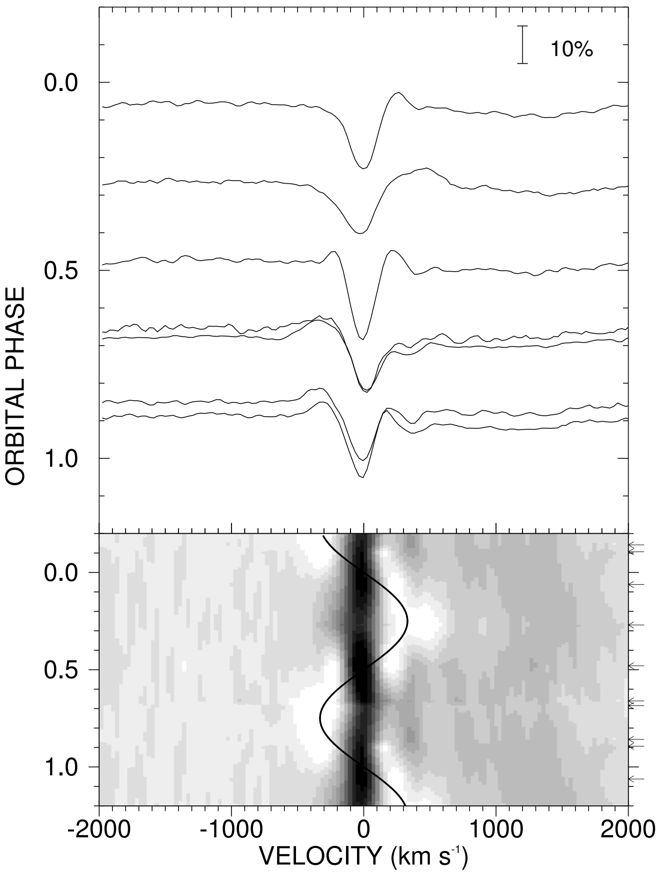

Figure 4.10 The variations of Hβ λ4861 as a function of orbital phase and velocity in the frame of the ON star. The intensity between observed spectra in the gray-scale image is calculated by a linear interpolation between the closest observed phases (shown by arrows along the right axis). The sinusoidal curve in the gray-scale image shows the relative velocity curve of the companion star. An emission component (bright in the gray-scale image) appears to follow the velocity curve for the companion star.

– distance relationship is $R_1/R_\odot = (10.4 \pm 0.8)\ d(\mathrm{kpc})$. There does appear to be a flux excess in the SED at wavelengths $> 8\mu$m that may result from systemic mass loss. Because the BSTAR2006 grid does not take winds into account, an SED from a CMFGEN model atmosphere (Hillier & Miller 1998) was fit with similar stellar parameters and a wind. The absolute fluxes from the CMFGEN model were systematically 5% higher than those from the BSTAR2006 SED over the optical to near-IR

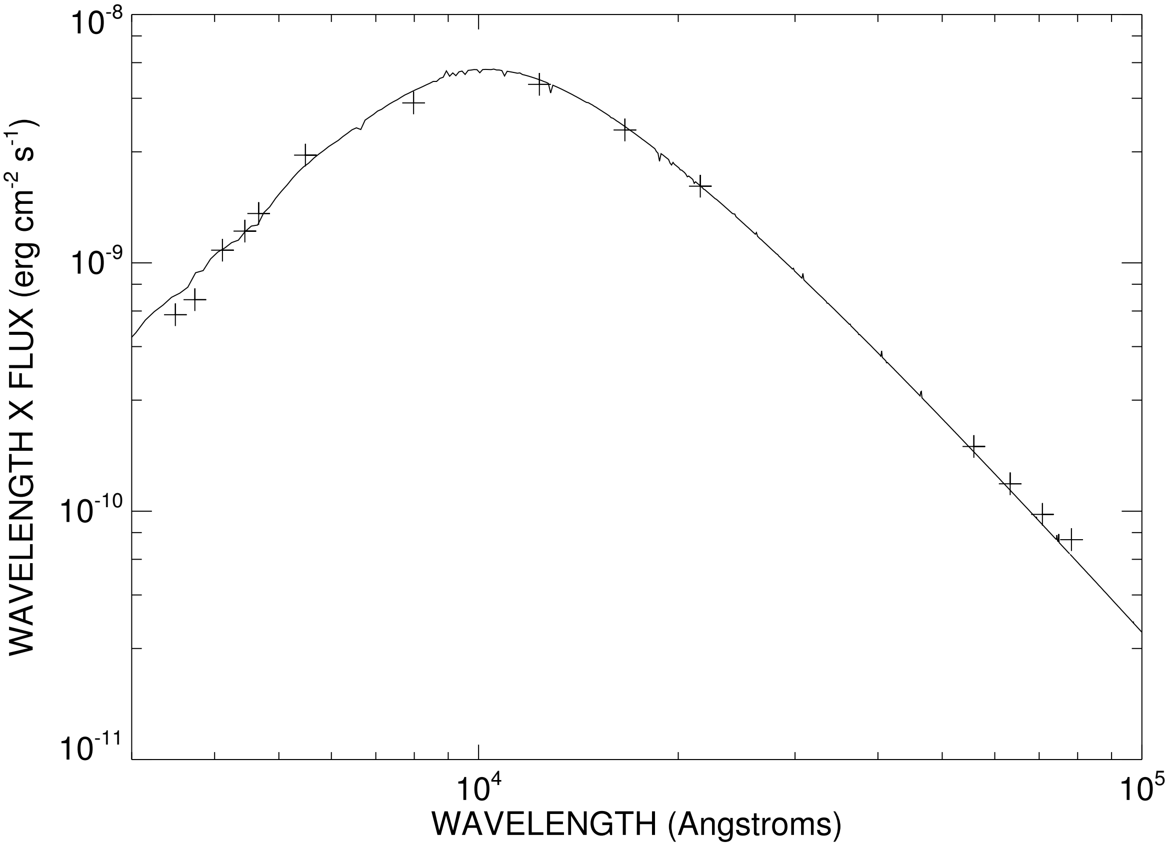

Figure 4.11 The spectral energy distribution for BD+36°4063. The plus signs indicate the observed fluxes while the solid line shows a reddened version of a BSTAR2006 flux model for the ON star.

range. However, there is no evidence of a marked IR excess near 10 μm from the wind in the CMFGEN model SED. This suggests that the observed excess may result instead from binary mass loss.

The available constraints on the masses of the stars are summarized in Figure 4.12. The mass ratio range derived from $v \sin i/K_1$ is indicated by the lines of constant slope. Next, the observed light curve can be used to constrain the orbital inclination. The ON star probably fills its Roche surface, and consequently the photometric variations are due to the star's tidal distortion (geometric shape and gravity darkening). The amplitude of the ellipsoidal light curve depends on the degree of Roche filling (assumed complete) and the orbital inclination (larger at higher inclination). Ideally one would create a model that includes both a Roche distorted mass donor and a disk surrounding the gainer (Djurašević et al. 2008), but given the small flux contribution of the disk and the relatively large errors in the photometric data, an approximate model was made assuming that the companion is a small spherical object (with the same temperature as the ON star) that acts only as a mild flux dilution source in the light curve of the tidally distorted ON star. The GENSYN binary code (Mochnacki & Doughty 1972) was used to create model I_C light curves for a grid of orbital inclinations, assuming that the ON star fills its Roche surface and that the companion has a radius that yields a monochromatic flux ratio, $F_2/F_1 = 0.1$ (matching that of the preliminary tomographic reconstruction). A best fit light curve (full amplitude ≈ 0.13 mag) then gives an inclination of $i = 49^\circ \pm 8^\circ$. The derived masses based on the spectroscopic mass function and this range in inclination are sketched as curved lines in Figure 4.12.

Combining the radius – distance relation derived from the SED with the projected rotational velocity (assuming a Roche filling, synchronously rotating, ON star) forms a distance – inclination relation, $\sin i = (1.15 \pm 0.16)/d(\mathrm{kpc})$. The inclination range shown in Figure 4.12 corresponds to distance range of 1.37 kpc ($i = 57^\circ$) to 1.76 kpc ($i = 41^\circ$), which agrees well with distance estimates for the Cyg OB1 association, $d = 1.25 - 1.83$ kpc (Uyanıker et al. 2001). One can also associate a stellar luminosity with any specific distance (or inclination) from the radius – distance relation. In the absence of mass transfer, the luminosity is expected to agree with the

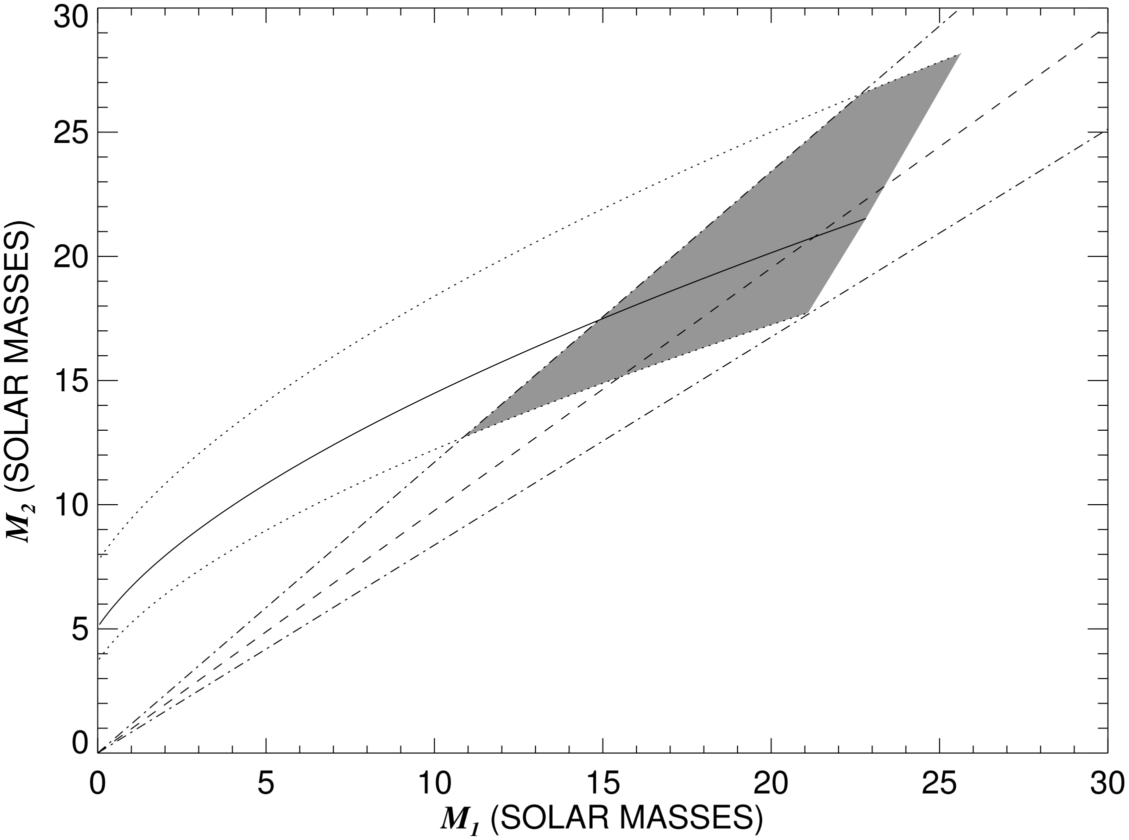

Figure 4.12 A mass plane diagram showing observational constraints on the masses of the ON star M_1 and the unseen companion M_2. The dashed line shows the mass ratio derived from $v \sin i / K_1$ and the adjacent dot-dashed lines give the associated $\pm 1\sigma$ error range. The solid line shows the relation from the spectroscopic mass function for an orbital inclination of $i = 49°$ derived from the light curve, while the dotted lines show the same for $i = 41°$ (*above*) and $i = 57°$ (*below*). These three lines are terminated where the ON star would be underluminous for its mass. The shaded region indicates the ranges meeting all the constraints.

mass – luminosity relation for single stars of its temperature (Schaller et al. 1992), so that one position along the constant inclination locus would be preferred. However, stars in binaries that suffer mass loss may appear overluminous for their mass, so in practice there is an upper limit along the inclination track where the star becomes more massive than expected for the luminosity. These terminal points are indicated in Figure 4.12. Because the Schaller et al. (1992) models do not account for rotation and because rapidly rotating stars may appear more luminous (Ekström et al. 2008), these end-point values should be taken as upper limits. The gray shaded region shows the preferred mass ranges that fulfill all the constraints, and the optimal fit occurs for $M_1 \approx M_2 \approx 21 M_\odot$.

The tentative picture that emerges from the spectroscopic analysis is that the ON star is transferring gas to a relatively faint disk that surrounds and obscures the companion star. The ON star must be very close to filling its Roche surface because evidence of its tidal distortion is seen in the light curve as ellipsoidal variations and in the deepening of lines at conjunctions. The emission features that follow the orbital radial velocity characteristics of the hidden mass gainer probably form in the thick disk. Thus, BD+36°4063 shares many features in common with the W Ser class of interacting binaries, but because the orbital period is much shorter and the mass ratio closer to unity than that found in other W Ser systems, this analysis suggests that BD+36°4063 represents an earlier and faster mass transfer stage of evolution. If the system is coeval with the stars of Cyg OB1 (with an age of approximately 7.5 Myr; Uyanıker et al. 2001), then the mass – radius – age relations for single-star evolutionary tracks (Schaller et al. 1992) suggest that the ON star probably began life with a mass of $25 M_\odot$ or less. Thus, the ON star has probably lost only a modest fraction of its original mass so far. BD+36°4063 offers an important glimpse of binary evolution at its most intense stage, and new observational efforts to probe the system and its environment are encouraged.

– 5 –

Double-Lined Spectroscopic Binaries

5.1 Introduction

Over the course of this research, I was fortunate enough to find three binaries, HD 42401, LH 54-425, and HI Mon, that exhibited two sets of lines in their spectra, i.e. SB2s. When spectra of each component of a binary system are combined with photometric variations in their light curves, the most important physical parameters of the stars, such as masses and radii, may be uniquely determined. These kinds of analyses are the pinnacle of my efforts in this dissertation. Two additional SB2 systems who analyses are still in the preliminary stages are also discussed, HD 103146 and HD 155775,.

5.2 HD 42401

5.2.1 Introduction and Observations

The star HD 42401 was first classified as B2 V by Walborn (1971). Since then, it has been used as a spectral standard for the B2 V type stars in a number of publications (Walborn & Fitzpatrick 1990; de Mello et al. 2000; Bagnuolo et al. 2001). The eclipsing nature of its light curve was first noticed with the *Hipparcos* satellite (HIP 29321), where it was classified as an Algol-type eclipsing binary and given the moniker V1388 Ori (Kazarovets et al. 1999). Three radial velocity measurements of HD 42401 by Fehrenbach et al. (1997) show a range from –103 to 36 km s^{-1}, but no further investigations were made into this probable velocity variable.

Observations of HD 42401 were made at the KPNO 0.9-m coudé feed telescope and the experimental setup is described in detail in Chapter 2. Exposure times were 1200 s resulting in a S/N $\simeq$ 100 pixel^{-1} with a resolving power of $R = 13,500$.

5.2.2 Radial Velocities

The narrow range of wavelength coverage in these spectra limits the lines that may be used for radial velocity analysis. Radial velocities were measured from three lines, He I $\lambda4387$, He I $\lambda4471$, and Mg II $\lambda4481$ via a template-fitting scheme (Gies et al. 2002) that measures velocities by using model templates weighted by a flux ratio to match both the shifts and line depths in the observed spectra. There is no evidence of emission or intrinsic line asymmetries in these lines or Hγ $\lambda4340$. The Hγ line was not used in the velocity analysis due to the combination of the extreme amount of blending and the large width of the line for each component in the system.

The BSTAR2006 grid of stellar models from Lanz & Hubeny (2007) was used to derive template spectra, shown in Figure 5.2. These models are based on the line blanketed, non-LTE, plane-parallel, hydrostatic atmosphere code TLUSTY and the radiative transfer code SYNSPEC (Hubeny 1988; Hubeny & Lanz 1995; Hubeny et al. 1998). In finding templates, initial values were used for temperatures, gravities, projected rotational velocities, and flux contributions from each star. These parameters for model templates were then checked by comparing the three lines used in radial velocity measurements against the tomographically reconstructed spectra of each star (see section 5.2.3). The parameters were changed and new templates made after initial fits to the light curve and radial velocity curves (see section 5.2.4) indicated slightly different values were more appropriate. The velocity analysis was then performed again until the best fit was obtained. In this way, an estimate of the monochromatic flux ratio was obtained in the blue spectra of $F_2/F_1 = 0.25 \pm 0.05$ based upon the relative line depths of the spectral components.

The template fitting scheme also needs preliminary estimates for the velocities of each component. To obtain these, spectra that clearly showed two sets of spectral lines were analyzed. Midpoints of spectral features were used to make crude estimates of radial velocities for each star. Preliminary orbital parameters were obtained by using the nonlinear, least-squares fitting program of Morbey & Brosterhus (1974). The preliminary velocities from this initial orbital solution were starting points for performing a nonlinear, least-squares fit of the composite profiles with the template spectra and calculating the shifts for each star. The fitting scheme searches a region of ±10 Å around the rest wavelength of each line, so preliminary velocities are mere starting points and need not be highly accurate. The values for radial velocity from the three lines in each spectrum were averaged, and the standard deviation of the mean value was calculated. Each of these values are listed in Table 5.1 for the primary and secondary stars. Also listed are the orbital phase for each observation and the observed minus calculated values for each data point. Phase zero is defined as the time of inferior conjunction of the primary star, $T_{\mathrm{IC},1}$ (time of secondary minimum in the light curve). Figure 5.1 shows two sample spectra at times of near quadrature according to this ephemeris.

HD 42401 is an eclipsing system, so during eclipse phases, velocity measurements may be affected by the Rossiter-McLaughlin effect in which the center of light of the eclipsed star will appear redshifted on ingress and blue shifted on egress because of

Table 5.1. HD 42401 Radial Velocity Measurements

Date (HJD−2,400,000)	Orbital Phase	V_1 (km s^{-1})	σ_1 (km s^{-1})	$(O-C)_1$ (km s^{-1})	V_2 (km s^{-1})	σ_2 (km s^{-1})	$(O-C)_2$ (km s^{-1})
54474.738	0.548	–36.3	5.4	6.9	90.6	3.8	12.9
54474.836	0.593	–71.7	3.3	–1.3	138.1	13.8	4.9
54476.690	0.441	82.7	0.4	2.3	–45.7	6.3	20.4
54476.735	0.461	65.6	3.3	–1.6	–21.1	8.3	18.1
54476.775	0.480	53.8	1.6	5.7	–35.8	21.7	–20.9
54477.672	0.890	–84.6	1.8	–3.8	152.6	6.9	1.2
54477.720	0.912	–70.4	4.0	–6.5	129.4	4.7	2.4
54477.800	0.949	–41.4	3.0	–8.9	84.4	2.0	–13.8
54478.660	0.342	139.3	0.9	–3.9	–160.9	5.4	8.2
54478.676	0.349	133.3	2.0	–6.3	–160.1	5.6	3.6
54478.718	0.368	125.0	1.9	–3.3	–156.2	5.4	–9.2
54478.779	0.396	109.6	4.1	0.3	–114.4	11.0	4.9
54478.840	0.424	87.6	2.0	–1.6	–76.1	16.9	10.9
54479.667	0.802	–128.4	0.9	–1.9	218.7	4.6	0.6
54479.718	0.825	–115.9	1.2	2.3	214.2	5.3	8.3
54479.760	0.845	–109.8	0.9	–0.8	194.8	2.0	2.4
54479.825	0.874	–90.2	0.5	1.3	174.5	2.6	7.5
54480.635	0.245	163.8	0.7	–1.5	–197.1	6.8	6.6
54480.684	0.267	163.2	3.8	–1.6	–196.5	5.7	6.2
54480.755	0.300	155.8	2.3	–3.3	–194.5	4.2	–1.0
54480.802	0.321	151.8	2.0	–0.5	–186.8	4.3	–3.9
54481.635	0.702	–127.3	2.5	1.6	240.8	6.7	20.8
54481.680	0.722	–135.7	2.4	–2.7	226.5	6.5	0.0
54481.728	0.744	–135.8	0.6	–1.1	222.2	2.5	–7.4
54481.794	0.775	–135.3	2.7	–2.5	234.0	4.6	6.9
54483.646	0.622	–94.4	2.2	–3.3	171.4	5.9	8.2
54483.687	0.640	–108.5	1.9	–5.8	180.2	2.5	–0.1
54483.757	0.672	–120.3	2.0	–1.5	200.8	2.9	–3.6
54483.839	0.710	–129.4	2.0	1.3	223.4	3.6	0.5

the rotational Doppler shifts of the visible portions. This effect will result in narrower line profiles as the red and blue shifted regions of the eclipsed star are blocked, and it is more prominent in broad-lined, rapidly rotating systems. HD 42401 is a short-period binary having relatively narrow lines, therefore the effect should be small. However, since the template method does not account for eclipses, deviations from orbital motion near eclipse phases are expected.

5.2.3 Tomographic Reconstruction

The Doppler tomography algorithm of Bagnuolo et al. (1994) was used to separate the primary and secondary spectra of HD 42401 for the F3KB CCD spectra. This iterative method uses the 24 observed composite spectra, their velocity shifts, and an assumed monochromatic flux ratio to derive individual component spectra. The best flux ratio was the one that best matched line depths in the reconstructions with those

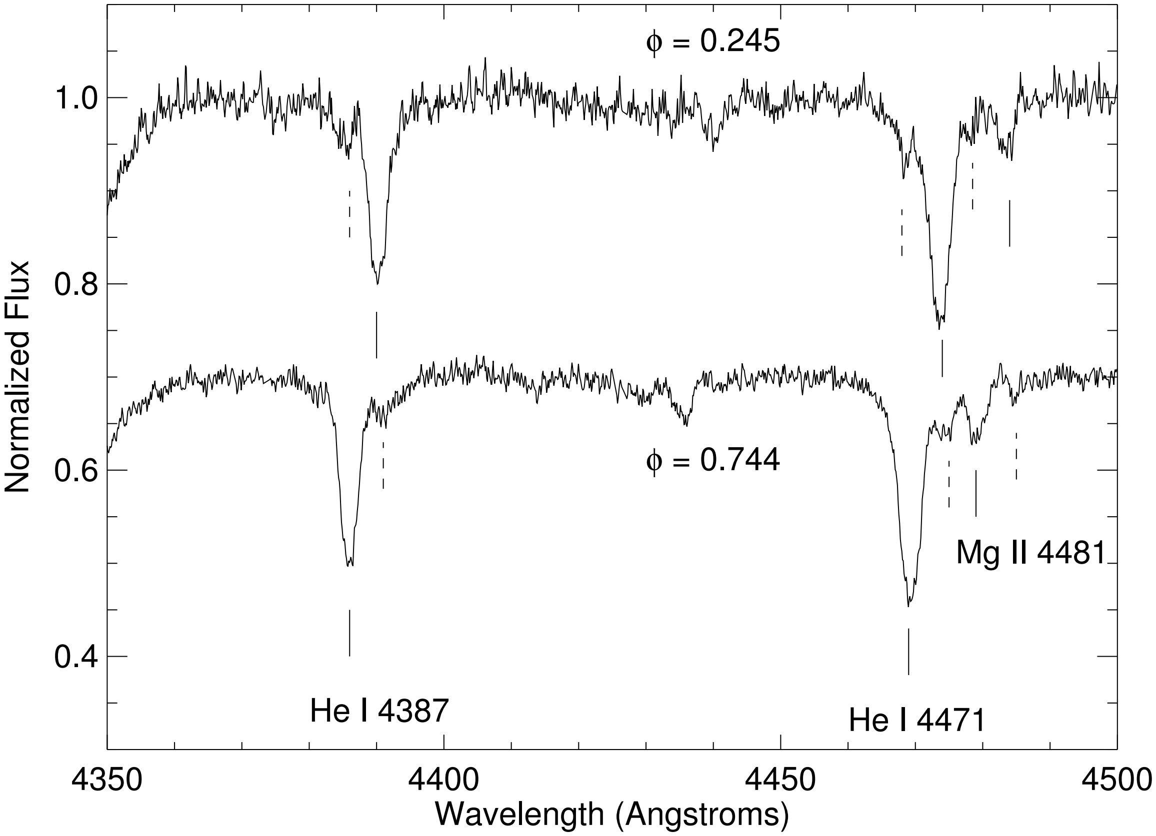

Figure 5.1 Two spectra of HD 42401 obtained near quadrature phases (offset for clarity). Solid lines indicate the positions of the primary component and dashed lines indicate those for the secondary component. The lines marked are those used in the velocity analysis.

in the model spectra. Figure 5.2 shows the reconstructed spectra for the primary and secondary with the best fit models over-plotted. The relative depths of He I $\lambda4471$ and Mg II $\lambda4481$ are good temperature indicators throughout the B-star sequence. Specifically, the He I $\lambda4471$ line gets weaker while the Mg II $\lambda4481$ line gets stronger as temperature decreases, as is seen in the spectrum of the secondary compared to that of the primary. The set of spectra from the F3KB instrument has only one spectrum that is close to an eclipse. Because there are many more spectra outside eclipse used

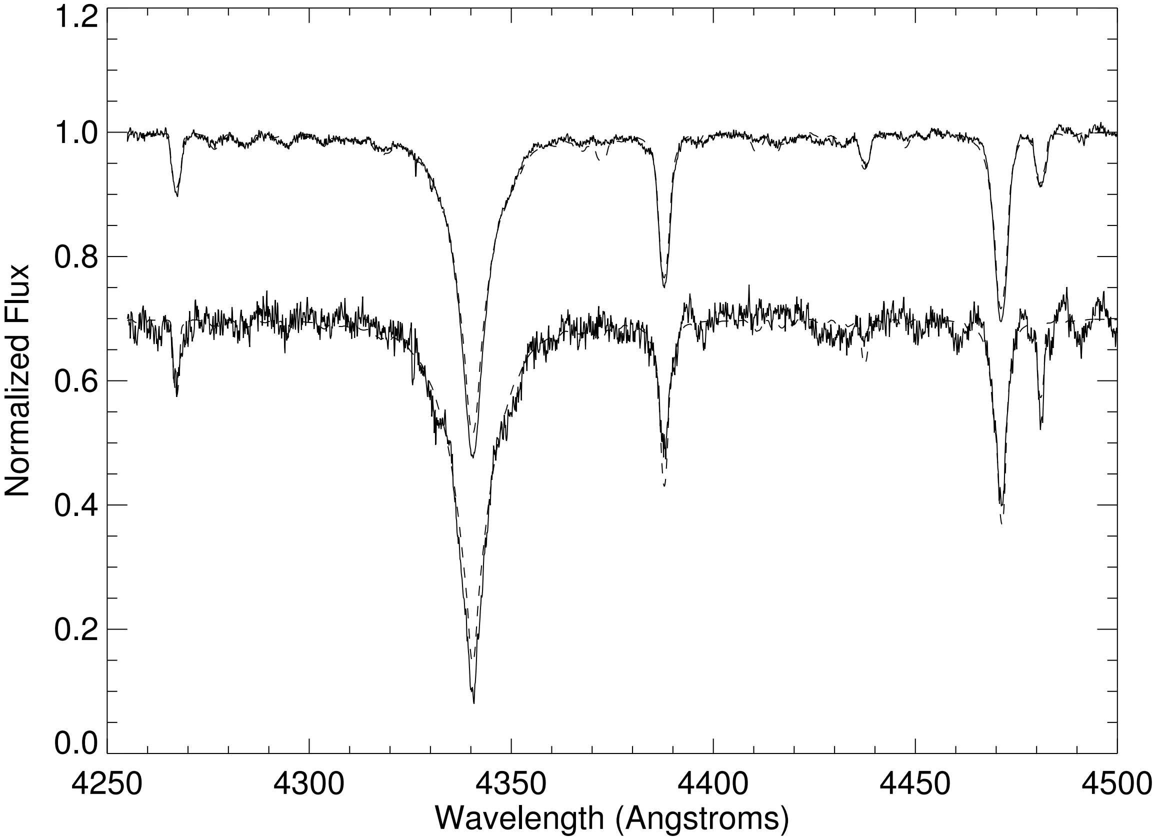

Figure 5.2 Tomographic reconstructions of the components of HD 42401 based on 24 spectra obtained with the F3KB instrument during 2008 January at KPNO. The top solid line represents the reconstructed spectrum of the primary and the bottom solid line is the reconstructed secondary spectrum offset by 0.3 for clarity. Overplotted for both are the model spectra for each (dashed lines). The stellar parameters for the model spectra are given in Table 5.2.

in the tomographic reconstruction, the final reconstructed spectra are insensitive to details of the Rossiter-McLaughlin effect. Indeed, tomographic reconstructions with the one eclipse spectrum omitted are negligibly different from those presented in Figure 5.2.

The final reconstructed spectra were fit with TLUSTY/SYNSPEC model synthesis spectra (see previous section). Fits to all three lines made in the velocity analysis

Table 5.2. Tomographic Spectral Reconstruction Parameters for HD 42401

Parameter	Primary	Secondary
Spectral Type[a] . .	B2.5 IV-V	B3 V
$T_{\rm eff}$ (kK)	20.5 ± 0.5	18.5 ± 0.5
log g (cgs)	3.75 ± 0.25	4.00 ± 0.25
v sin i (km s^{-1})	125 ± 10	75 ± 15
F_2/F_1 (blue)	0.25 ± 0.05	

[a] These spectral types are estimated from derived values of $T_{\rm eff}$ and log g.

were used to estimate the projected rotational velocity $v \sin i$, and the temperature and surface gravity of each star were estimated by comparing the reconstructed and model profiles for a grid of test values. These parameter values are listed in Table 5.2.

The narrow wavelength range of the spectra is insufficient to attempt classical spectral typing. However, an estimate may be made of the spectral types for each star in the HD 42401 system by comparing the derived effective temperatures with a spectral type versus effective temperature relation. According to Table 2 of Böhm-Vitense (1981) the effective temperature and gravity (see next section) of the primary of HD 42401 are most consistent with a B2.5 IV-V star while the secondary matches most closely with a B3 V star, and these classifications are listed in Table 5.2.

5.2.4 Combined Radial Velocity and Light Curve Solution

The ASAS V-band light curve for HD 42401 (ASAS 061059+1159.7) was extracted and points removed that had a grade of anything less than "A" – the highest quality data.

The Eclipsing Light Curve (ELC) code (Orosz & Hauschildt 2000) was used to find orbital and astrophysical parameters for the HD 42401 system. ELC fits the radial velocity and light curves simultaneously, giving a joint orbital ephemeris based on both sets of data. The best fit for the radial velocity curve is shown in Figure 5.3 (upper panel) along with the observed minus $(O-C)$ calculated residuals (lower panel). ELC treats calculation of velocities during eclipse via a flux-weighted velocity centroid as described in Wilson & Sofia (1976). The model velocity curves match the data well and the Rossiter-McLaughlin effect is clearly seen in the best fit as a slight redshift going into eclipse and a slight blueshift leaving eclipse. The best fit for the V-band light curve is shown in Figure 5.4. Figures 5.5 and 5.6 show the details of the fit for the light curve in the region of the primary and secondary eclipses, respectively.

The genetic optimizer mode of ELC was used initially to explore wide ranges of values for the period, epoch of inferior conjunction of the primary $T_{\rm IC,1}$, inclination, mass ratio, primary velocity semiamplitude, and Roche lobe filling factor, f, for each star. The Roche lobe filling factor is defined by Orosz & Hauschildt (2000) as the ratio of the radius of the star toward the inner Lagrangian point (L_1) to the distance to L_1 from the center of the star, $f \equiv x_{\rm point}/x_{L1}$.

The use of ELC included fixing the temperature of each star to the values found in the tomographic reconstructions and also fixing the radius ratio (R_1/R_2) based upon the temperatures, surface fluxes, and monochromatic flux ratio of the two stars. Non-zero eccentricities for the HD 42401 system were explored during fitting but rejected based on the higher χ^2 values for those fits.

To estimate the uncertainties based on the best fit, the values of the seven fitted

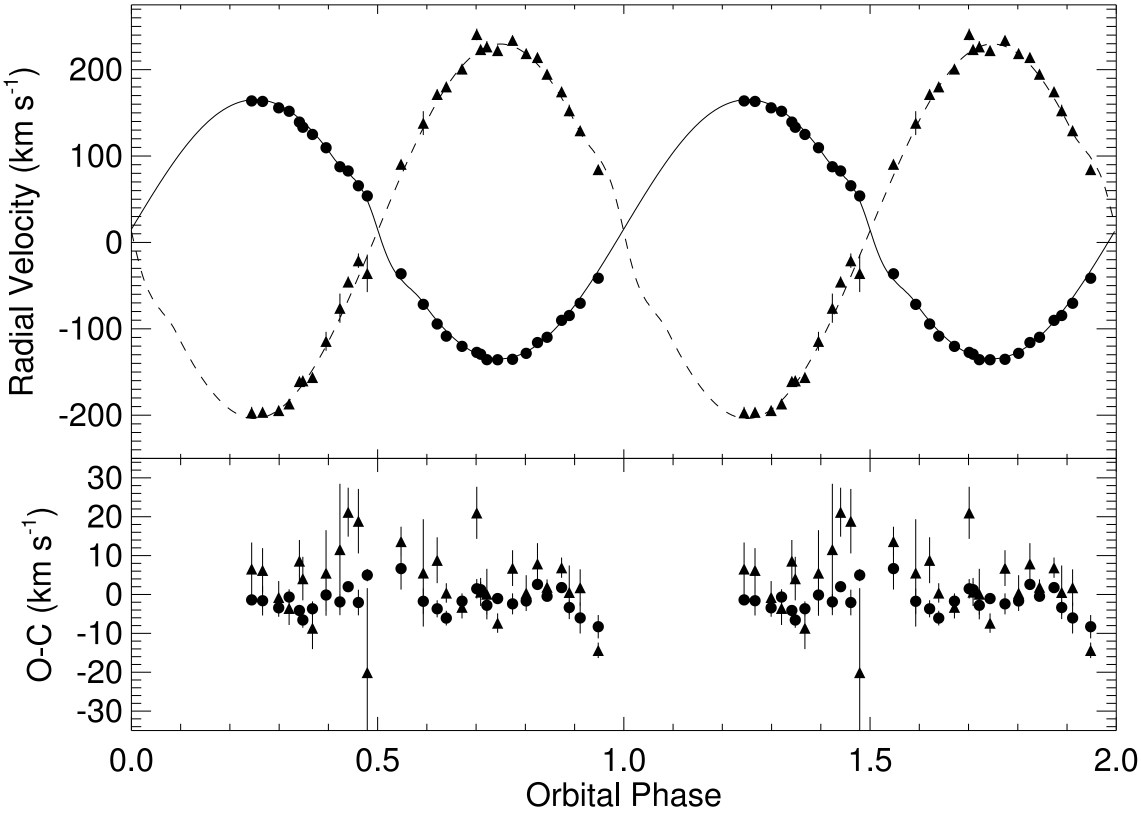

Figure 5.3 Radial velocity curves for HD 42401. Primary radial velocities are shown by filled dots and secondary radial velocities are shown by filled triangles with associated uncertainties shown as vertical lines. The solid line is the best fit solution for the primary and the dashed line is the same for the secondary. The lower panel shows the observed minus calculated values for each measurement with uncertainties.

parameters were varied in the calculation of $\sim 3 \times 10^6$ light and radial velocity curves. The well-explored χ^2 surface was then projected as a function of each fitted parameter or astrophysical parameter of interest. The lowest χ^2 value is found for each parameter, and the 1σ uncertainty may be estimated by the locus of minima where $\chi^2 \leq \chi^2_{\rm min} + 1$. These values and uncertainties are listed in Table 5.3 for the orbital parameters and Table 5.4 for the astrophysical parameters. Also listed are $R_{\rm eff}$, the effective radius of a sphere with the same volume, $R_{\rm pole}$, the polar radius of

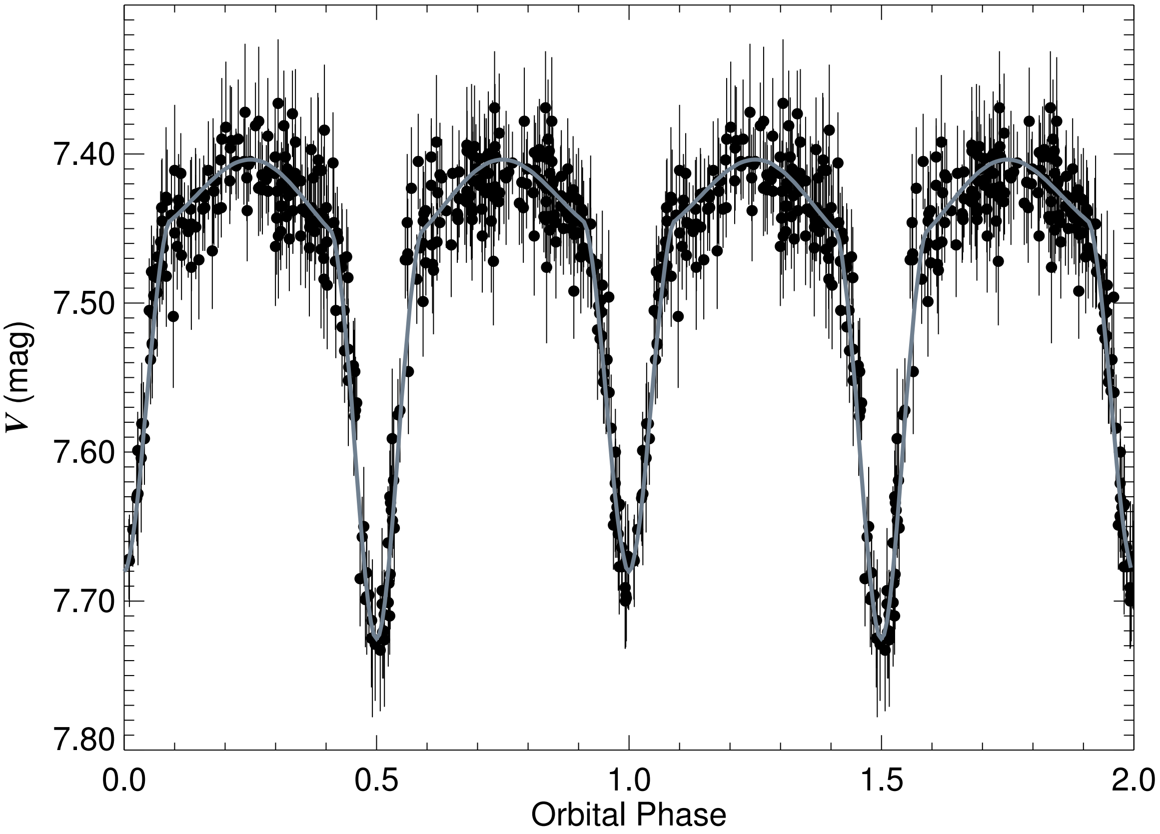

Figure 5.4 V-band light curve for HD 42401. These data were taken from the All Sky Automated Survey database (Pojmanski 2002) and are presented here in phase according to our best fit solution. The model is the thick gray line and the data are the filled dots with V uncertainties represented by vertical lines. Phase zero corresponds to inferior conjunction of the primary star.

each star, and R_{point}, the radius of the each star toward the inner Lagrangian point. The derived period of P= 2.18706 ± 0.00005 days for HD 42401 agrees well with the value found by the *Hipparcos* satellite of 2.18709 ± 0.00050 days (ESA 1997).

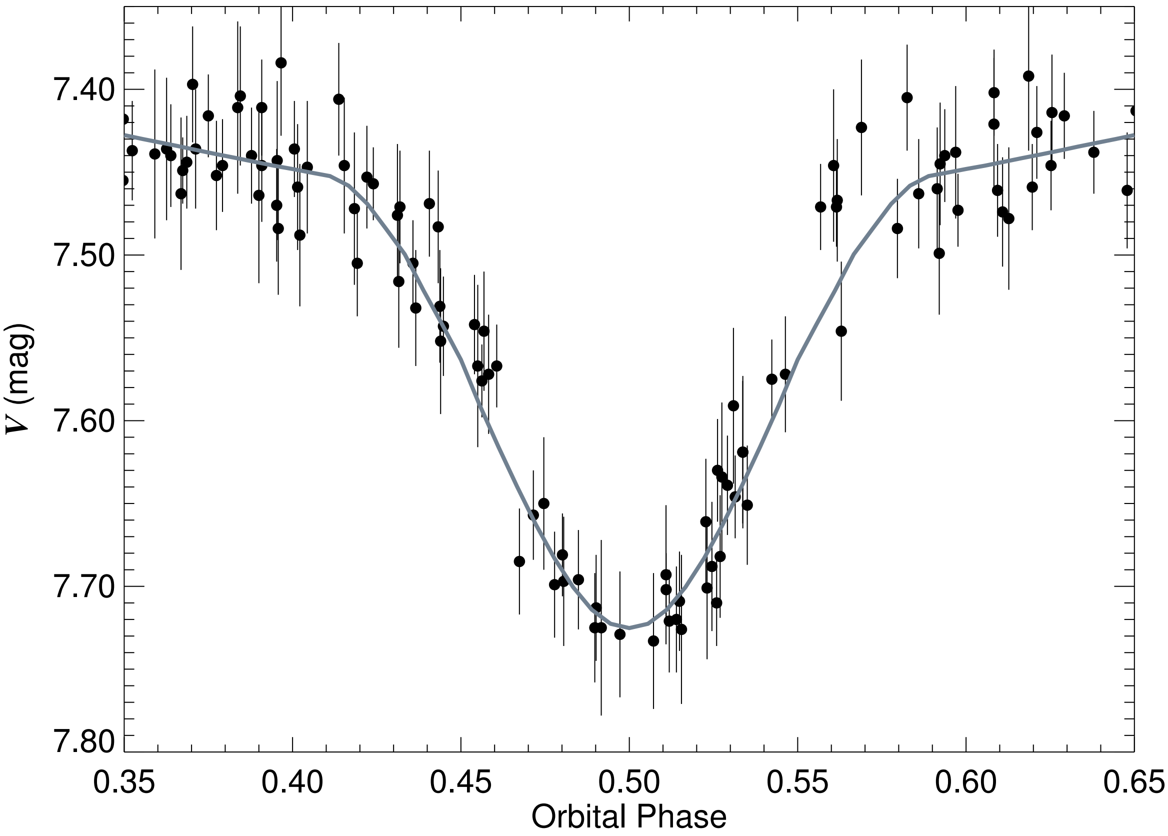

Figure 5.5 V-band light curve for HD 42401 around the time of primary eclipse. As with Figure 5.4, the model is the thick gray line and the data are filled dots with vertical lines representing uncertainties. Residuals are distributed as expected around the best fit.

5.2.5 Discussion

As is seen in Table 5.4, both stars are well within their Roche radii but experience tidal distortions that are seen in the light curve as ellipsoidal variations outside of eclipse phases (Fig. 5.4). The rotational velocities derived from the tomographic reconstructions (Table 5.2) match very well with the synchronous rotation values found by ELC (Table 5.4), indicating that this system has achieved synchronous rotation, and is therefore not very young.

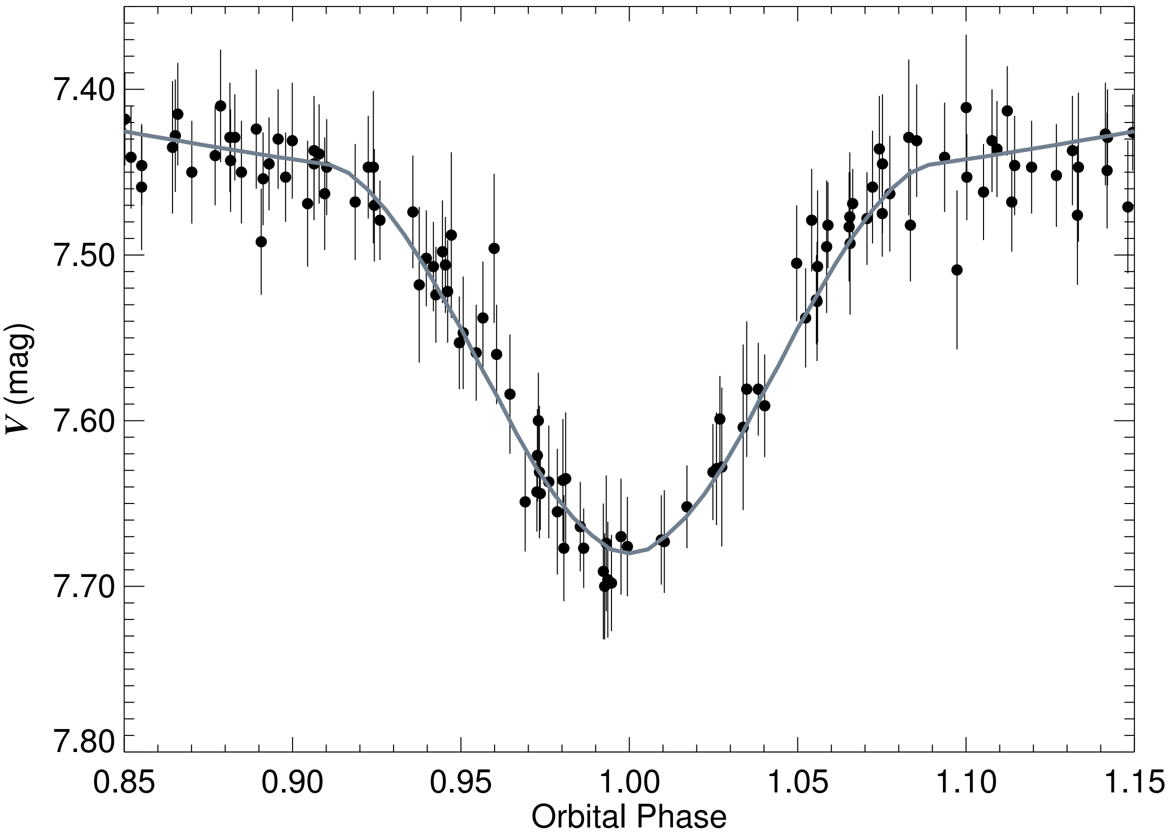

Figure 5.6 V-band light curve for HD 42401 around the time of secondary eclipse. As with Figure 5.4, the model is the thick gray line and the data are filled dots with vertical lines representing uncertainties. Here, as in Fig. 5.5, the residuals are distributed as expected around the best fit.

To make an estimate of the age of the system, the effective temperatures from Table 5.2 and radii from Table 5.4 are used to plot the two stars of HD 42401 on a theoretical H-R diagram and to compare their locations to evolutionary tracks. The result is shown in Figure 5.7, plotted against evolutionary tracks for stars of 5, 7, and 9 $M_\odot$ from Schaller et al. (1992) as well as isochrones from Lejeune & Schaerer (2001) for solar metallicity with ages of 21.9, 25.1, 27.5, and 31.6 Myr. The locations of the stars are most consistent with an age of $\sim$25 Myr. The model tracks shown

Table 5.3. Circular Orbital Solution for HD 42401

Element	Value
P (days)	2.18706 ± 0.00005
$T_{\mathrm{IC},1}$ (HJD–2,400,000) ...	54477.9130 ± 0.0002
K_1 (km s^{-1})............	151.4 ± 0.3
K_2 (km s^{-1})............	217.9 ± 1.0
γ_1 (km s^{-1})	15.32 ± 0.07
γ_2 (km s^{-1})	12.9 ± 0.2
rms (primary) (km s^{-1}) .	3.7
rms (secondary) (km s^{-1})	9.7
rms (photometry) (mag).	0.007

Table 5.4. ELC Model Parameters for HD 42401

Parameter	Primary	Secondary
Inclination (deg)...	75.5 ± 0.2	
M ($M_\odot$)..........	7.42 ± 0.08	5.16 ± 0.03
R_{eff} ($R_\odot$)..........	5.60 ± 0.04	3.76 ± 0.03
R_{pole}[a]($R_\odot$).........	5.40 ± 0.02	3.70 ± 0.01
R_{point}[b]($R_\odot$)........	5.97 ± 0.02	3.87 ± 0.01
v_{sync} sin i (km s^{-1})	125.5 ± 0.9	84.3 ± 0.6
log g (cgs).........	3.812 ± 0.005	3.999 ± 0.006
Filling factor	0.674 ± 0.005	0.588 ± 0.010
a_{tot} ($R_\odot$)..........	16.48 ± 0.05	
F_2/F_1	0.27 ± 0.04	

[a] Polar radius.

[b] Radius toward the inner Lagrangian point.

in Figure 5.7 are for non-rotating stellar models. The present ratios of spin angular velocity to critical angular velocity are $\Omega/\Omega_{\mathrm{crit}} = 0.45$ and 0.31 for the primary and secondary, respectively (assuming synchronous rotation), and the evolutionary tracks for such moderate rotation rates are only slightly steeper and more extended in time than those illustrated (Ekström et al. 2008). Thus, the derived age may slightly underestimate the actual value.

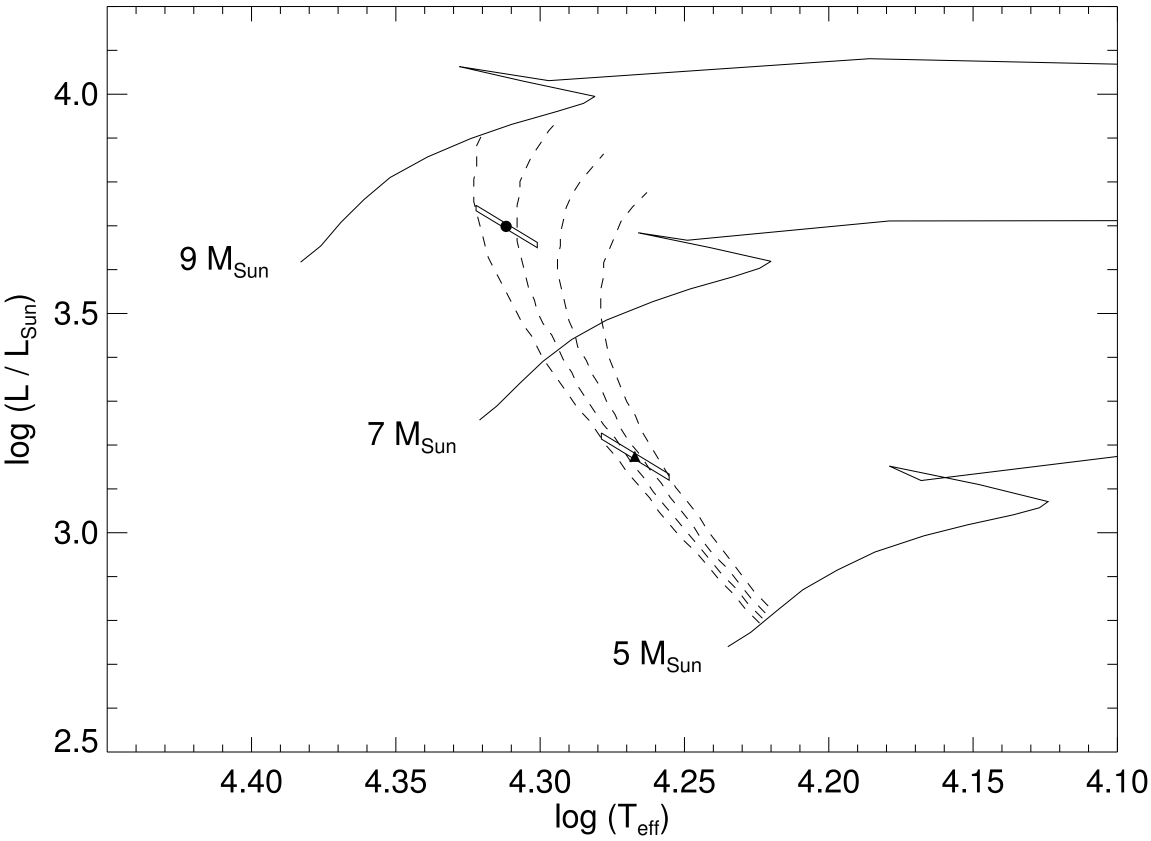

Figure 5.7 A theoretical H-R diagram showing the location of the primary star (*filled circle*) and secondary star (*filled triangle*) of HD 42401 including uncertainty regions for each. Also plotted are evolutionary tracks for stars of various masses from Schaller et al. (1992) and isochrones (*vertical dashed lines*) from Lejeune & Schaerer (2001) for solar metallicity with ages of 21.9, 25.1, 27.5, and 31.6 Myr going from left to right. The positions of the two stars are consistent with an age of ∼25 Myr.

Both stars appear (in Fig. 5.7) to be overluminous for the derived masses of 7.42 $M_{\odot}$ for the primary and 5.16 $M_{\odot}$ for the secondary. Table 3 of Harmanec (1988) lists astrophysical parameters for stars as a function of spectral type for main sequence stars based on empirical data from eclipsing binaries. The mass and effective temperature of the primary fit between the listed values for spectral types B2 (mean of 8.6 $M_{\odot}$) and B3 (mean of 6.1 $M_{\odot}$), but the radius is much larger than the means for comparable spectral types and matches a B0.5 star (mean of 5.5 $R_\odot$). The mass of the secondary is consistent with the B4 spectral type (mean of 5.1 $M_\odot$) while the effective temperature and radius appear more consistent with the B3 spectral type. In a study of eclipsing binaries in the Small Magellanic Cloud, Hilditch et al. (2005) found several systems of comparable mass that, like HD 42401, are overluminous compared to model predictions. However, these findings for HD 42401 seem in conflict with the results of Malkov (2003) who shows that early B-type stars that are in close systems and rotate more slowly than single stars are on average smaller than those same single stars. In a subsequent paper, Malkov (2007) studied well-separated binaries in an effort to use the properties of their component stars for a more direct comparison with single stars. His resulting mass-luminosity-radius relations, when applied to results derived here for HD 42401, predict less luminous, hotter and smaller components. This is perhaps not surprising, due to the age of HD 42401 and the evolution of its components from the zero age main sequence.

The distance to the system can be estimated by fitting an SED to various photometric measurements. The spectra were not flux calibrated, so to create an SED, literature photometry of the system must be used. HD 42401 is a relatively bright ($V \sim 7.4$) system and has thus been well studied. The problem arises in estimating the phase at which a particular observation in the historical literature was made. Two observations of HD 42401 were taken by *IUE* at $\phi = 0.12 \pm 0.07$ based on the orbital ephemeris in Table 5.3. The uncertainty in this estimate comes from the uncertainties in the values for $T_{\mathrm{IC},1}$ and period and the number of orbits between the *IUE* observations and observations analyzed here. The range in uncertainty for the orbital phase of the *IUE* data brings it close to eclipse, and this was supported by initial SED fits including the *IUE* data that indicated a lower UV flux than indicated by other measurements. Thus, the *IUE* measurements have not been used. There are various other measurements that also were sufficiently close to eclipses to be omitted in SED fitting. Fortunately, 2MASS (Cutri et al. 2003) measurements were obtained at $\phi = 0.16 \pm 0.03$ and are therefore far enough away from eclipse, within uncertainties, to be used. The only other points used were Johnson UBV magnitudes. To obtain these values, the value at quadrature from the ASAS light curve of $V = 7.40$ was used along with colors of $(B - V) = -0.042$ and $(U - B) = -0.620$, which are averages of several observations listed by Mermilliod & Mermilliod (1994). The SED fit is shown in Figure 5.8 along with the U, B, V, J, H, K_s magnitudes. Two model spectra from Lanz & Hubeny (2007) were computed for the effective temperatures and gravities of each star given in Table 5.2, and these were scaled in the blue by the flux ratio of 0.25 ± 0.05 found from the tomographic reconstructions. This fit of the SED results in a limb-darkened, angular diameter for the primary of $\theta_{\rm LD} = 62.7 \pm 1.1$ μas with a reddening of $E(B - V) = 0.15 \pm 0.01$ mag and a ratio of total-to-selective extinction of $R = 3.24 \pm 0.10$. By directly comparing this angular diameter with the value for the radius of the primary, the distance of the system is estimated to be $d = 832 \pm 89$ pc. This distance and reddening are in excellent agreement with the values in Bowen et al. (2008) of $E(B - V) = 0.15 \pm 0.02$ mag and $d = 0.8$ kpc.

HD 42401 has Galactic coordinates of $\ell = 197\overset{\circ}{.}64$ and $b = -3\overset{\circ}{.}33$ (Reed 2005). This is close to the Galactic open cluster NGC 2169 at $\ell = 195\overset{\circ}{.}61$ and $b = -2\overset{\circ}{.}93$ (separation $\sim 2\overset{\circ}{.}07$). Abt (1977) found that the earliest spectral type of the cluster

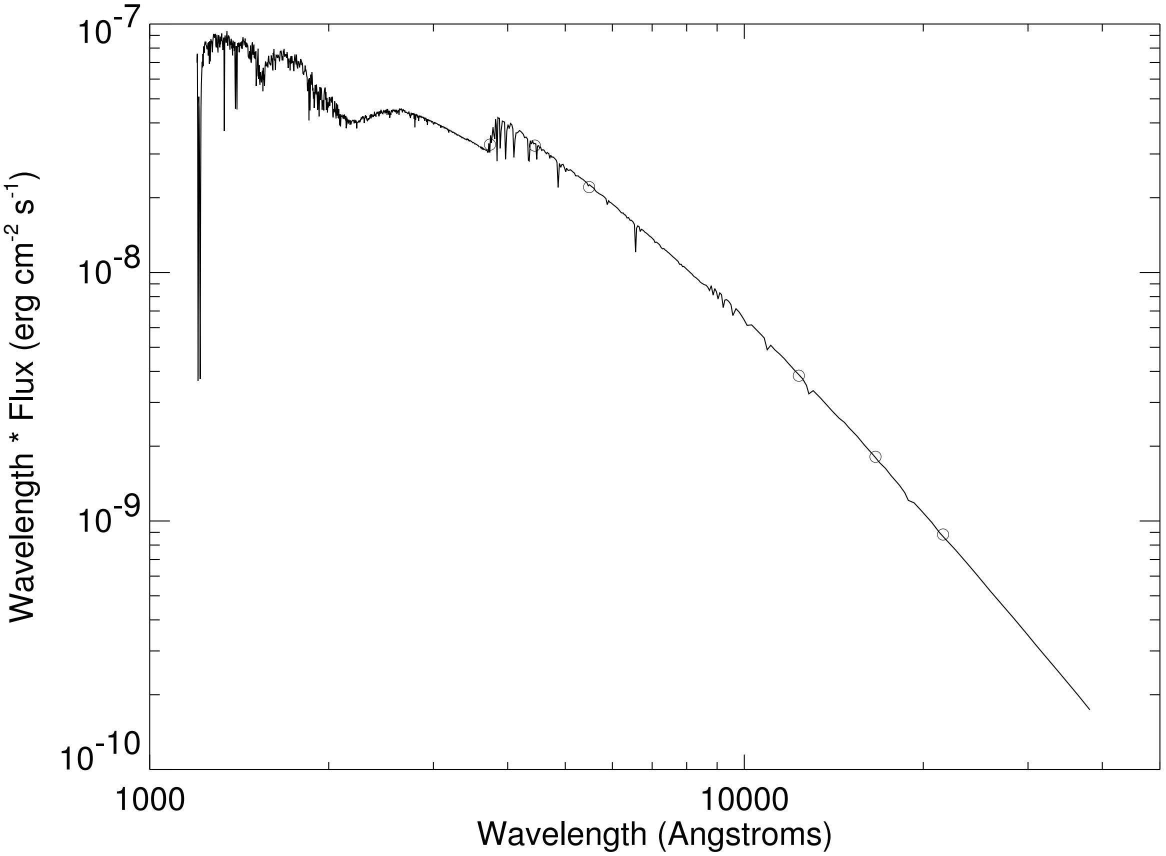

Figure 5.8 The spectral energy distribution and fit for the combined light of the HD 42401 components (*solid line*) to Johnson U, B, V, J, H, K_s photometry (*open circles*).

members of NGC 2169 was B2 III. Jeffries et al. (2007) find a reddening value of $E(B-V) = 0.20 \pm 0.01$ mag and a distance of $\sim$ 1060 pc to NGC 2169. Proper motions for the objects are similar as well, with HD 42401 having $\mu_\alpha\ cos\ \delta = -2.25 \pm 1.41$ mas yr^{-1} and $\mu_\delta = -2.71 \pm 0.53$ mas yr^{-1} (ESA 1997) and NGC 2169 having $\mu_\alpha\ cos\ \delta = -2.17 \pm 1.41$ mas yr^{-1} and $\mu_\delta = -2.52 \pm 0.53$ mas yr^{-1} (Kharchenko et al. 2005). The systemic velocity derived here for HD 42401 is $\sim$ 14 km s^{-1} and the average of 8 stars in NGC 2169 is 22 km s^{-1} (Kharchenko et al. 2005). While the proximity of HD 42401 to NGC 2169 is intriguing and the fact that the earliest star has a similar spectral type to the components of HD 42401, actual cluster membership is unlikely. The age of NGC 2169 in the literature ranges from 9 ± 2 Myr (Jeffries et al. 2007) to 7.8 Myr (Kharchenko et al. 2005), too young to fit comfortably with the data for the components of HD 42401 in Figure 5.7. Kharchenko et al. (2005) determined the corona radius of NGC 2169 by matching stellar densities of the cluster to that of the background and found an angular size of 0.15 degrees. The distance on the sky of HD 42401 from NGC 2169 is about 14 times this radius. The difference in distances to the two objects and their separation on the sky make cluster membership even more unlikely. However, it is possible that a wave of star formation associated with the Orion arm of the Galaxy swept through the region, leaving HD 42401 behind as it moved on and eventually led to the creation of NGC 2169.

5.3 LH54-425

5.3.1 Introduction and Observations

The earliest type star in the Large Magellanic Cloud LH 54 OB association is [L72] LH 54-425 (Hill et al. 1994), also known as L54S-4 (Oey 1996). Its spectral type was classified by Oey & Smedley (1998) as O4 III(f*). Its binary nature was unknown until Ostrov (2002) noted the ellipsoidal variations in the V-band photometry and obtained six spectroscopic observations of the system. The light and radial velocity curves from that study were used to estimate the masses of the two stars at 100 $M_\odot$ and 50 $M_\odot$. The lack of phase coverage for the radial velocity data did not allow for a more rigorous analysis of physical parameters.

Two sets of observations were used in this analysis. The first set was obtained at the CTIO 1.5-m telescope and is described in Chapter 2. A total of 48 spectra were obtained with exposure times of 1800 s, resulting in a S/N $\sim$ 70. The second set of data were given to me by Alceste Bonanos after talking with her at International Astronomical Union conference 250 in December 2007. These observations were obtained with the echelle spectrograph on the 2.5-m DuPont telescope at Las Campanas Observatory binned 2×2 with a resolving power of ≈ 27000 (from measurements of arc lamp spectra). Exposures were combined where there were two, and the spectral flux was normalized. Orders were merged and cosmic rays removed. For continuity of analysis, these data were clipped and re-sampled to match the wavelength and lower resolution CTIO data.

5.3.2 Radial Velocities and Orbital Elements

Radial velocities were measured using a template-fitting scheme (Gies et al. 2002) for the five lines Hδ λ4101, He II λ4200, Hγ λ4340, He II λ4541, and He II λ4686. These were the only prominent lines in the spectrum of each star. The spectra show no evidence for wind effects in the lines used to derive the orbital solution. No clear emission features and no asymmetries of absorption features were seen in the hydrogen lines or the He II λ4686 line.

The He II $\lambda\lambda$4542, 4686 lines were used to derive matching template spectra for the primary and secondary components. Template spectra were obtained from the grid of O-type stellar models from Lanz & Hubeny (2003). In order to find matching templates, approximations were initially used for the temperatures, gravities, projected rotational velocities, and flux contributions from each star. These initial parameters for model templates were then checked after velocity analysis by studying the properties of the tomographically reconstructed spectra of the components, as shown below.

The template fitting scheme also needs preliminary estimates of the velocities for the primary and secondary. To obtain these estimates, the He II $\lambda4541$ line for each star was fit using Gaussian functions with the "splot" routine and deblend option in IRAF. Radial velocity shifts were then calculated for all spectra with well separated lines, and these were used to obtain initial orbital parameters. The preliminary velocity from the initial orbital solution gave a starting point to perform a non-linear, least squares fit of the composite profiles with the template spectra and to calculate the shifts for each star. The five values for radial velocity from each set of five lines in an individual spectrum were then averaged to obtain a mean value, and the standard deviation of the mean value was calculated. Each of these values are listed in Table 5.5 for the primary and secondary stars, as well as the orbital phase for each observation and the observed minus calculated values for each point. Zero phase is defined to be the time of inferior conjunction of the primary star, $T_{\mathrm{IC},1}$.

An orbital fit of the radial velocity data was made using the non-linear, least-squares fitting program of Morbey & Brosterhus (1974). Equal weights were assigned to each data point because all the spectra were comparable in S/N ratio, spectral coverage, resolving power, and quality of radial velocities derived. It should be noted that for massive binaries, discrepancies in systemic velocities between components may be attributed to differences in their expanding atmospheres and/or differences in the shapes of template spectral lines, so systemic velocities were fit for each component. Fits with non-zero eccentricities were explored, none of which gave as good

Table 5.5. LH 54–425 Radial Velocity Measurements

Date (HJD$-$2,400,000)	Orbital Phase	V_1 (km s^{-1})	σ_1 (km s^{-1})	$(O-C)_1$ (km s^{-1})	V_2 (km s^{-1})	σ_2 (km s^{-1})	$(O-C)_2$ (km s^{-1})
52714.5496	0.080	393.0	6.7	–4.1	126.4	20.7	–16.2
52714.5756	0.092	398.5	12.9	–11.1	72.8	49.6	–47.5
52714.6009	0.103	414.3	4.9	–6.7	90.9	42.1	–9.2
52714.6312	0.116	430.9	11.7	–3.1	91.2	14.6	14.0
52714.6586	0.129	431.4	15.6	–13.7	39.1	38.6	–18.4
52715.5251	0.514	269.6	9.7	–11.8	405.9	16.7	57.1
52715.5487	0.525	263.0	9.1	–4.8	404.0	23.1	31.4
52715.5725	0.535	231.3	5.7	–23.8	423.6	11.5	28.5
52715.5971	0.546	242.3	11.1	0.9	384.8	9.1	–34.4
52715.6216	0.557	213.4	5.0	–14.5	418.4	14.3	–24.4
52716.5492	0.970	245.8	19.2	–16.0	389.8	20.5	4.4
52716.5722	0.980	234.2	17.4	–40.4	398.1	17.8	35.6
52716.5952	0.990	252.9	24.1	–34.6	354.5	27.1	15.3
52716.6182	0.000	343.9	31.6	43.4	231.1	35.6	–84.7
52717.5139	0.399	443.8	14.0	23.5	149.6	39.9	43.9
52717.5370	0.409	419.3	16.6	10.1	147.8	39.3	22.5
52717.5642	0.421	404.9	10.2	8.8	171.2	21.5	22.8
52717.5878	0.432	387.5	15.0	3.5	183.0	23.3	13.3
52717.6122	0.443	378.2	16.3	6.8	198.6	17.0	6.8
52718.5139	0.844	139.1	6.4	5.6	621.2	55.7	7.8
52718.5370	0.854	137.6	20.6	–3.3	595.3	28.4	–5.0
52718.5600	0.864	142.0	9.3	–7.0	563.3	26.1	–22.8
52718.5831	0.875	151.1	10.2	–6.6	575.4	26.5	4.6
52718.6060	0.885	157.9	7.4	–9.2	536.5	18.1	–17.8
53017.5789	0.915	152.5	12.4	–44.9	469.5	23.3	–31.0
53017.7698	0.000	323.6	25.6	23.8	259.5	36.7	–57.5
53018.5366	0.341	499.9	22.4	30.8	67.6	46.7	48.4
53019.5645	0.798	102.2	11.9	–6.7	654.1	12.7	–1.9
53019.7591	0.785	160.2	21.6	–6.8	555.3	18.5	0.8
53020.5382	0.232	515.8	11.4	17.4	–10.0	42.2	24.9
53021.5305	0.673	149.7	15.4	28.0	662.8	8.9	32.1
53021.7435	0.768	104.3	6.8	3.2	670.6	3.7	1.5
53022.5223	0.114	437.1	23.5	5.0	135.2	47.4	54.7
53023.5216	0.559	249.2	10.4	23.7	419.2	8.9	–27.8
53027.5315	0.344	441.2	14.8	–26.2	25.6	8.6	3.5
53028.5271	0.786	118.3	17.8	13.2	674.8	17.5	12.3
53028.7270	0.875	165.0	8.0	6.9	591.8	37.4	21.7
53029.5269	0.231	518.6	9.8	20.2	19.6	32.4	54.4
53030.5260	0.676	131.5	10.3	11.4	631.7	15.5	–1.9
53030.7169	0.761	96.7	10.5	–3.6	683.5	20.2	13.2
53031.5200	0.118	475.7	22.6	40.1	118.6	20.8	44.2
53032.5246	0.565	234.0	18.9	15.5	487.5	48.1	28.3
53032.7225	0.653	146.3	3.9	12.1	569.6	21.2	–38.7
53033.5391	0.017	346.1	6.3	25.4	209.5	20.0	–69.8
53710.7543[a]	0.347	539.9	39.3	75.4	31.7	33.4	5.4
53711.7167[a]	0.776	77.1	52.7	–29.5	688.2	79.4	23.6
53748.5493	0.165	458.6	11.7	–13.4	14.7	21.9	4.2
53752.6857	0.006	304.4	25.3	–2.3	282.6	31.5	–22.0
53753.5655	0.397	454.1	15.9	32.0	73.8	23.6	–28.8
53755.7542	0.371	438.2	9.6	–8.5	–3.4	20.9	–62.5
53765.6205[a]	0.761	55.1	21.2	–49.6	623.4	64.7	–44.4
53766.6131[a]	0.203	526.3	43.6	40.6	–54.9	78.2	–37.6

[a] Data from the echelle spectrograph on the 2.5 m DuPont telescope at Las Campanas.

a fit as a circular orbital solution. Fits were also made for subsets of measurements near conjunction (phases near 0.0 and 0.5) and quadrature (phases near 0.25 and 0.75). These tests revealed that the important spectroscopic elements, such as the velocity semi-amplitudes, did not vary by more than 3σ from the best fits for any subset. The results for the orbit using spectroscopic data only are listed in column 3

Table 5.6. Circular Orbital Solutions for [L72] LH 54-425

Element	Combined Solution	Spectroscopic Solution
P (days).................	2.24741 ± 0.00004	2.24746 ± 0.00010
$T_{\mathrm{IC},1}$ (HJD–2,400,000) ...	53029.007 ± 0.003	53029.016 ± 0.007
K_1 (km s^{-1}).............	201.6 ± 3.8	210.8 ± 3.0
K_2 (km s^{-1}).............	359.1 ± 4.5	350.8 ± 5.2
γ_1 (km s^{-1})..............	299.7 ± 0.6	303.1 ± 2.0
γ_2 (km s^{-1})..............	316.7 ± 2.2	317.7 ± 3.3
rms (Primary) (km s^{-1}) .	19.4	21.9
rms (Secondary) (km s^{-1})	33.2	32.8
rms (Photometry) (mag).	0.007	...

of Table 5.6. The radial velocity measurements and final orbital velocity curves (see below) are shown in Figure 5.9.

5.3.3 Tomographic Reconstruction

A Doppler tomography algorithm (Bagnuolo et al. 1994) was used to separate the primary and secondary spectra of [L72] LH 54-425. This is an iterative method that uses the 48 observed composite spectra from CTIO, their velocity shifts, and an assumed monochromatic flux ratio (F_2/F_1) to derive the individual component spectra. A range of flux ratios was explored to find a value that best matched the line depths in the reconstructions with those in model spectra. Figure 5.10 shows the reconstructed spectra for the primary and secondary, as well as synthetic spectra just below each. Few lines are present in the spectra. However, the relative strength of the He I λ4471 in the secondary is the major difference between the two spectra and indicates the cooler temperature of the secondary.

These reconstructed spectra were fit with TLUSTY/SYNSPEC model synthesis

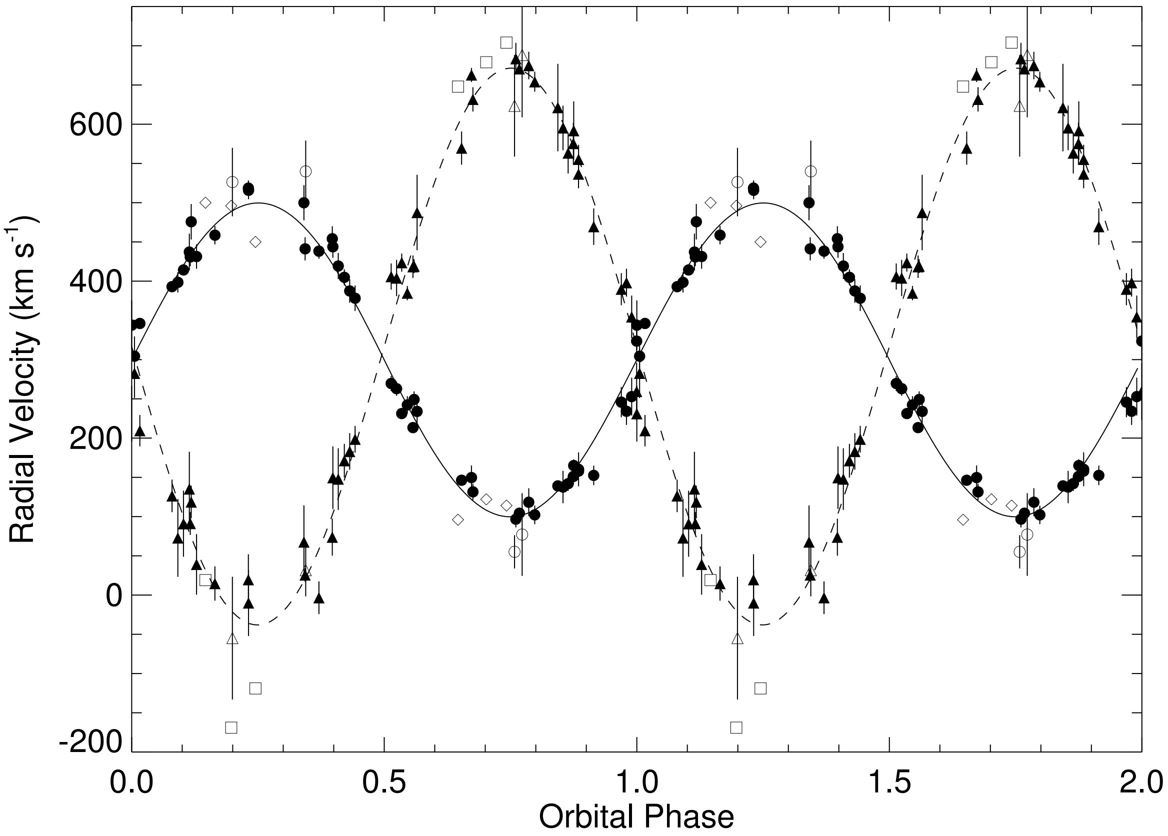

Figure 5.9 Radial velocity curves for [L72] LH 54-425. Primary radial velocities are shown by filled dots and secondary radial velocities are represented by filled triangles with associated uncertainties shown as vertical lines for both. The open circles and triangles represent the echelle data from Las Campanas. The open diamonds and squares are the radial velocity measurements from Ostrov (2002) for the primary and secondary, respectively. The Ostrov data were not used in model fits. The solid line is the best combined fit solution for the primary, and the dotted line is the same for the secondary.

spectra. These matches allow for estimates of stellar parameters listed in Table 5.7. The width of the He II $\lambda4542$ line was used to estimate the projected rotational velocity $v \sin i$ for each star by comparing the reconstructed and model profiles for a grid of test $v \sin i$ values. Matches were made to the Hγ $\lambda4340$ and He I $\lambda4471$ lines to obtain the temperature and surface gravity estimates. Finally, the ratios of

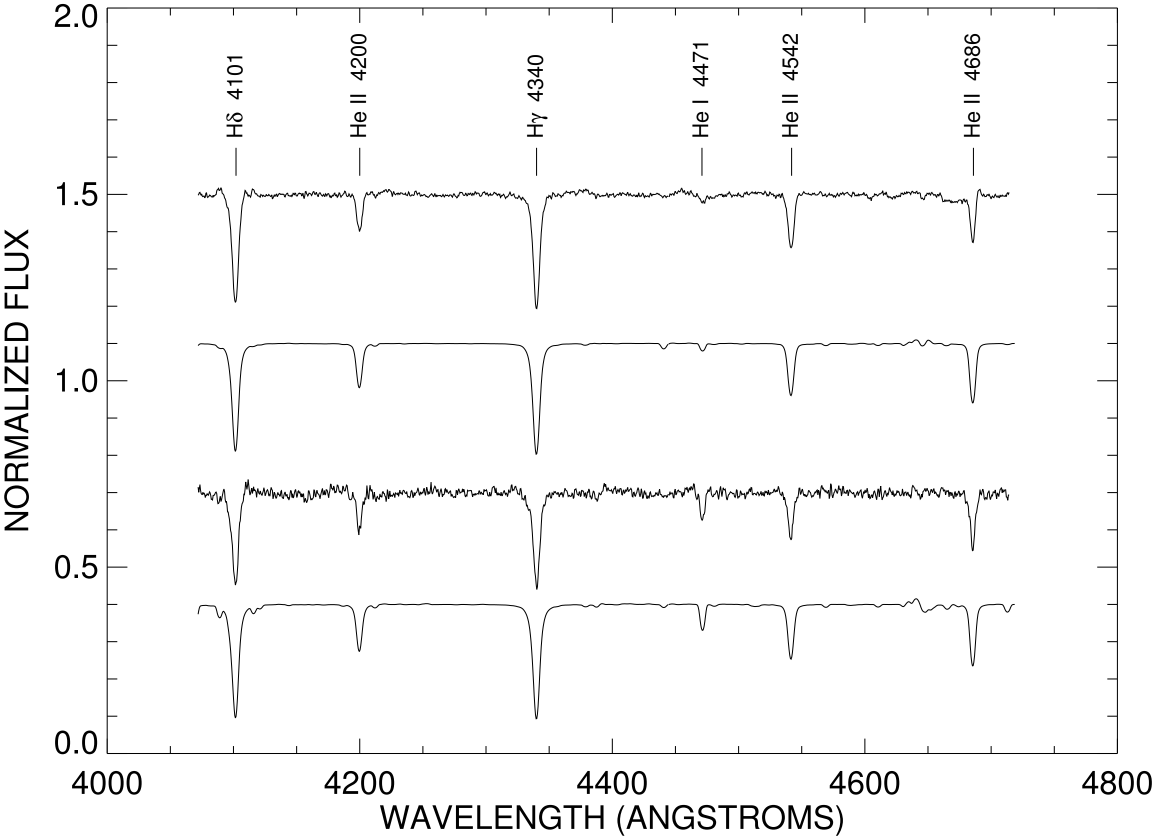

Figure 5.10 Tomographic reconstructions of the components of [L72] LH 54-425 based on 48 spectra obtained from 2003 through 2006 at CTIO. Plotted from top to bottom are line identifications with vertical tick marks, the primary spectrum, the model primary spectrum (Lanz & Hubeny 2003), the secondary spectrum, and the model secondary spectrum. The stellar parameters for the model spectra are given in Table 5.7.

the reconstructed to synthetic spectral line depths were used to estimate that the monochromatic flux ratio (F_2/F_1) in the blue spectra is 0.45 ± 0.10.

A visual inspection of the reconstructed spectra match best the O3 V example in Figure 6 of Walborn et al. (2002) for the primary and the O5 V example in Figure 7 of Walborn et al. (2002), and these are the spectral types we list in Table 5.7. Unfortunately, the wavelength coverage does not include the N IV $\lambda4058$ feature

Table 5.7. Tomographic Spectral Reconstruction Parameters for [L72] LH 54-425

Parameter	Primary	Secondary
Spectral Type	O3 V	O5 V
$T_{\rm eff}$ (kK)	45 ± 1	41 ± 1
log g (cgs)	4.0 ± 0.2	4.0 ± 0.2
v sin i (km s^{-1})	197 ± 5	182 ± 8
F_2/F_1 (blue)	0.45 ± 0.05	

suggested in Walborn et al. (2002) for spectral classification of the hottest O-stars. The N III λ4634–42 feature is another good diagnostic for classification of early O-type stars, but is too weak in these spectra for measurement. Instead, the equivalent width ratio of He I λ4471/He II λ4542 calibrated in Mathys (1988) for each of the reconstructed spectra is used to obtain a spectral class. This measurement results in a spectral class for the primary of O3 and of O5.5 for the secondary. The best matched effective temperatures from the TLUSTY/SYNSPEC models were combined with the $T_{\rm eff}$ versus spectral type calibration of Martins et al. (2005) to estimate spectral types of O3 V for the primary and O5 V for the secondary. These spectral types and effective temperatures are also consistent with those shown in Figure 1 of Mokiem et al. (2007) for LMC O-type dwarfs.

5.3.4 Combined Radial Velocity and Light Curve Solution

Light curve data were taken from the V-band observations listed in Table 1 of Ostrov (2002). New orbital parameters were then found using ELC. The resulting light curve is shown in Figure 5.11, and the radial velocity curves are shown in Figure 5.9, along with the radial velocity measurements from Ostrov (2002), which were not used for

Table 5.8. ELC Model Parameters for [L72] LH 54-425

Parameter	Distorted Secondary		Distorted Primary[a]	
···	Primary	Secondary	Primary	Secondary
Inclination (deg)	52^{+2}_{-3}		55 ± 1	
M ($M_\odot$)	53^{+7}_{-4}	32^{+4}_{-2}	47 ± 2	28 ± 1
$R_{\rm eff}$ ($R_\odot$)	$11.0^{+0.7}_{-0.3}$	$9.7^{+1.0}_{-0.2}$	11.4 ± 0.1	8.1 ± 0.1
$R_{\rm pole}{}^{\rm b}(R_\odot)$	$10.7^{+0.3}_{-0.2}$	$9.2^{+0.3}_{-0.2}$	10.9 ± 0.1	7.8 ± 0.1
$R_{\rm point}{}^{\rm c}(R_\odot)$	$11.7^{+0.4}_{-0.2}$	$11.1^{+0.4}_{-0.2}$	12.3 ± 0.2	8.6 ± 0.1
$v_{\rm sync}$ sin i (km s^{-1})	197 ± 5	173 ± 7	209 ± 5	148 ± 6
log g (cgs)	$4.08^{+0.01}_{-0.01}$	$3.94^{+0.02}_{-0.01}$	4.00 ± 0.02	4.07 ± 0.01
Filling Factor	$0.66^{+0.04}_{-0.02}$	$0.80^{+0.08}_{-0.02}$	$0.72^{+0.03}_{-0.02}$	$0.64^{+0.03}_{-0.02}$
$a_{\rm tot}$ ($R_\odot$)	$31.6^{+1.0}_{-0.6}$		30.4 ± 0.4	
F_2/F_1 (blue)	$0.70^{+0.05}_{-0.01}$		0.46 ± 0.02	

[a] Preferred solution, see text.

[b] Polar radius.

[c] Radius toward the inner Lagrangian point.

any fit here. ELC's genetic optimizer was used to explore the parameter space and was given wide ranges for each value of period, epoch of inferior conjunction of the primary $T_{\rm IC,1}$, inclination, mass ratio, primary velocity semi-amplitude, and Roche-lobe filling factor for each star. The Roche-lobe filling factor is defined as the ratio of the radius of the star toward the inner Lagrangian Point (L_1) to the distance to L_1 from the center of the star, $f \equiv x_{\rm point}/x_{L1}$ (Orosz & Hauschildt 2000); the fits show that the stars do not fill their Roche lobes (see Table 5.8). A by-product of the exploration of parameter space by ELC was a determination of systemic velocities for each component (see Table 5.6.

The temperatures of each star were set and not fit because these were well constrained by analysis of the reconstructed spectra discussed previously. As with

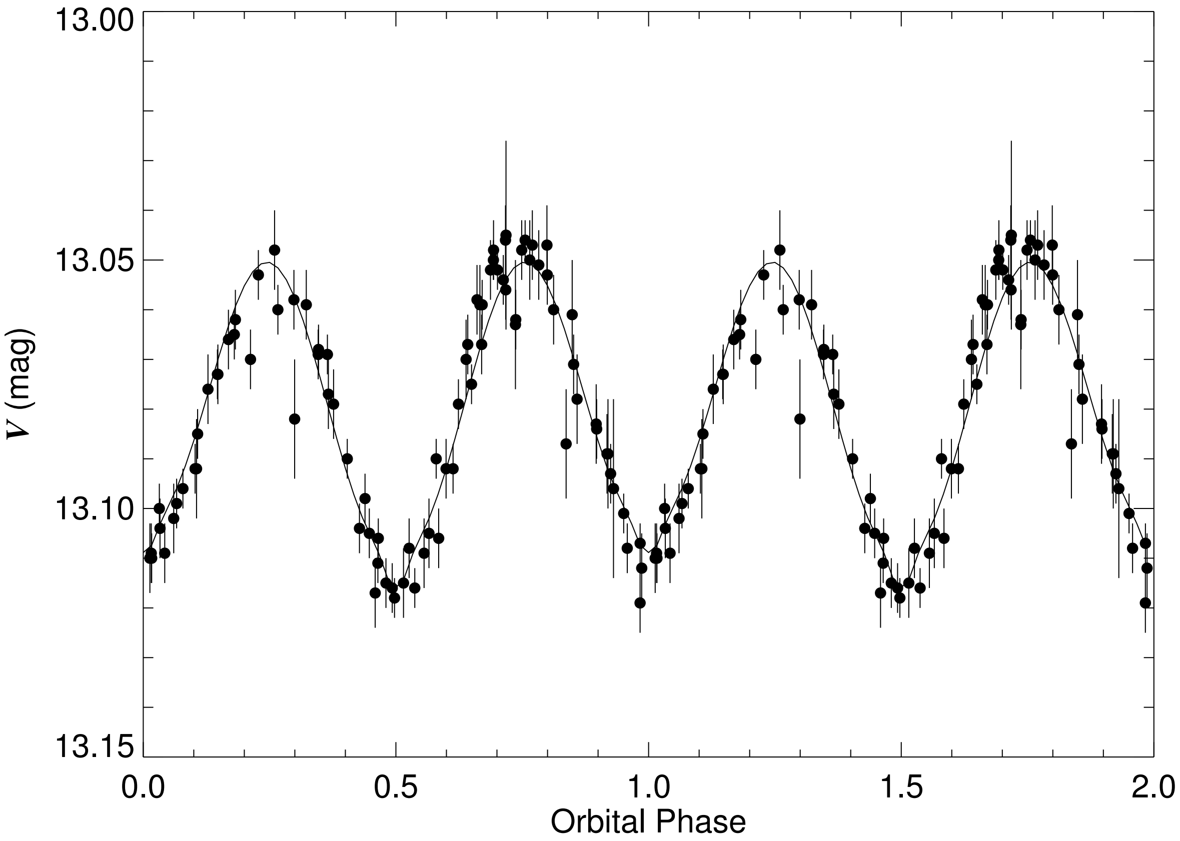

Figure 5.11 V-band light curve for [L72] LH 54-425. These data were taken from Ostrov (2002) and are presented here in phase according to our best combined solution. The model is the solid line and the data are represented by filled dots with V uncertainties shown by line segments. Phase zero corresponds to inferior conjunction of the primary star (which differs by 0.5 phase from that adopted by Ostrov 2002).

the fits of only radial velocities discussed in section 5.3.2, circular orbital solutions proved best.

To estimate the 1, 2, and 3σ uncertainties associated with the fitted parameters, the method discussed in Orosz et al. (2002) was followed. The values of the seven fitted parameters (plus the two systemic velocities) listed above were varied in the calculation of $\sim 3.6\times 10^6$ light and radial velocity curves. This procedure resulted in thorough sampling near the χ^2_{min} point, making the multi-dimensional surface well populated. This allowed for projection of the χ^2 surface as a function of each parameter or fitted value of interest. The lowest χ^2 is then found for each parameter of interest, and the 1, 2, and 3σ uncertainties may be estimated by the regions where $\chi^2 \leq \chi^2_{min}$ +1, +4, and +9, respectively. The uncertainties listed in the Tables are 1σ uncertainties.

Special attention was paid to the inclination of the system. The well-sampled light curve from Ostrov (2002) allows for an exploration of the important parameters that cause the ellipsoidal variations in this system: inclination and Roche-lobe filling factors for each star. Ellipsoidal light variations occur in systems where one or both of the components are tidally distorted due to the proximity of its companion. At different orbital phases, the observer sees varying amounts of light from the system, based upon the interplay between the amount of tidal distortion, the observed cross-section of the two stars, and the inclination of the system. As was expected, it was found that for lower inclinations, i.e., viewing the system more face-on, the sizes and tidal distortions of the stars needed to become larger in order to match the modulation of the light curve. Thus, restricting the stars to radii within their Roche lobes ultimately limits the lowest acceptable inclination, while the lack of observed eclipses establishes the maximum inclination.

Again, using the genetic algorithm in ELC, the range of inclination values suggested in Ostrov (2002) was explored and the fill factors for each star were allowed to vary over a wide range while keeping the other parameters fixed. The results of this analysis are plotted as contours of 1, 2, and 3σ confidence intervals in Figures 5.12 and 5.13. In the best overall fit, the estimated filling factors are larger for the secondary, so most of the ellipsoidal variation is due to the tidal distortion of the secondary (Fig. 5.12). It is interesting to note that the contours suggest a rather steep surface toward higher inclinations, indicating a hard upper limit for the inclination of 56° at the 3σ level. Lower inclinations are not as probable, and fill factors for the secondary get too large to match the light curve as the secondary star approaches a fill factor of 1.0, thus completely filling its Roche-lobe. These characteristics help to constrain the inclination of the system to be $i = 52^{+2}_{-3}$ degrees. The corresponding masses and other parameters are listed in Table 5.8. Included are values for $v_{\rm sync}\ \sin\ i$, the projected rotational velocity assuming synchronous rotation, $R_{\rm eff}$, the effective radius for a sphere of the same volume, and the sizes of the stars along different directions.

The orbital parameters for the best fit are listed in Table 5.6. The spectroscopic solution and the combined solution from ELC match very well. It should be noted that the parameters in Table 5.8 with asymmetric uncertainties are a result of the asymmetry in the uncertainties for the inclination.

The possibility of the primary being the more tidally distorted star was also explored. Simulations were run again, keeping the same parameters from Table 5.6 and varying only the filling factors and inclination. Thus, the radial velocity curve does not change and the light curve is fit to roughly the same degree of accuracy as before, so the fits in Figures 5.9 and 5.11 need not be changed. The contour plot for this scenario, again with confidence intervals of 1, 2, and 3σ, is shown in Figure 5.13. The fit gives an inclination of $i = 55 \pm 1$ degrees. This corresponds to slightly different values of masses and radii, listed alongside the overall best fit in Table 5.8. The small range in inclination leads to a small range in the masses and radii of the components

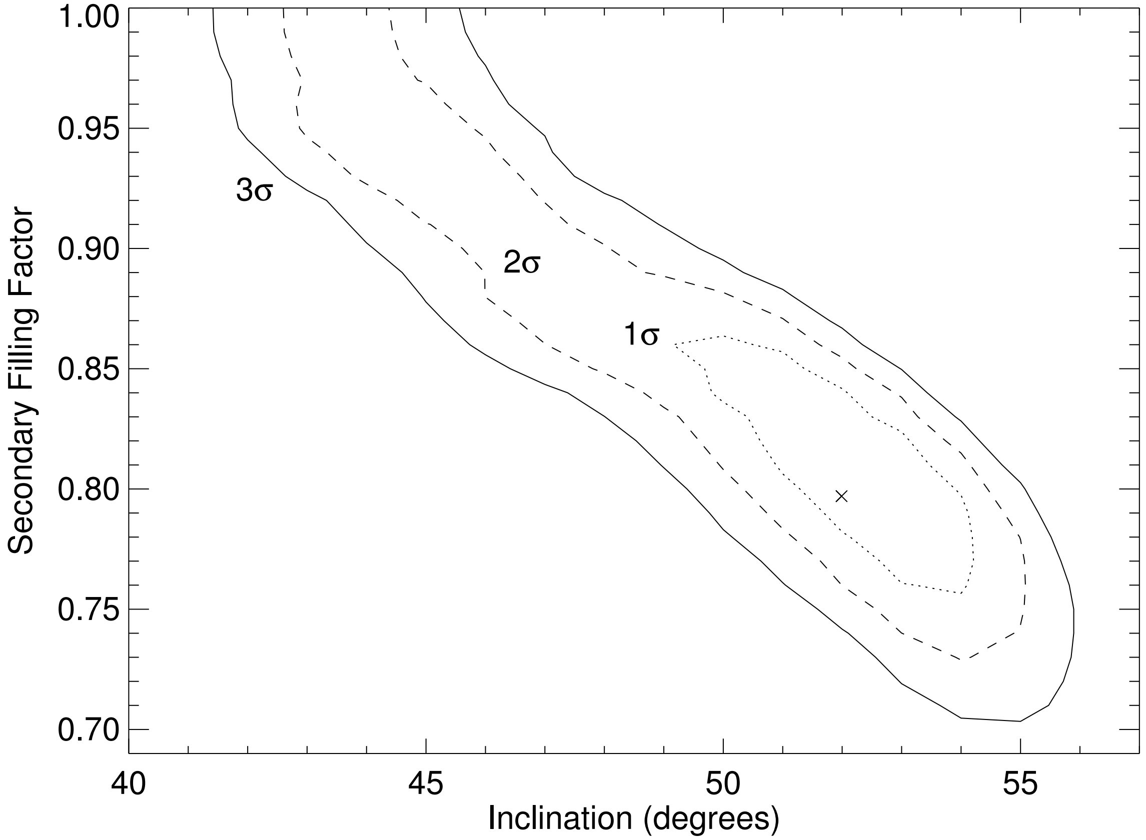

Figure 5.12 χ^2 surface contours of the residuals from the combined velocity and light curve data as a function of orbital inclination and secondary Roche-lobe filling factor of the best fit solution. The best fit position is represented by the "x" inside the 1σ contour. The range of filling factor is quite large, while the inclination is reasonably well constrained.

of the system. This restricted fit has a reduced χ^2 of 2.69 versus 2.54 for the case where the secondary is more tidally distorted.

A contact binary is another possible configuration for the system. This possibility was not explored because in a contact system, the sum of the values of $v \sin i$ and the sum of the velocity semiamplitudes would be comparable. For the fits of [L72] LH 54-425 (see Tables 5.6 and 5.7), the sums of these values differ by at least 300 km s^{-1}.

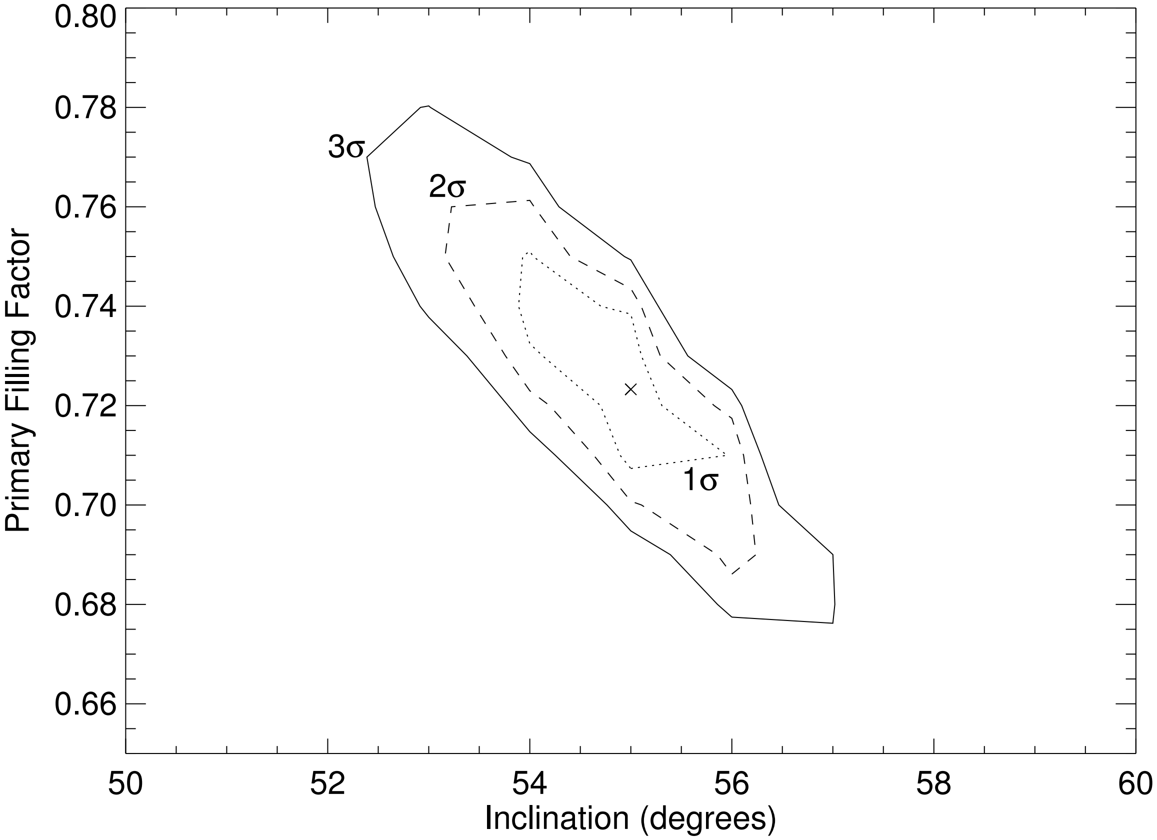

Figure 5.13 χ^2 surface contours of the combined fit residuals as a function of the orbital inclination and Roche-lobe filling factor of the primary star for the case where the primary is the more tidally distorted star. The best fit position is represented by the "x" inside the 1σ contour. The parameter space is more confined than for the best fit, and the contours are smaller around the best inclination for this configuration.

5.3.5 Discussion

Which of the two models is most consistent with the available data? The answer to this question lies in comparing the consequences of each solution.

To begin the comparison, the temperatures and radii output from ELC were used to obtain an estimate of the monochromatic flux ratio F_2/F_1. The case where the secondary is more tidally distorted yields a model flux ratio of $0.70\ ^{+0.05}_{-0.01}$, while the primary as the more tidally distorted star gives a flux ratio of 0.46 ± 0.02, in agreement with the value of 0.45 ± 0.05 derived from the tomographic reconstructions.

Theory suggests (Ekström et al. 2008) that for massive stars, the main sequence radius scales as $R \sim M^{0.6}$. Applying this as another consistency check, one can substitute velocity semiamplitudes to estimate the expected ratio of radii, $R_2/R_1 \sim (K_1/K_2)^{0.6}$ which, from the values in Table 5.6, is 0.707 ± 0.10. The ratio of effective radii estimated from the output of ELC (Table 5.8) is $\sim 0.88^{+0.03}_{-0.05}$ for the fit with the secondary as the more tidally distorted and $\sim 0.71 \pm 0.010$ for the primary being more tidally distorted. Once again the fit with the primary as the more tidally distorted matches theory more closely.

Ignoring the tidal distortions, the luminosity may be estimated by applying the Stefan-Boltzmann equation $L = 4\pi R^2 \sigma T_{\rm eff}^4$, and combining this with temperature estimates, each component can be placed in a theoretical H-R diagram. This is presented in Figure 5.14, along with evolutionary tracks from Schaerer et al. (1993) for stars of varying mass with a metallicity of $Z = 0.008$ which is appropriate for the LMC. The 1σ uncertainty regions are consistent with an age of ~1.5 Myr for the model consisting of the primary as the more tidally distorted star, and both stars appear to be co-evolutionary. The tidally distorted secondary fit appears a bit older, roughly matching the 2 Myr isochrone. This fit also indicates that the secondary is more evolved than the primary and is overluminous for its derived mass. Therefore, it seems the fit with the primary being more tidally distorted is more consistent with evolutionary tracks. These approximate ages are also consistent within uncertainties with the estimate from Oey & Smedley (1998) of ~2-3 Myr for the LH 54 OB associ-

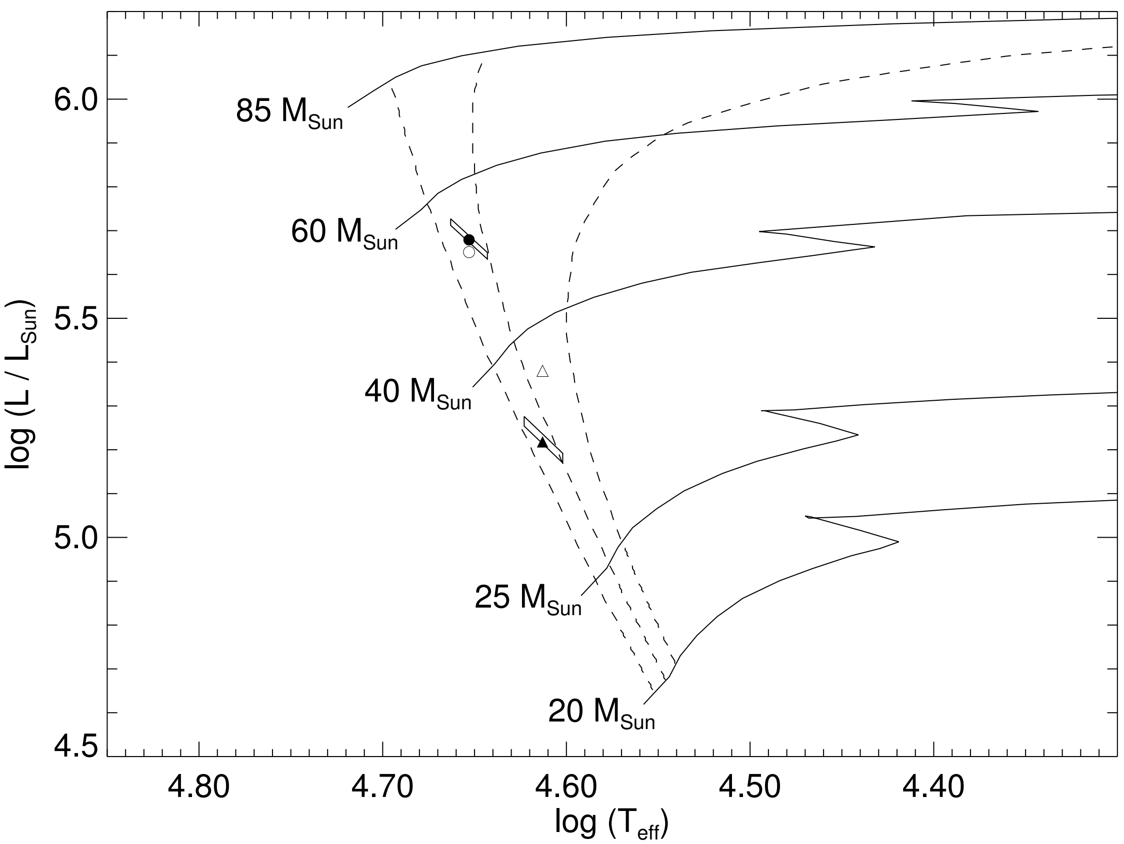

Figure 5.14 An H-R diagram showing the location of the primary star (*filled circle*) and secondary star (*filled triangle*) of [L72] LH 54-425 for our fit where the primary is the more tidally distorted star. The open symbols represent the fit where the secondary is the more tidally distorted star. Also plotted are evolutionary tracks for stars of various masses from Schaerer et al. (1993) for an LMC metallicity. The boxes around the filled data points correspond to the 1-σ uncertainties in the derived values of T_{eff} and R from the fits where the primary star is the more tidally distorted star. The vertical dashed lines correspond to isochrones from Lejeune & Schaerer (2001), also for an LMC metallicity, of 1, ~2 and ~3.2 Myr going from left to right. The positions of the two stars are consistent with an age of ~1.5 Myr.

ation. According to Table 1 of Schaerer et al. (1993), even the oldest age of ~2 Myr puts [L72] LH 54-425 in the part of its life when it is still burning hydrogen, and it will continue to do so for another ~1.5–2 Myr.

For the next comparison, the luminosities calculated above are used to obtain a bolometric absolute magnitude, assuming a solar bolometric absolute magnitude of 4.74 mag (Cox 2000). Next, a bolometric correction is applied for each star based on the spectral types derived here from Table 4 of Martins et al. (2005) to obtain absolute V magnitudes. These magnitudes are then combined to obtain an absolute V magnitude for the system. Finally, the distance modulus is computed for the system by using the maximum magnitude of the system from the photometric data and $E(B-V) = 0.10$ mag (Oey & Smedley 1998). The resulting distance modulus from the fit with the more tidally distorted secondary is 18.65 mag while the distance modulus for the tidally distorted primary fit is 18.55 mag. Both of these numbers are consistent with the HST Key Project distance modulus to the LMC of 18.50 ± 0.10 mag (Freedman et al. 2001), with the tidally distorted primary fit being slightly better. Note that each of the contour plots in Figures 5.12 and 5.13 seem to have a best fit valley in χ^2 as a function of inclination and filling factor. As one travels along this valley to higher inclinations, the dimensions of the system get smaller, including the sizes of the two stars. This makes the stars intrinsically fainter, and they must lie at a closer distance to match the observed V photometry. In contrast, the lower inclinations mean the stars are larger and lie at greater distances. The overall agreement in distance modulus between the model results and those for the LMC indicate that the final filling factor estimates are reliable.

The two models are most different in the $v_{\rm sync} \sin i$ values output from ELC. The observed $v \sin i$ values from the reconstructed spectra are 197 ± 5 km s^{-1} for the primary and 182 ± 8 km s^{-1} for the secondary. The ELC fit for the more distorted secondary gives values of 197 ± 5 km s^{-1} and 173 ± 7 km s^{-1} for the primary and secondary, respectively, while the ELC fit for the more distorted primary gives 209 ± 5 km s^{-1} and 148 ± 6 km s^{-1}. Both cases agree within uncertainties for the primary's line broadening, but the predicted $v \sin i$ for the secondary is too small for the case where the primary is the more tidally distorted star. However, due to the youth of the system, the assumption of synchronous rotation may not be appropriate. There may not have yet been enough time for tidal forces to synchronize the spin with the orbit. More ELC fits were performed assuming a faster rotation for the secondary and these show that the same physical parameters are obtained for a non-synchronous rotation scenario.

Given the above tests, it seems the fit with the primary as the more tidally distorted star is the more likely configuration. For this case, the masses and radii are $M_1 = 47 \pm 2\ M_\odot$ and $R_1 = 11.4\ \pm\ 0.1\ R_\odot$ for the primary and $M_2 = 28 \pm 1\ M_\odot$ and $R_2 = 8.1\ \pm\ 0.1\ R_\odot$ for secondary. These masses are significantly less than the 100 $M_\odot$ and 50 $M_\odot$ values obtained by Ostrov (2002). Part of the reason lies in the data set we obtained for radial velocities of the system. As is shown in Figure 5.9, two secondary velocity values derived by Ostrov (2002) near phase 0.25 are the ones that drove the estimate for the velocity semi-amplitude up, and consequently the mass ratio down. This, in addition to the lower inclination adopted by Ostrov (2002), leads to the differences in masses between the two analyses. The temperatures derived here are also slightly lower than those given in Ostrov (2002) in his Table 3, due to his use of a different, older temperature versus spectral-type calibration (Aller et al. 1982). The primary star can be compared with the primary in R136-38 (Massey et al. 2002), which is also an O3 V. Massey et al. (2002) derive a mass for their O3 V star of

$56.9 \pm 0.6\ M_\odot$, in closer agreement with our value of 47 $M_\odot$ than that of 100 $M_\odot$ found by Ostrov (2002). The derived radius for the primary in LH 54-425 is slightly larger than that for the primary in R136-38 of 9.3 $R_\odot$ (Massey et al. 2002). This may be due to the extreme youth of R136-38, which appears to be near the zero-age main sequence (see Fig. 6 in Massey et al. 2002), while the position of [L72] LH 54-425 in the H-R diagram (our Fig. 5.14) indicates the primary is slightly evolved. These numbers are consistent with the fact that the LH 54 OB association, at ∼2–3 Myr (Oey & Smedley 1998), is slightly older than the R136 cluster with an age of ∼1–2 Myr (Massey & Hunter 1998).

5.4 HI Mon

5.4.1 Introduction and Observations

The photometric variability of HI Mon (HD 51076) was first noted in Wachmann (1968). The system was classified as an "OB" type in Vogt (1976) and has been listed as an early B-type system since Eggen (1978), although no spectra for the system have been previously published.

Eleven spectra were obtained of HI Mon during the December CTIO 4-m Blanco observing run (see Chapter 2). Exposure times were typically 180 s in order to obtain a S/N ∼ 100 per pixel in each spectrum. HI Mon was originally part of the ASAS eclipsing binaries study outlined in Chapter 6.

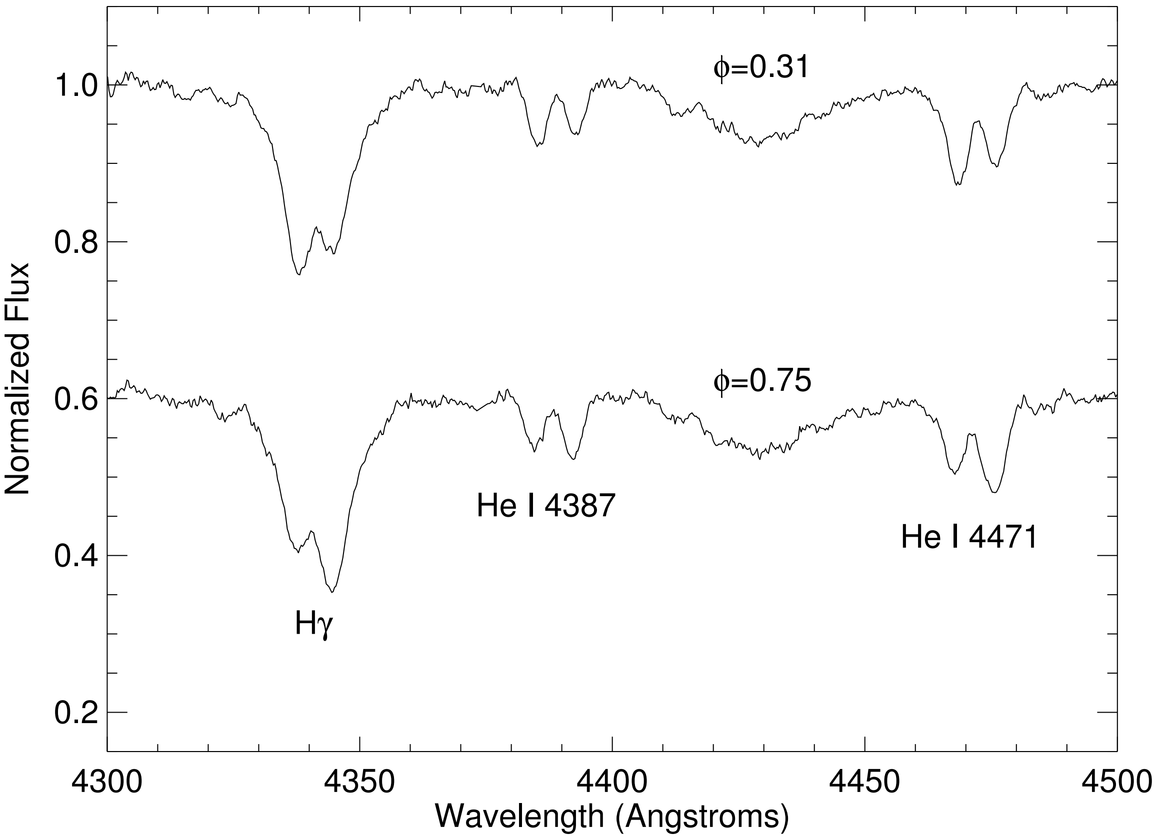

Figure 5.15 Two spectra of HI Mon near opposing quadrature phases (offset for clarity). The primary in each spectrum is represented by the deeper lines.

5.4.2 Radial Velocities

Radial velocities were measured using four spectral lines, He I $\lambda4026$, Hδ $\lambda4101$, He I $\lambda4143$, and Hγ $\lambda4340$. A template-fitting scheme (Gies et al. 2002) was used that measures velocities by using model spectra weighted by a flux ratio to match both the shifts and line depths in the observed spectra. No evidence was found for emission or intrinsic line asymmetries in any spectral feature. Two observations near quadrature (orbital phase 0.31 and 0.75) are shown in Figure 5.15.

The BSTAR2006 grid of stellar models from Lanz & Hubeny (2007) was used to

Table 5.9. HI Mon Radial Velocity Measurements

Date (HJD−2,400,000)	Orbital Phase	V_1 (km s^{-1})	σ_1 (km s^{-1})	$(O-C)_1$ (km s^{-1})	V_2 (km s^{-1})	σ_2 (km s^{-1})	$(O-C)_2$ (km s^{-1})
55190.776	0.119	–90.2	4.5	15.7	257.3	2.4	3.0
55190.837	0.157	–131.9	4.9	11.9	306.7	7.2	8.0
55191.769	0.750	312.2	8.2	0.8	–224.0	7.1	1.9
55191.818	0.780	306.7	8.2	–0.8	–219.4	8.2	1.2
55191.846	0.798	298.4	7.9	–2.8	–211.1	8.5	1.8
55192.648	0.308	–166.6	2.6	–0.3	329.9	3.8	1.7
55192.680	0.328	–157.6	2.2	–4.1	311.5	4.8	–2.1
55192.797	0.402	–82.2	3.6	–3.9	221.1	4.1	–5.8
55192.838	0.429	–52.1	5.4	–9.2	185.7	6.5	–17.0
55193.777	0.024	–0.9	13.5	17.3	107.4	12.4	3.6
55193.828	0.057	–40.4	7.8	12.0	156.4	8.2	–4.6

derive template spectra. The process of finding templates yielded initial values for temperatures, gravities, projected rotational velocities, and relative flux contributions from each star. Parameters for model templates were then checked against spectral features in the tomographically reconstructed spectra of each star (Section 5.4.3). The parameters were changed and new templates were made after initial fits to the light and radial velocity curves (Section 5.4.4) indicated that slightly different values were more appropriate. The velocity analysis was performed again until the best fit was obtained. Based on the relative line depths of spectral components, the observational monochromatic flux ratio in the blue is estimated to be $F_2/F_1 = 0.70 \pm 0.05$.

The four values for velocity from each spectrum for each component were averaged, and the standard deviation of the mean was calculated. Each of these values is listed in Table 5.9, along with the observation date, orbital phase, and observed minus calculated values.

5.4.3 Tomographic Reconstruction

The Doppler tomography algorithm of Bagnuolo et al. (1994) was used to separate the primary and secondary spectra of HI Mon. This iterative method uses the 11 observed composite spectra, their observed velocity shifts, and an assumed monochromatic flux ratio to derive individual component spectra. The best flux ratio was the one that best matched the line depths in the reconstructions with those in the model spectra. Figure 5.16 shows the reconstructed spectra for the primary and secondary, along with the best fit model spectra for each. The region containing the diffuse interstellar absorption band around λ4428 Å and other interstellar features were removed when performing the reconstruction, as otherwise this introduced noise into the final reconstructed spectra. Of particular importance are the fits of the wings of the Hγ λ4340 line, as these are produced by linear Stark broadening and are good estimators for the gravities of the stars. The relative depths of the He I λ4471 and Mg II λ4481 lines give an indication of the temperature in early B-type stars. It should be mentioned that fast rotation can lead to changing depths of these features, but these stars are not seen to be rotating faster than $\sim$ 200 km s^{-1}, where such complications may arise.

The final reconstructed spectra were fitted with TLUSTY/SYNSPEC model synthesis spectra. Estimates listed in Table 5.10 were made by comparing the reconstructed and model spectral line profiles against a grid of test values (see Williams et al. 2008; Williams 2009). Spectral type estimates were obtained by comparing the effective temperature against Table 2 of Böhm-Vitense (1981) and Table 3 of Harmanec (1988). The gravities of each star indicate they are main sequence objects, so final estimates for the spectral types are B0 V and B0.5 V.

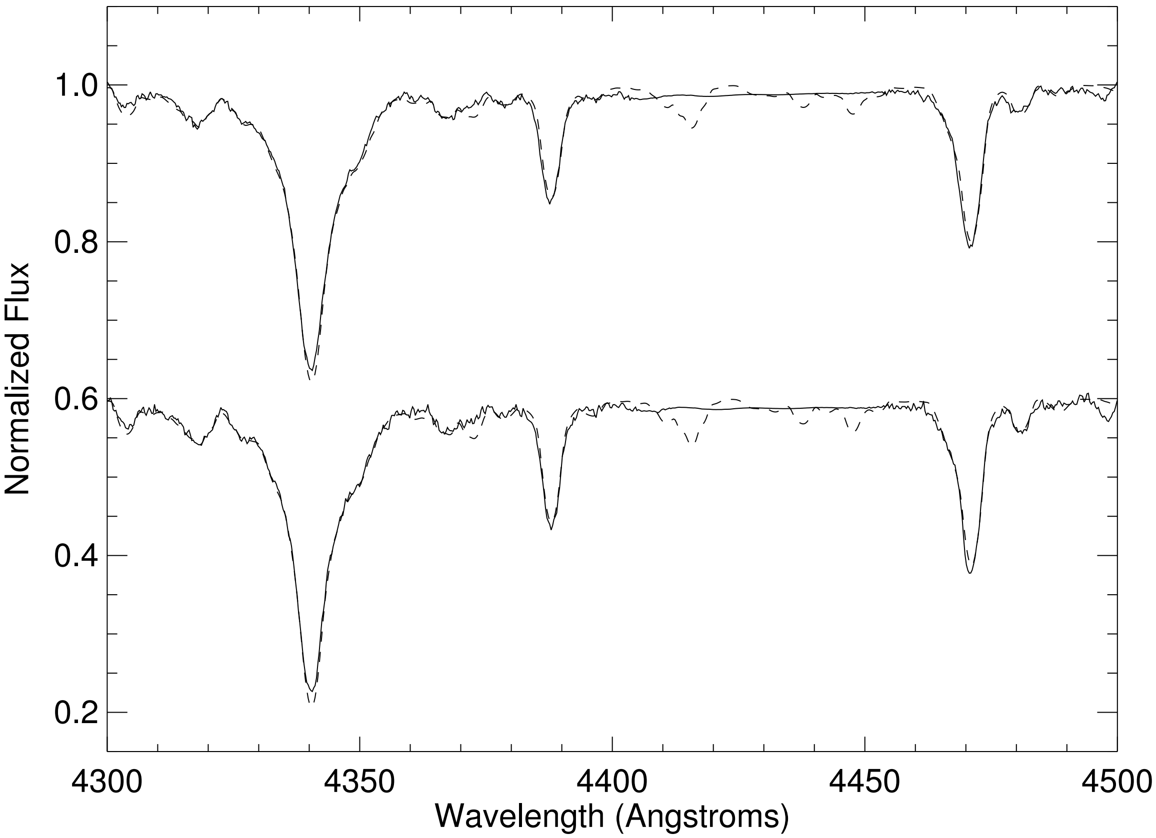

Figure 5.16 Tomographic reconstructions of the components of HI Mon based on the 9 spectra obtained outside of eclipse phases. The top solid line represents the primary and the bottom solid line is the reconstructed secondary spectrum offset by 0.4 for clarity. Overplotted for both are the model spectra for each shown by dashed lines. The stellar parameters for the model spectra are given in Table 4. Note also that the region containing the diffuse interstellar band near 4428Å has been removed for the tomographic reconstruction.

5.4.4 Combined Radial Velocity and Light-Curve Solution

ELC was used to fit both the light curve and the radial velocity curves simultaneously. The parameters allowed to vary included the orbital period, epoch of inferior conjunction of the primary, $T_{\mathrm{IC},1}$, inclination, mass ratio, primary velocity semiamplitude, effective temperatures of each star, and Roche lobe filling factor, f, for each

Table 5.10. Tomographic Spectral Reconstruction Parameters for HI Mon

Parameter	Primary	Secondary
Spectral Type[a] . .	B0 V	B0.5 V
T_{eff} (kK)	30.0 ± 0.5	29.0 ± 0.5
log g (cgs)	4.1 ± 0.2	4.1 ± 0.2
v sin i (km s^{-1})	150 ± 25	150 ± 25
F_2/F_1 (blue)	0.70 ± 0.05	

[a] These spectral types are estimated from derived values of T_{eff} and log g.

star. The Roche lobe filling factor is defined by Orosz & Hauschildt (2000) as the ratio of the radius of the star toward the inner Lagrangian point (L_1) to the distance to L_1 from the center of the star, $f \equiv x_{\mathrm{point}}/x_{\mathrm{L1}}$. Nonzero eccentricities for HI Mon were explored during initial fitting, but rejected based on the higher χ^2 values for those fits. HI Mon is therefore a "false member" of candidate eccentric systems listed in Hegedus (1988). The resulting best fit velocity curves are shown in Figure 5.17 and the best fit light curve is shown in Figure 5.18. During eclipses (at phase 0.0 and 0.5 in both Figures 5.17 and 5.18), bumps in the radial velocity curve can be seen due to the rotational Doppler shifts of the unobscured portions of the eclipsed star. This changes the shape of the observed spectral features, and gives rise to the velocity change, a perturbation known as the Rossiter-McLaughlin effect.

To estimate uncertainties based on the best fit, the nearly 40,000 recorded χ^2 values for each fit to the light and radial velocity curves performed by ELC were used. The well explored χ^2 surface was projected onto each parameter of interest. The lowest χ^2 value is found for each parameter and the 1σ uncertainty estimated from the

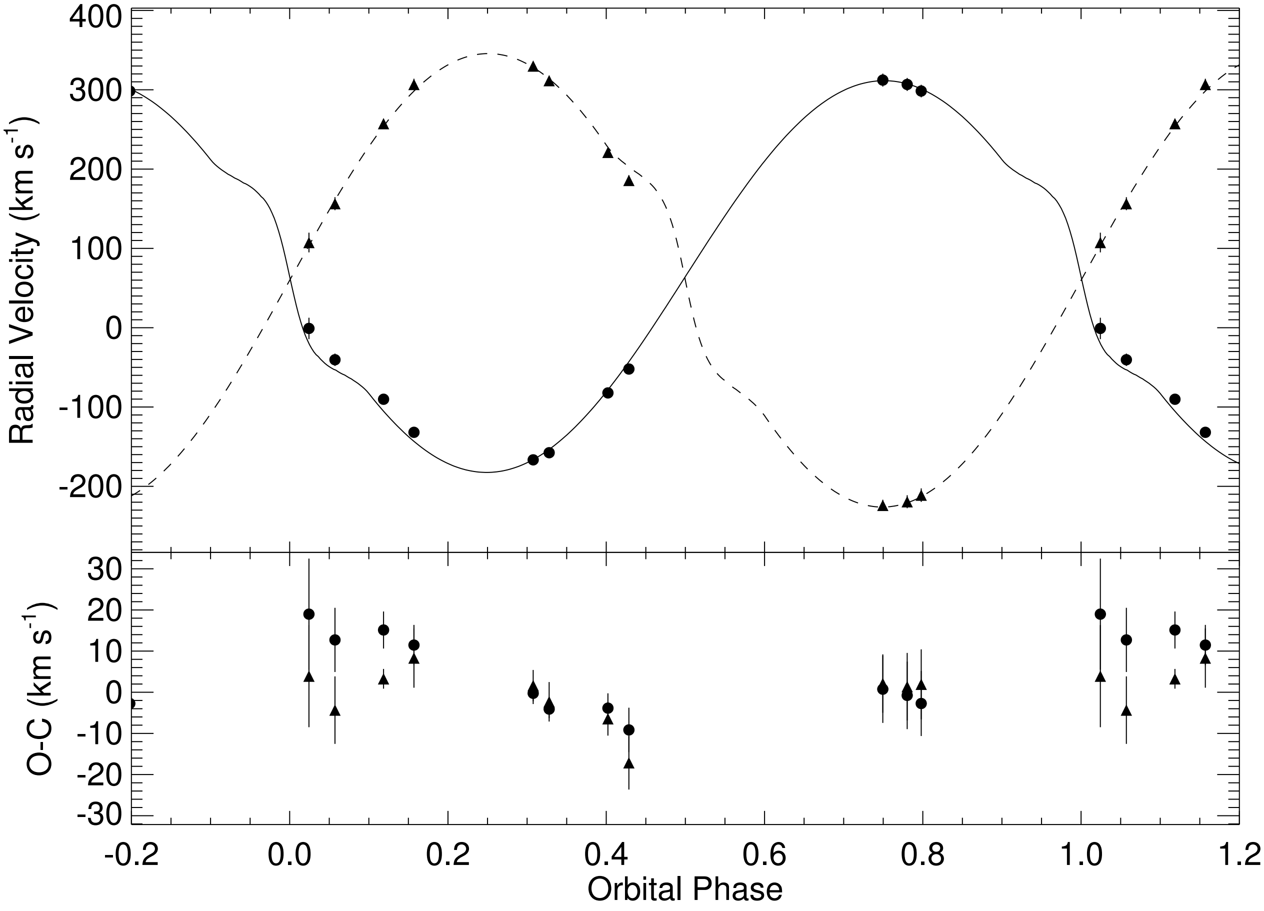

Figure 5.17 Radial velocity curves for HI Mon. Primary radial velocities are represented by filled dots and secondary radial velocities by filled triangles with associated uncertainties shown as vertical lines for both. The solid line is the best-fit solution for the primary and the dashed line is the best-fit solution for the secondary. The lower panel shows the observed minus calculated values for each measurement with uncertainties.

region where $\chi^2 \leq \chi^2_{\rm min} + 1$. These values are listed in Table 5.11 for the circular orbital solution and astrophysical parameters of interest are listed in Table 5.12.

Comparing these results with those from the on-line catalog of Pilecki, Pojmański, & Szczygieł[1] shows the importance of including spectra in the analysis of eclipsing binary systems. The inclination derived here of 80.2 ± 0.8 degrees agrees well with

---

[1] http:/www.astrouw.edu.pl/asas/?page=eclipsing

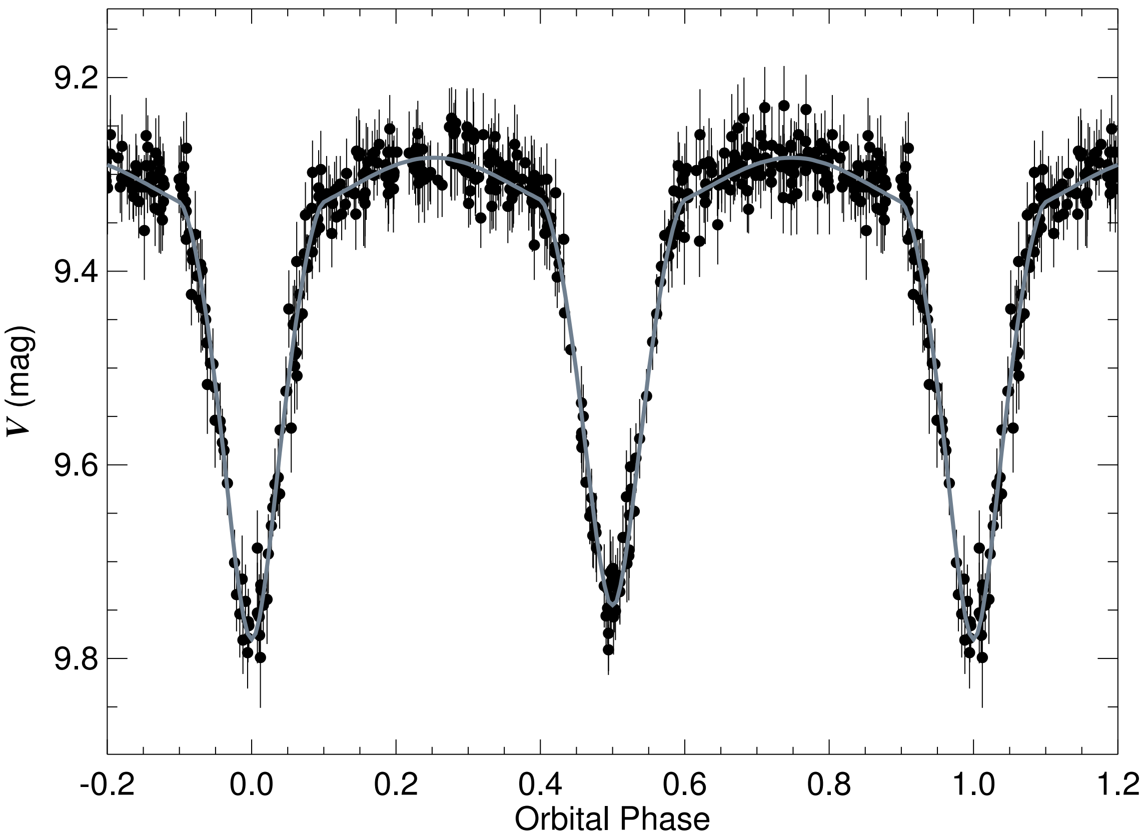

Figure 5.18 V-band light curve for HI Mon taken from the ASAS database (Pojmanski 2002) and presented here in phase according to the best-fit solution. The model is the thick gray line and data are the filled dots with uncertainties represented by vertical lines. Phase zero for this plot corresponds to mid-eclipse of the primary star.

Table 5.11. Circular Orbital Solution for HI Mon

Element	Value
P (days)	1.5744300 ± 0.0000008
T_0 (HJD–2,400,000)	54935.5331 ± 0.0005
K_1 (km s^{-1}).............	248.8 ± 1.9
K_2 (km s^{-1}).............	288.2 ± 2.4
γ_1 (km s^{-1})	64.5 ± 1.3
γ_2 (km s^{-1})	59.8 ± 1.2
rms (primary) (km s^{-1}) .	9.6
rms (secondary) (km s^{-1})	6.5
rms (photometry) (mag).	0.02

Table 5.12. ELC Model Parameters for HI Mon

Parameter	Primary	Secondary
Inclination (deg)...	80.0 ± 0.2	
M ($M_\odot$)..........	14.2 ± 0.3	12.2 ± 0.2
$R_{\rm eff}$ ($R_\odot$)..........	5.13 ± 0.11	4.99 ± 0.07
$R_{\rm pole}$[a]($R_\odot$).........	4.99 ± 0.11	4.83 ± 0.07
$R_{\rm point}$[b]($R_\odot$)........	5.40 ± 0.11	5.30 ± 0.07
$v_{\rm sync}$ sin i (km s^{-1})	162.5 ± 7.2	157.9 ± 2.7
log g (cgs).........	4.17 ± 0.04	4.13 ± 0.04
$T_{\rm eff}$ (kK)..........	29.5 ± 0.6	28.4 ± 0.4
Filling factor......	0.62 ± 0.01	0.65 ± 0.02
$a_{\rm tot}$ ($R_\odot$)..........	16.96 ± 0.11	
F_2/F_1 (blue).......	0.81 ± 0.09	

[a] Polar radius.

[b] Radius toward the inner Lagrangian point.

their inclination of 80.9 degrees. Also matching reasonably well is the temperature ratio from this work 0.963, with 0.971 in their catalog. Their estimates for the polar radius of each star relative to its Roche lobe polar radius are 0.793 and 0.830 for the primary and secondary, respectively. These values are slightly larger than the values derived from the best ELC fit of 0.751 and 0.777, most likely due to the additional constraints used in our analysis from the spectra. The most discrepant set of values are for the temperatures of the individual stars. They list 8110 K for the primary and 7870 K for the secondary. They arrive at the value for the primary based on the $(V-I)$ color index. There are several problems with estimating the temperature of intermediate mass stars with only a color index. First, interstellar extinction has not been taken into account. Distances for mid to early B-type stars of the magnitude ranges covered in the ASAS (V ~7-12) are more than one kpc. Because these intermediate mass stars are typically found in or near the Galactic plane, where extinction is more pronounced, any estimate of the temperature based on photometry will be affected by an unknown amount. Also, because the temperatures of intermediate mass binaries are high, their photometric colors sample the Rayleigh-Jeans tail of the energy distribution and the color differences are small. For example, the difference in $(V-I)$ is only 0.05 mag between a 20 kK star and a 25 kK star (Bessell et al. 1998). Both of these factors illustrate the need for spectroscopy to understand the nature of these intermediate mass or more massive binaries.

5.4.5 Discussion

With a modest number of spectra (11 total), the masses and radii of each component in HI Mon have been estimated to better than 3% accuracy, as is seen in Table 5.12. Both stars are within their Roche lobes but experience tidal distortion, as evidenced in the light curve in Figure 5.18. Tidal evolution in the HI Mon system is also seen in the fact that the projected rotational velocities from the tomographic reconstructions (Table 5.10) and from the synchronous rates from ELC (Table 5.12) are consistent within uncertainties. This indicates that the system has had sufficient time to undergo tidal evolution in order to attain synchronous rotation.

To make a more quantitative estimate of the age of the system, the effective temperatures and effective radii of each component from Table 5.12 were used to compute the luminosity and then plotted on a theoretical H-R diagram to compare their locations with evolutionary tracks. Because the stars are tidally distorted, the effective radius of each star is the radius of a sphere with the same volume. Figure 5.19 shows evolutionary tracks from Schaller et al. (1992) for stars of 12 and 15 $M_\odot$ and isochrones from Lejeune & Schaerer (2001) for solar metallicity for ages of 1.5, 2.5, and 3.5 Myr. The ages of the stars are most consistent with an age of 2.5 Myr. The evolutionary tracks from Schaller et al. (1992) are for nonrotating stellar models. The ratios of spin angular velocity to critical angular velocity are $\Omega/\Omega_{crit} = 0.43$ for the primary and 0.41 for the secondary. The evolutionary tracks for these moderate rotation rates are only slightly steeper and more extended in time than those illustrated (Ekström et al. 2008). Thus, this derived age is a lower limit.

The distance to the system can also be estimated by fitting an SED to photometric measurements from the literature (because the spectra were not flux calibrated). Measurements from Vogt (1976) for U, B, and V values were used, noting that the V-band measurement of maximum light from the ASAS light curve is consistent with these measures, meaning they were likely not taken during eclipse. In addition, 2MASS (Skrutskie et al. 2006) measurements were used to constrain the near-IR part of the SED. Strömgren photometric system measurements reported by Eggen (1978) were not consistent with the other photometry and were not used in the calculation of the SED. Perhaps one or more measurements were taken during or near an eclipse phase. The SED fit is shown in Figure 5.20 with the U, B, V, J, H, and K_s magnitudes transformed to fluxes using the calibrations of Colina et al. (1996) and Cohen et al. (2003). Model spectra for each star from Lanz & Hubeny (2007) with parameters for the best fit from ELC (Table 5.12) were scaled in the blue by the flux ratio (also Table 5.12) of 0.73 ± 0.08 and added to form the total SED of the system. This fit of the SED results in a limb-darkened angular diameter for the primary of $\theta_{\rm LD} = 21.5 \pm 0.7$ μas, a reddening of $E(B-V) = 0.35 \pm 0.02$ mag,

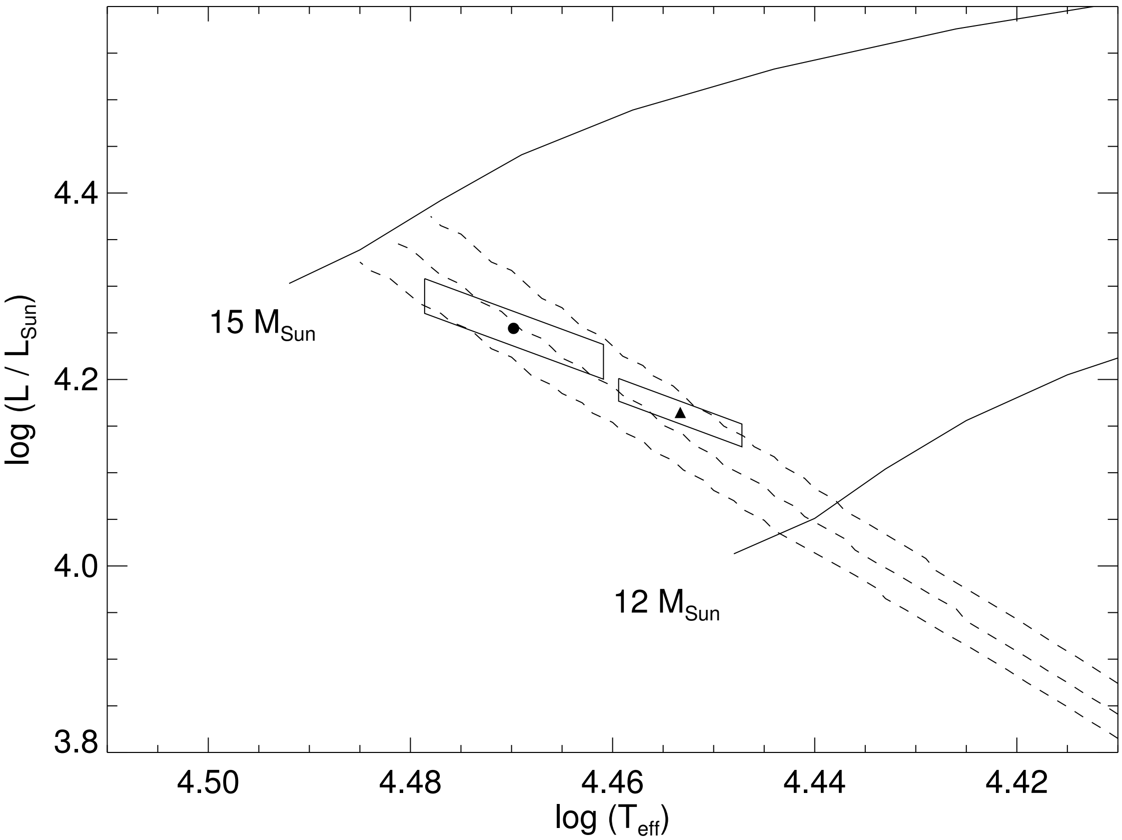

Figure 5.19 Theoretical H-R diagram showing the location of the primary star (filled circle) and secondary star (filled triangle) of HI Mon including uncertainty regions for each. Also plotted are the evolutionary tracks for stars of 12 $M_\odot$ and 15 $M_\odot$ from Schaller et al. (1992) and isochrones from Lejeune & Schaerer (2001) for solar metallicity with ages of 1.5, 2.5, and 3.5 Myr going from lower left to upper right. The positions of the two components of HI Mon are consistent with an age of ~2.5 Myr.

and a ratio of total-to-selective extinction of $R = 3.2 \pm 0.1$. This reddening value matches reasonably well with the values in the literature of 0.30 (Eggen 1978) and 0.38 (Vogt 1976). Combining this angular diameter with the physical radius for the primary from Table 5.12, the distance to HI Mon is estimated to be 2.26 ± 0.04 kpc. By contrast, this value is not consistent with previous photometric distance estimates for HI Mon of 3.89 kpc (Eggen 1978) and 3.98 kpc (Vogt 1976).

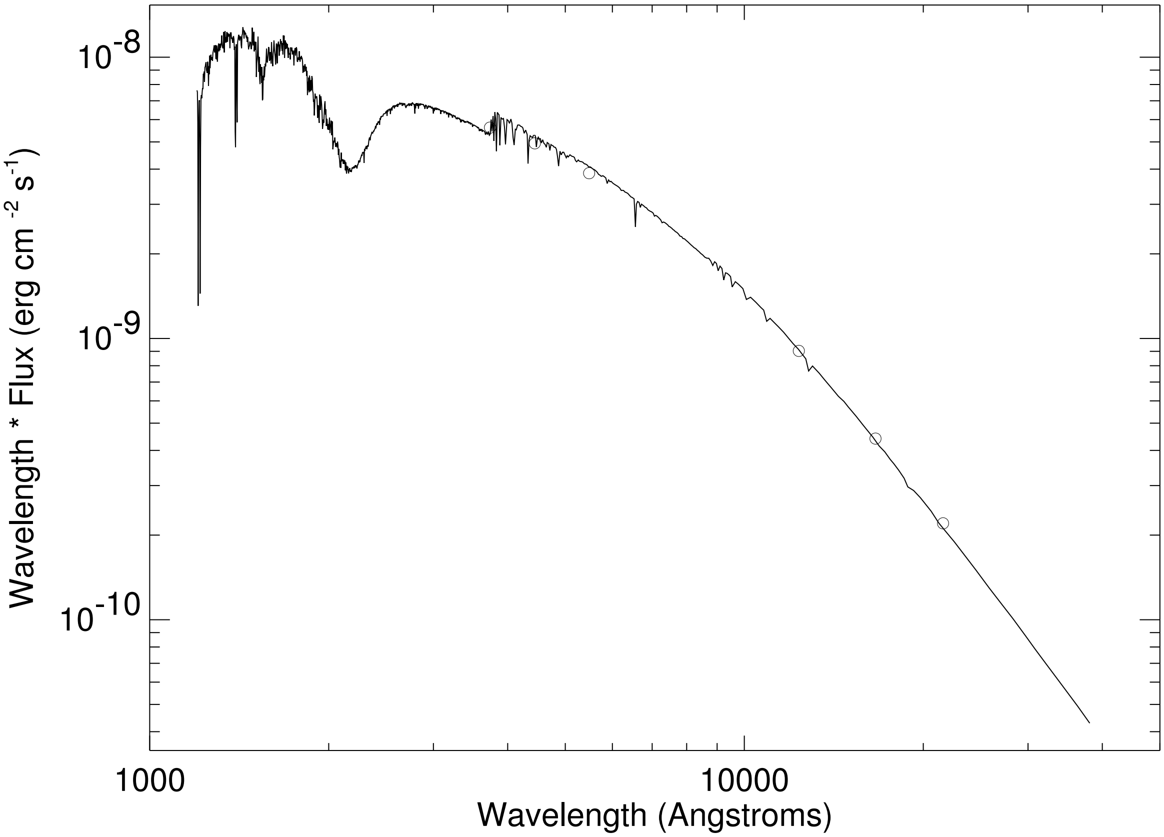

Figure 5.20 Spectral energy distribution and fit for the combined light of the HI Mon components (solid line) to Johnson U, B, V, J, H, K_S photometry (open circles).

HI Mon has galactic coordinates of $\ell = 217^\circ\!.03$ and $b = -0^\circ\!.87$ (Reed 2005). The closest galactic cluster is NGC 2311, which is located at $\ell = 217^\circ\!.76$ and $b = -0^\circ\!.69$ (Piatti et al. 2010). Piatti et al. (2010) find a distance to the cluster of 2.2 ± 0.4 kpc and a reddening of $E(B - V) = 0.25 \pm 0.05$. However, they find an age for the cluster of ∼100 Myr, making HI Mon far too young to be associated with NGC 2311. The distance found here for HI Mon and its location suggest it is part of "Group A" as defined by Vogt (1976). This group is an association of luminous stars in the constellation of Monoceros at a distance of about 2.2 kpc that is part of the local arm of the Galaxy.

5.5 HD 103146

5.5.1 Introduction and Observations

The photometric variability of HD 103146 (also known as VZ Cen) was first reported by Leavitt & Pickering (1913) and it was categorized as an Algol-type (EA) eclipsing binary by Giuricin et al. (1983). The combined spectral type for the system is given by Houk (1975) as B2 III/IV. A radial velocity of -37.0 km s^{-1} based on four measurements was reported by Feast & Thackeray (1963). This velocity is the only one published for this system, although a $v \sin i$ measurement of 156 km s^{-1} based on two observations was reported by Balona (1975). The only light curve analysis published was performed by Brancewicz & Dworak (1980).

Spectroscopic observations were obtained at the CTIO 1.5-m telescope and are described in Chapter 2. Light curve data were extracted from the *Hipparcos* epoch photometry search facility webpage[2] and converted to Johnson V magnitudes via the relation in Harmanec (1998).

5.5.2 Preliminary Radial Velocities

Radial velocities were measured using the same template-fitting scheme as above (Gies et al. 2002) for four lines: He I $\lambda\lambda 4143, 4387, 4471$ and Mg II $\lambda 4481$. The matching template for the primary was extracted from the BSTAR 2006 grid (Lanz & Hubeny 2007). The secondary is much cooler than the primary, and the template

---

[2] http://www.rssd.esa.int/index.php?page=Epoch_Photometry&project=HIPPARCOS

model used came from the grid described in Jeffery et al. (2001) that covers stars cooler than 15 kK. The final templates were T_{eff} =26 kK, $\log g = 4.0$, and $v \sin i = 75$ km s^{-1} for the primary, and 15 kK, 3.5, and 90 km s^{-1} for the secondary. The major obstacle in completing the analysis of this system has been finding acceptable model templates for the secondary. Technically, 15 kK is the bottom end of the BSTAR 2006 grid. However, those models did not fit the tomographically reconstructed spectra well. The models by Jeffery et al. (2001) use different input physics than the models from the BSTAR 2006 grid, with the most notable difference being the lack of non-LTE treatment in the Jeffery et al. (2001) models. Despite these issues, preliminary velocities were measured with these models and are listed in Table 5.13. Also listed are the dates of observation, uncertainties and $(O - C)$ values based on the fit described in section 5.5.4.

5.5.3 Tomographic Reconstruction

Again, as for previously discussed systems, the Doppler tomography algorithm of Bagnuolo et al. (1994) was used to reconstruct component spectra. These spectra, along with the current best fit model spectra, are shown in Figure 5.21. This plot beautifully illustrates the He I λ4471 and Mg II λ4481 behavior in the B-star temperature sequence. The much hotter primary has very strong He I λ4471 with very weak Mg II λ4481, while the depths of these two lines in the secondary are nearly equal. The reconstructed spectra in Figure 5.21 show signs of an incorrect monochromatic flux ratio (of 0.75) used. In particular, the line depths for the secondary are too shallow, and therefore the preliminary model spectrum was chosen based on the relative line

Table 5.13. HD 103146 Preliminary Radial Velocity Measurements

Date (HJD−2,400,000)	Orbital Phase	V_1 (km s^{-1})	σ_1 (km s^{-1})	$(O-C)_1$ (km s^{-1})	V_2 (km s^{-1})	σ_2 (km s^{-1})	$(O-C)_2$ (km s^{-1})
53018.767	0.209	59.9	4.4	4.9	–236.5	9.0	16.5
53018.833	0.222	55.2	2.9	–1.2	–250.7	15.2	6.1
53019.749	0.408	24.2	10.1	1.4	–174.0	9.4	–15.2
53020.732	0.607	–57.9	8.8	10.2	106.5	11.2	–9.5
53020.807	0.622	–77.7	6.5	–4.1	111.6	5.0	–20.9
53021.727	0.809	–89.8	6.3	2.0	195.7	4.0	10.5
53023.716	0.213	52.0	8.1	–3.5	–252.8	6.4	1.5
53027.816	0.044	–2.2	8.9	–3.8	–103.5	6.2	–0.4
53028.718	0.227	58.6	9.9	1.8	–244.1	8.1	13.9
53028.800	0.244	67.1	11.9	9.5	–248.8	9.3	11.1
53029.757	0.438	17.7	11.3	5.6	–132.5	7.7	–13.5
53030.708	0.631	–79.0	5.4	–2.4	123.0	12.5	–18.3
53031.632	0.819	–93.2	9.8	–3.3	185.6	4.2	5.5
53031.794	0.852	–81.2	8.3	0.6	175.0	7.2	17.3
53032.713	0.038	–6.6	12.2	–5.2	–135.5	10.8	–40.4
53033.793	0.257	59.1	5.7	1.5	–249.7	8.1	10.2
53152.476	0.337	61.7	6.5	15.2	–210.8	1.6	18.1
53152.700	0.382	43.0	9.8	10.4	–213.4	11.3	–25.3
53153.455	0.536	–42.3	9.0	4.4	39.1	8.5	17.4
53153.689	0.583	–73.1	7.2	–14.7	63.1	3.1	–23.5
53154.482	0.744	–96.3	8.9	0.7	198.7	9.2	–0.7
53154.660	0.780	–95.3	6.1	0.4	210.9	11.6	15.2
53155.479	0.946	–40.4	5.1	5.0	92.5	9.0	39.0
53156.458	0.145	40.3	5.7	–1.0	–219.1	9.6	–3.8
53156.668	0.187	41.2	6.5	–10.5	–246.5	0.6	–2.5
53158.464	0.552	–53.9	10.1	–3.8	47.0	16.2	2.2
53158.606	0.581	–53.0	10.3	4.4	63.5	6.2	–20.2
53159.450	0.752	–93.8	9.5	3.3	223.0	17.3	23.5
53159.658	0.794	–93.4	9.6	0.7	201.0	6.8	9.6
53160.448	0.954	–48.1	8.6	–6.5	55.9	4.8	11.9
53160.668	0.999	–29.3	5.5	–9.1	20.9	5.8	49.0
53161.461	0.160	47.6	11.8	2.1	–215.9	14.4	11.2
53161.660	0.200	55.3	6.7	1.4	–239.9	5.3	10.0
53162.601	0.391	43.7	8.9	14.4	–181.6	4.8	–3.2
53163.447	0.563	–47.6	7.9	4.1	54.4	6.7	–5.6
53164.445	0.765	–98.0	8.1	–1.3	204.1	16.8	5.6
53748.863	0.338	36.3	5.1	–9.8	–213.3	8.2	14.5
53752.785	0.134	29.8	4.5	–8.2	–212.2	7.7	–6.3
53753.680	0.316	50.5	8.6	–0.7	–247.3	6.4	–5.1
53756.694	0.927	–50.1	4.0	3.7	81.9	6.9	6.4
53758.840	0.363	42.1	9.3	2.9	–211.5	16.4	–3.7
53759.846	0.567	–49.1	9.1	3.2	52.9	5.6	–12.5
53868.776	0.668	–87.6	8.1	–0.5	167.6	4.6	–4.0
53872.470	0.417	33.1	5.9	14.3	–163.4	10.8	–16.5
53874.655	0.861	–84.8	4.5	–5.7	177.4	4.8	27.3
53876.466	0.228	51.7	5.7	–5.2	–257.5	7.3	0.5
53877.465	0.431	9.3	7.8	–4.4	–132.0	2.5	–2.6

depths of the 4471/4481 lines. The temperature listed for the primary in section 5.5.2 of 26 kK must be an upper limit. Closer inspection of the reconstructed spectrum for the primary and the model template in Figure 5.21 shows that the He II $\lambda\lambda 4200, 4541$ lines are present in the model but not the reconstructed spectrum. Clearly, more analysis is needed.

5.5.4 Combined Radial Velocity and Light Curve Solution

ELC was used to fit the *Hipparcos* photometry and preliminary radial velocities in Table 5.13. Based on the symmetry of the light curve, only circular orbit fits were

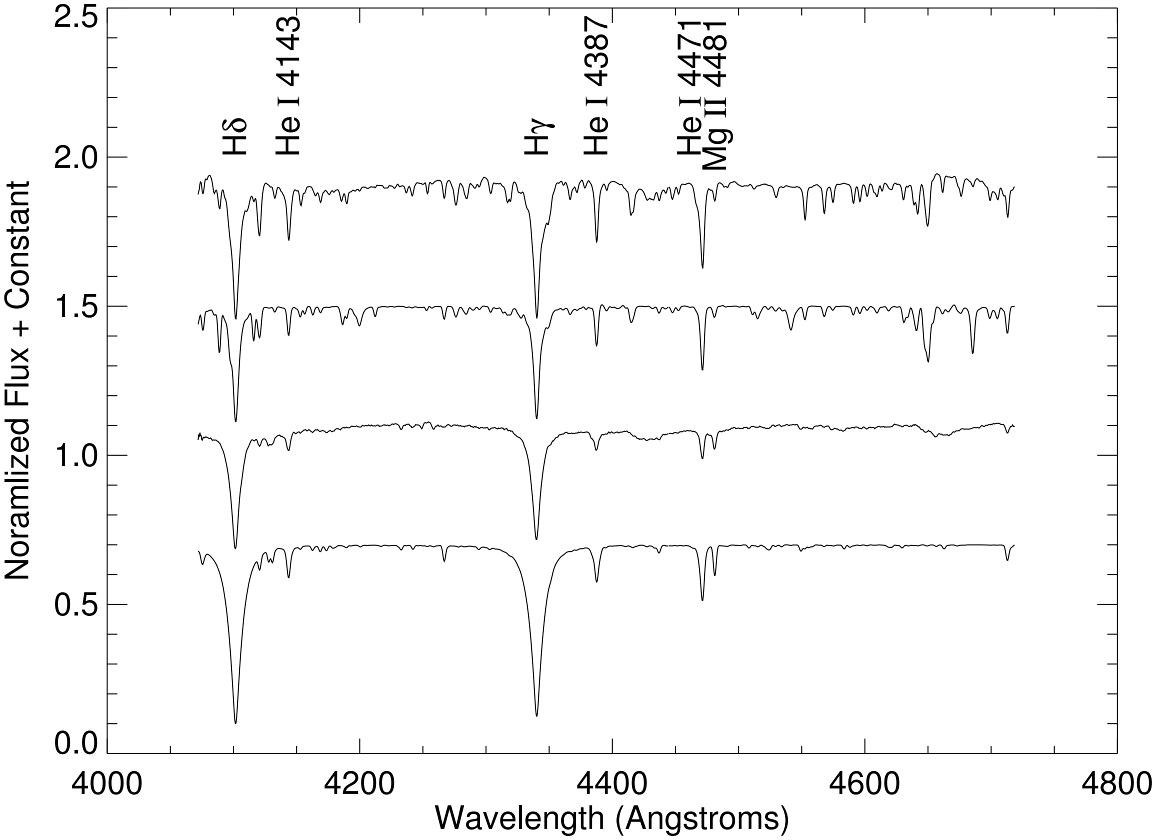

Figure 5.21 From bottom to top are plotted the secondary model spectrum, the reconstructed secondary spectrum, the model spectrum for the primary, and the reconstructed spectrum for the primary. Several prominent spectral features are labeled, including ones used for measuring velocities.

attempted. Orbital and astrophysical parameters from the current ELC fit are listed in Table 5.14. No uncertainties are listed due to the lack of time to fully flesh out this solution. The best fit radial velocity curves are plotted with the data in Figure 5.22, and the light curve is plotted in Figure 5.23. The fits themselves are very good, but the astrophysical parameters used by ELC to make those fits are not matching information from reconstructed spectra. Let's compare values from Brancewicz & Dworak (1980) with those derived here. For $a_{\rm tot}$, they find 35.54 $R_\odot$, close to the

31.8 $R_\odot$ from the best ELC fit. They also list the secondary star as filling 97% of its Roche-lobe, while the preliminary ELC fit runs up against the hard limit set for the parameter space of 99%. They list the radius of the secondary to be larger than the radius of the primary, similar to the values in Table 5.14. Given the cool T_{eff} of the secondary, the only way it could be seen is if it has a larger radius than the primary. They give an estimate for the mass ratio based on applying their findings to a mass-luminosity relation and arrive at $q = 0.70$, not matching well with the output from ELC fits to the radial velocity curves that gives a mass ratio of 0.33.

The lack of constraints to model fits from the reconstructed component spectra means ELC will go to wider ranges of values to fit the data. For example, even rudimentary fits to the reconstructed spectra show that the secondary does not have a log g of 3.16, as the ELC fits would indicate. The light curve shows almost 0.1 mag of ellipsoidal variation outside of eclipses, indicating that the stars are extremely tidally distorted. Certainly with a mass ratio from the velocity semiamplitudes of 0.33, and with what appears to be an evolved secondary component, HD 103146 will prove to be an interesting system once the analysis is complete.

Table 5.14. Circular Orbital Solution and Astrophysical Parameters for HD 103146

Element	Value
P (days)	4.92876
T_0 (HJD–2,400,000)	53027.5965
K_1 (km s^{-1})	77.4
K_2 (km s^{-1})	237.9
γ_1 (km s^{-1})	–19.7
γ_2 (km s^{-1})	–30.3
Inclination (deg)	74.6
M_1 ($M_\odot$)	13.5
M_2 ($M_\odot$)	4.4
Primary Filling Factor	0.36
Secondary Filling Factor	0.99[a]
$R_{\rm eff,1}$ ($R_\odot$)	7.0
$R_{\rm eff,2}$ ($R_\odot$)	9.1
log g_1 (cgs)	3.87
log g_2 (cgs)	3.16
$a_{\rm tot}$ ($R_\odot$)	31.8
rms (primary) (km s^{-1})	6.4
rms (secondary) (km s^{-1})	16.7
rms (photometry) (mag)	0.016

[a] Hard limit of ELC fit.

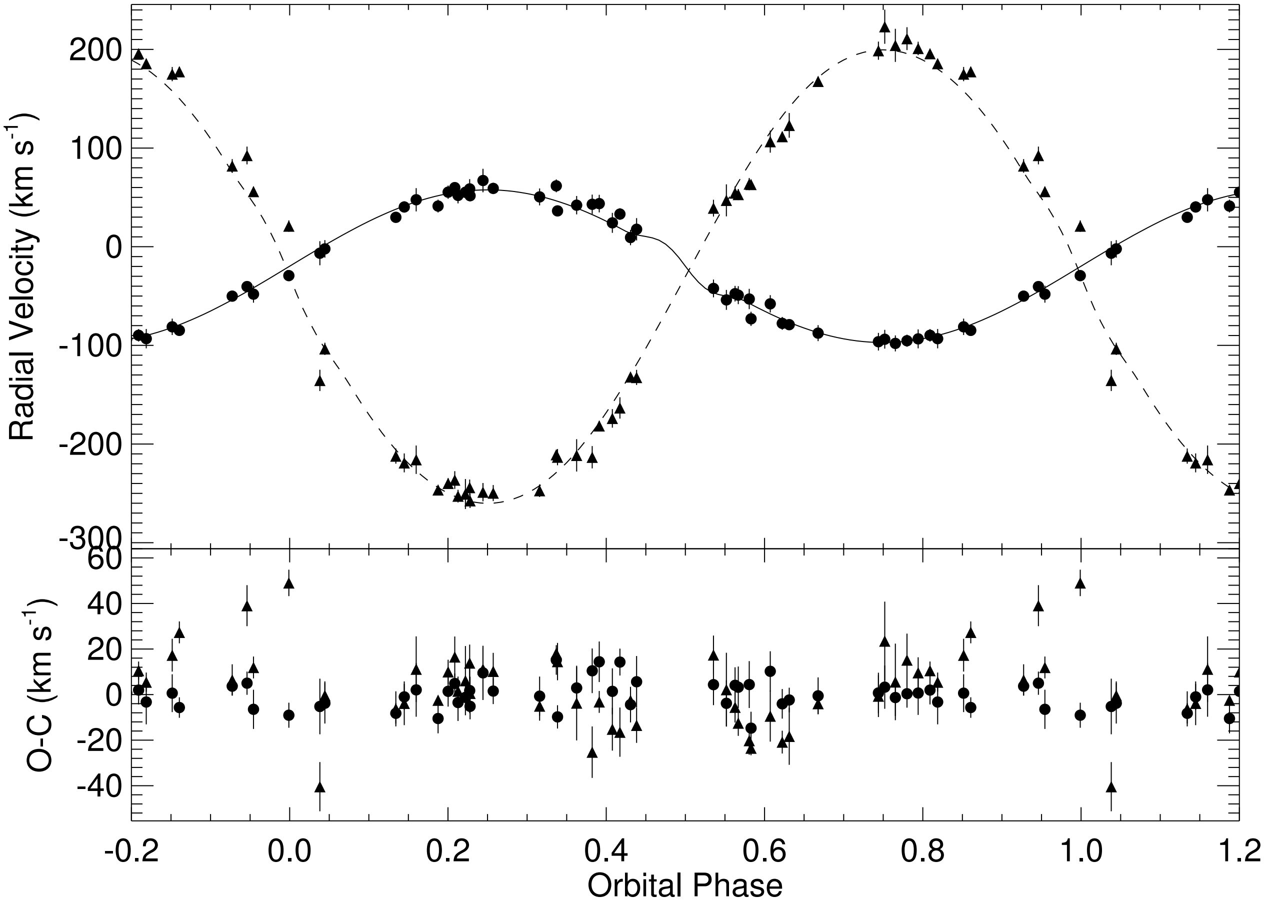

Figure 5.22 Radial velocity curves for HD 103146. Primary radial velocities are shown as circles and secondary velocities are triangles, both with uncertainties represented by vertical lines. The solid line is the best fit for the primary and the dashed line is the best fit for the secondary. Plotted below this are the $(O - C)$ values for each measurement.

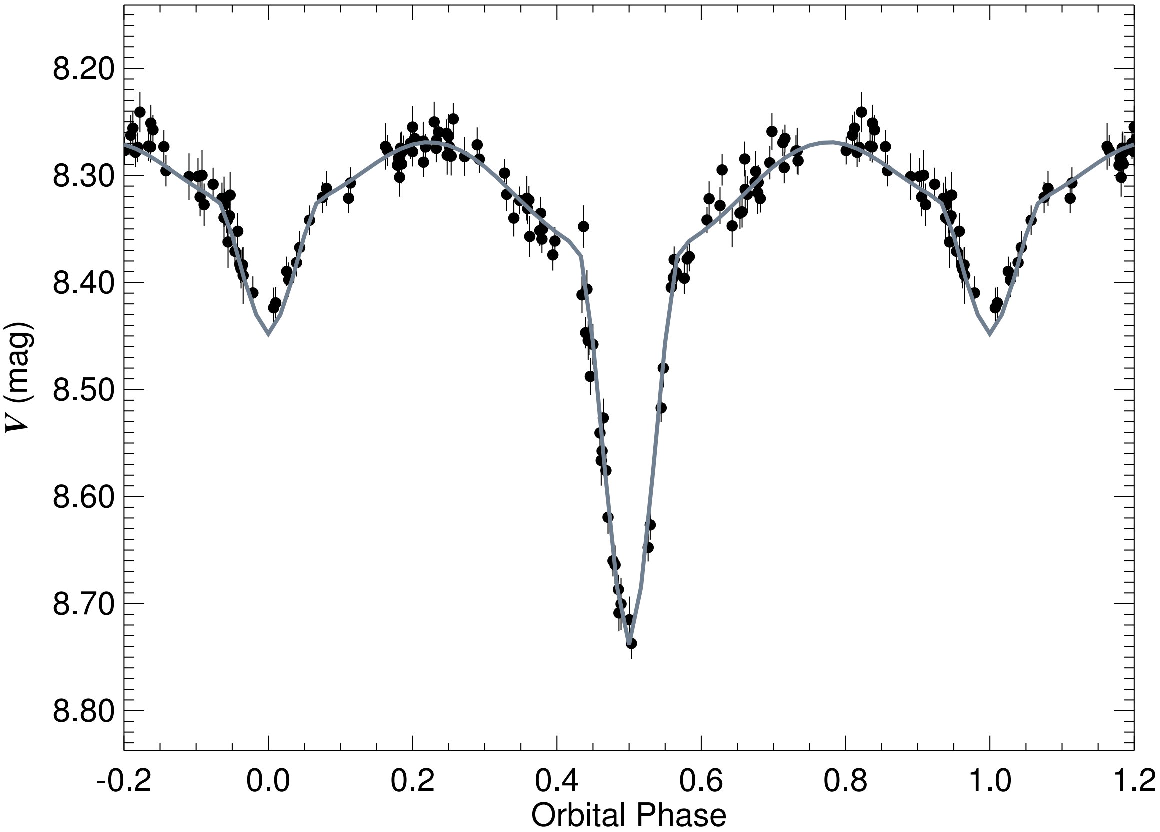

Figure 5.23 V-band light curve for HD 103146 transformed from *Hipparcos* data and plotted as circles with vertical lines for uncertainties. The best fit light curve output from ELC is the solid gray line.

5.6 HD 155775

5.6.1 Introduction and Observations

The previous efforts on HD 155775 have been summarized by Stickland & Lloyd (2001), and no work has been done since then. HD 155775 has been known to be a double-lined spectroscopic binary since the work by Feast et al. (1955). An unpublished SB1 orbit was mentioned in Garmany et al. (1980), claiming a 7 day orbital period and 120 km s^{-1} velocity amplitude. The single $v \sin i$ measurement in the literature is 135 km s^{-1} by Howarth et al. (1997). The most recent spectral classification is O9.5 by Conti et al. (1977). The first light curve published for HD 155775 was reported by Balona (1992), showing ellipsoidal variation with a period of just over 1.5 days.

The *Hipparcos* photometry was extracted from the epoch photometry search webpage and converted to Johnson V magnitudes by using the relation in Harmanec (1998), as for HD 103146. All spectroscopic observations were made with the CTIO 1.5 m and are, as usual, discussed further in Chapter 2.

5.6.2 Preliminary Radial Velocities

Radial velocities for HD 155775 were once again measured using the template-fitting scheme outlined by Gies et al. (2002). The three lines used in the velocity analysis were He I $\lambda\lambda 4143, 4387, 4471$. Model templates for the components were made from the OSTAR 2002 grid (Lanz & Hubeny 2003) for the primary, with $T_{\rm eff} = 32$ kK, $\log g = 4.0$, and $v \sin i = 150$ km s^{-1}, and the BSTAR 2006 grid (Lanz & Hubeny 2007) was used to obtain the template for the secondary of $T_{\rm eff} = 23$ kK, $\log g = 4.0$,

Table 5.15. HD 155775 Preliminary Radial Velocity Measurements

Date (HJD−2,400,000)	Orbital Phase	V_1 (km s^{-1})	σ_1 (km s^{-1})	$(O-C)_1$ (km s^{-1})	V_2 (km s^{-1})	σ_2 (km s^{-1})	$(O-C)_2$ (km s^{-1})
53152.737	0.701	–105.4	5.9	–2.6	175.7	11.9	0.2
53153.633	0.292	122.9	10.9	0.2	–162.8	14.9	8.2
53154.871	0.109	91.9	9.6	7.8	–121.4	10.0	–11.1
53155.734	0.678	–99.3	7.3	–2.8	164.4	12.8	–1.7
53156.621	0.264	135.3	10.7	8.9	–162.8	5.0	13.7
53157.888	0.100	90.6	13.7	11.9	–109.4	8.9	–7.3
53158.859	0.740	–104.5	10.8	3.9	182.9	2.7	–0.8
53159.621	0.186	125.6	13.5	7.5	–160.5	15.6	2.3
53159.860	0.401	65.3	7.4	–12.0	–85.9	10.5	16.2
53160.584	0.879	–54.7	9.7	18.0	132.4	20.0	4.6
53160.846	0.052	56.2	10.8	9.3	–63.7	11.0	–9.9
53161.610	0.556	–44.9	14.6	–14.0	69.3	18.9	3.8
53161.869	0.727	–110.2	8.1	–2.9	175.5	8.3	–6.6
53162.566	0.186	125.6	13.7	7.5	–160.5	16.2	2.3
53162.867	0.385	86.9	9.0	0.4	–92.9	7.9	23.2
53163.572	0.850	–80.8	10.0	5.8	135.9	16.2	–13.2
53164.814	0.670	–95.3	9.1	–1.7	163.4	16.0	1.7
53868.899	0.268	120.9	8.9	–5.2	–180.4	5.6	–4.5
53872.605	0.714	–111.7	8.6	–6.3	165.8	8.1	–13.6
53874.848	0.194	120.4	10.1	0.3	–152.4	11.2	13.4
53876.704	0.419	76.8	10.3	10.4	–77.4	12.3	7.8
53891.766	0.357	93.2	8.6	–7.4	–152.5	6.2	–14.7

and $v \sin i = 150$ km s^{-1}. These templates were used to measure the preliminary velocities listed in Table 5.15. Also listed are the dates of observation, uncertainties and $(O-C)$ values as computed from the fits discussed in section 5.6.4.

5.6.3 Tomographic Reconstruction

Similar to the previous sections, the Doppler tomography algorithm of Bagnuolo et al. (1994) was used to reconstruct the component spectra. Figure 5.24 shows the reconstructed primary and secondary spectra with their respective model templates plotted underneath and line identifications on top. A monochromatic flux ratio of 0.45 was used to reconstruct these individual spectra. Based on the reconstructed spectra, however, the two stars appear to be quite similar and are both early B-type stars. This may mean the flux ratio of 0.45 is too small.

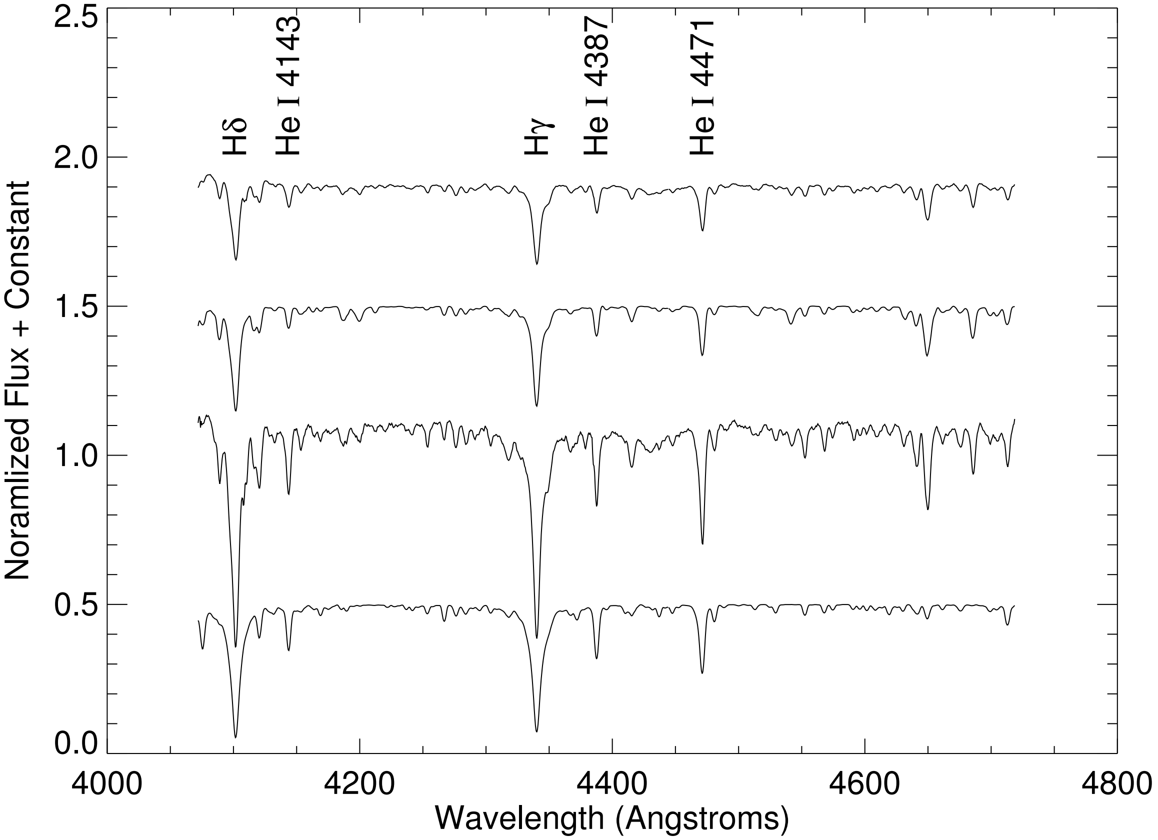

Figure 5.24 From bottom to top are plotted the secondary model spectrum, the reconstructed secondary spectrum, the model spectrum for the primary, and the reconstructed spectrum for the primary. Several prominent spectral features are labeled, including ones used for measuring velocities.

5.6.4 Radial Velocity Curve Solution

The ellipsoidal *Hipparcos* light curve and radial velocities were fit with ELC's genetic optimizer. Thus far, only circular orbits have been explored. Similarities between the ellipsoidal nature of the light curve for LH 54-425 and HD 155775 also hint toward the eccentricity being close to, if not equal to, zero. The radial velocity curves also do not obviously exhibit non-sinusoidal, and therefore eccentric orbit, behavior.

Attempts to fit the light curve and radial velocity curves simultaneously did not converge to a physically satisfying solution. Therefore, Figure 5.26 shows the *Hipparcos* light curve phased with $P = 1.5155426$ days and $T_0 = 2453156.9658$ based on times of minima from Balona (1992), the *Hipparcos* data, and from preliminary fits to the spectroscopic data. Given the temperature of the secondary's model template, there is a possibility that it may be a β Cephei star. β Cephei stars are early B-type stars in an advanced state of core-hydrogen burning that pulsate via opacity-driven modes throughout their interior (Dziembowski & Pamiatnykh 1993). They typically have pulsation periods between 2 and 12 hours, making a 1.5 day period a possible alias. They also have photometric variations less than 0.1 mag. However, the spectra do not exhibit the kind of behavior outlined in the study by Freyhammer et al. (2005) on HD 92024, where pulsations were seen to affect the velocity measurements of this star in a close binary orbit.

Could HD 155775 be a contact system, where the photospheres of the stars physically touch each other? There are several hints that this may be the case. First, in a contact binary system, the sum of the velocity semiamplitudes and the sum of the $v \sin i$ measurements should be roughly equal, as is the case for HD 155775 based on the preliminary model template fits and the values in Table 5.16. Second, the mass ratio ($q = 0.66$) and orbital period for HD 155775 match closely with the values of two other massive contact binaries, TU Mus (Penny et al. 2008) and V382 Cyg (Değirmenci et al. 1999). Third, in a contact binary system, the spectral lines for the two stars will never fully separate because of the contact configuration. Even at quadrature phases, spectra for HD 155775 in its spectrum stack do not separate. The main difference between HD 155775 and the two contact systems is the lack of deep

Table 5.16. Spectroscopic Orbital Solution for HD 155775

Element	Value
P (days)	1.51547[a]
T_0 (HJD–2,400,000)	53159.2525
K_1 (km s^{-1})............	117.7
K_2 (km s^{-1})............	179.6
γ_1 (km s^{-1})	9.1
γ_2 (km s^{-1})	3.4
rms (primary) (km s^{-1}) .	7.8
rms (secondary) (km s^{-1})	10.2

[a] Orbital period fixed to this value

eclipses in the light curve for HD 155775. This may indicate the system has a modest inclination, and this is supported by the comparatively small velocity semiamplitudes derived here of 117.7 and 179.6 km s^{-1} as opposed to those for TU Mus of 214.8 and 344.5 km s^{-1}.

The radial velocities are quite well fit (Fig. 5.25), so perhaps further exploration in the parameter space is all that is needed to reach a combined light curve and radial velocity curves solution. The results of this fit are listed in Table 5.16 for spectroscopic values only. Once again, no uncertainties were computed, because this is not the final fit for this system. No matter what the actual physical configuration may be for HD 155775, it should be a very interesting system, and may be quite a rare massive contact binary system.

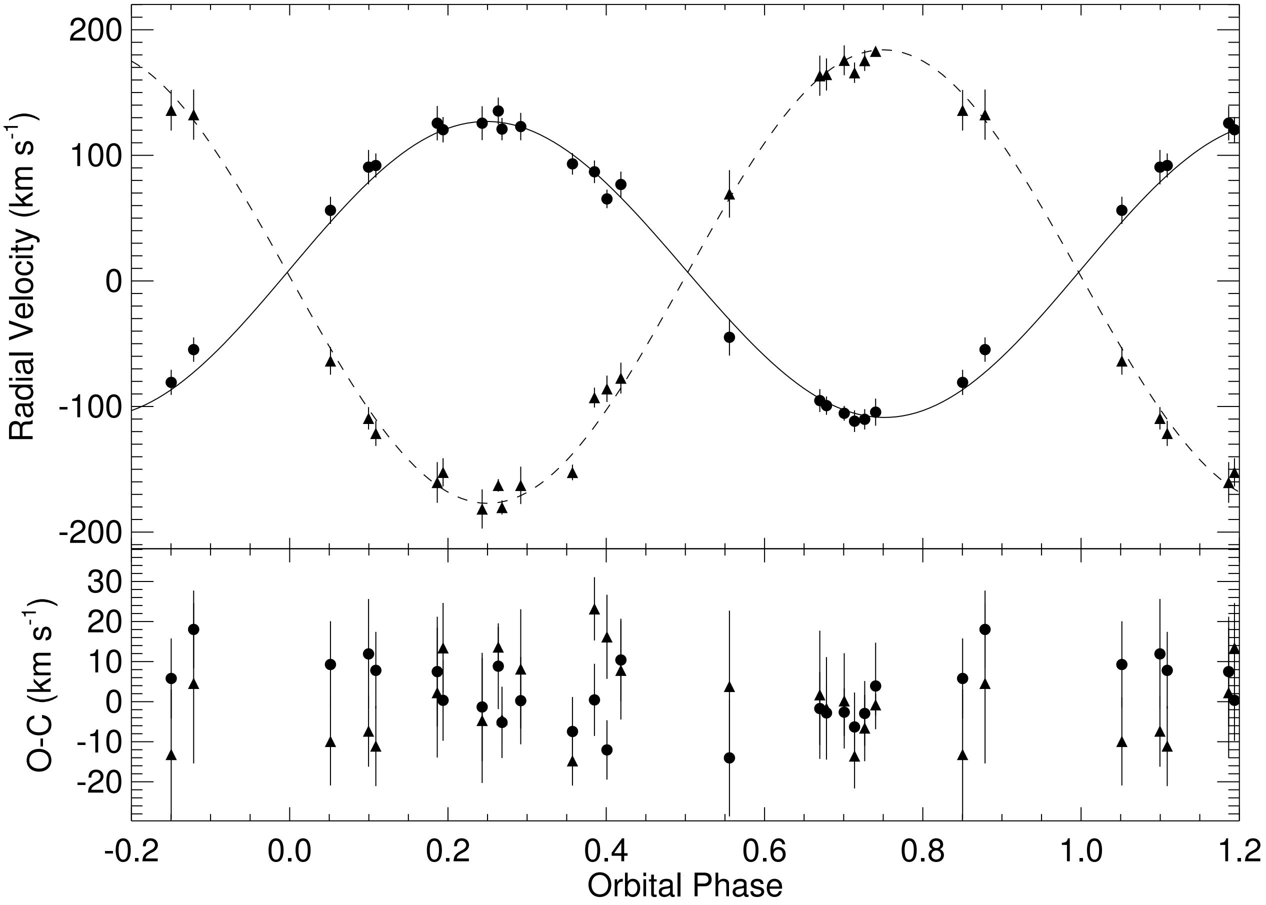

Figure 5.25 Radial velocity curves for HD 155775. Primary radial velocities are shown as circles and secondary velocities are triangles, both with uncertainties represented by verticl lines. The solid line is the best fit for the primary and the dashed line is the best fit for the secondary. Plotted below this are the $(O - C)$ values for each measurement.

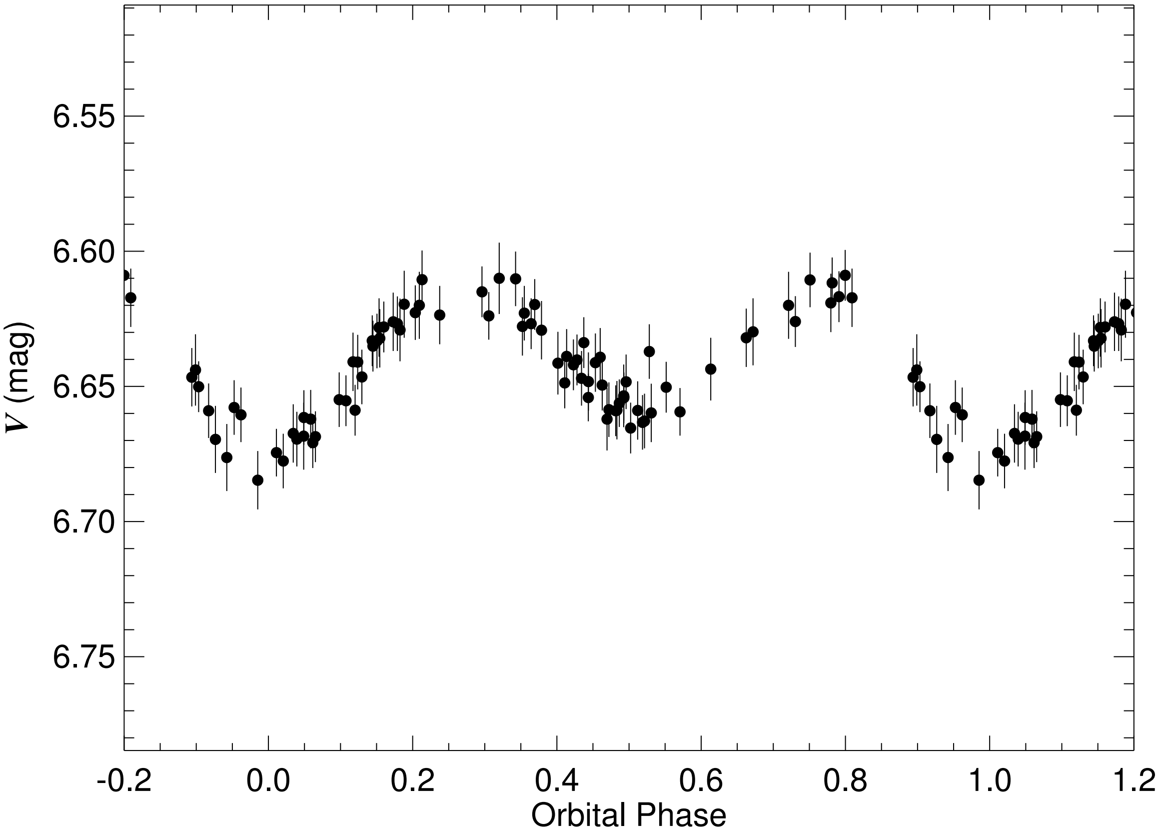

Figure 5.26 V-band light curve for HD 155775 transformed from *Hipparcos* data and plotted as circles with vertical lines representing uncertainties.

– 6 –

Future Spectroscopic Targets: Light Curves of Candidate Intermediate Mass Binary Systems

6.1 Introduction

In recent years large scale photometric surveys such as the ASAS (Pojmanski 2002) have preceded other surveys looking for transiting exoplanets. One byproduct of these searches will be a very large number of well sampled eclipsing binary light curves. The impetus behind the project outlined in this chapter was to find candidate intermediate and high mass binary systems with the eventual goal of obtaining fundamental parameters by observing these systems spectroscopically and resolving double lines. The applicability and validity of this technique has been demonstrated for lower mass systems in the recent effort by Deb & Singh (2011).

This chapter discusses the methods used to select probable intermediate mass binary eclipsing systems from the ASAS Catalog of Variable Stars. The final section covers the light curve analysis, estimation of uncertainties, the comparison of these results with previously published studies, and wraps up with an examination of the previously published spectral types as a check to see if intermediate mass systems were indeed selected.

6.2 Sample Selection

The sample selection criteria are based upon an ongoing spectroscopic observing program with the DeVeny Spectrograph (formerly the White Spectrograph on the 2.1-m telescope at Kitt Peak National Observatory) on the 1.8-m Perkins telescope at the Anderson Mesa Station of Lowell Observatory. The ASAS Catalog of Variable Stars

(Pojmanski 2002, 2003; Pojmanski & Maciejewski 2004, 2005; Pojmanski et al. 2005) which is a subset of the 3rd data release (Pojmanski 2002) was searched.[1] The ASAS Catalog of Variable Stars lists preliminary orbital periods for the identified eclipsing binaries. Furthermore, Pilecki, Pojmański, & Szczygieł have prepared an on-line catalog[2] that provides estimates of the system parameters based upon the V- and I-band light curves. Several thousand individual light curves were visually inspected and photometry was extracted for those systems that met specific criteria. First, systems were selected that were typically north of $-25°$ with a few exceptions near this cutoff limit. The most southern object is HD 122026 at $-27°$ while the most northern object is DR Vul with a declination of $+26°$. The data releases so far from the ASAS have reached a northern limit of $+28°$, a hard limit for the time being. In order to meet the exposure time limits for the instrumental spectral resolving power of the DeVeny of $R = \lambda \ / \ \Delta\lambda \sim 5000$, a limiting V magnitude of 11 was adopted. Then, only light curves that had a primary eclipse depth greater than 0.1 mag were selected to ensure only systems with well defined photometric variations were included. To further ensure that the secondary spectral lines will be readily detected, light curves were chosen where the ratio of eclipse depths was not greater than ~ 0.25 for the secondary-to-primary ratio. Contact systems were avoided and only light curves with “EA” and “EB” designations (Giuricin et al. 1983) were selected. This criterion was enforced in order to study systems where the stars have yet to interact with each other and have evolved thus far as individual stars.

---

[1] http://www.astrouw.edu.pl/asas/?page=main

[2] http:/www.astrouw.edu.pl/asas/?page=eclipsing

With this first cut of light curves, the corresponding J,H,K_s magnitudes were extracted from the 2MASS catalog (Skrutskie et al. 2006) for each object. Using the maximum brightness from the ASAS V-band light curve and the 2MASS K magnitude, $(V-K)$ colors were computed for each candidate object. For many objects there is an unknown amount of interstellar reddening, which will cause the $(V-K)$ color to increase and indicate a star with a cooler spectral type. Therefore, to look for intermediate mass binary candidates ($> 3M_\odot$), Table A5 in Kenyon & Hartmann (1995) was used to eliminate later spectral types based on the apparent $(V-K) < 0.7$, corresponding to a spectral type earlier than F0 V. To add an additional constraint, the reddening-free Q parameter in the infrared from Comerón et al. (2002) was computed with the 2MASS values. Stars with $Q < 0.1$ usually correspond to main sequence stars with masses greater than 1.4 $M_\odot$.

Observational parameters for candidate systems meeting all criteria are listed in Table 6.1. Column 1 lists the ASAS identification tag in the ASAS catalog of variable stars or general photometry catalog. In column 2 are alternate object names. Following this, columns 3 and 4 contain the right ascension and declination of the objects in the 2000.0 epoch. Columns 5 and 6 list the $(V-K)$ and Q values as discussed above. Next is column 7, showing the spectral classification found in the literature for each object while column 8 lists the reference for each entry. Column 7 demonstrates that most of the systems are intermediate mass binaries with an A- or B-type primary star. Column 9 lists whether the system was known to be a binary before the ASAS Catalog of Variable stars and gives the reference to the work where the system was first discovered to be a binary. It should be noted that only 21 of the 56 candidates listed in Table 6.1 are contained in the on-line atlas of Pilecki, Pojmański, & Szczygieł.

Table 6.1: Observational System Parameters

ASAS ID (1)	Other ID (2)	RA (J2000.0) (3)	Declination (J2000.0) (4)	$V-K$ (mag) (5)	Q (mag) (6)	Spectral Classification (7)	Classification Reference[a] (8)	Discovery Reference[a] (9)
053838+0901.2	HD 37396	05 38 38.1	+09 01 10.7	0.33	−0.10	A0	1	14
054816+2046.1	HD 247740	05 48 16.5	+20 46 10.3	0.18	−0.14	B8	1	ASAS
060857+1128.9	HD 252416	06 08 57.2	+11 25 56.2	0.19	0.00	B8	1	ASAS
060927−1501.7	TYC 5933−142−1	06 09 26.6	−15 01 42.7	0.31	−0.10	…	…	ASAS
062556−1254.5	HD 45263	06 25 56.1	−12 54 29.1	0.26	−0.07	B9 IV	2	ASAS
063347−1410.5	HD 46621	06 33 46.8	−14 10 30.9	0.28	0.14	A1 IV/V	2	ASAS
064010−1140.3	HD 47845	06 40 09.4	−11 40 17.8	0.47	0.05	A2 IV	3	ASAS
064118−0551.1	2MASS06411762−0551065	06 41 17.6	−05 51 06.9	0.43	−0.04	…	…	ASAS
064538+0219.4	HD 48866	06 45 37.8	+02 19 21.1	−0.04	−0.10	A (V)+A (V)	3	15
064609−1923.8	HD 49125	06 46 09.4	−19 23 50.1	−0.03	−0.08	B9 V	2	ASAS
064715+0225.6	HD 289072	06 47 14.6	+02 25 34.3	0.37	−0.03	B5	4	ASAS
064745+0122.3	V448 Mon	06 47 45.0	+01 22 18.0	0.14	0.09	B5	4	16
065534−1013.2	HD 51082	06 55 33.9	−10 13 12.6	0.02	−0.15	A0 V	3	17
065549−0402.6	HI Mon	06 55 49.1	−04 02 35.8	0.22	−0.04	B3/5 II	3	18
070105−0358.2	HD 52433	07 01 05.1	−03 58 15.5	−0.17	0.02	B3 III	3	19
070238+1347.0	HD 52637	07 02 38.2	+13 46 58.6	0.23	0.03	A0	1	20
070636−0437.4	AO Mon	07 06 36.3	−04 37 24.5	−0.43	−0.04	B3+B5	5	21
070943+2341.7	BD +23 1621	07 09 43.3	+23 41 42.8	0.70	0.01	…	…	ASAS
070946−2005.5	NSV 3433	07 09 46.2	−20 05 35.2	−0.09	0.01	…	…	17
071010−0035.1	HD 54780	07 10 10.4	−00 35 08.7	0.22	−0.17	B5/7 (III)	3	15
071203−0139.1	HD 55236	07 12 03.5	−01 39 04.2	0.54	0.04	A2 III/IV	3	ASAS
071702−1034.9	HD 56544[b]	07 17 02.4	−10 34 56.6	−0.30	0.02	A0	1	ASAS
072201−2552.6	CX CMa	07 22 01.0	−25 52 35.9	−0.30	−0.10	B5 V	6	21
073053+0513.7	HD 59607	07 30 53.5	+05 13 37.3	−0.27	−0.11	B8	1	ASAS

Continued on next page…

Table 6.1 – Continued

ASAS ID (1)	Other ID (2)	RA (J2000.0) (3)	Declination (J2000.0) (4)	$(V-K)$ (mag) (5)	Q (mag) (6)	Spectral Classification (7)	Classification Reference[a] (8)	Discovery Reference[a] (9)
073348−0940.9	HD 60389	07 33 48.4	−09 40 52.6	0.45	−0.02	G6 V	3	22
074355−2517.9	HD 62607	07 43 55.2	−25 17 53.7	0.08	−0.08	B9.5 V	2	ASAS
074717−0519.8	HD 63141	07 47 17.3	−05 19 51.1	0.29	−0.01	A0 V	3	17
074928−0721.6	BD −06 2317	07 49 27.5	−07 21 36.0	0.23	−0.05	A0	7	ASAS
075052+0048.0	HD 63818	07 50 52.4	+00 48 04.1	−0.06	−0.07	A0	1	ASAS
080617−0426.8	V871 Mon	08 06 17.3	−04 26 46.8	0.64	0.02	A3/5mA7-F0	3	23
081749−2659.7	HD 69797	08 17 48.7	−26 59 37.5	0.66	−0.22	A1 V	8	ASAS
083245+0247.3	BD +03 2001	08 32 45.3	+02 47 16.5	0.79	0.07	A2	9	ASAS
084831−2609.8	TT Pyx	08 48 30.9	−26 09 47.8	0.16	−0.08	B9.5 IV	2	24
101120−1956.3	HD 88409	10 11 19.5	−19 56 20.4	0.49	0.04	A5 II/III	2	ASAS
135949−2745.5	HD 122026	13 59 49.3	−27 45 26.4	0.52	0.03	A1/2 III/IV	8	ASAS
160851−2351.0	TYC 6780−1523−1	16 08 51.0	−23 51 01.4	1.56	0.09	…	…	ASAS
165354−1301.9	HD 152451	16 53 54.2	−13 01 57.5	1.85	0.14	A9 V	2	ASAS
170158+2348.4	HD 154010	17 01 57.5	+23 48 22.5	0.56	−0.01	A2	1	ASAS
173421−1836.3	HD 159246	17 34 21.1	−18 36 21.7	0.57	−0.08	B9 III	2	ASAS
174104+0747.1	V506 Oph	17 41 04.3	+07 47 04.3	1.12	0.10	A9	10	25
175659−2012.2	HD 312444	17 56 58.8	−20 12 05.7	1.46	−0.04	A3	3	ASAS
175859−2323.1	HD 313508	17 58 59.3	−23 23 07.9	0.68	−0.76	B8	3	ASAS
180903−1824.5	HD 165890	18 09 02.9	−18 24 29.5	0.66	−0.01	B7/8 Ib	2	ASAS
181025+0047.7	HD 166383	18 10 25.7	+00 47 47.0	0.88	0.15	B3/5 II/III	3	ASAS
181328−2214.3	HD 166851	18 13 28.0	−22 14 07.2	0.67	−0.03	B9 III/IV	2	ASAS
181909−1410.0	HD 168207	18 19 09.0	−14 10 00.6	1.05	0.05	B1/2(N)	2	ASAS
183129−1918.8	BD −19 5039	18 31 28.9	−19 18 47.3	0.90	0.02	B3 V	11	ASAS
183219−1117.4	BD −11 4667	18 32 19.0	−11 17 23.6	2.21	0.02	B1:V:pe	12	26
184223+1158.9	BD +11 3569	18 42 23.2	+11 58 57.4	−0.24	0.01	A2	9	ASAS
184327+0841.5	TYC 1025−1524−1	18 43 26.9	+08 41 32.1	0.53	0.00	…	…	ASAS

Continued on next page…

Table 6.1 – Continued

ASAS ID (1)	Other ID (2)	RA (J2000.0) (3)	Declination (J2000.0) (4)	$(V-K)$ (mag) (5)	Q (mag) (6)	Spectral Classification (7)	Classification Reference[a] (8)	Discovery Reference[a] (9)
184436−1923.4	YY Sgr	18 44 35.9	−19 23 22.7	0.41	0.12	B5+B6	13	27
185051−1354.6	HD 174397	18 50 51.3	−13 54 33.1	1.40	0.01	A9	2	ASAS
194334−0904.0	V1461 Aql	19 43 34.1	−09 04 02.1	1.17	0.19	A0 III	3	20
195342+0205.4	HD 188153	19 53 42.0	+02 05 21.2	0.32	−0.01	A0	1	ASAS
195613+1630.9	HD 354110	19 56 13.1	+16 30 59.1	0.19	−0.01	B8	3	ASAS
205642+1153.0	HD 199428	20 56 42.0	+11 53 02.3	0.54	−0.02	A2	1	ASAS

[a] References: 1−Cannon & Pickering (1924), 2−Houk & Smith-Moore (1988), 3−Houk & Swift (1999), 4−Nesterov et al. (1995), 5−Struve (1945), 6−Milone (1986), 7−Ochsenbein (1980), 8−Houk & Cowley (1982), 9−Heckmann (1975), 10−Brancewicz & Dworak (1980), 11−Wallerstein (1960), 12−Morgan et al. (1955), 13−Lacy (1993), 14−Vogt et al. (2004), 15−Poretti et al. (2005), 16−Wachmann (1964), 17−Strohmeier et al. (1965), 18−Wachmann (1968), 19−Otero et al. (2004), 20−Kazarovets et al. (1999), 21−Hoffmeister (1931), 22−Strohmeier (1966), 23−Wils & Dvorak (2003), 24−Hoffmeister (1933), 25−Hoffmeister (1935), 26−Bidelman (1982), 27−Zinner (1930)

[b] Misidentified in link between the Simbad Database and 2MASS catalog.

Table 6.2: Derived System Parameters

ASAS ID (1)	Other ID (2)	P (d) (3)	T_o (HJD−2,400,000) (4)	i (°) (5)	e (6)	ω (°) (7)
053838+0901.2	HD 37396	1.2266800(7)	54900.7215(9)	76.3(2)	0.0	···
054816+2046.1	HD 247740	2.432420(3)	54883.284(3)	81.9(3)	0.0	···
060857+1128.9	HD 252416	1.9064750(3)	54937.317(1)	87.8(3)	0.0	···
060927−1501.7	TYC 5933−142−1	0.8770790(4)	54901.1184(4)	76.1(8)	0.0	···
062556−1254.5	HD 45263	5.059505(1)	54949.571(1)	89.6(2)	0.0	···
063347−1410.5	HD 46621	1.5958525(7)	54953.602(1)	81.1(2)	0.0	···
064010−1140.3	HD 47845	5.285090(4)	53847.994(2)	88.1(1)	0.0	···
064118−0551.1	2MASS06411762−0551065	2.7575000(2)	54931.373(2)	77.8(2)	0.0	···
064538+0219.4	HD 48866	1.568196(1)	54905.362(1)	74.4(5)	0.0	···
064609−1923.8	HD 49125	2.9038975(3)	54908.0579(2)	88.6(2)	0.050(2)	53.1(3)
064715+0225.6	HD 289072	3.47257(2)	54931.694(2)	76.2(2)	0.029(6)	130(7)
064745+0122.3	V448 Mon	1.1184750(5)	54933.5519(4)	74.9(2)	0.0	···
065534−1013.2	HD 51082	2.186880(3)	54586.250(3)	81.2(2)	0.0	···
065549−0402.6	HI Mon	1.5744300(8)	54935.531(1)	80.2(3)	0.0	···
070105−0358.2	HD 52433	5.95577(2)	54603.119(4)	79.9(6)	0.089(5)	64(3)
070238+1347.0	HD 52637	1.918694(5)	54809.539(3)	75.0(3)	0.0	···
070636−0437.4	AO Mon	1.8847476(1)	54965.283(2)	85.3(2)	0.020(4)	73.6(6)
070943+2341.7	BD +23 1621	1.676100(1)	54944.097(2)	72.5(3)	0.0	···
070946−2005.5	NSV 3433	1.7568950(1)	55003.386(1)	85(2)	0.0	···
071010−0035.1	HD 54780	2.228764(5)	54963.206(4)	71.8(3)	0.0	···
071203−0139.1	HD 55236	1.2834150(5)	54944.918(1)	78.9(5)	0.0	···
071702−1034.9	HD 56544	1.276465(2)	55004.4228(5)	77.2(6)	0.0	···
072201−2552.6	CX CMa	0.95462500(2)	55007.3937(9)	81.8(2)	0.0	···
073053+0513.7	HD 59607	4.1393500(5)	54962.5048(4)	84.4(1)	0.0	···
073348−0940.9	HD 60389	2.549608(3)	54576.370(2)	76.6(2)	0.0	···
074355−2517.9	HD 62607	3.863847(3)	54606.582(3)	82.5(3)	0.0	···
074717−0519.8	HD 63141	4.593948(6)	54958.146(3)	85.2(1)	0.0	···
074928−0721.6	BD −06 2317	2.152188(1)	54966.080(2)	76(2)	0.0	···
075052+0048.0	HD 63818	2.0543180(7)	54966.5836(9)	80.2(2)	0.127(1)	0(3)
080617−0426.8	V871 Mon	4.335950(6)	54962.886(3)	82.3(5)	0.007(4)	283(12)
081749−2659.7	HD 69797	1.743810(5)	54931.5924(1)	87.2(2)	0.0	···
083245+0247.3	BD +03 2001	1.657400(3)	54936.661(1)	78.4(3)	0.0	···
084831−2609.8	TT Pyx	3.031555(1)	54987.7394(5)	89.8(8)	0.0	···
101120−1956.3	HD 88409	1.563820(3)	54902.837(1)	79.8(2)	0.0	···
135949−2745.5	HD 122026	6.13316(1)	55002.281(2)	88.2(1)	0.0	···
160851−2351.0	TYC 6780−1523−1	4.660068(4)	54801.473(2)	81.5(3)	0.0	···
165354−1301.9	HD 152451	2.207586(2)	54804.513(1)	83.1(1)	0.210(8)	160.3(6)
170158+2348.4	HD 154010	4.76987(3)	54700.586(2)	86.1(1)	0.0	···
173421−1836.3	HD 159246	5.216893(7)	54807.6262(9)	89.9(3)	0.0	···
174104+0747.1	V506 Oph	1.060427(1)	54806.6806(9)	89.9(6)	0.0	···
175659−2012.2	HD 312444	3.089370(2)	54803.4897(5)	82.8(2)	0.0	···
175859−2323.1	HD 313508	1.540495(5)	55006.0287(9)	79.2(2)	0.0	···
180903−1824.5	HD 165890	3.707515(8)	54807.317(4)	81.0(3)	0.0	···
181025+0047.7	HD 166383	3.18867(2)	54808.142(7)	72.1(1.7)	0.0	···
181328−2214.3	HD 166851	4.47977(3)	54803.530(11)	89.7(5)	0.0	···
181909−1410.0	HD 168207	1.786820(8)	54803.012(2)	75.0(2)	0.0	···
183129−1918.8	BD −19 5039	2.455005(8)	54949.213(2)	74.6(2)	0.0	···
183219−1117.4	BD −11 4667	4.95238(2)	55038.859(5)	83.3(9)	0.0	···
184223+1158.9	BD +11 3569	1.497118(3)	55008.3686(9)	81.2(3)	0.005(80)	160(24)
184327+0841.5	TYC 1025−1524−1	2.1392220(4)	55044.8479(9)	86.0(1)	0.298(1)	283.0(1)
184436−1923.4	YY Sgr	2.628448(2)	55027.735(1)	88.1(1)	0.117(1)	214.1(5)
185051−1354.6	HD 174397	3.145935(6)	55047.307(2)	78.0(2.4)	0.0	···
194334−0904.0	V1461 Aql	1.76306(1)	55040.5114(1)	82.3(2)	0.0	···
195342+0205.4	HD 188153	1.608120(2)	55040.4270(8)	73.2(2)	0.042(4)	24.5(7)
195613+1630.9	HD 354110	3.444576(3)	55036.802(1)	85.1(2)	0.011(1)	205(26)
205642+1153.0	HD 199428	4.124500(5)	55047.555(2)	89.7(2)	0.193(20)	346.2(4)

6.3 Light Curve Analysis

For each system, the V-band light curve was fit using ELC. The program solves for orbital and physical parameters relevant to the light curve. These parameters include the epoch of mid-eclipse of the primary star T_0, the orbital period P, the orbital inclination i, the Roche lobe filling factor of each star, the temperature of each star, and in cases with elliptical orbits, the eccentricity and longitude of periastron of the primary ω. In ELC, the primary is defined as the more massive star. It should be noted that the sizes and temperatures of the stars are relative, and without spectroscopic analysis, their true values cannot be determined.

In finding a best fit light curve for each system, the solutions with ELC create $\sim 40,000$ simulated light curves and record the χ^2 statistic associated with each light curve. In order to estimate uncertainties, χ^2 is projected over the range of each parameter of interest and attention is focused on the region around $\chi^2_{\rm min}$. The resulting χ^2 curves are not symmetric about the minimum, so the final estimate for the uncertainty of any particular parameter was the larger of the two adjoining $\chi^2_{\rm min} + 1$ values. The best fit values are listed in Table 6.2, with uncertainties listed in parentheses in units of the last digit quoted. Column 1 in Table 6.2 lists the ASAS ID and column 2 gives the alternate ID. The orbital period for each system is given in column 3. The period uncertainties are smaller in the shorter period systems due to the large number of orbits covered in the ASAS. Column 4 is the epoch of mid-eclipse of the primary. Note that this is different than the epoch of periastron for binaries with eccentric orbits. The ASAS Catalog of Variable Stars also lists P and T_0. The orbital periods listed here do not differ greatly, but the reference epochs were chosen to be more recent than those listed in Pojmanski (2002), reflecting times closer to when spectroscopic observations may be taken. Next is the orbital inclination in column 5, followed by the eccentricity of the orbit in column 6, and the longitude of periastron in column 7, where applicable. The value of the eccentricity found for BD+11°3569 of 0.006 ± 0.002 is only 3σ different than zero. Given the typical uncertainty in the ASAS data, any system listed with $e = 0.0$ probably has an eccentricity no greater than 0.01. It should also be noted that the longitude of periastron given here follows the spectroscopic orbit definition, i.e., measured from the plane of the sky through the center of mass to the primary.

To check the accuracy of these results, the values listed in Table 2 can be compared with those previously published. For example, a detailed light curve study of YY Sgr was made by Lacy (1993). His fit gives a longitude of periastron of 214.52 ± 0.46 deg, matching the value derived here of 214.1 ± 0.5 deg within uncertainties. The eccentricity in Lacy's work of 0.1573 ± 0.0008 and the inclination of 88.89 ± 0.12 deg are close to the values reported here of 0.117 ± 0.001 and 88.1 ± 0.1 deg, respectively, but still differ by more than 3σ. This is most likely due to the differences in the data analyzed. The data set in Lacy (1993) consists of 717 measures most of which were made during eclipses where the above parameters are best constrained. The data set used here includes 601 measures more or less evenly distributed around the orbit, and thus eclipses are not as well measured and the resulting parameters are not as accurate nor as well constrained. Future observations, specifically targeted to obtain data during eclipses, will help resolve these differences.

One of the goals in selecting the candidates in Tables 6.1 and 6.2 is to collect a set of data for early-type eclipsing binaries. Using previously published spectral classifications (Column 7 of Table 6.1) a histogram is constructed of the number of objects as a function of spectral type in Figure 6.1. This plot may be somewhat biased, as several spectral types are from Cannon & Pickering (1924). Subtle differences in the He I 4471 Å line are the determinant for discerning late-B from early-A spectral types. Early photographic plate spectra may not have been sufficiently sensitive to

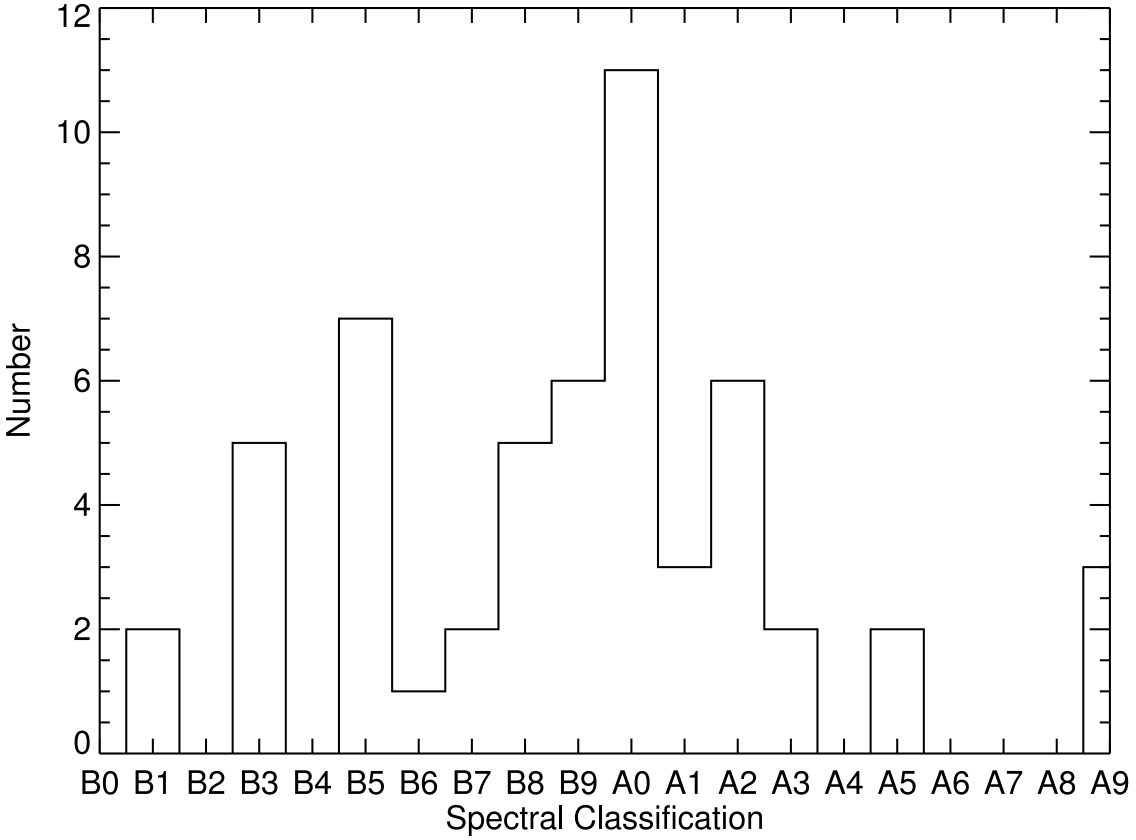

Figure 6.1 A histogram of published spectral types for target objects.

the changes in this temperature region, and several systems are likely consequently lumped into the "A0" category. Regardless, this plot shows that for the objects with published spectra, this data set has met the goal of finding systems earlier than F0. In fact, more stars (30) are hotter than A0 than stars (17) cooler than A0. Note that HD 60389, with a spectral type estimate of G6 V (Houk & Swift 1999) does not appear in this figure. Note also that not all systems discussed here have spectral types, and some previously known systems have spectral type estimates for both stars plotted in the histogram. Plots of light curve solutions and ASAS data for the full sample are given in Appendix A.

– 7 –

Summary

7.1 Introduction

The bulk of the work done in the course of this dissertation has been described in the previous chapters. First is a look at systems that were not analyzed in time for inclusion into this dissertation. Next is a qualitative look at values derived here compared with models used throughout the dissertation. To complete the dissertation, a rundown of some of the lessons learned is discussed in the final section.

7.2 Future Work

Several systems could not be analyzed and presented in this dissertation, mainly because of difficulties with the analysis. These systems are listed in Table 7.1, along with the number of spectra gathered thus far, whether or not the system has a variable light curve, and a comment on why work was stopped.

There are several listed reasons why work was halted on these systems. The first is related to the multiplicity of O-type systems. Because these systems are typically greater than 1 kpc away, there is a significant chance that some targets consist of at least three stars in a hierarchical system close together, with light from all three (or more) stars present in the spectra. If high angular resolution techniques cannot resolve close companions in these systems, analysis of a close binary system becomes very difficult when trying to account for the third star's light. Several of the systems show line asymmetries in certain spectra, but no clear separation of the spectral features of each component. Other systems have two well defined eclipses in the light

Table 7.1. Systems Awaiting Further Analysis

System Name	N	Varying Light Curve?	Comment
HD 56995	22	Y	eclipsing LC, triple?
HD 64315	46	Y	quadruple, ellipsoidal LC variations
HD 92024	32	Y	β Cep system, complex spectra
HD 101205	22	Y	eclipsing LC, triple?
HD 113659	23	Y	eclipsing LC, triple?
HD 114026	30	Y	eclipsing LC, triple?
HD 150136	33	N	triple system
CPD−35°2209	14	N	SB2, eccentric, insufficient data
CPD−40°2666	18	Y	eclipsing LC, line asymmetries
HD 152246	26	N	line asymmetries
HD 153426	16	N	line asymmetries
HD 158186	24	Y	eclipsing LC, unseen companion
HD 165246	24	Y	eclipsing LC, triple?
HD 167971	9	Y	eclipsing LC, insufficient data?
LS 1874	41	N	line asymmetries
LS 3052	24	Y	eclipsing LC, very faint companion
NGC 6231 SBL 314	14	N	line asymmetries
NGC 6231 SBL 521	17	Y	unknown orbital period

curve, but no companion can be seen in the spectra, even at quadrature phases. These systems may be hierarchical triples, where the brightest component has broad deep lines masking the SB2 nature of the two fainter, eclipsing components. Whatever the reason analyses were stopped on the systems in Table 7.1, these are great targets for techniques not explored in this dissertation.

7.3 Spectroscopic Binary Parameter Space

What can be said about the completeness of this survey? Beyond what limit is it likely that all spectroscopic variables have been detected? In order to address this query, it is appropriate to explore the parameter space of physical properties of the binaries studied. The parameters explored here will include the mass ratio, assuming a primary mass of 25 $M_\odot$ corresponding to a O7 V star in the calibration of Martins et al. (2005), the log of the semimajor axis a in astronomical units (AU), the log of the orbital period in years, and the difference in V-band magnitude. Let's start with the equation listed in the introduction of this dissertation,

$$M_{1,2}\sin^3 i = 1.036149 \times 10^{-7}(1-e^2)^{3/2}(K_1+K_2)^2 K_{2,1}P.$$

Let's also assume circular orbits ($e = 0$), a most likely inclination value of $\langle \sin i \rangle = \pi/4$, and also take the average value of $v \sin i$ from Penny & Gies (2009) of 130 km s^{-1} from a study of rotation rates of O-stars. Some algebra and substitution gives the following form of the above equation in terms of the orbital period:

$$P = M\frac{(167.2\ km\ s^{-1})}{K_1^3}\frac{q^3}{1+q^2}$$

Now, we assume the lowest detected K_1 value from HD 152147 of ∼13 km s^{-1}, assume a range of q (mass ratio) values and calculate a range of orbital periods. This gives the solid, labeled line in Figure 7.1 marked $K_1 = 13$ km s^{-1}.

The hashed region in Figure 7.1 that lies mostly above the 100 km s^{-1} line is the region where the analyses performed here would have detected any SB2 systems. The region is bounded on the bottom by the mass ratio and flux ratio (ΔV) estimated detection limits corresponding to a ΔV of 2.5 or a flux ratio of 0.1. The right hand boundary of this region is determined by the typcial time frame of observations, about two weeks, or log $P = -1.4$, the longest orbital period possible to detect in our data sets. If any binary resided in this region of parameter space, it would have been detected in this survey as an SB2 system. The second line for 13 km s^{-1}, delineates

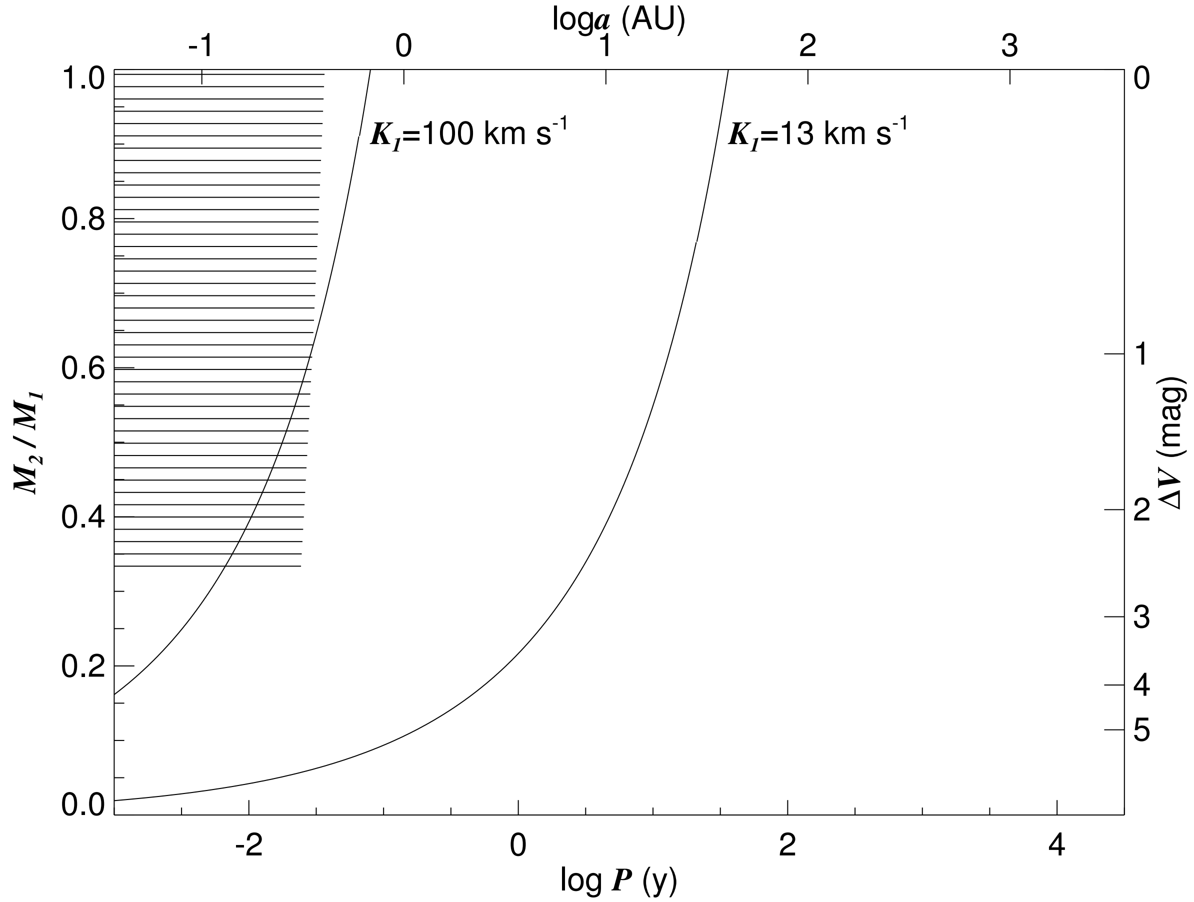

Figure 7.1 This is a plot of the parameter space of spectroscopic binaires. The shaded region in the upper left shows where SB2 systems would be detected given the time observed and sensitivity of the data. The overplotted lines display the regions above which SB1s with the labeled K_1 values would be detected, including the SB1 in this work with the lowest detected K_1 value of 13 km s^{-1} (HD 152147).

the region above which a system would have been detected in this survey as an SB1, again given the limits in time sampling, for log $P = -1.4$ in order to determine an orbit for such a system. To detect more of the systems residing in the region to the right of the log $P = -1.4$ boundary, the same observations would need to be taken over a longer time period. Therefore, this study, even with observations made over 10 years (log $P = 1.0$) will only be able to detect SB1s above the 13 km s^{-1} line. Any binaries that reside to the right of this line would have to be detected via other methods, such as long-baseline interferometry, speckle interferometry, and direct imaging as you move further to the right toward longer period systems.

This plot reveals the high sensitivity of long-term spectroscopic surveys to variability, even at the modest resolution used for the majority of the data in this dissertation ($R \sim 3000$). The utility of such surveys in helping to fill in this region of parameter space ($a = 5 - 100$ AU), particularly for massive stars, is one of the least explored parts of this parameter space according to the review by Sana et al. (2011). The binary fraction of massive stars will only increase with longer period spectroscopic detections that could be made with future work similar to the work done here.

7.4 Results

Astrophysical parameters were computed for six stars in three binary systems, LH 54-425, HI Mon, and HD 42401. Single lined orbits were computed for 5 systems, and interesting characteristics were explored for two more SB1-like systems. Only a few parameters are computed for the stars discussed in Chapters 3 and 4. With only an effective temperature derived, it is difficult to plot the Chapter 3 and 4 stars on an H-R Diagram. The spectral classification was estimated for each of these stars based on the Martins et al. (2005) relations. An estimate for the luminosity from column 6 of Tables 4, 5, and 6 in Martins et al. (2005) for each object could then be obtained from those same relations in order to place each object on an H-R diagram.

Figure 7.2 shows the H-R diagram for all O-type objects and some B-type objects analyzed in this dissertation. The early B-type components of HI Mon are located at the bottom right of the plot, and serve as a reference for the bottom of the region

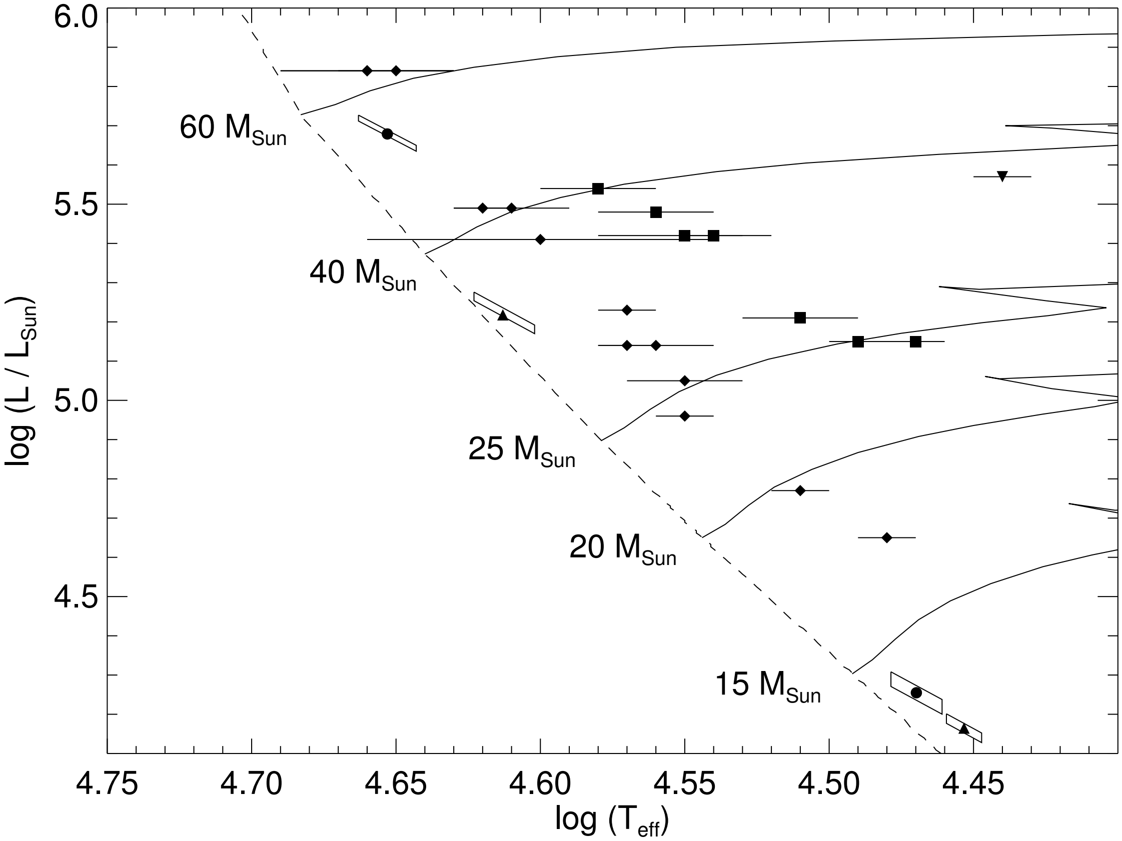

Figure 7.2 A theoretical H-R diagram showing objects from Chapters 3 and 4. Also plotted are the components of LH 54-425 and HI Mon for comparison. Main sequence stars are filled diamonds, giants are filled squares, and the supergiant is the filled downward facing triangle. Uncertainties in $T_{\rm eff}$ are represented by horizontal lines. A zero age main sequence from Lejeune & Schaerer (2001) is shown by a dashed line, and evolutionary tracks for stars of various masses from Schaller et al. (1992) are shown as labeled solid lines.

occupied by O-type objects. The components of LH 54-425 are also plotted as they were in Figure 5.14. Main sequence objects are filled diamonds, with uncertainties in the effective temperatures shown as horizontal lines. Giants are shown by filled squares and HD 152147, the sole supergiant, is a filled, downward pointing triangle. Evolutionary tracks for stars of mass 15, 20, 25, 40, and 60 $M_\odot$ from Schaller et al. (1992) are plotted along with a zero age main sequence (ZAMS, dashed line) from

Lejeune & Schaerer (2001). Immediately noticeable is the delineation between main sequence and evolved components. Also equally noticeable are the distances of objects in Chapters 3 and 4 from the ZAMS. Are all of these main sequence objects slightly evolved, or is there a systematic difference between the calibration in Martins et al. (2005) and the ZAMS obtained from Lejeune & Schaerer (2001)? Questions like these are beyond the scope of this dissertation, but hint at the kind of analyses that can be done with the work done here.

7.5 Lessons Learned

Perhaps the most important lesson learned in the course of this work is that there are so few "nice" double-lined eclipsing (or even ellipsoidal) systems among the O-type stars. Rather than chalk it up to some sinister and cynical conspiracy, perhaps it is just another human life lesson: live fast and die young. Chasing after the Steve McQueen's of the stellar world has proven not only taxing, but extremely difficult! There are so few, and they seem to refuse to fit into the nice, simple categories that a general scientific taxonomy prefers.

Other lessons learned are perhaps the every day type of lessons one is supposed to learn in graduate school. Watch your double, floating, and integer arrays while programming. As my father would say, side projects are "the devil's doin". One of the multitude of side projects made it into this dissertation: the ASAS light curves work that was the culmination of summer research done by John Helsel. Work with Melissa Hursey, a student teacher working under John Wilson, made it into print (Williams et al. 2010b), but efforts with data from NASA's Kepler Mission have not. These projects are complementary to the work I present in this dissertation. I encourage folks to go read them, or at least watch out for future publications on Kepler data by yours truly.

I have also learned how to do proper historical bibliographies on bright stars. You are only truly doing those stars, and the astronomy community as a whole, justice if you reference people like Annie Jump Cannon, Henrietta Leavitt, and Otto Struve. I am therefore quite proud of the following "references" section, despite failing to find references from authors with names starting with "Q" or "X" – the only two letters missing.

REFERENCES

Abt, H. A. 1977, PASP, 89, 646

Africano, J. L., Cobb, C. L., Dunham, D. W., Evans, D. S., Fekel, F. C., & Vogt, S. S. 1975, AJ, 80, 689

Aller, L. H. et al. 1982, Landolt-Börnstein: Numerical Data and Functional Relationships in Science and Technology (New York: Springer-Verlag)

Aragona, C., McSwain, M. V., Grundstrom, E. D., Marsh, A. N., Roettenbacher, R. M., Hessler, K. M., Boyajian, T. S., & Ray, P. S. 2009, ApJ, 698, 514

Ardeberg, A., & Maurice, E. 1977, A&AS, 28, 153

Bagnuolo, Jr., W. G., Gies, D. R., Hahula, M. E., Wiemker, R., & Wiggs, M. S. 1994, ApJ, 423, 446

Bagnuolo, Jr., W. G., Riddle, R. L., Gies, D. R., & Barry, D. J. 2001, ApJ, 554, 362

Balona, L. A. 1975, MmRAS, 78, 51

——. 1992, MNRAS, 254, 404

Berger, D. H., & Gies, D. R. 2001, ApJ, 555, 364

Bessell, M. S. 1990, PASP, 102, 1181

Bessell, M. S., & Brett, J. M. 1988, PASP, 100, 1134

Bessell, M. S., Castelli, F., & Plez, B. 1998, A&A, 333, 231

Bidelman, W. P. 1982, IBVS, 2112

Blaauw, A. 1993, in Massive Stars: Their Lives in the Interstellar Medium, ASP Conference Series, Vol. 35, ed. J. P. Cassinelli & E. B. Churchwell (San Francisco: ASP), 207

Boggs, D., & Bohm-Vitense, E. 1989, ApJ, 339, 209

——. 1990, ApJ, 358, 441

Böhm-Vitense, E. 1981, ARA&A, 19, 295

Böhm-Vitense, E., Hodge, P., & Boggs, D. 1984, ApJ, 287, 825

Bolton, C. T., & Rogers, G. L. 1978, ApJ, 222, 234

Bouret, J.-C., Lanz, T., & Hillier, D. J. 2005, A&A, 438, 301

Bowen, D. V. et al. 2008, ApJS, 176, 59

Brancewicz, H. K., & Dworak, T. Z. 1980, Acta Astron., 30, 501

Brinkmann, W. et al. 1997, A&A, 323, 739

Buscombe, W., & Kennedy, P. M. 1969, MNRAS, 143, 1

Cannon, A. J., & Pickering, E. C. 1924, Annals of the Astronomical Observatory Henry Draper (HD) Catalog and HD Extension (Cambridge, MA: Harvard College)

Carraro, G., Romaniello, M., Ventura, P., & Patat, F. 2004, A&A, 418, 525

Cohen, M., Wheaton, W. A., & Megeath, S. T. 2003, AJ, 126, 1090

Colina, L., Bohlin, R. C., & Castelli, F. 1996, HST Instrument Science Report CAL/SCS-008 (Baltimore, MD: STScI)

Comerón, F. et al. 2002, A&A, 389, 874

Conti, P. S., & Ebbets, D. 1977, ApJ, 213, 438

Conti, P. S., & Leep, E. M. 1974, ApJ, 193, 113

Conti, P. S., Leep, E. M., & Lorre, J. J. 1977, ApJ, 214, 759

Cox, A. N. 2000, Allen's Astrophysical Quantities 4th ed. (New York: AIP Press)

Crampton, D. 1972, MNRAS, 158, 85

Crawford, D. L. 1975, PASP, 87, 481

Cutri, R. M. et al. 2003, 2MASS All Sky Catalog of Point Sources (Pasadena, CA: IPAC/Caltech)

Daflon, S., Cunha, K., de Araújo, F. X., Wolff, S., & Przybilla, N. 2007, AJ, 134, 1570

de Geus, E. J. 1992, A&A, 262, 258

de Mello, D. F., Leitherer, C., & Heckman, T. M. 2000, ApJ, 530, 251

Deb, S., & Singh, H. P. 2011, MNRAS, 412, 1787

Değirmenci, Ö. L., Sezer, C., Demircan, O., Erdem, A., Özdemir, S., Ak, H., & Albayrak, B. 1999, A&AS, 134, 327

Diaz-Cordoves, J., & Gimenez, A. 1992, A&A, 259, 227

Djurašević, G., Vince, I., & Atanacković, O. 2008, AJ, 136, 767

Droege, T. F., Richmond, M. W., Sallman, M. P., & Creager, R. P. 2006, PASP, 118, 1666

Dubus, G., Cerutti, B., & Henri, G. 2010, A&A, 516, A18

Dziembowski, W. A., & Pamiatnykh, A. A. 1993, MNRAS, 262, 204

Eggen, O. J. 1978, AJ, 83, 288

Eggleton, P. P. 1983, ApJ, 268, 368

Ekström, S., Meynet, G., Maeder, A., & Barblan, F. 2008, A&A, 478, 467

ESA. 1997, The *Hipparcos* and *Tycho* Catalogues (ESA SP-1200)(Noordwijk: ESA)

Feast, M. W., & Thackeray, A. D. 1963, MmRAS, 68, 173

Feast, M. W., Thackeray, A. D., & Wesselink, A. J. 1955, MmRAS, 67, 51

——. 1957, MmRAS, 68, 1

Fehrenbach, C., Duflot, M., Mannone, C., Burnage, R., & Genty, V. 1997, A&AS, 124, 255

Fitzpatrick, E. L. 1999, PASP, 111, 63

Freedman, W. L., & Madore, B. F. 2010, ARA&A, 48, 673

Freedman, W. L. et al. 2001, ApJ, 553, 47

Freyhammer, L. M., Hensberge, H., Sterken, C., Pavlovski, K., Smette, A., & Ilijić, S. 2005, A&A, 429, 631

Fullerton, A. W. 1990, PhD thesis, University of Toronto

Garmany, C. D., Conti, P. S., & Massey, P. 1980, ApJ, 242, 1063

Garmany, C. D., & Vacca, W. D. 1991, PASP, 103, 347

Garrison, R. F., Hiltner, W. A., & Schild, R. E. 1977, ApJS, 35, 111

Gies, D. R. 1987, ApJS, 64, 545

Gies, D. R., & Bolton, C. T. 1986a, ApJS, 61, 419

——. 1986b, ApJ, 304, 371

Gies, D. R., Fullerton, A. W., Bolton, C. T., Bagnuolo, Jr., W. G., Hahula, M. E., & Wiemker, R. 1994, ApJ, 422, 823

Gies, D. R., Penny, L. R., Mayer, P., Drechsel, H., & Lorenz, R. 2002, ApJ, 574, 957

Gilfanov, M., & Bogdán, Á. 2010, Nature, 463, 924

Giuricin, G., Mardirossian, F., & Mezzetti, M. 1983, A&AS, 54, 211

Gray, D. F. 2005, The Observation and Analysis of Stellar Photospheres (3rd ed.; Cambridge: Cambridge Univ. Press)

Gray, R. O. 1998, AJ, 116, 482

Grundstrom, E. D. 2007, PhD thesis, Georgia State University

Grundstrom, E. D. et al. 2007a, ApJ

Grundstrom, E. D., Gies, D. R., Hillwig, T. C., McSwain, M. V., Smith, N., Gehrz, R. D., Stahl, O., & Kaufer, A. 2007b, ApJ

Hanson, M. M., Conti, P. S., & Rieke, M. J. 1996, ApJS, 107, 281

Hanson, M. M., Howarth, I. D., & Conti, P. S. 1997, ApJ, 489, 698

Hanuschik, R. W. 1995, A&A, 295, 423

Harmanec, P. 1988, Bull. Astron. Inst. Czech., 39, 329

——. 1998, A&A, 335, 173

Harries, T. J., Howarth, I. D., & Evans, C. J. 2002, MNRAS, 337, 341

Harris, III, D. L. 1955, ApJ, 121, 554

Hauck, B., & Mermilliod, M. 1998, A&AS, 129, 431

Hayford, P. 1932, Lick Observatory Bulletin, 16, 53

Heckmann, O. 1975, AGK3. Star catalogue of positions and proper motions north of −2.5 deg. declination, ed. W. Dieckvoss (Hamburg-Bergedorf: Hamburger Sternwarte)

Hegedus, T. 1988, Bull. Inf. CDS, 35, 15

Hernández, J., Calvet, N., Hartmann, L., Briceño, C., Sicilia-Aguilar, A., & Berlind, P. 2005, AJ, 129, 856

Hilditch, R. W., Howarth, I. D., & Harries, T. J. 2005, MNRAS, 357, 304

Hill, R. J., Madore, B. F., & Freedman, W. L. 1994, ApJS, 91, 583

Hillier, D. J., & Miller, D. L. 1998, ApJ, 496, 407

Hiltner, W. A. 1956, ApJS, 2, 389

Hinton, J. A. et al. 2009, ApJ, 690, L101

Hoffmeister, C. 1931, AN, 242, 129

——. 1933, AN, 247, 281

——. 1935, AN, 255, 401

Hoffmeister, V. H., Chini, R., Scheyda, C. M., Schulze, D., Watermann, R., Nürnberger, D., & Vogt, N. 2008, ApJ, 686, 310

Høg, E. et al. 2000, A&A, 355, L27

Hoogerwerf, R., de Bruijne, J. H. J., & de Zeeuw, P. T. 2000, ApJ, 544, L133

Houck, J. R. et al. 2004, ApJS, 154, 18

Houk, N. 1975, Michigan Catalogue of Two-dimensional Spectral Types for the HD Stars, Vol. 1 (Ann Arbor: Univ. of Michigan)

Houk, N., & Cowley, A. P. 1982, Michigan Catalogue of Two-dimensional Spectral Types for the HD Stars, Vol. 3 (Ann Arbor: Univ. of Michigan)

Houk, N., & Smith-Moore, M. 1988, Michigan Catalogue of Two-dimensional Spectral Types for the HD Stars, Vol. 4 (Ann Arbor: Univ. of Michigan)

Houk, N., & Swift, C. 1999, Michigan Catalogue of Two-dimensional Spectral Types for the HD Stars, Vol. 5 (Ann Arbor: Univ. of Michigan)

Howarth, I. D., Siebert, K. W., Hussain, G. A. J., & Prinja, R. K. 1997, MNRAS, 284, 265

Huang, W., & Gies, D. R. 2006, ApJ, 648, 580

——. 2008, ApJ, 683, 1045

Hubeny, I. 1988, Comput. Phys. Commun., 52, 103

Hubeny, I., Heap, S. R., & Lanz, T. 1998, in ASP Conf. Ser., Vol. 131, Boulder Munich II: Properties of Hot Luminous Stars, ed. I. Howarth (San Francisco, CA:

ASP), 108

Hubeny, I., & Lanz, T. 1995, ApJ, 439, 875

Humphreys, R. M. 1978, ApJS, 38, 309

Ishihara, D. et al. 2010, A&A, 514, A1

Jeffery, C. S., Woolf, V. M., & Pollacco, D. L. 2001, A&A, 376, 497

Jeffries, R. D., Oliveira, J. M., Naylor, T., Mayne, N. J., & Littlefair, S. P. 2007, MNRAS, 376, 580

Kaltcheva, N. T., & Georgiev, L. N. 1994, MNRAS, 269, 289

Kazarovets, E. V., Samus, N. N., Durlevich, O. V., Frolov, M. S., Antipin, S. V., Kireeva, N. N., & Pastukhova, E. N. 1999, IBVS, 4659

Kenyon, S. J., & Hartmann, L. 1995, ApJS, 101, 117

Kessel-Deynet, O., & Burkert, A. 2003, MNRAS, 338, 545

Kharchenko, N. V., Piskunov, A. E., Röser, S., Schilbach, E., & Scholz, R. 2005, A&A, 438, 1163

Kilkenny, D., & Hill, P. W. 1975, MNRAS, 172, 649

Klinglesmith, D. A., & Sobieski, S. 1970, AJ, 75, 175

Kobulnicky, H. A., & Kiminki, D. C. 2011, Bull. Soc. Roy. Sci. de Liege, 80, 616

Koen, C., & Eyer, L. 2002, MNRAS, 331, 45

Kopal, Z. 1959, Close Binary Systems (New York: Wiley)

Kurucz, R. L. 1979, ApJS, 40, 1

Lacy, C. H. S. 1993, AJ, 105, 637

Langer, N., Cantiello, M., Yoon, S., Hunter, I., Brott, I., Lennon, D., de Mink, S., & Verheijdt, M. 2008, in Massive Stars as Cosmic Engines, Proc. IAU, Vol. 3, Symp.

S250, ed. F. Bresolin, P. A. Crowther, & J. Puls (Cambridge: Cambridge Univ. Press), 167

Lanz, T., & Hubeny, I. 2003, ApJS, 146, 417

——. 2007, ApJS, 169, 83

Leavitt, H. S., & Pickering, E. C. 1913, Harvard College Observatory Circular, 179, 1

Lee, H., & Chen, W. P. 2007, ApJ, 657, 884

Lejeune, T., & Schaerer, D. 2001, A&A, 366, 538

Levato, H., Malaroda, S., Morrell, N., Garcia, B., & Hernandez, C. 1991, ApJS, 75, 869

Levato, H., Morrell, N., Garcia, B., & Malaroda, S. 1988, ApJS, 68, 319

Lucarelli, F. et al. 2010, The Astronomer's Telegram, 2761, 1

Lucy, L. B. 1967, ZAp, 65, 89

——. 1968, ApJ, 153, 877

Lucy, L. B., & Sweeney, M. A. 1971, AJ, 76, 544

MacConnell, D. J., & Bidelman, W. P. 1976, AJ, 81, 225

Maíz-Apellániz, J., Walborn, N. R., Galué, H. Á., & Wei, L. H. 2004, ApJS, 151, 103

Malkov, O. Y. 2003, A&A, 402, 1055

——. 2007, MNRAS, 382, 1073

Martins, F., Schaerer, D., & Hillier, D. J. 2005, A&A, 436, 1049

Mason, B. D. 1996, AJ, 112, 2260

Mason, B. D., Gies, D. R., Hartkopf, W. I., Bagnuolo, Jr., W. G., ten Brummelaar, T., & McAlister, H. A. 1998, AJ, 115, 821

Mason, B. D., Hartkopf, W. I., Gies, D. R., Henry, T. J., & Helsel, J. W. 2009, AJ, 137, 3358

Mason, B. D., Wycoff, G. L., Hartkopf, W. I., Douglass, G. G., & Worley, C. E. 2001, AJ, 122, 3466

Massey, P., DeGioia-Eastwood, K., & Waterhouse, E. 2001, AJ, 121, 1050

Massey, P., & Hunter, D. A. 1998, ApJ, 493, 180

Massey, P., & Johnson, J. 1993, AJ, 105, 980

Massey, P., Johnson, K. E., & Degioia-Eastwood, K. 1995, ApJ, 454, 151

Massey, P., Penny, L. R., & Vukovich, J. 2002, ApJ, 565, 982

Mathys, G. 1988, A&AS, 76, 427

——. 1989, A&AS, 81, 237

Mazeh, T., & Goldberg, D. 1992, ApJ, 394, 592

McCuskey, S. W., Pesch, P., & Snyder, G. A. 1974, AJ, 79, 597

McSwain, M. V., Grundstrom, E. D., Gies, D. R., & Ray, P. S. 2010, ApJ, 724, 379

Megier, A., Strobel, A., Galazutdinov, G. A., & Krełowski, J. 2009, A&A, 507, 833

Mermilliod, J., & Mermilliod, M. 1994, Catalogue of Mean UBV Data on Stars (Berlin: Springer-Verlag)

Mermilliod, J. C. 1991, Catalogue of Homogeneous Means in the UBV System (Lusanne: Inst. d'Astronomie, Univ. de Lausanne)

Merrill, P. W., & Burwell, C. G. 1943, ApJ, 98, 153

Milone, E. F. 1986, ApJS, 61, 455

Mirabel, I. F. 2007, Ap&SS, 309, 267

Mochnacki, S. W., & Doughty, N. A. 1972, MNRAS, 156, 51

Mokiem, M. R. et al. 2007, A&A, 465, 1003

Morbey, C. L., & Brosterhus, E. B. 1974, PASP, 86, 455

Morgan, W. W., Code, A. D., & Whitford, A. E. 1955, ApJS, 2, 41

Munari, U., Sordo, R., Castelli, F., & Zwitter, T. 2005, A&A, 442, 1127

Nazarenko, V. V., & Glazunova, L. V. 2006, Astronomy Reports, 50, 369

Nazé, Y. 2009, A&A, 506, 1055

Neckel, T., & Klare, G. 1980, A&AS, 42, 251

Nesterov, V. V., Kuzmin, A. V., Ashimbaeva, N. T., Volchkov, A. A., Röser, S., & Bastian, U. 1995, A&AS, 110, 367

Neubauer, F. J. 1943, ApJ, 97, 300

Nielbock, M., Chini, R., Jütte, M., & Manthey, E. 2001, A&A, 377, 273

Nomoto, K., Thielemann, F., & Yokoi, K. 1984, ApJ, 286, 644

Ochsenbein, F. 1980, Bull. Inf. CDS, 19, 74

Oey, M. S. 1996, ApJS, 104, 71

Oey, M. S., & Smedley, S. A. 1998, AJ, 116, 1263

Ogura, K., & Ishida, K. 1976, PASJ, 28, 35

Oktariani, F., & Okazaki, A. T. 2009, PASJ, 61, 57

Olivares, E. F. et al. 2010, ApJ, 715, 833

Orosz, J. A. et al. 2002, ApJ, 568, 845

Orosz, J. A., & Hauschildt, P. H. 2000, A&A, 364, 265

Ostrov, P. G. 2002, MNRAS, 336, 309

Otero, S. A., Wils, P., & Dubovsky, P. A. 2004, IBVS, 5570

Ott, C. D., Burrows, A., Thompson, T. A., Livne, E., & Walder, R. 2006, ApJS, 164, 130

Paredes, J. M. 2008, in AIP Conf. Proc., Vol. 1085, Proc. 4th International Meeting on High Energy Gamma-Ray Astronomy, ed. F. A. Aharonian, W. Hofmann, & F. Rieger (San Francisco, CA: ASP), 157

Patriarchi, P., Morbidelli, L., & Perinotto, M. 2003, A&A, 410, 905

Penny, L. R. 1996, ApJ, 463, 737

Penny, L. R., & Gies, D. R. 2009, ApJ, 700, 844

Penny, L. R., Ouzts, C., & Gies, D. R. 2008, ApJ, 681, 554

Penny, L. R., Sprague, A. J., Seago, G., & Gies, D. R. 2004, ApJ, 617, 1316

Peters, G. J. 1983, PASP, 95, 311

Petrie, R. M., & Lee, E. K. 1965, Publ. Dom. Ap. Obs. Victoria, 12, 435

Petrie, R. M., & Pearce, J. A. 1961, Publ. Dom. Ap. Obs. Victoria, 12, 1

Piatti, A. E., Clariá, J. J., & Ahumada, A. V. 2010, MNRAS, 408, 1147

Pittori, C. et al. 2009, A&A, 506, 1563

Plavec, M. J. 1980, in Close Binary Stars: Observations and Interpretation (IAU Symp. 88), ed. M. J. Plavec, D. M. Popper, & R. K. Ulrich (Dordrecht: Reidel), 251

Pojmanski, G. 2002, Acta Astron., 52, 397

——. 2003, Acta Astron., 53, 341

Pojmanski, G., & Maciejewski, G. 2004, Acta Astron., 54, 153

——. 2005, Acta Astron., 55, 97

Pojmanski, G., Pilecki, B., & Szczygiel, D. 2005, Acta Astron., 55, 275

Popper, D. M. 1944, ApJ, 100, 94

Poretti, E. et al. 2005, AJ, 129, 2461

Povich, M. S. et al. 2009, ApJ, 696, 1278

Preibisch, T., & Zinnecker, H. 1999, AJ, 117, 2381

Prša, A., & Zwitter, T. 2005, ApJ, 628, 426

Rauw, G., Sana, H., Gosset, E., De Becker, M., Arias, J., Morrell, N., Eenens, P., & Stickland, D. 2005, in Massive Stars and High-Energy Emission in OB Associations, JENAM 2005, ed. G. Rauw, et al. (Liège: Univ. Liège), 85

Reed, B. C. 2005, AJ, 130, 1652

Repolust, T., Puls, J., & Herrero, A. 2004, A&A, 415, 349

Riess, A. G. et al. 1998, AJ, 116, 1009

Romero, G. E., Okazaki, A. T., Orellana, M., & Owocki, S. P. 2007, A&A, 474, 15

Ryans, R. S. I., Dufton, P. L., Rolleston, W. R. J., Lennon, D. J., Keenan, F. P., Smoker, J. V., & Lambert, D. L. 2002, MNRAS, 336, 577

Salpeter, E. E. 1955, ApJ, 121, 161

Sana, H., & Evans, C. J. 2010, ArXiv e-prints

Sana, H., Gosset, E., Rauw, G., Sung, H., & Vreux, J.-M. 2006, A&A, 454, 1047

Sana, H., James, G., & Gosset, E. 2011, MNRAS, Submitted

Schaerer, D., Meynet, G., Maeder, A., & Schaller, G. 1993, A&AS, 98, 523

Schaller, G., Schaerer, D., Meynet, G., & Maeder, A. 1992, A&AS, 96, 269

Schild, R. E. 1970, ApJ, 161, 855

Schild, R. E., Hiltner, W. A., & Sanduleak, N. 1969, ApJ, 156, 609

Skilton, J. L. et al. 2009, MNRAS, 399, 317

Skrutskie, M. F. et al. 2006, AJ, 131, 1163

Smartt, S. J., Eldridge, J. J., Crockett, R. M., & Maund, J. R. 2009, MNRAS, 395, 1409

Smith, N., Gehrz, R. D., Stahl, O., Balick, B., & Kaufer, A. 2002, ApJ, 578, 464

Snow, Jr., T. P., York, D. G., & Welty, D. E. 1977, AJ, 82, 113

Solivella, G. R., & Niemela, V. S. 1986, Rev. Mexicana Astron. Astrofis., 12, 188

Sterken, C. et al. 1993, A&AS, 102, 79

Stickland, D. J., & Lloyd, C. 2001, The Observatory, 121, 1

Strohmeier, W. 1966, IBVS, 158

Strohmeier, W., Knigge, R., & Ott, H. 1965, IBVS, 107

Struve, O. 1944, ApJ, 100, 189

——. 1945, ApJ, 102, 74

Tamblyn, P., Rieke, G. H., Hanson, M. M., Close, L. M., McCarthy, Jr., D. W., & Rieke, M. J. 1996, ApJ, 456, 206

Tarasov, A. E. 2000, in The Be Phenomenon in Early-Type Stars (ASP Conf. Ser. 214), ed. M. A. Smith, H. F. Henrichs, & J. Fabregat (San Francisco: ASP), 644

Tavani, M. et al. 2009, A&A, 502, 995

ten Brummelaar, T. A. et al. 2005, ApJ, 628, 453

Thackeray, A. D., Tritton, S. B., & Walker, E. N. 1973, MmRAS, 77, 199

Thackeray, A. D., & Wesselink, A. J. 1965, MNRAS, 131, 121

Thompson, G. I., Nandy, K., Jamar, C., Monfils, A., Houziaux, L., Carnochan, D. J., & Wilson, R. 1978, Catalogue of stellar ultraviolet fluxes (TD1): A Compilation of Absolute Stellar Fluxes Measured by the Sky Survey Telescope (S2/68) Aboard the ESRO satellite TD-1 (London: The Science Research Council, UK)

Torres, G., Andersen, J., & Giménez, A. 2010, A&A Rev., 18, 67

Tovmassian, H. M., Epremian, R. A., Hovhannessian, K., Cruz-Gonzalez, G., Navarro, S. G., & Karapetian, A. A. 1998, AJ, 115, 1083

Turner, N. H., ten Brummelaar, T. A., Roberts, L. C., Mason, B. D., Hartkopf, W. I., & Gies, D. R. 2008, AJ, 136, 554

Uyanıker, B., Fürst, E., Reich, W., Aschenbach, B., & Wielebinski, R. 2001, A&A, 371, 675

van Altena, W. F., & Jones, B. F. 1972, A&A, 20, 425

van Hamme, W. 1993, AJ, 106, 2096

van Hamme, W., & Wilson, R. E. 2003, in ASP Conf. Ser., Vol. 298, GAIA Spectroscopy: Science and Technology, ed. U. Munari (San Francisco, CA: ASP), 323

van Leeuwen, F. 2007, A&A, 474, 653

Vercellone, S. et al. 2008, ApJ, 676, L13

Vogt, N. 1976, A&A, 53, 9

Vogt, N., Kroll, P., & Splittgerber, E. 2004, A&A, 428, 925

Wachmann, A. A. 1964, Astron. Abh. Hamburg. Sternw., 7, 155

——. 1968, Astron. Abh. Hamburg. Sternw., 7, 381

Wade, R. A., & Rucinski, S. M. 1985, A&AS, 60, 471

Walborn, N. R. 1971, ApJS, 23, 257

——. 1972, AJ, 77, 312

——. 1973, AJ, 78, 1067

Walborn, N. R., & Fitzpatrick, E. L. 1990, PASP, 102, 379

Walborn, N. R., & Howarth, I. D. 2000, PASP, 112, 1446

Walborn, N. R. et al. 2002, AJ, 123, 2754

Walker, M. F. 1957, ApJ, 125, 636

Wallerstein, G. 1960, ApJ, 132, 37

Wegner, W. 1994, MNRAS, 270, 229

——. 2003, AN, 324, 219

Wellstein, S., Langer, N., & Braun, H. 2001, A&A, 369, 939

Williams, S. J. 2009, AJ, 137, 3222

Williams, S. J., Gies, D. R., Helsel, J. W., Matson, R. A., & Caballero-Nieves, S. M. 2011, AJ, 142, 5

Williams, S. J. et al. 2008, ApJ, 682, 492

Williams, S. J., Gies, D. R., Matson, R. A., & Huang, W. 2009, ApJ, 696, L137

Williams, S. J., Gies, D. R., Matson, R. A., Touhami, Y., Grundstrom, E. D., Huang, W., & McSwain, M. V. 2010a, ApJ, 723, L93

Williams, S. J., Wilson, J. W., Hursey, M., & Caballero-Nieves, S. M. 2010b, Journal of Double Star Observations, 6, 15

Wils, P., & Dvorak, S. W. 2003, IBVS, 5425

Wilson, R. E., & Devinney, E. J. 1971, ApJ, 166, 605

Wilson, R. E., & Sofia, S. 1976, ApJ, 203, 182

Wolff, S. C., Strom, S. E., Dror, D., & Venn, K. 2007, AJ, 133, 1092

Woosley, S. E., & Bloom, J. S. 2006, ARA&A, 44, 507

Woźniak, P. R. et al. 2004, AJ, 127, 2436

Yudin, R. V. 2001, A&A, 368, 912

Zhang, P., Chen, P. S., & Yang, H. T. 2005, New Astron., 10, 325

Zhao, M. et al. 2008, ApJ, 684, L95

Zinnecker, H., & Yorke, H. W. 2007, ARA&A, 45, 481

Zinner, E. 1930, Astronomische Nachrichten, 239, 59

Zucker, S. 2003, MNRAS, 342, 1291

Zwitter, T. et al. 2008, AJ, 136, 421

Appendices

– A –

ASAS Light Curves

This Appendix presents the light curve figures discussed in Chapter 6. These plots contain the ASAS data with uncertainties, phased to the derived orbits listed in Table 6.2. These best fit orbits are shown by grey lines passing through the data between orbital phases −0.2 to 1.2 to show the primary eclipse in its entirety. There are several systems that have interesting features in their light curves. For example, Figure A.19 shows the light curve for NSV 3433. It shows one of the larger temperature differences between components in this sample. It also shows an illumination effect on the secondary by the flux of the hotter primary. The out-of-eclipse flux is higher just before and after the secondary eclipse, indicating that the side of the secondary facing the primary is slightly hotter and giving off more light at this orbital phase. Figure A.29 illustrates the light curve of HD 63818. This system has a moderately high eccentricity (0.132) with $\omega = 343°$, meaning the periastron of the orbit is near the plane of the sky. This causes the secondary eclipse to be shifted from the circular case where it would be at 0.5 in orbital phase. A particularly illustrative example of this is TYC 1025-1524-1 seen in Figure A.50. The widths of the eclipses are different owing to an eccentricity of ∼0.367. Periastron occurs near phase 0.02 ($\omega = 280°$), and the deeper, narrow eclipse at phase 0.0 results from the rapid and close passage of the secondary star in front of the primary star. Several systems have very well constrained light curves such as HD 48866 in Figure A.9 and TT Pyx seen in Figure A.33 that will make for highly accurate determinations of mass and radius when combined with double-lined spectroscopic orbits, and therefore, they represent the jewels of the collection.

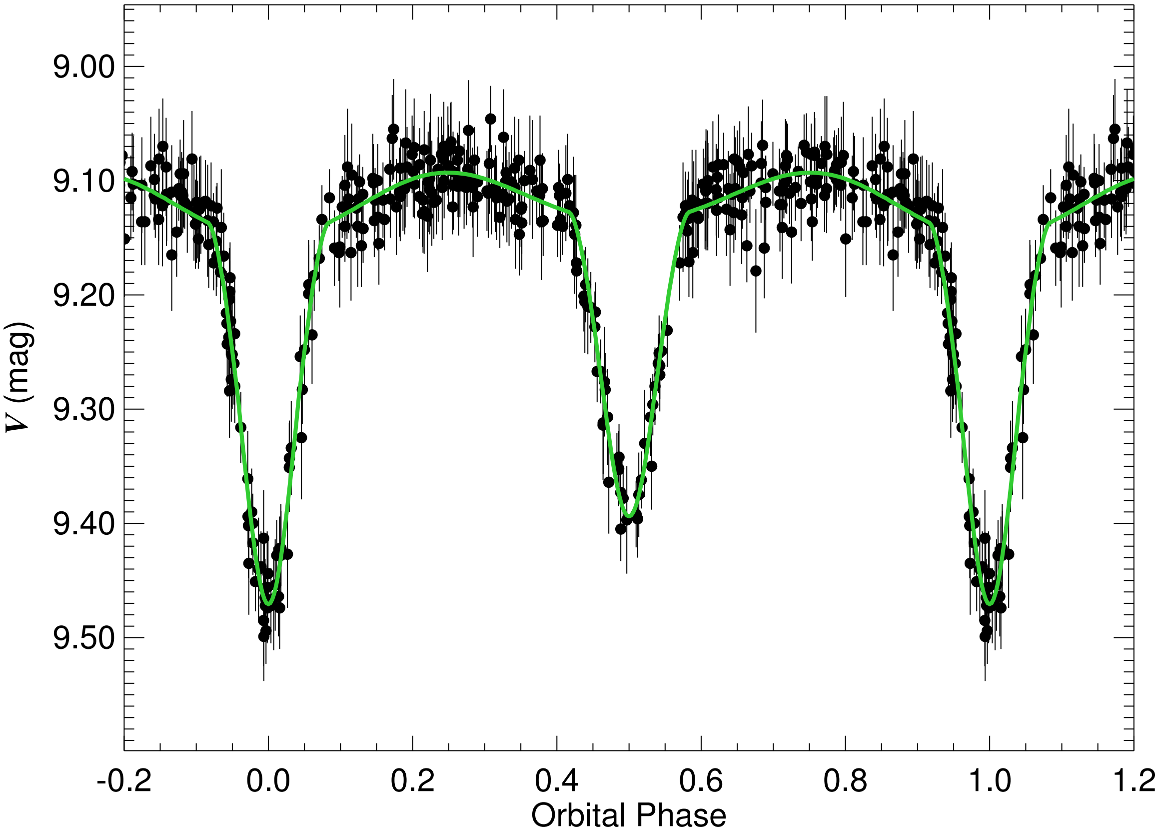

Figure A.1 The ASAS $V-$band light curve for ASAS 053838+0901.2 (HD 37396). Filled circles with lines represent data with associated uncertainties. The best fit orbital solution listed in Table 6.2 is shown as a solid line passing through the data.

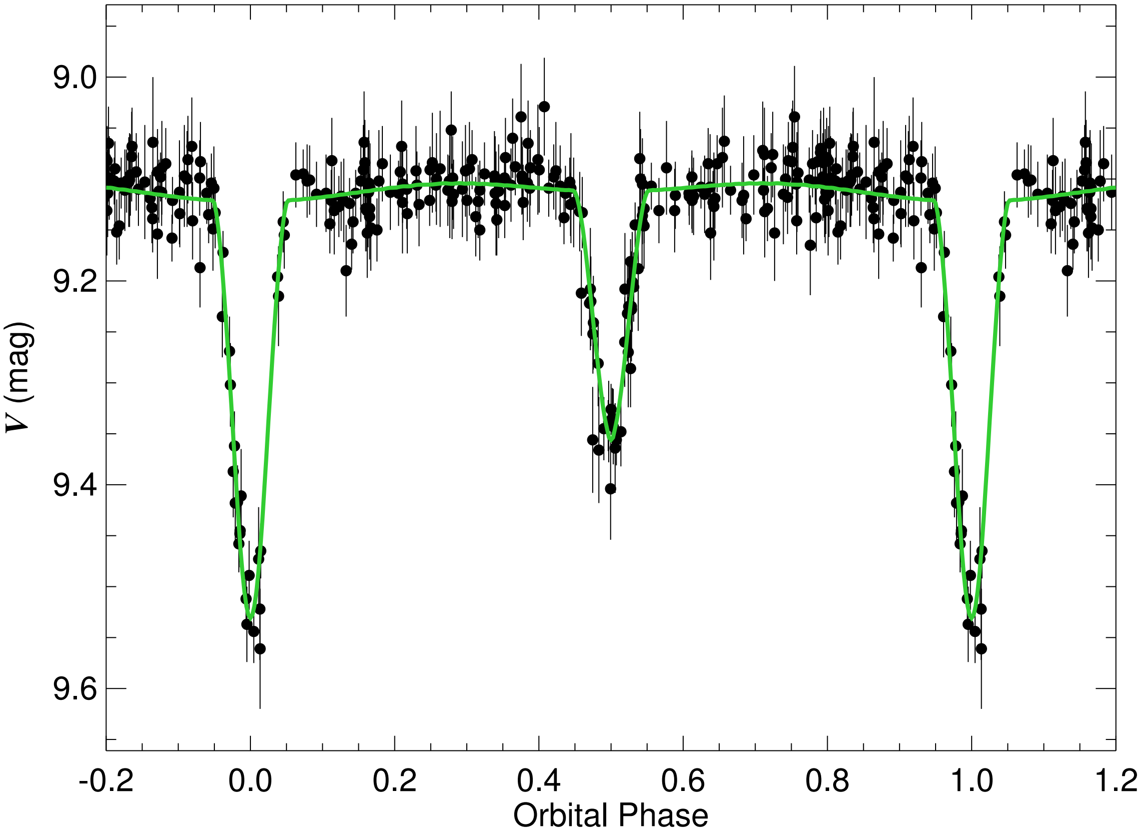

Figure A.2 The ASAS $V-$band light curve for ASAS 054816+2046.1 (HD 247740). Filled circles with lines represent data with associated uncertainties. The best fit orbital solution listed in Table 6.2 is shown as a solid line passing through the data.

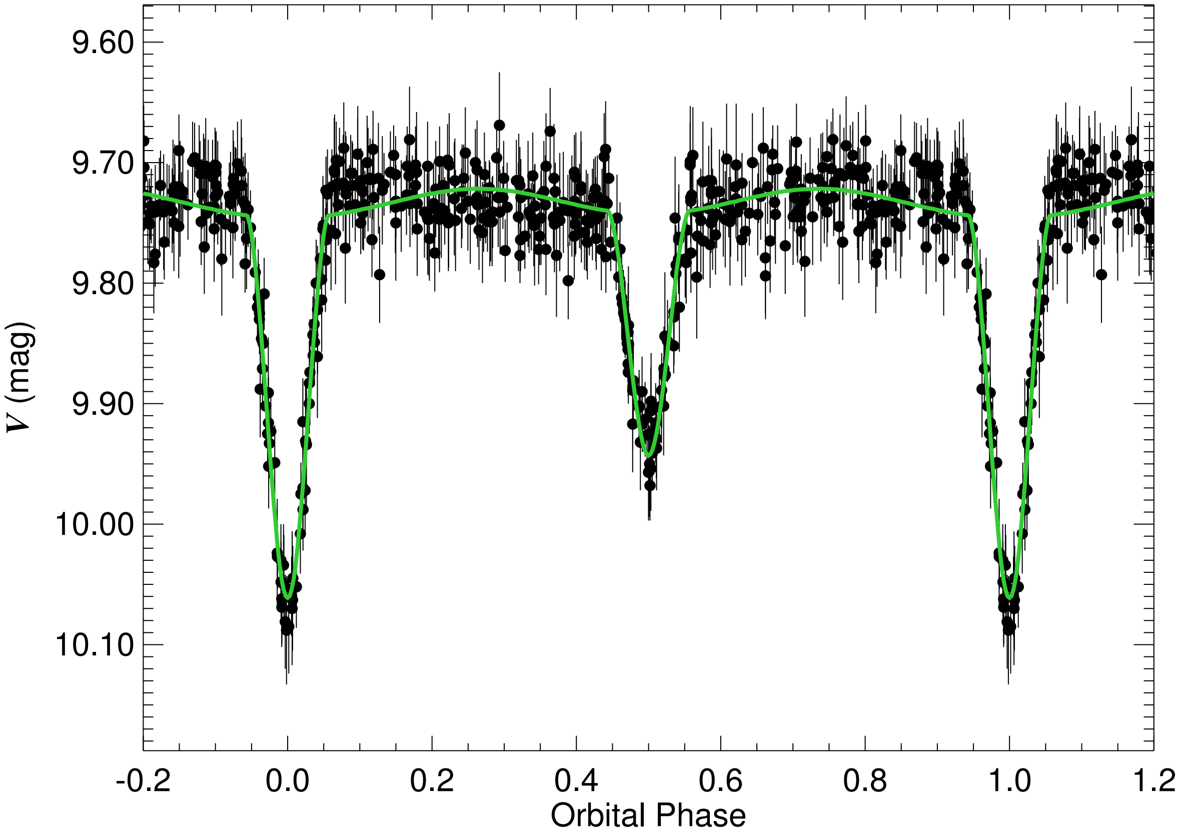

Figure A.3 The ASAS $V-$band light curve for ASAS 060857+1128.9 (HD 252416). Filled circles with lines represent data with associated uncertainties. The best fit orbital solution listed in Table 6.2 is shown as a solid line passing through the data.

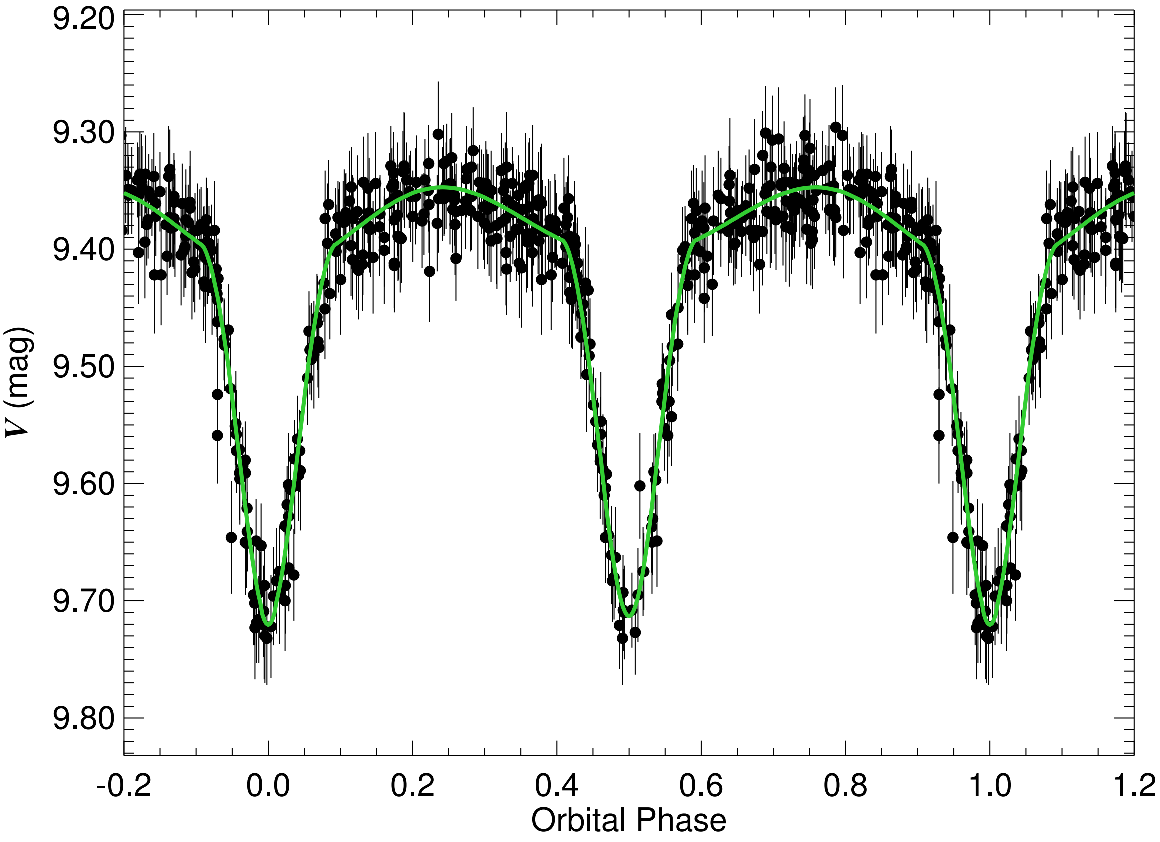

Figure A.4 The ASAS $V-$band light curve for ASAS 060927$-$1501.7 (TYC 5933-142-1). Filled circles with lines represent data with associated uncertainties. The best fit orbital solution listed in Table 6.2 is shown as a solid line passing through the data.

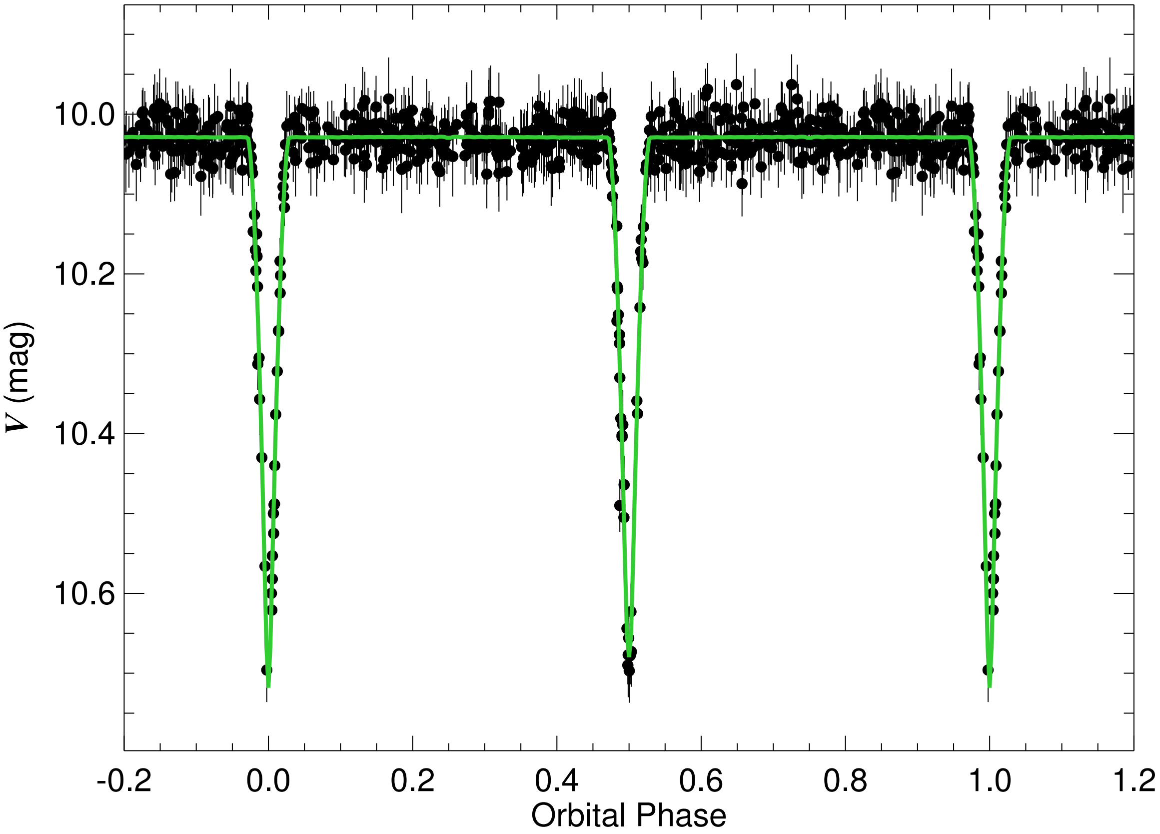

Figure A.5 The ASAS *V* band light curve for ASAS 062556−1254.5 (HD 45263). Filled circles with lines represent data with associated uncertainties. The best fit orbital solution listed in Table 6.2 is shown as a solid line passing through the data.

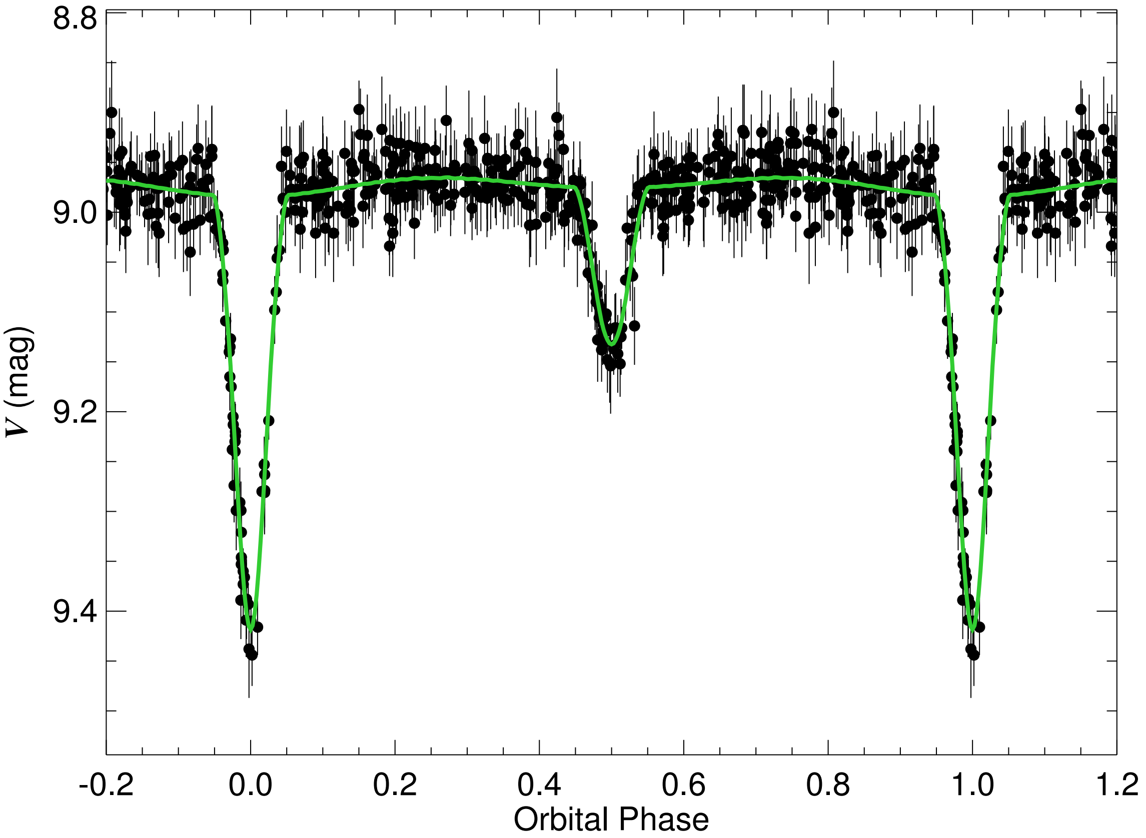

Figure A.6 The ASAS $V-$band light curve for ASAS 063347−1410.5 (HD 46621). Filled circles with lines represent data with associated uncertainties. The best fit orbital solution listed in Table 6.2 is shown as a solid line passing through the data.

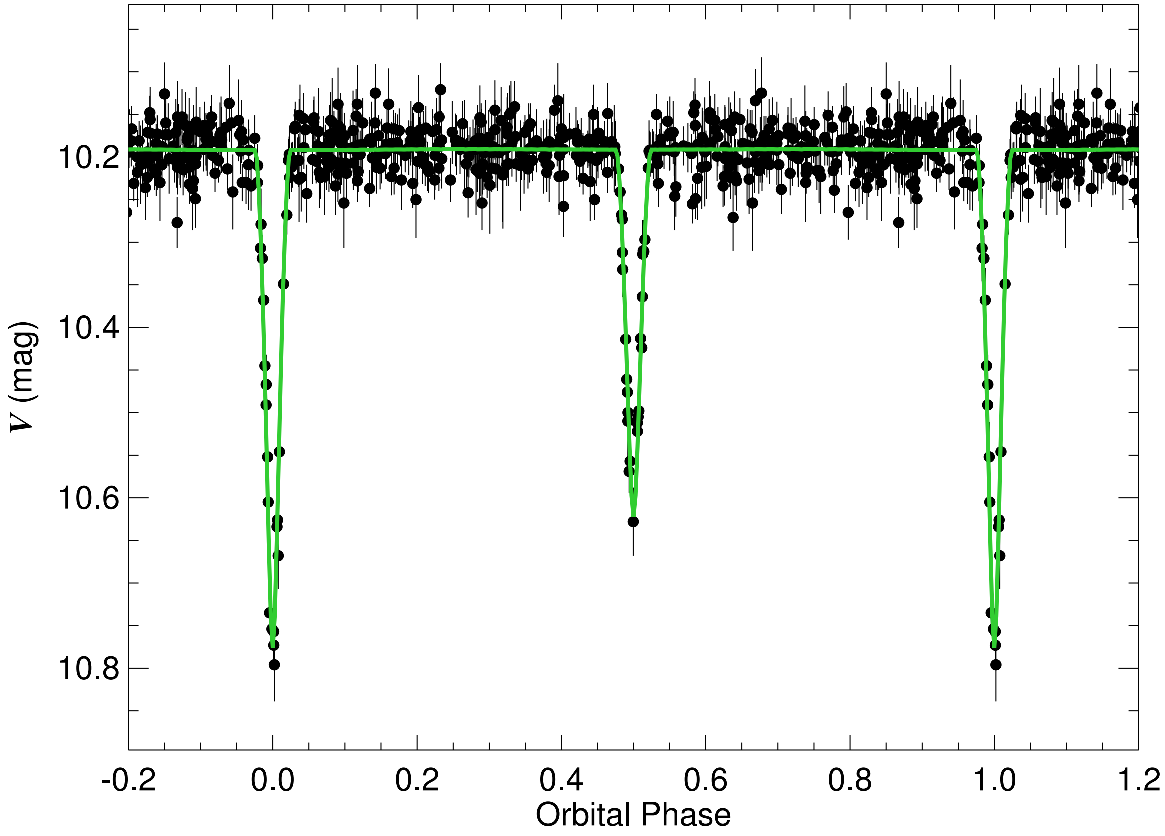

Figure A.7 The ASAS $V-$band light curve for ASAS 064010−1140.3 (HD 47845). Filled circles with lines represent data with associated uncertainties. The best fit orbital solution listed in Table 6.2 is shown as a solid line passing through the data.

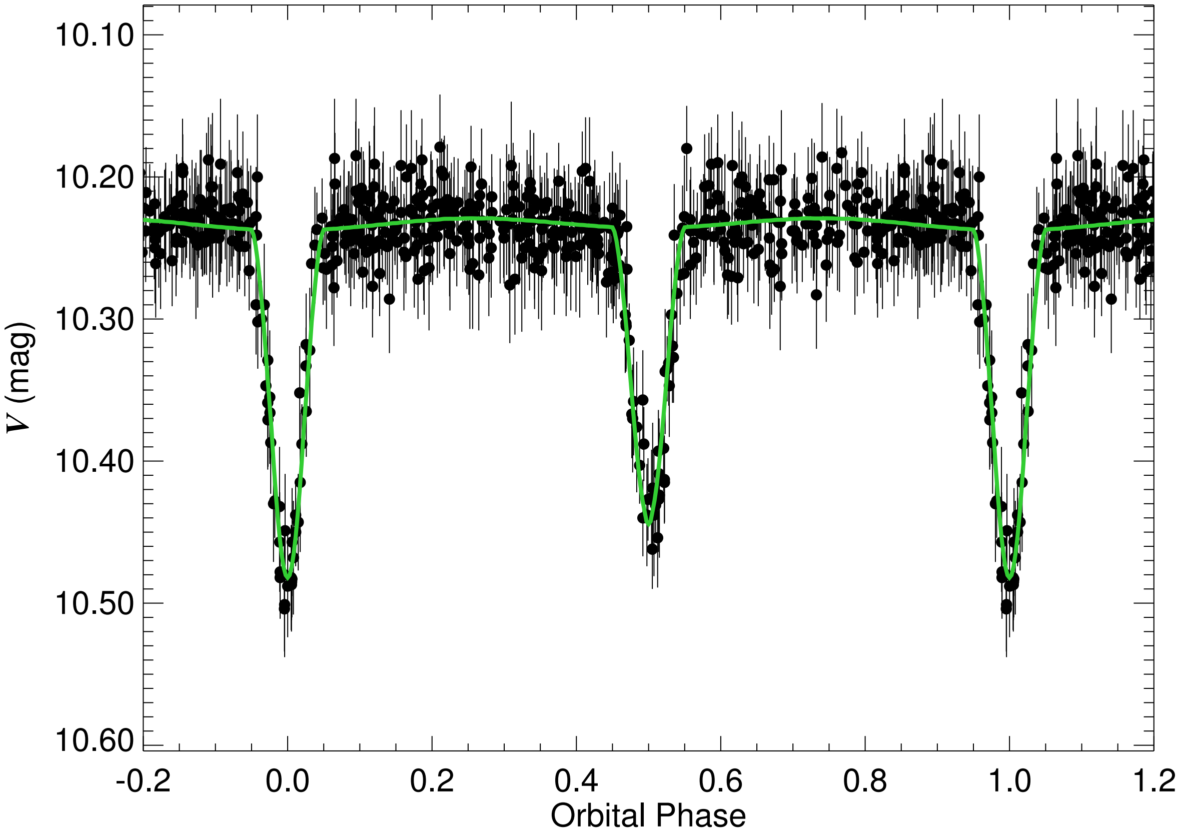

Figure A.8 The ASAS $V-$band light curve for ASAS 064118−0551 (2MASS 06411762−0551065). Filled circles with lines represent data with associated uncertainties. The best fit orbital solution listed in Table 6.2 is shown as a solid line passing through the data.

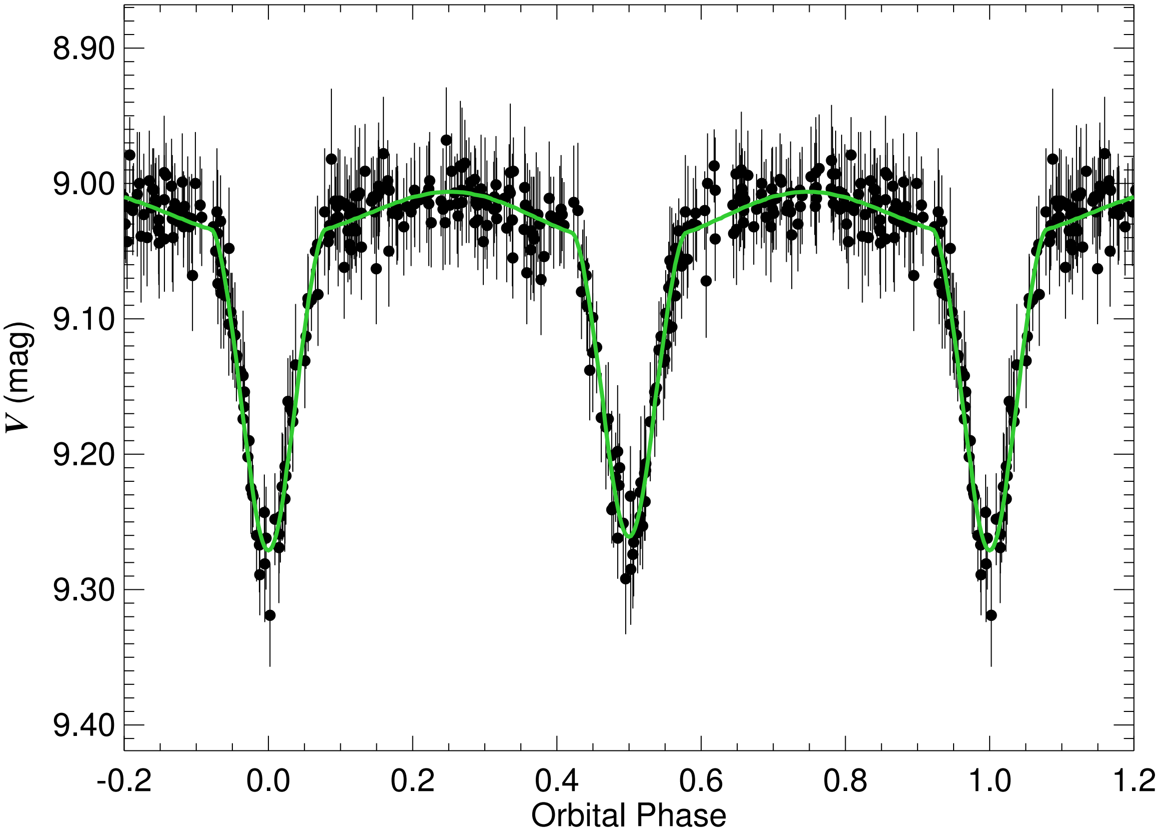

Figure A.9 The ASAS $V-$band light curve for ASAS 064539+0219.4 (HD 48866). Filled circles with lines represent data with associated uncertainties. The best fit orbital solution listed in Table 6.2 is shown as a solid line passing through the data.

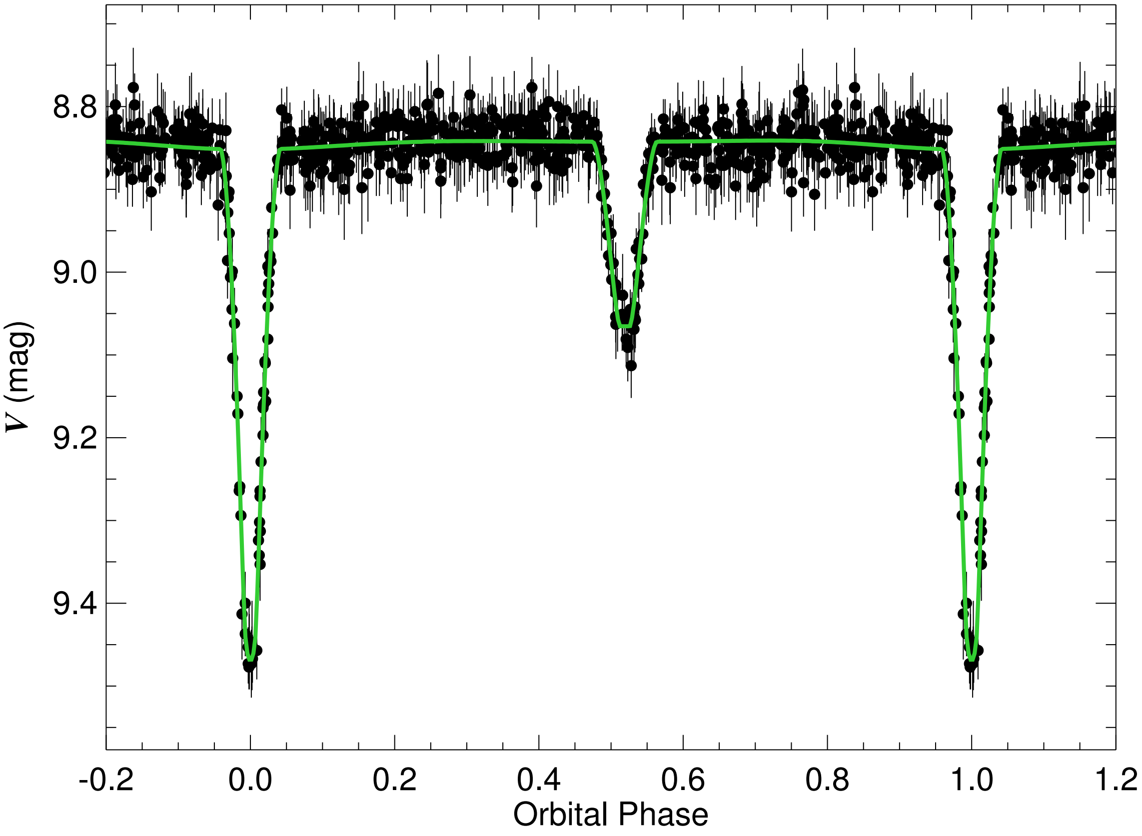

Figure A.10 The ASAS $V-$band light curve for ASAS 064609−1923.8 (HD 49125). Filled circles with lines represent data with associated uncertainties. The best fit orbital solution listed in Table 6.2 is shown as a solid line passing through the data.

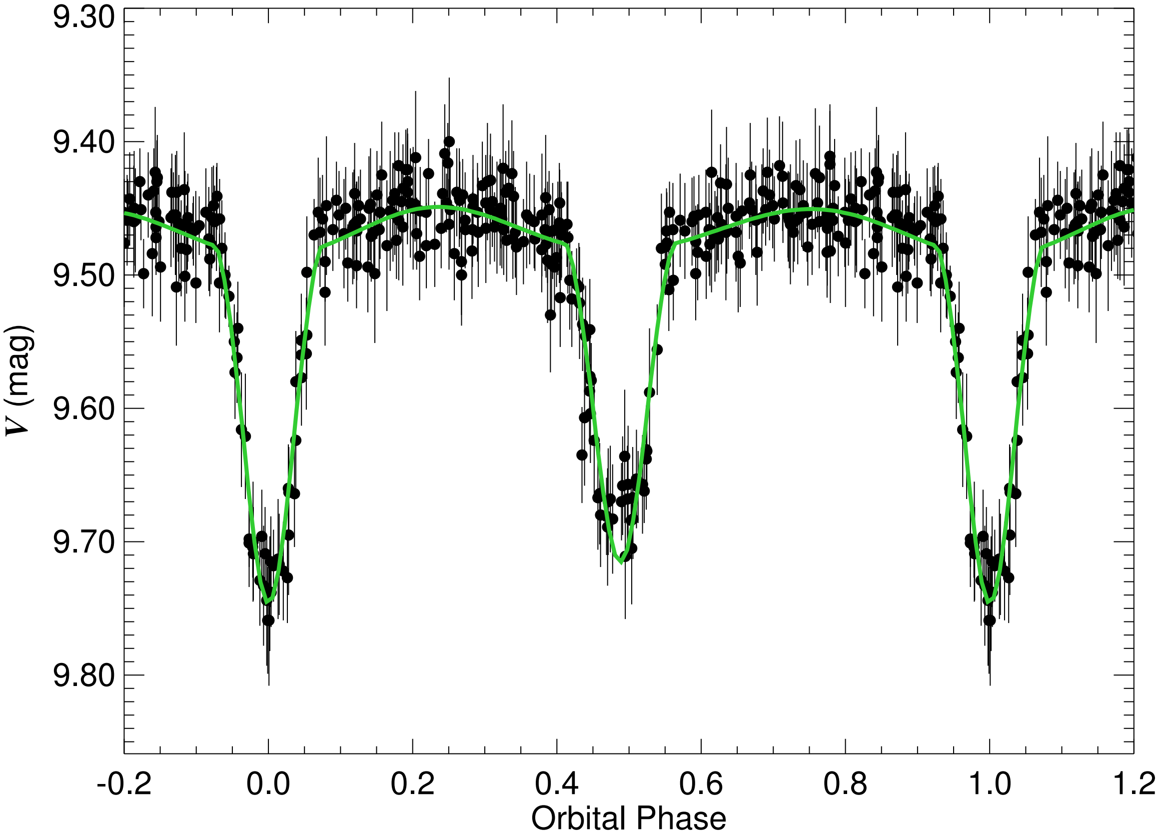

Figure A.11 The ASAS $V-$band light curve for ASAS 064715+0225.6 (HD 289072). Filled circles with lines represent data with associated uncertainties. The best fit orbital solution listed in Table 6.2 is shown as a solid line passing through the data.

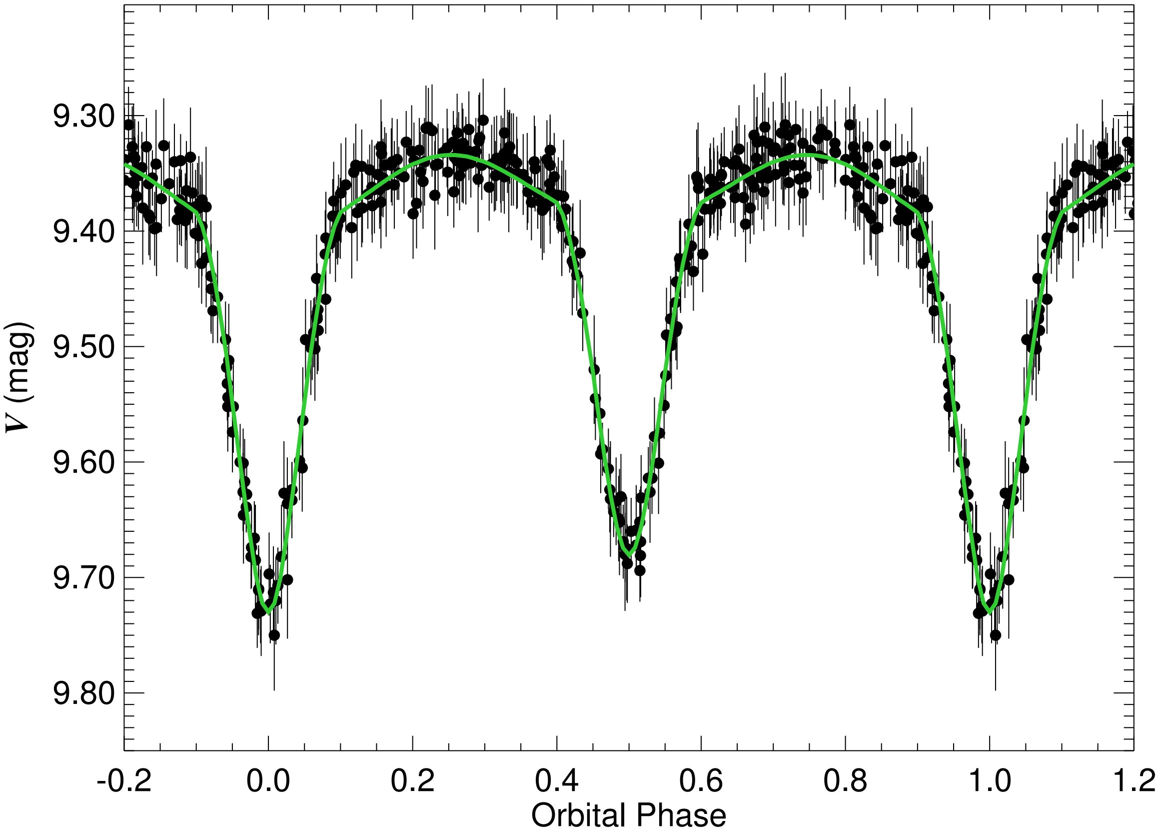

Figure A.12 The ASAS V−band light curve for ASAS 064745+0122.3 (V448 Mon). Filled circles with lines represent data with associated uncertainties. The best fit orbital solution listed in Table 6.2 is shown as a solid line passing through the data.

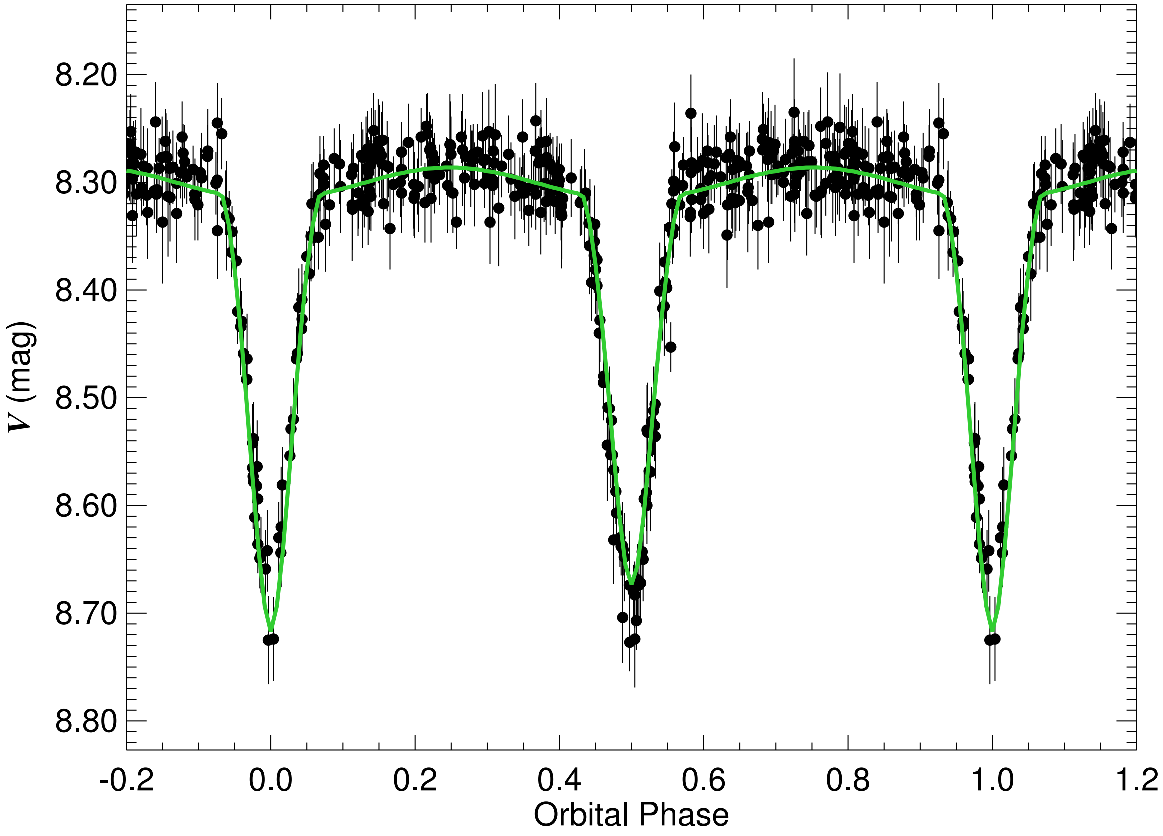

Figure A.13 The ASAS $V-$band light curve for ASAS 065534−1013.2 (HD 51082). Filled circles with lines represent data with associated uncertainties. The best fit orbital solution listed in Table 6.2 is shown as a solid line passing through the data.

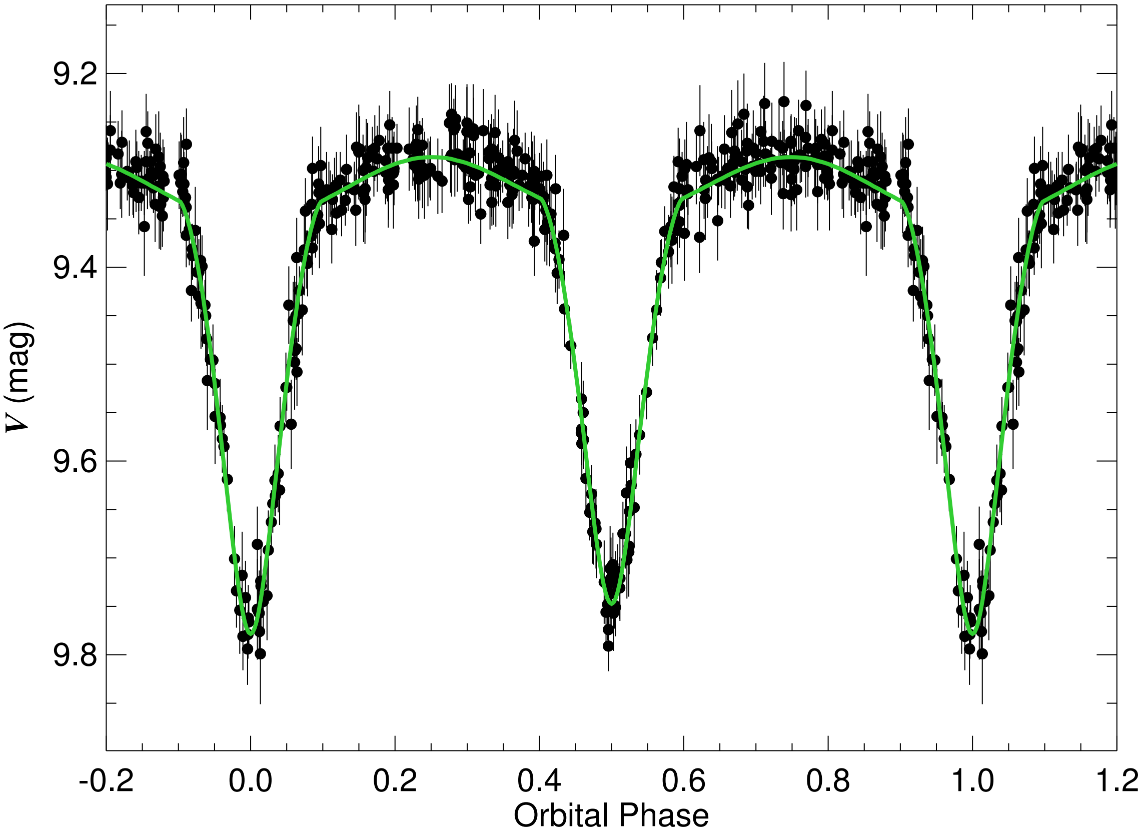

Figure A.14 The ASAS $V-$band light curve for ASAS 065549−0402.6 (HI Mon). Filled circles with lines represent data with associated uncertainties. The best fit orbital solution listed in Table 6.2 is shown as a solid line passing through the data.

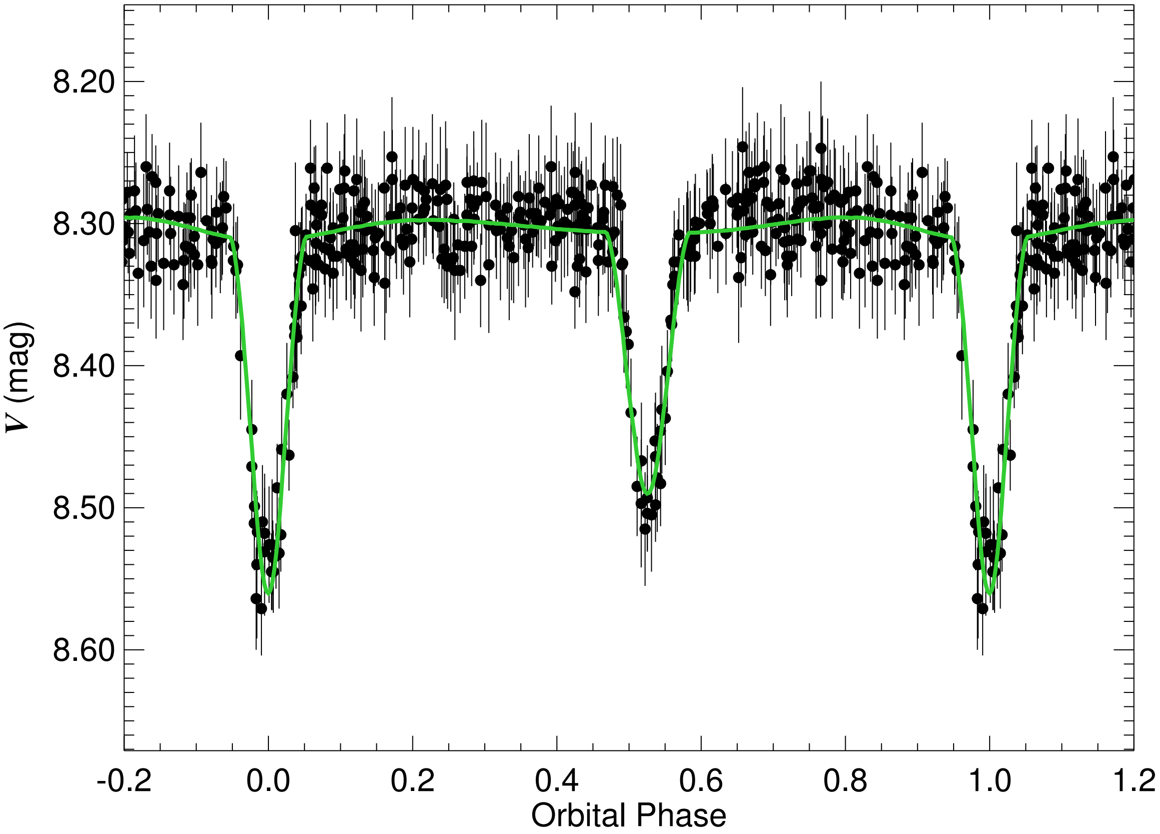

Figure A.15 The ASAS $V-$band light curve for ASAS 070105$-$0358.2 (HD 52433). Filled circles with lines represent data with associated uncertainties. The best fit orbital solution listed in Table 6.2 is shown as a solid line passing through the data.

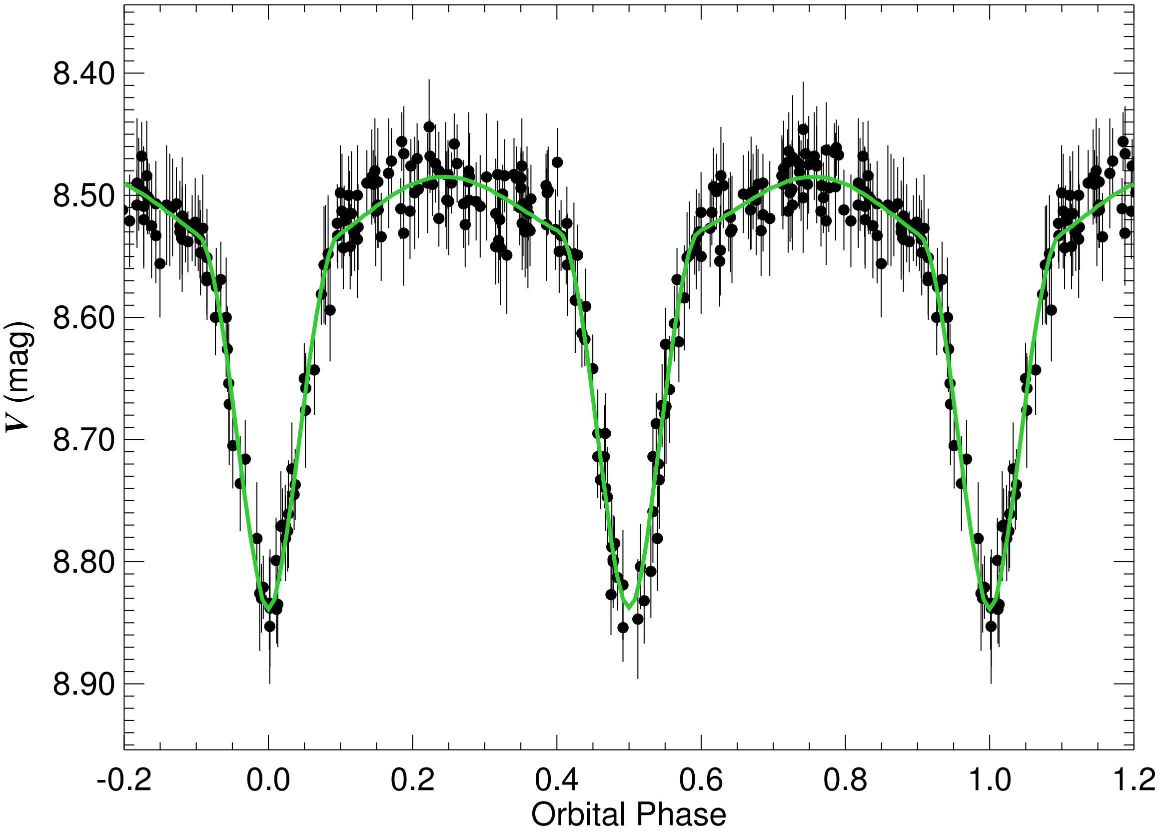

Figure A.16 The ASAS $V-$band light curve for ASAS 070238+1347.0 (HD 52637). Filled circles with lines represent data with associated uncertainties. The best fit orbital solution listed in Table 6.2 is shown as a solid line passing through the data.

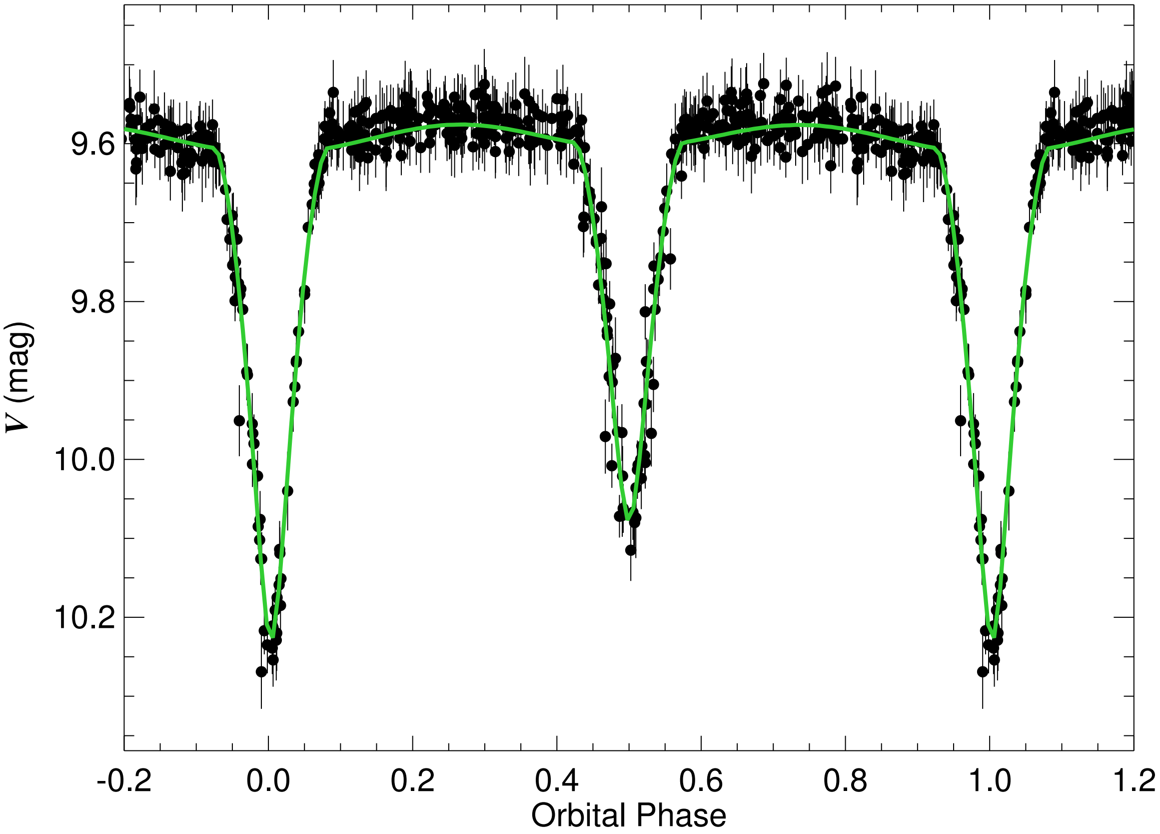

Figure A.17 The ASAS $V-$band light curve for ASAS 070636$-$0437.4 (AO Mon). Filled circles with lines represent data with associated uncertainties. The best fit orbital solution listed in Table 6.2 is shown as a solid line passing through the data.

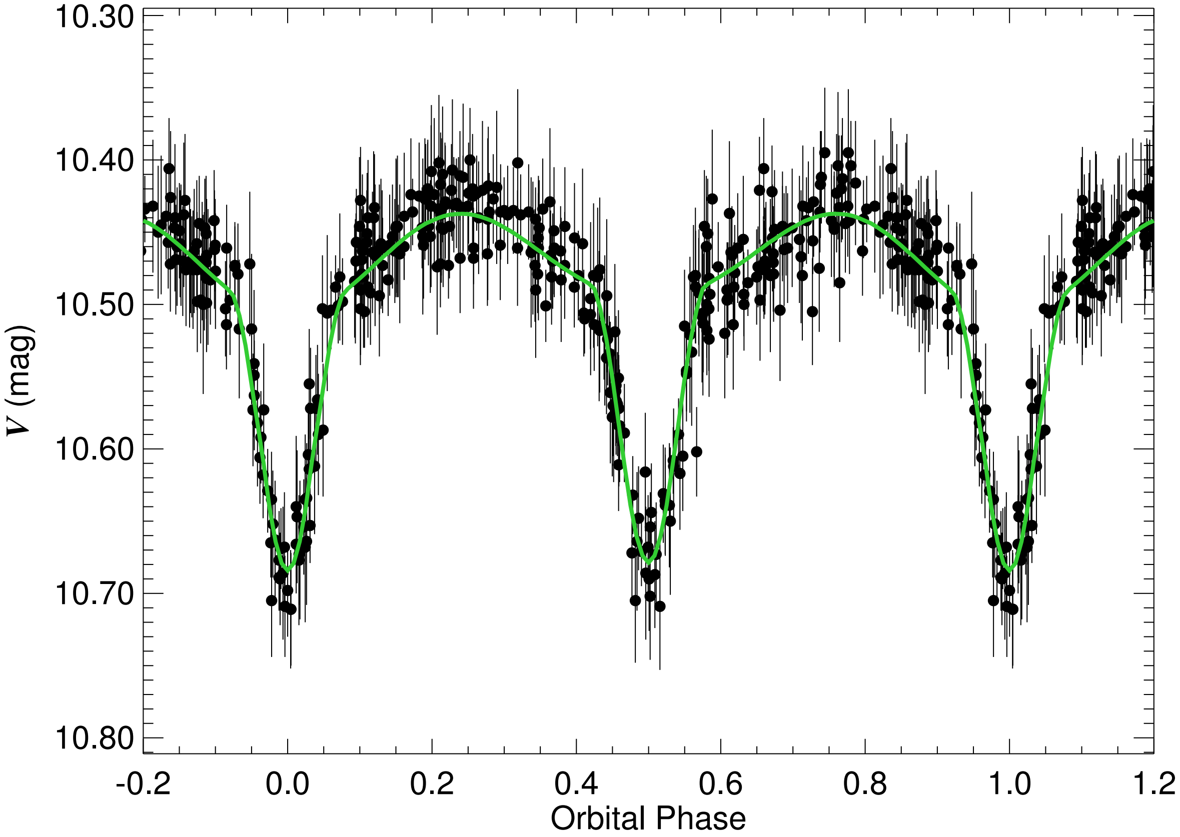

Figure A.18 The ASAS $V-$band light curve for ASAS 070943+2341.7 (BD+23°1621). Filled circles with lines represent data with associated uncertainties. The best fit orbital solution listed in Table 6.2 is shown as a solid line passing through the data.

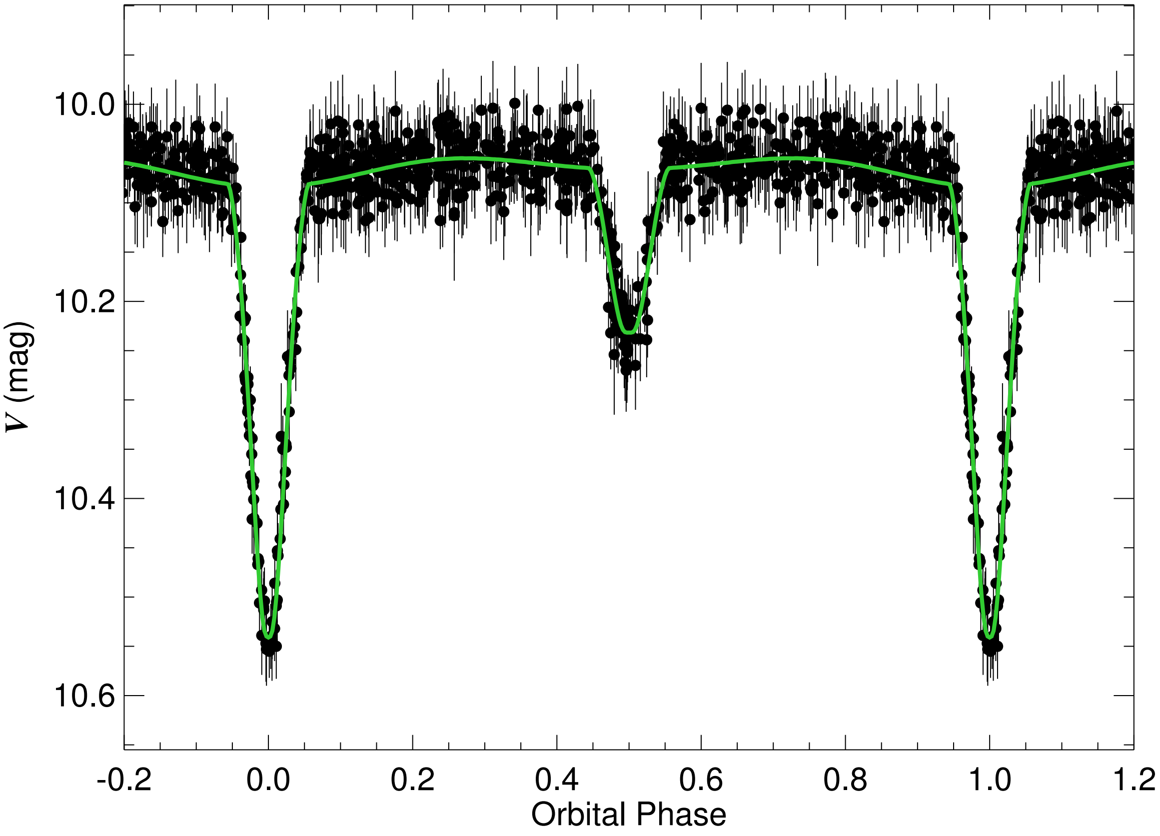

Figure A.19 The ASAS $V-$band light curve for ASAS 070946−2005.5 (NSV 3433). Filled circles with lines represent data with associated uncertainties. The best fit orbital solution listed in Table 6.2 is shown as a solid line passing through the data.

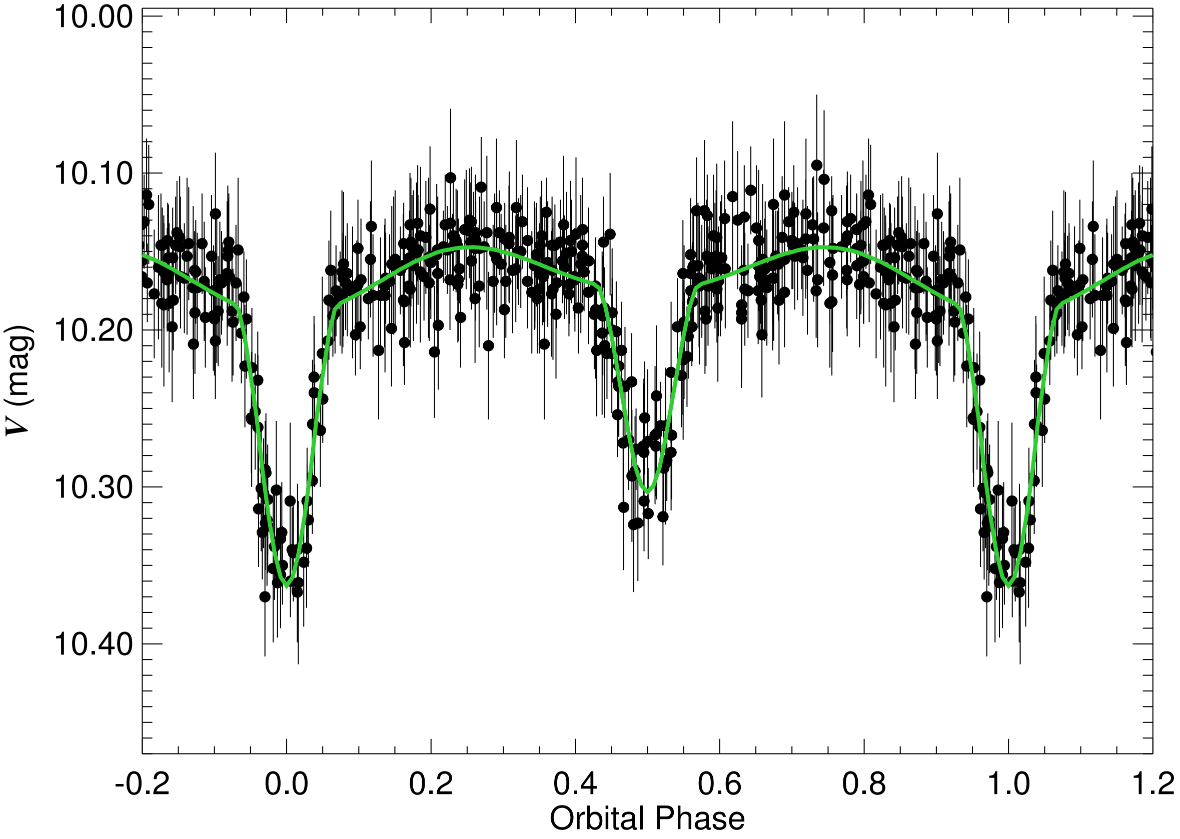

Figure A.20 The ASAS $V-$band light curve for ASAS 071010−0035.1 (HD 54780). Filled circles with lines represent data with associated uncertainties. The best fit orbital solution listed in Table 6.2 is shown as a solid line passing through the data.

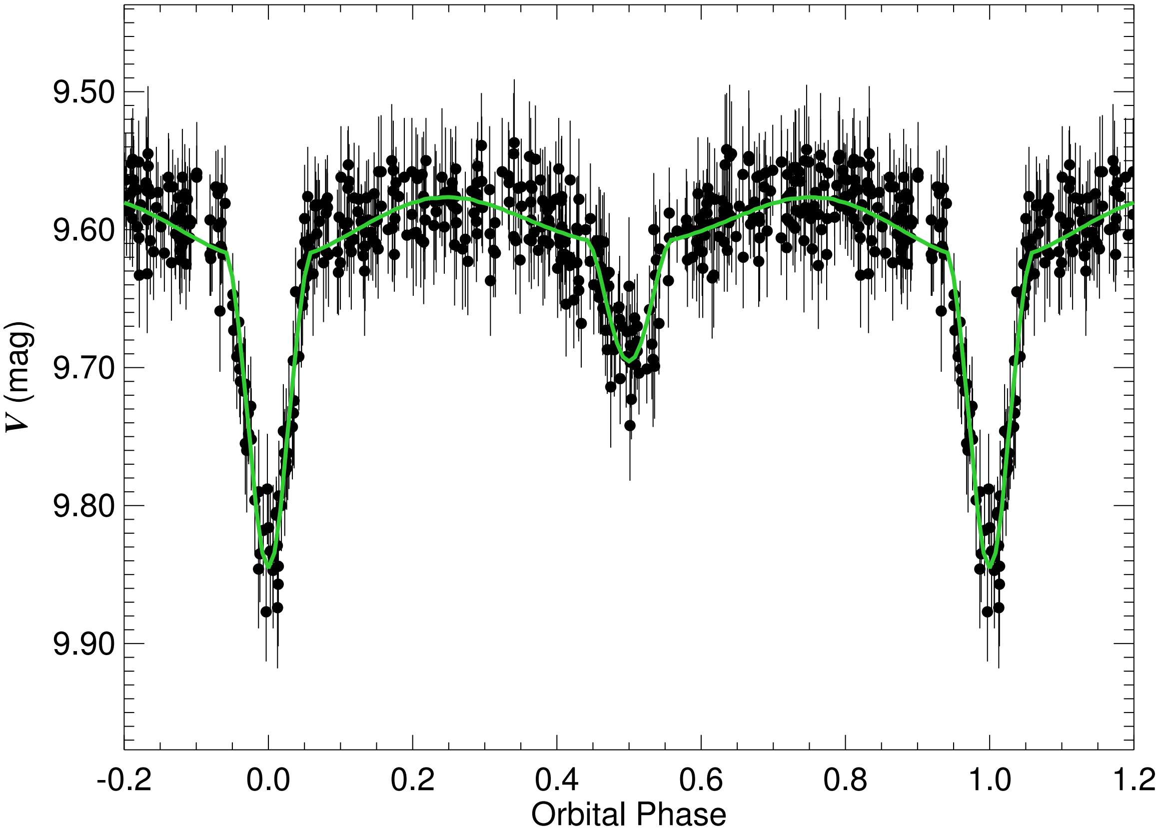

Figure A.21 The ASAS $V-$band light curve for ASAS 071203$-$0139.1 (HD 55236). Filled circles with lines represent data with associated uncertainties. The best fit orbital solution listed in Table 6.2 is shown as a solid line passing through the data.

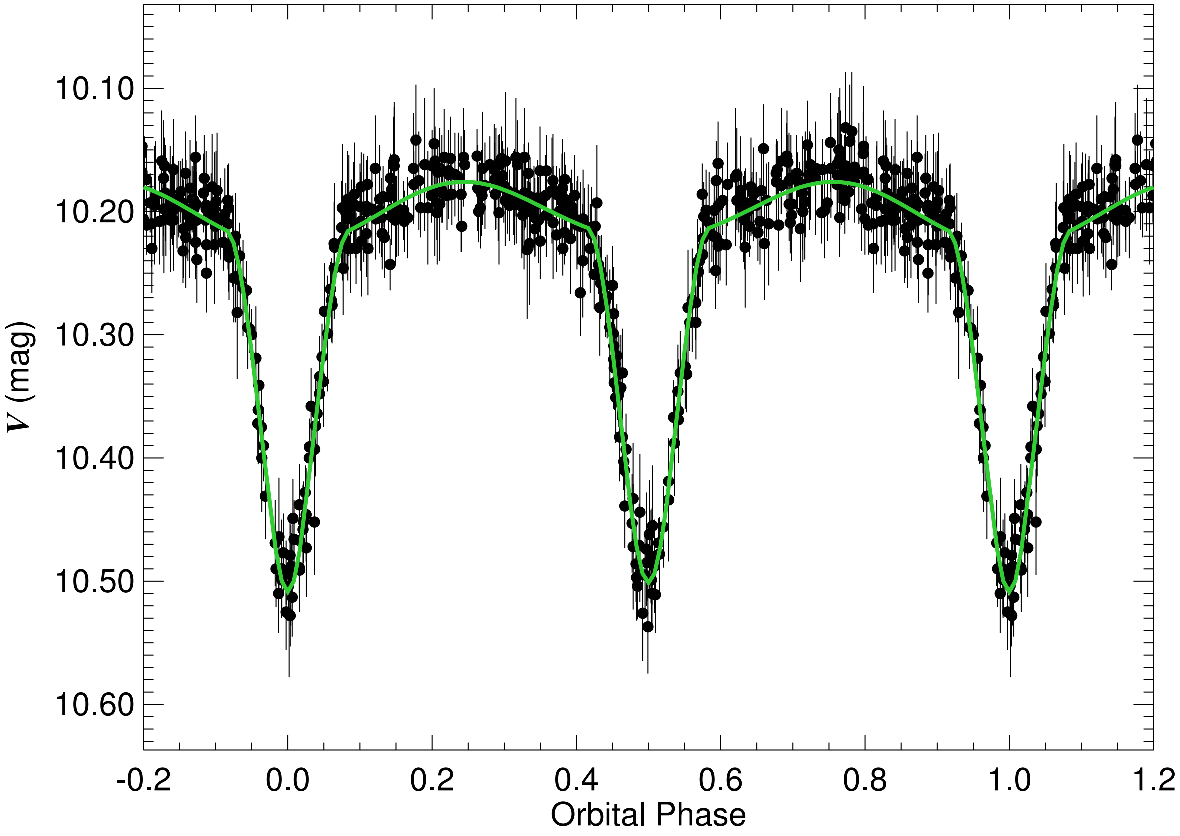

Figure A.22 The ASAS $V-$band light curve for ASAS 071702$-$1034.9 (HD 56544). Filled circles with lines represent data with associated uncertainties. The best fit orbital solution listed in Table 6.2 is shown as a solid line passing through the data.

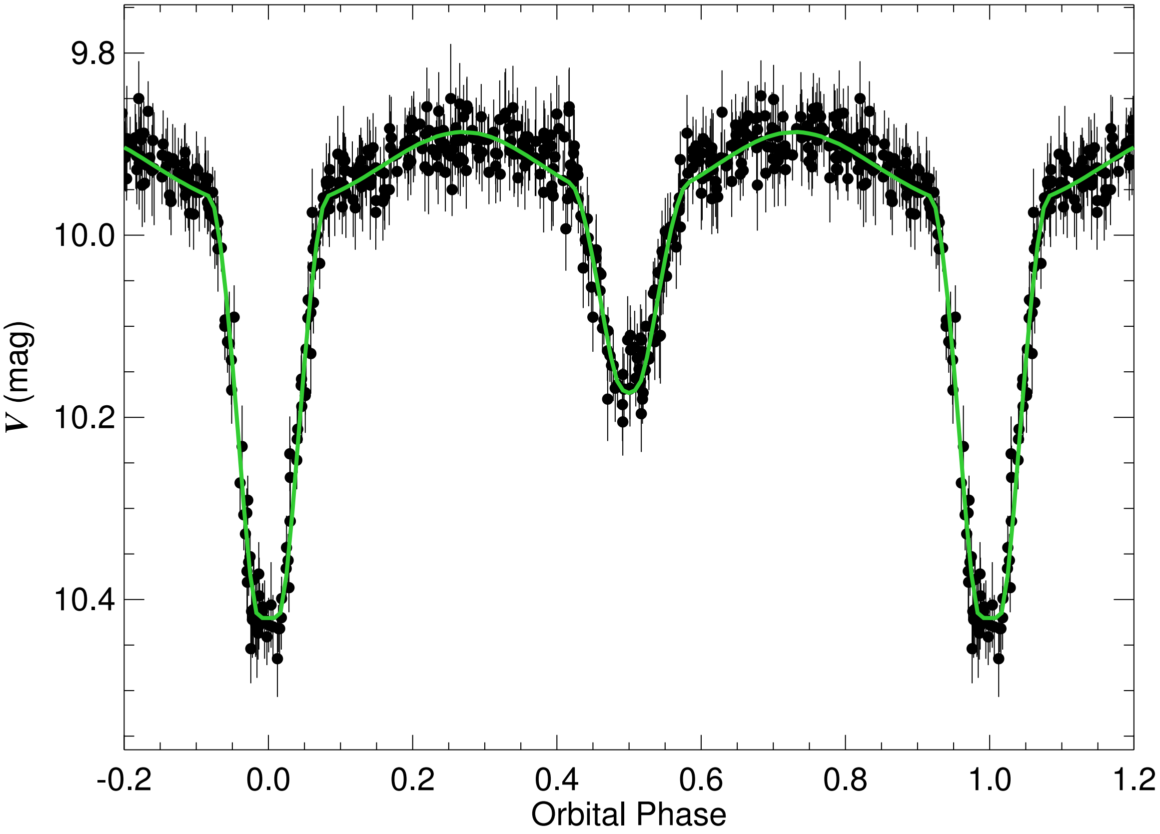

Figure A.23 The ASAS $V-$band light curve for ASAS 072201$-$2552.6 (CX CMa). Filled circles with lines represent data with associated uncertainties. The best fit orbital solution listed in Table 6.2 is shown as a solid line passing through the data.

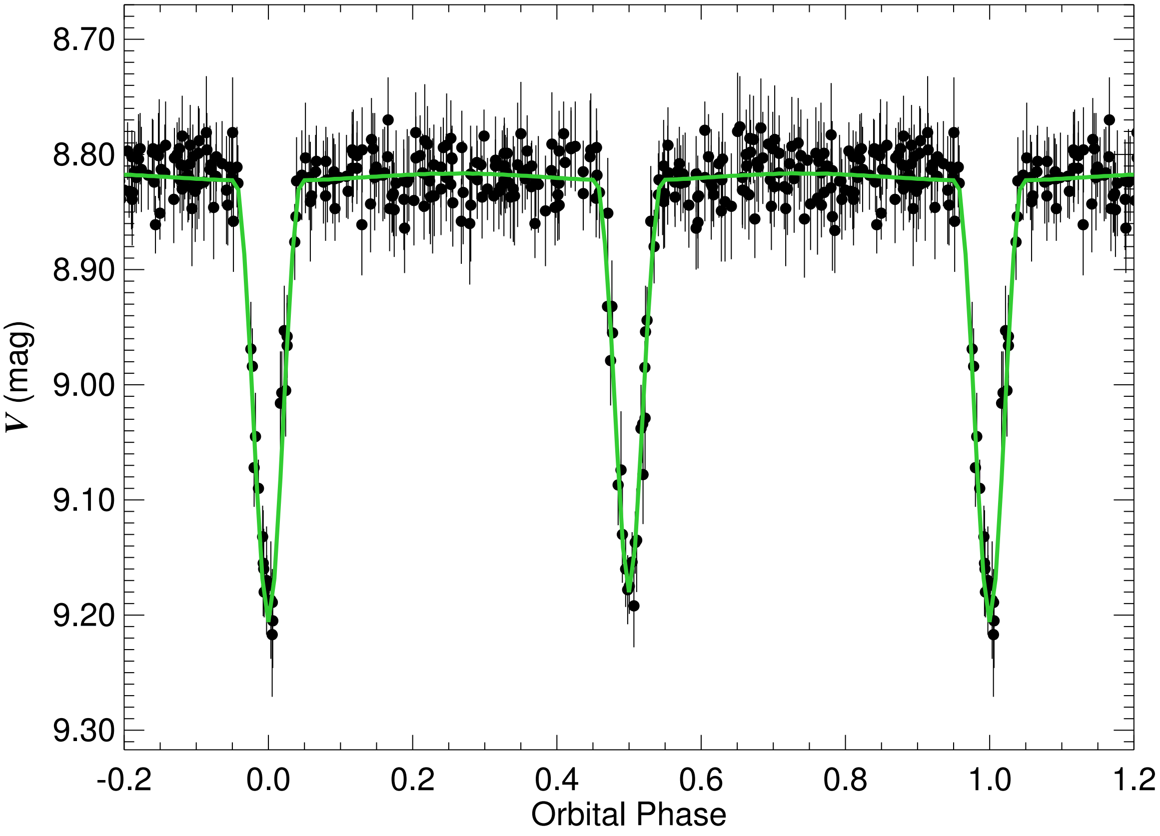

Figure A.24 The ASAS $V-$band light curve for ASAS 073053+0513.7 (HD 59607). Filled circles with lines represent data with associated uncertainties. The best fit orbital solution listed in Table 6.2 is shown as a solid line passing through the data.

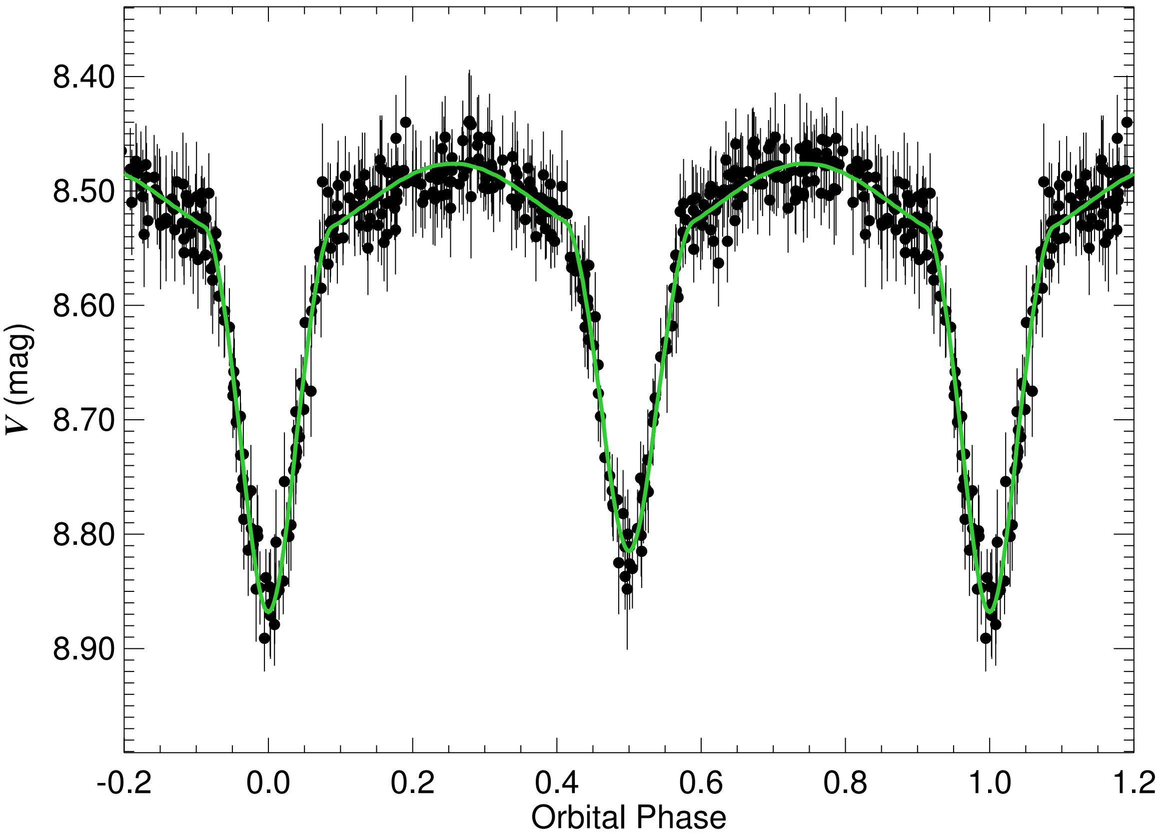

Figure A.25 The ASAS $V-$band light curve for ASAS 073348−0940.9 (HD 60389). Filled circles with lines represent data with associated uncertainties. The best fit orbital solution listed in Table 6.2 is shown as a solid line passing through the data.

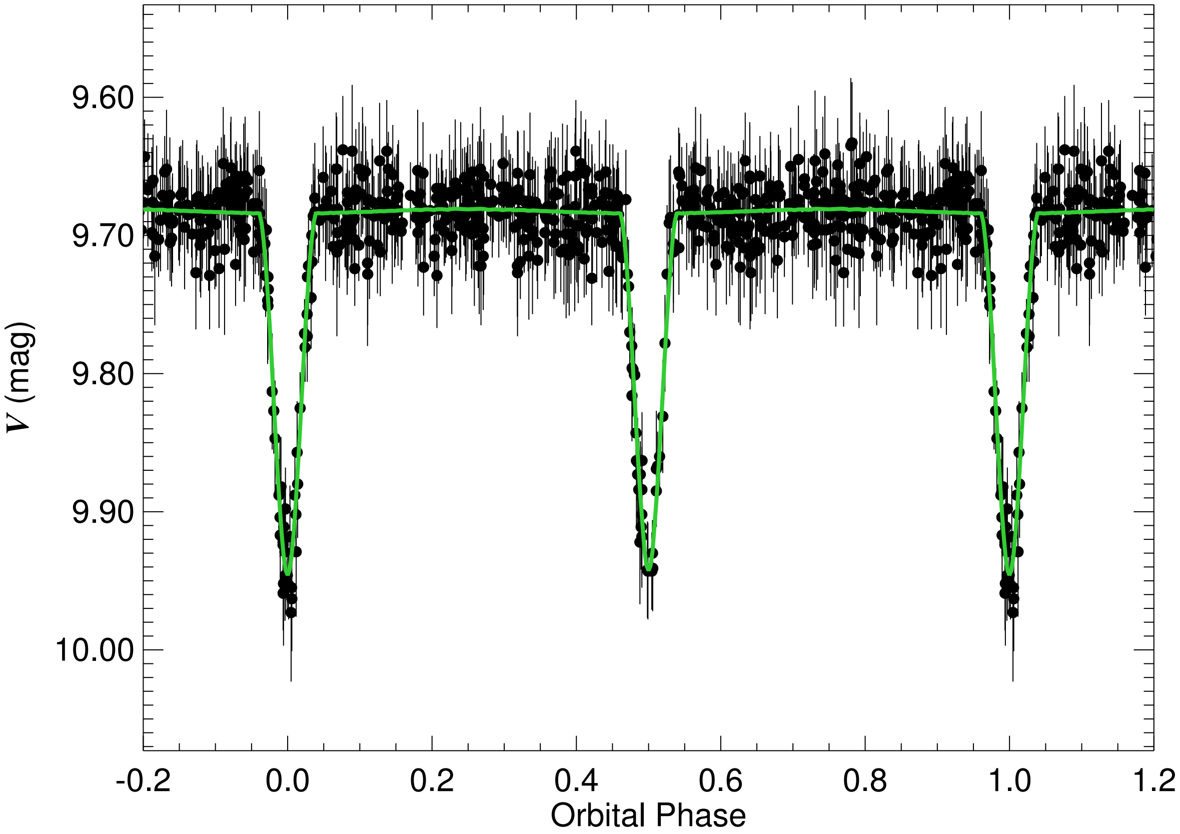

Figure A.26 The ASAS $V-$band light curve for ASAS 074355−2517.9 (HD 62607). Filled circles with lines represent data with associated uncertainties. The best fit orbital solution listed in Table 6.2 is shown as a solid line passing through the data.

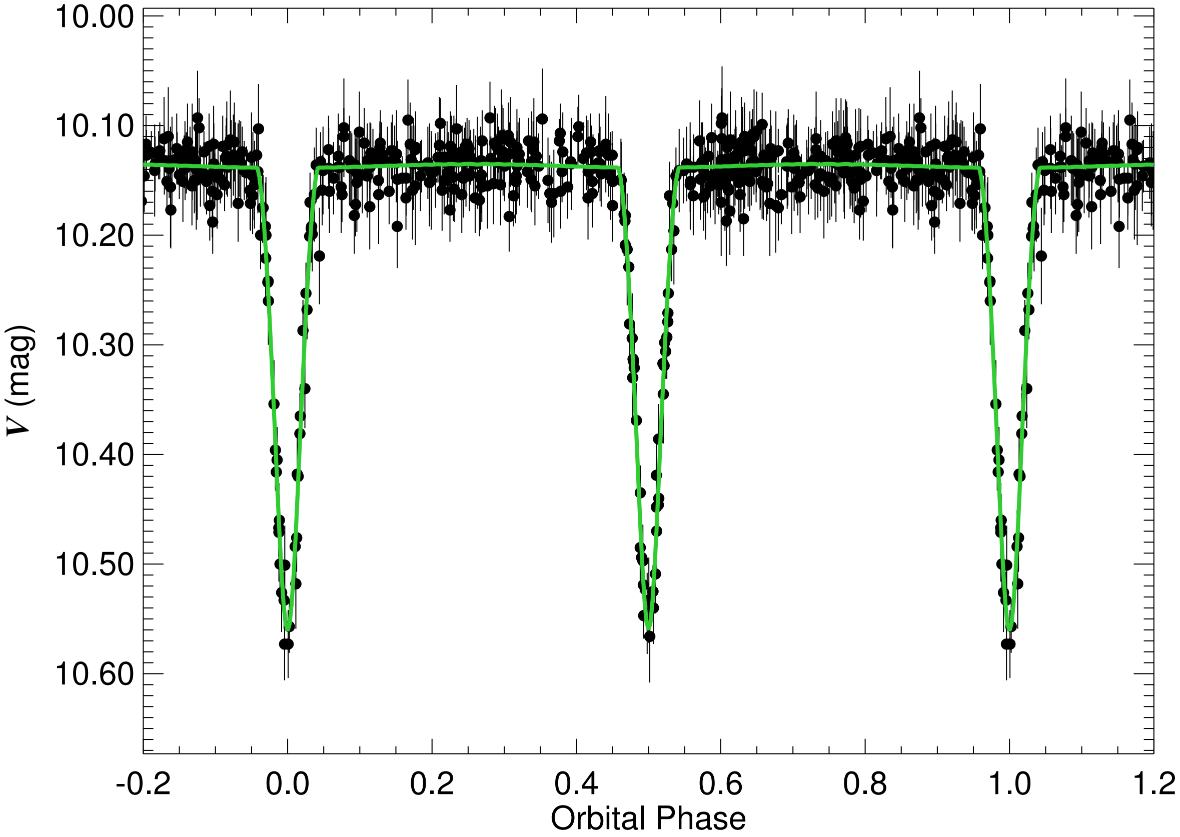

Figure A.27 The ASAS $V-$band light curve for ASAS 074714$-$0519.8 (HD 63141). Filled circles with lines represent data with associated uncertainties. The best fit orbital solution listed in Table 6.2 is shown as a solid line passing through the data.

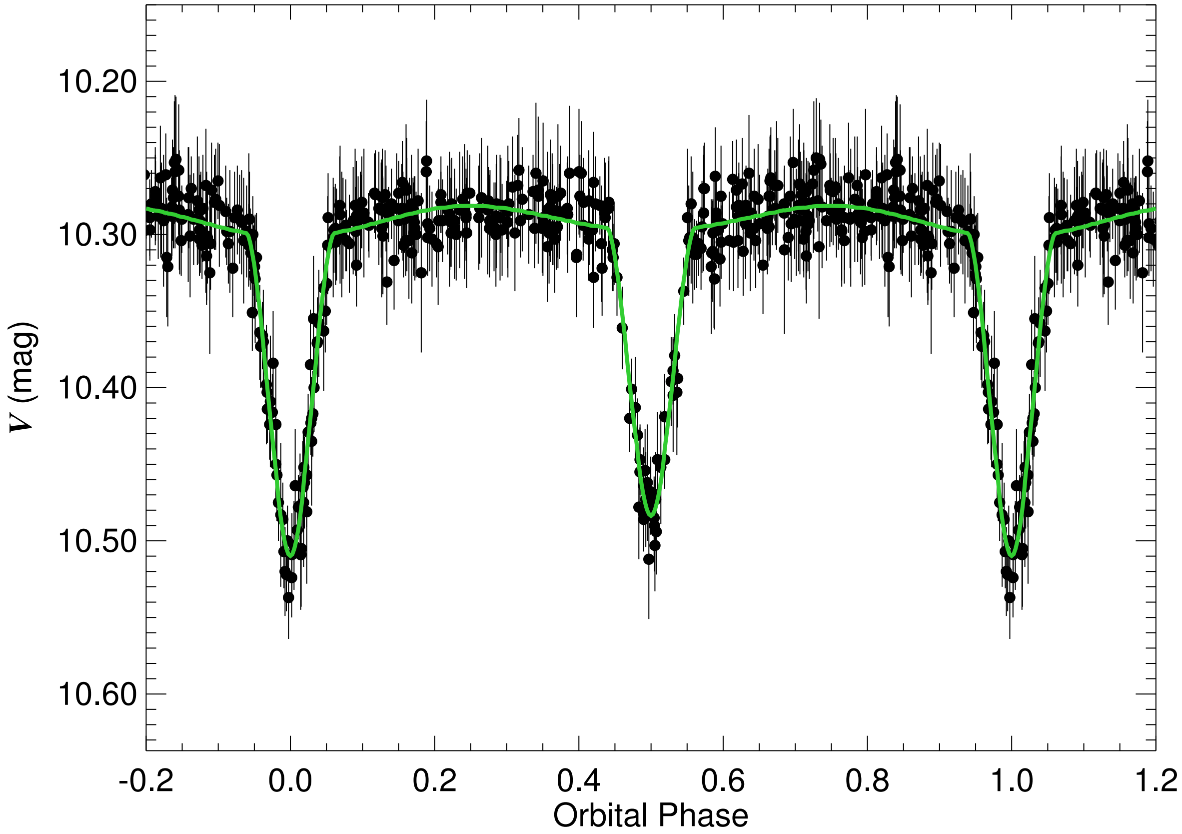

Figure A.28 The ASAS $V-$band light curve for ASAS 074928−0721.6 (BD−06°2317). Filled circles with lines represent data with associated uncertainties. The best fit orbital solution listed in Table 6.2 is shown as a solid line passing through the data.

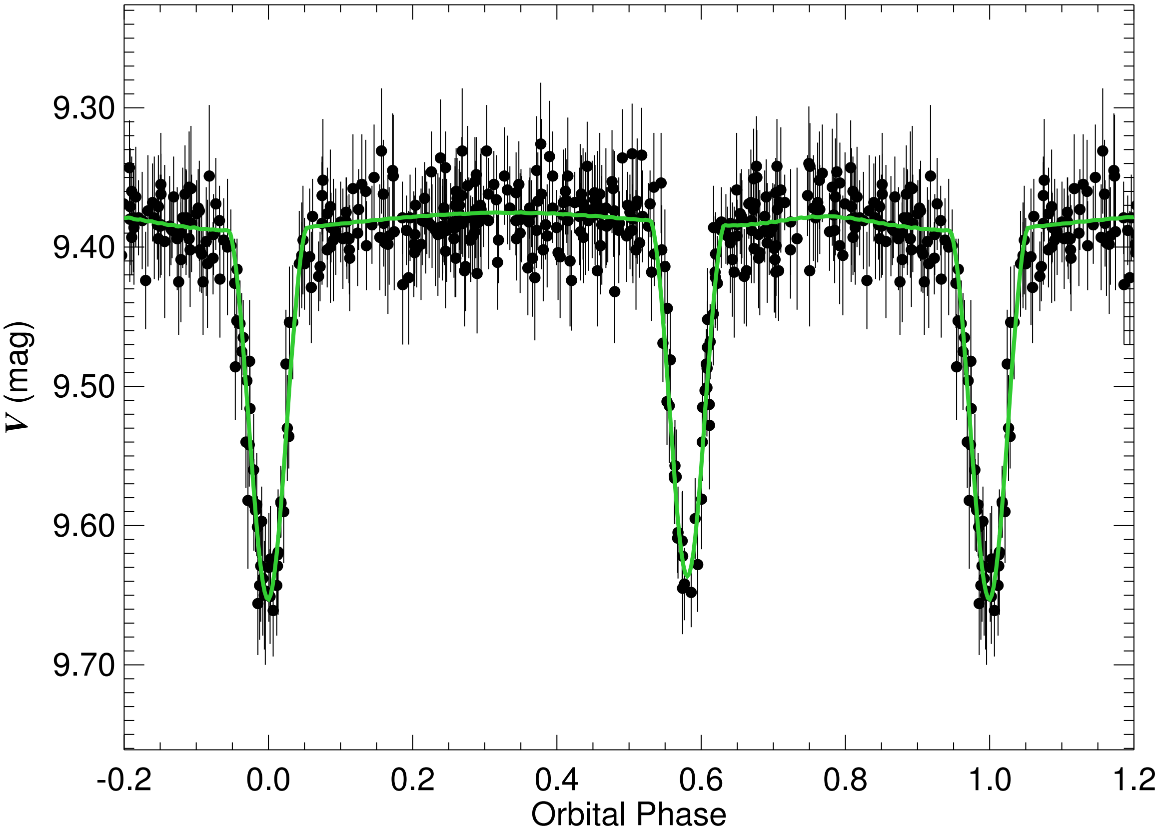

Figure A.29 The ASAS $V-$band light curve for ASAS 075052+0048.0 (HD 63818). Filled circles with lines represent data with associated uncertainties. The best fit orbital solution listed in Table 6.2 is shown as a solid line passing through the data.

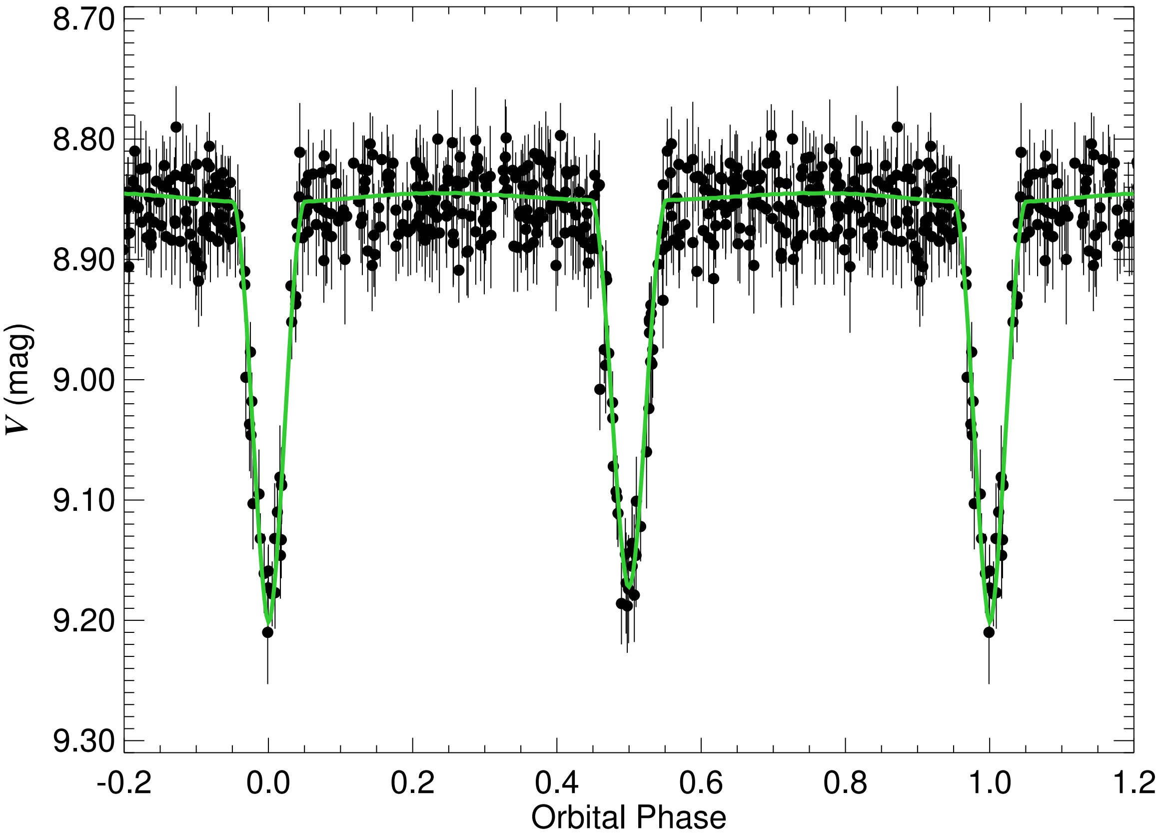

Figure A.30 The ASAS $V-$band light curve for ASAS 080617$-$0426.8 (V871 Mon). Filled circles with lines represent data with associated uncertainties. The best fit orbital solution listed in Table 6.2 is shown as a solid line passing through the data.

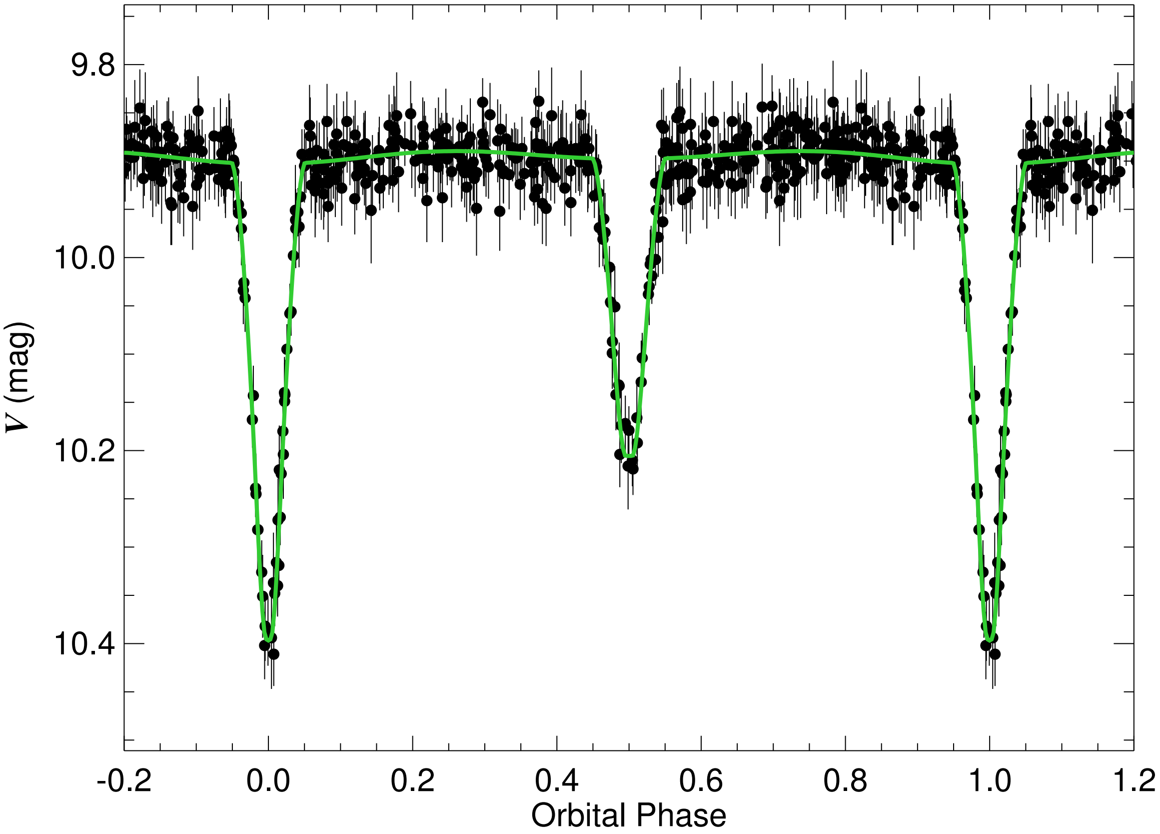

Figure A.31 The ASAS $V-$band light curve for ASAS 081749$-$2659.7 (HD 69797). Filled circles with lines represent data with associated uncertainties. The best fit orbital solution listed in Table 6.2 is shown as a solid line passing through the data.

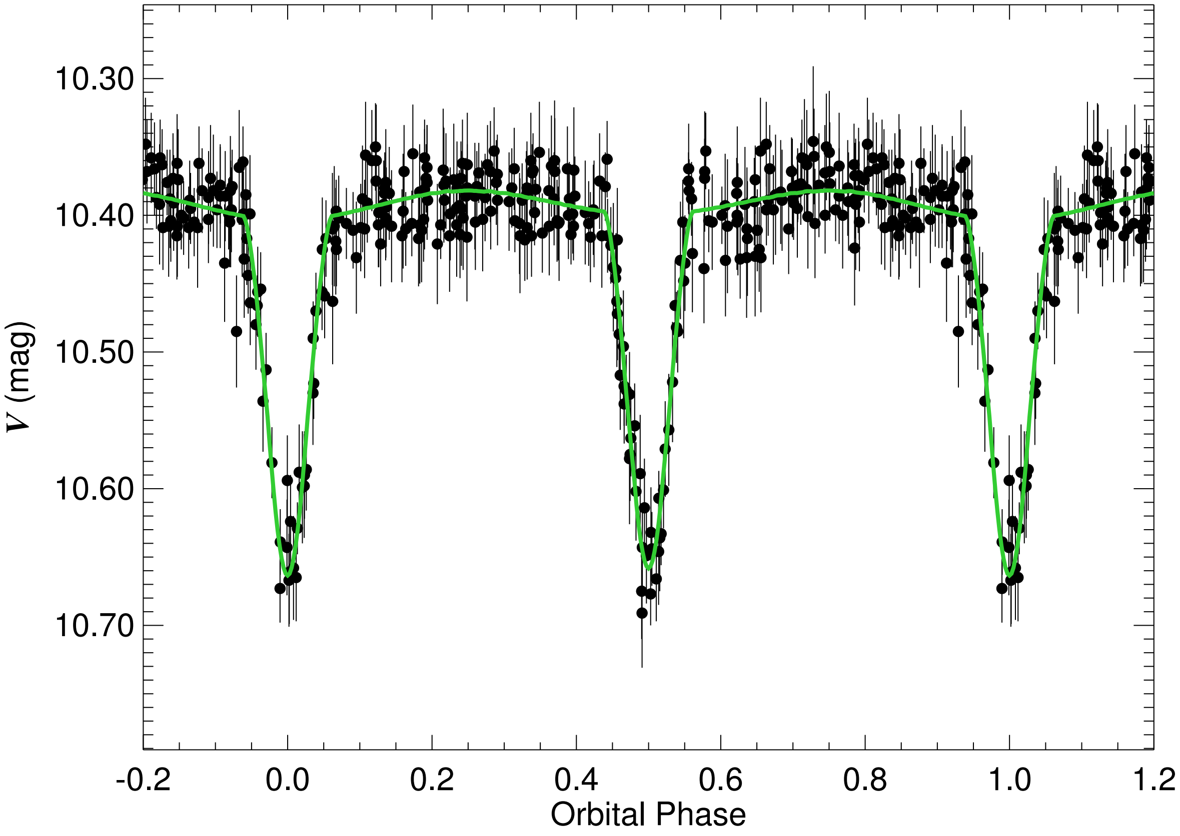

Figure A.32 The ASAS $V-$band light curve for ASAS 083245+0247.3 (BD+03°2001). Filled circles with lines represent data with associated uncertainties. The best fit orbital solution listed in Table 6.2 is shown as a solid line passing through the data.

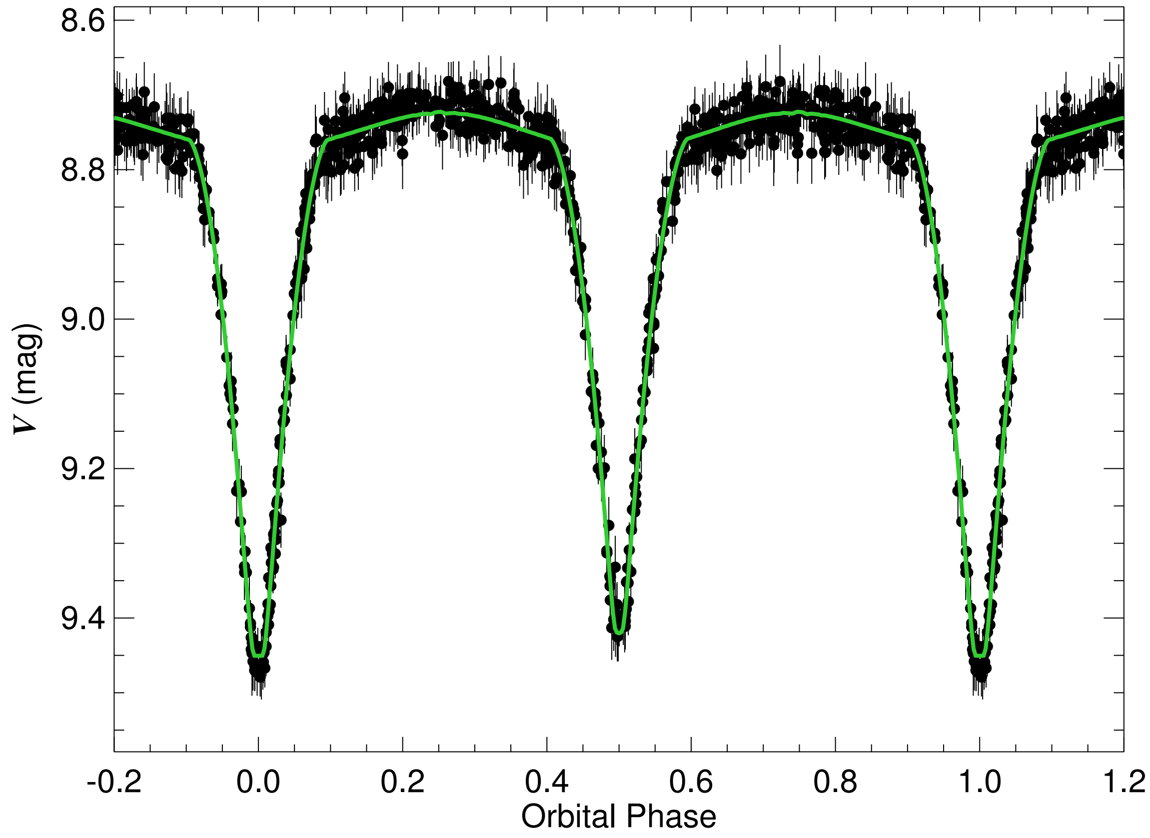

Figure A.33 The ASAS $V-$band light curve for ASAS 084831−2609.8 (TT Pyx). Filled circles with lines represent data with associated uncertainties. The best fit orbital solution listed in Table 6.2 is shown as a solid line passing through the data.

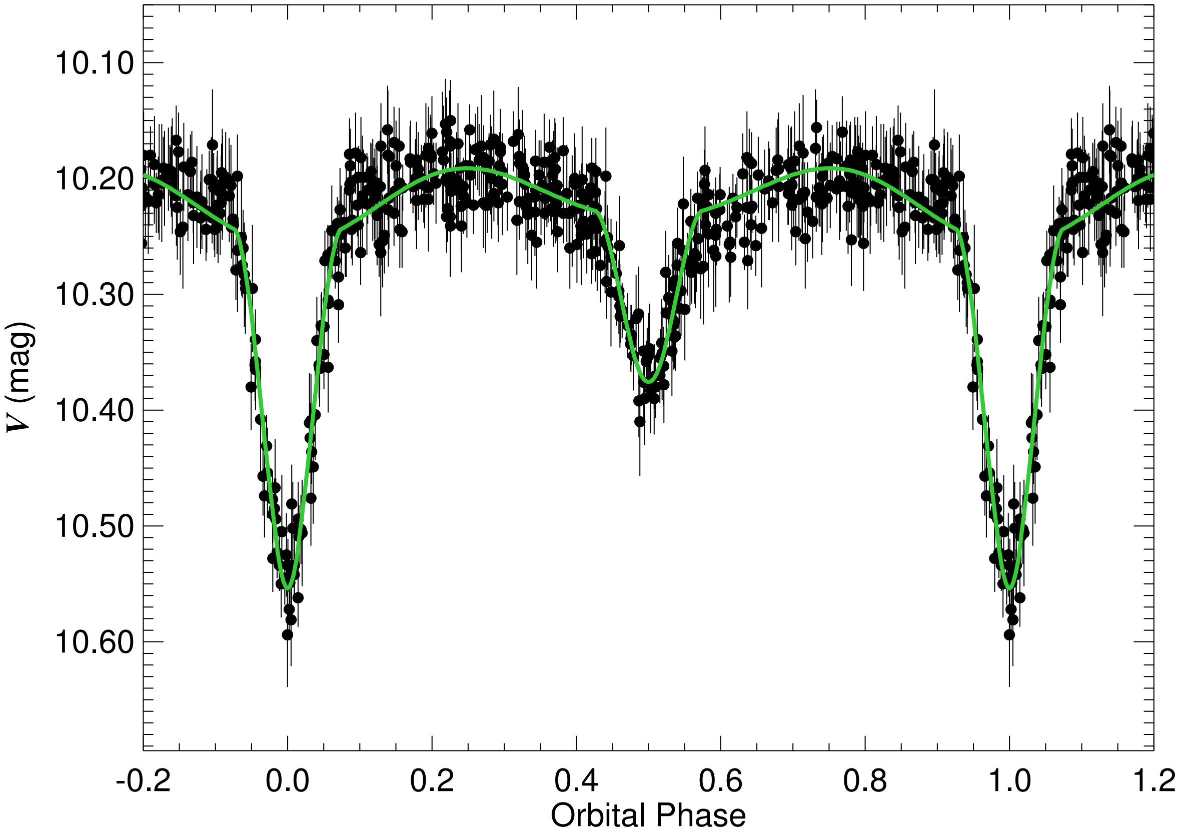

Figure A.34 The ASAS $V-$band light curve for ASAS 101120−1956.3 (HD 88409). Filled circles with lines represent data with associated uncertainties. The best fit orbital solution listed in Table 6.2 is shown as a solid line passing through the data.

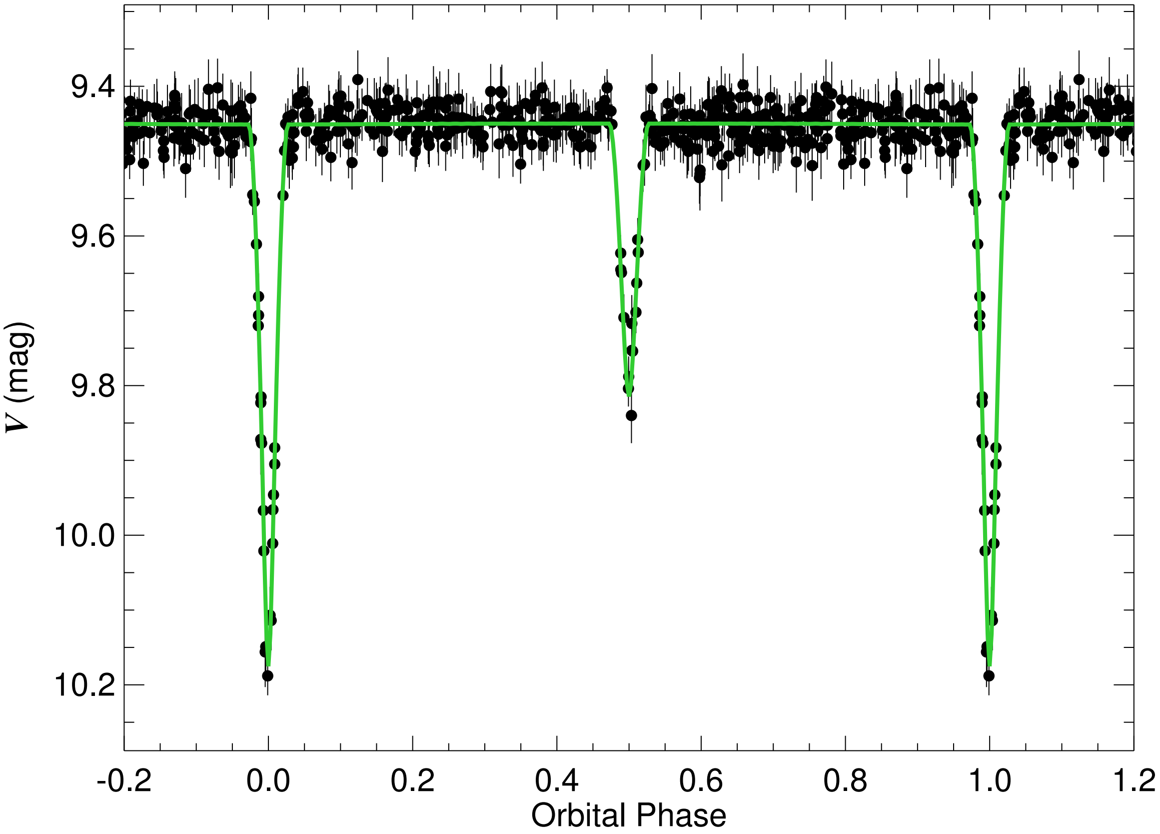

Figure A.35 The ASAS $V-$band light curve for ASAS 135949−2745.5 (HD 122026). Filled circles with lines represent data with associated uncertainties. The best fit orbital solution listed in Table 6.2 is shown as a solid line passing through the data.

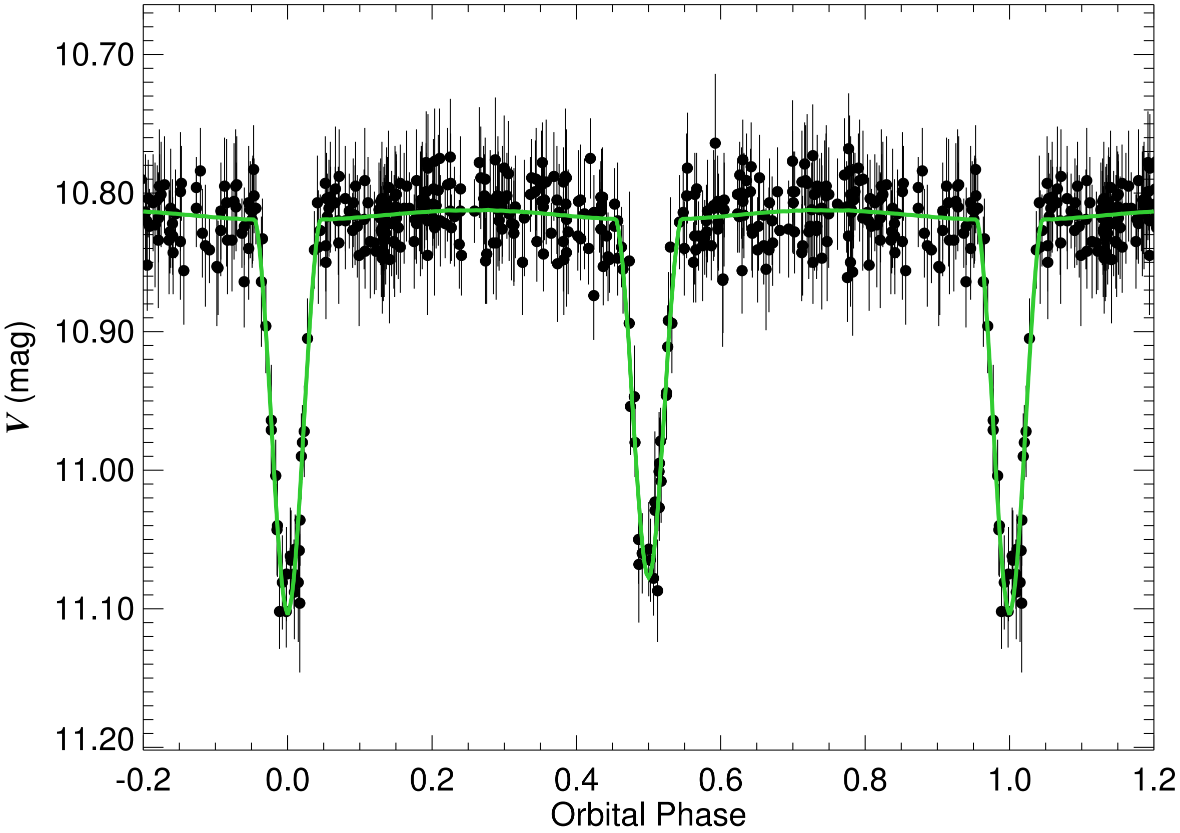

Figure A.36 The ASAS $V-$band light curve for ASAS 160851$-$2351.0 (TYC 6780-1523-1). Filled circles with lines represent data with associated uncertainties. The best fit orbital solution listed in Table 6.2 is shown as a solid line passing through the data.

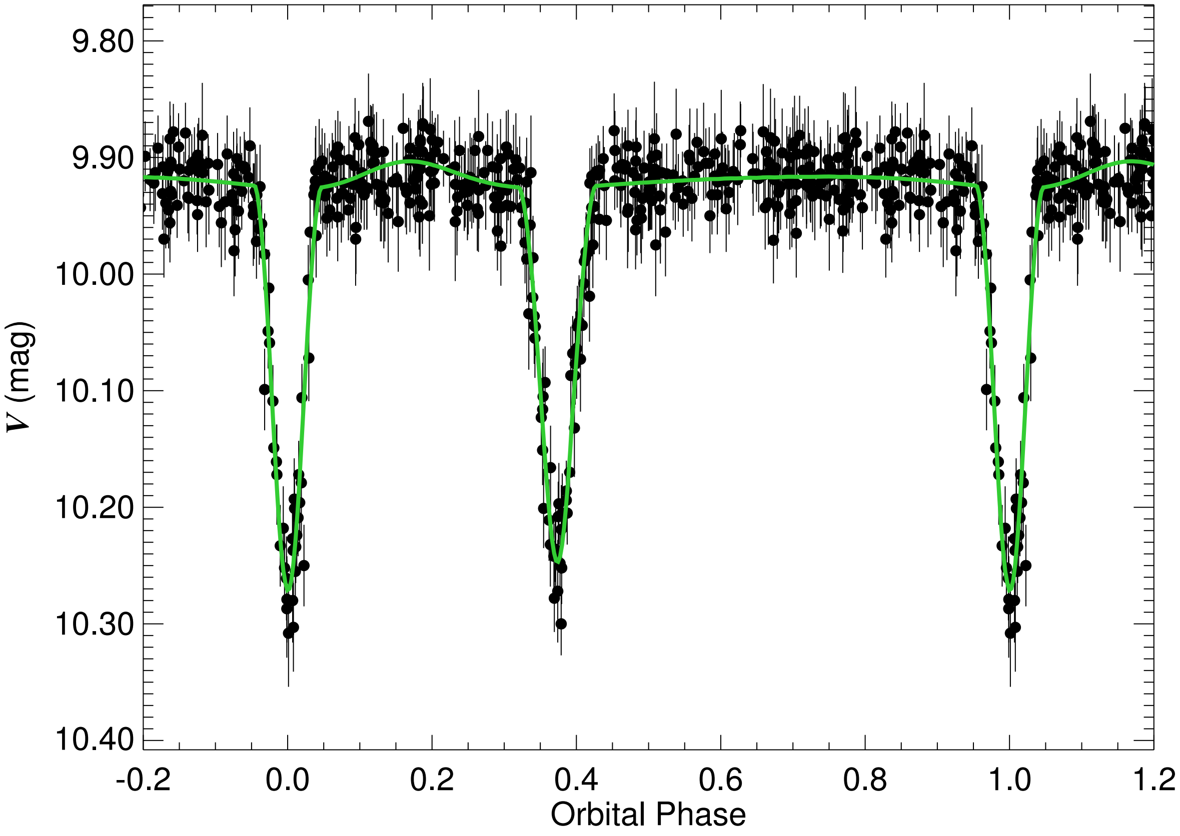

Figure A.37 The ASAS $V-$band light curve for ASAS 165354−1301.9 (HD 152451). Filled circles with lines represent data with associated uncertainties. The best fit orbital solution listed in Table 6.2 is shown as a solid line passing through the data.

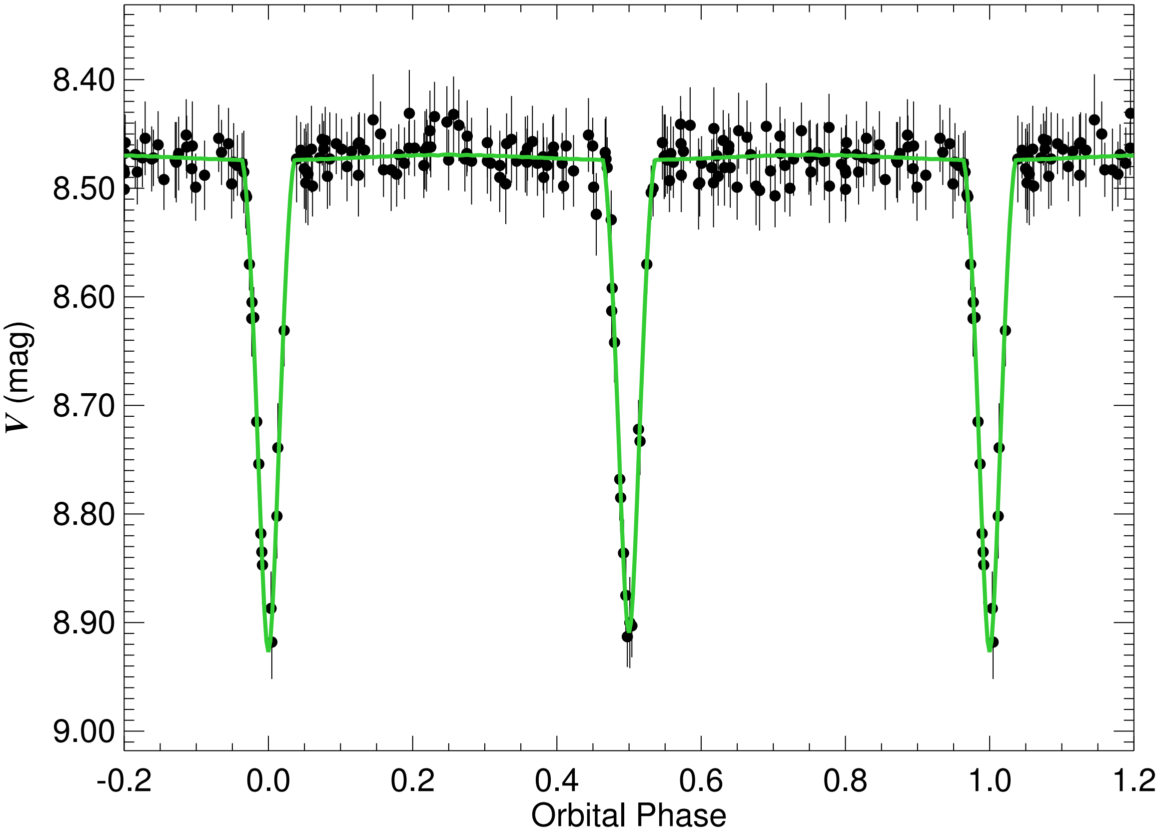

Figure A.38 The ASAS $V-$band light curve for ASAS 170158+2348.4 (HD 154010). Filled circles with lines represent data with associated uncertainties. The best fit orbital solution listed in Table 6.2 is shown as a solid line passing through the data.

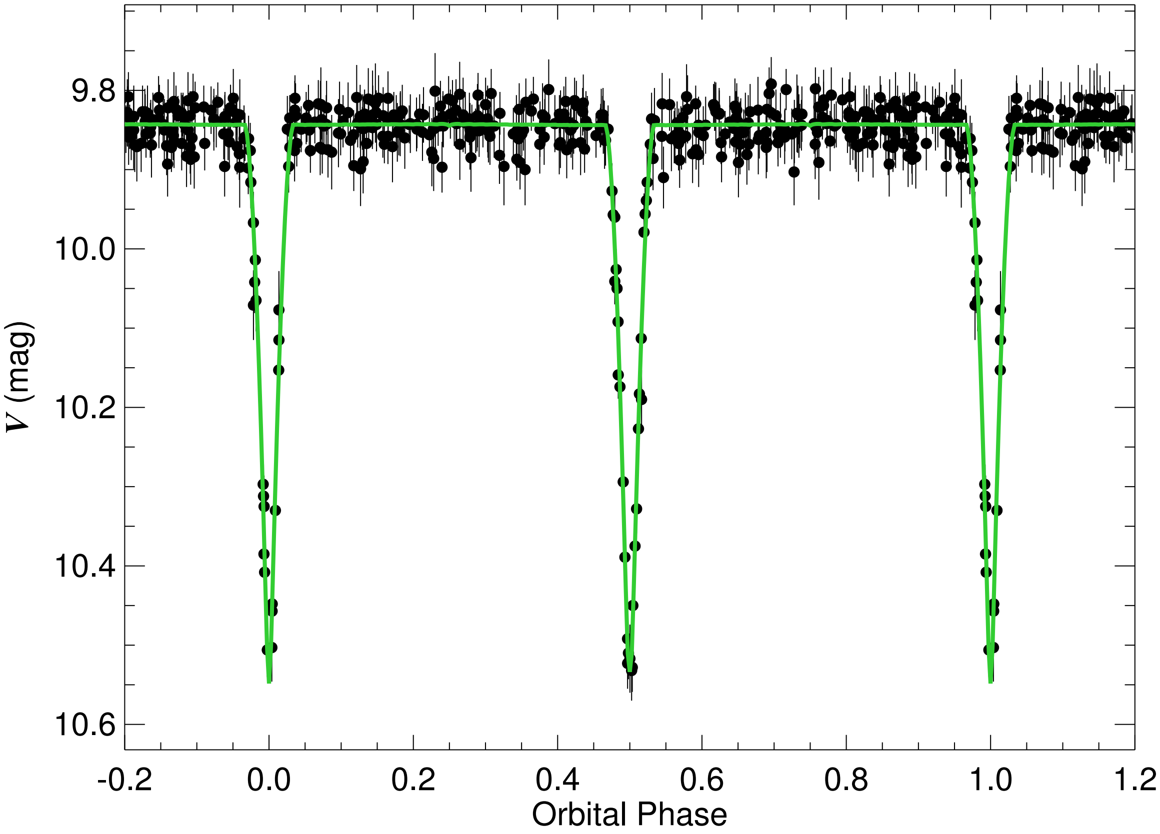

Figure A.39 The ASAS $V-$band light curve for ASAS 173421−1836.3 (HD 159246). Filled circles with lines represent data with associated uncertainties. The best fit orbital solution listed in Table 6.2 is shown as a solid line passing through the data.

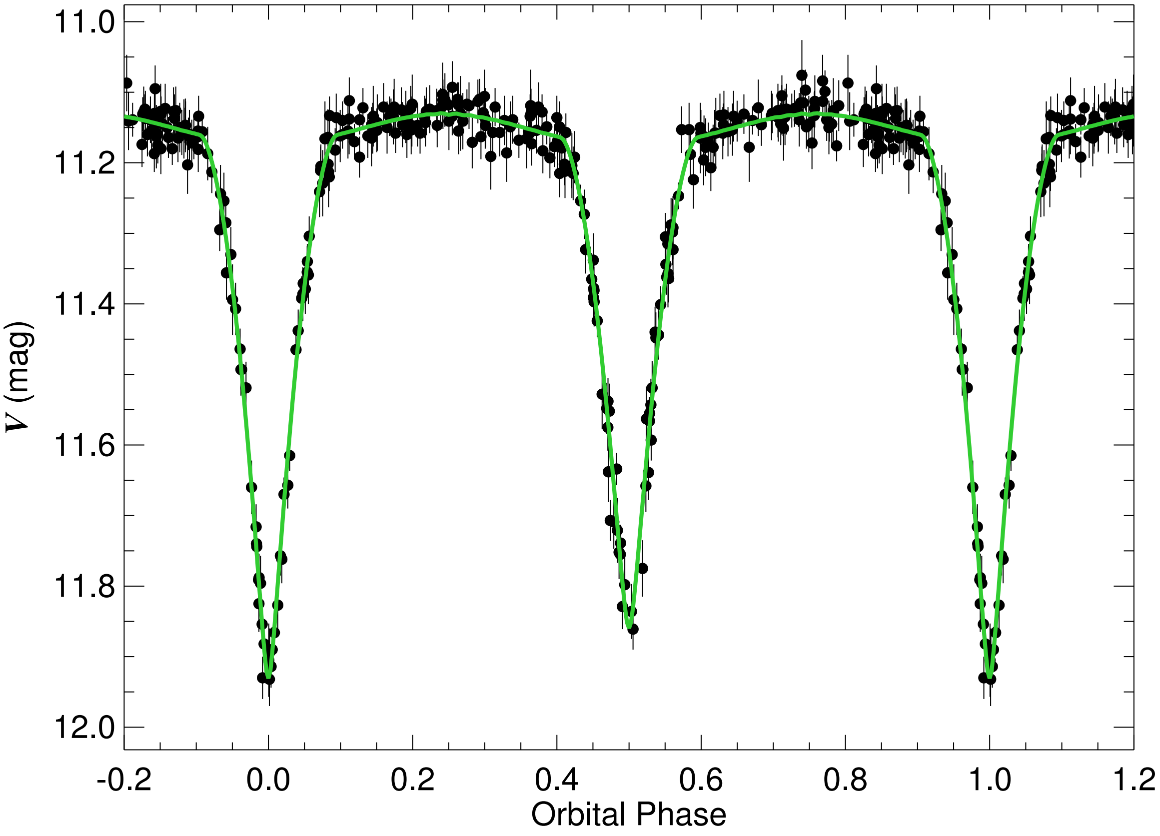

Figure A.40 The ASAS $V-$band light curve for ASAS 174104+0747.1 (V506 Oph). Filled circles with lines represent data with associated uncertainties. The best fit orbital solution listed in Table 6.2 is shown as a solid line passing through the data.

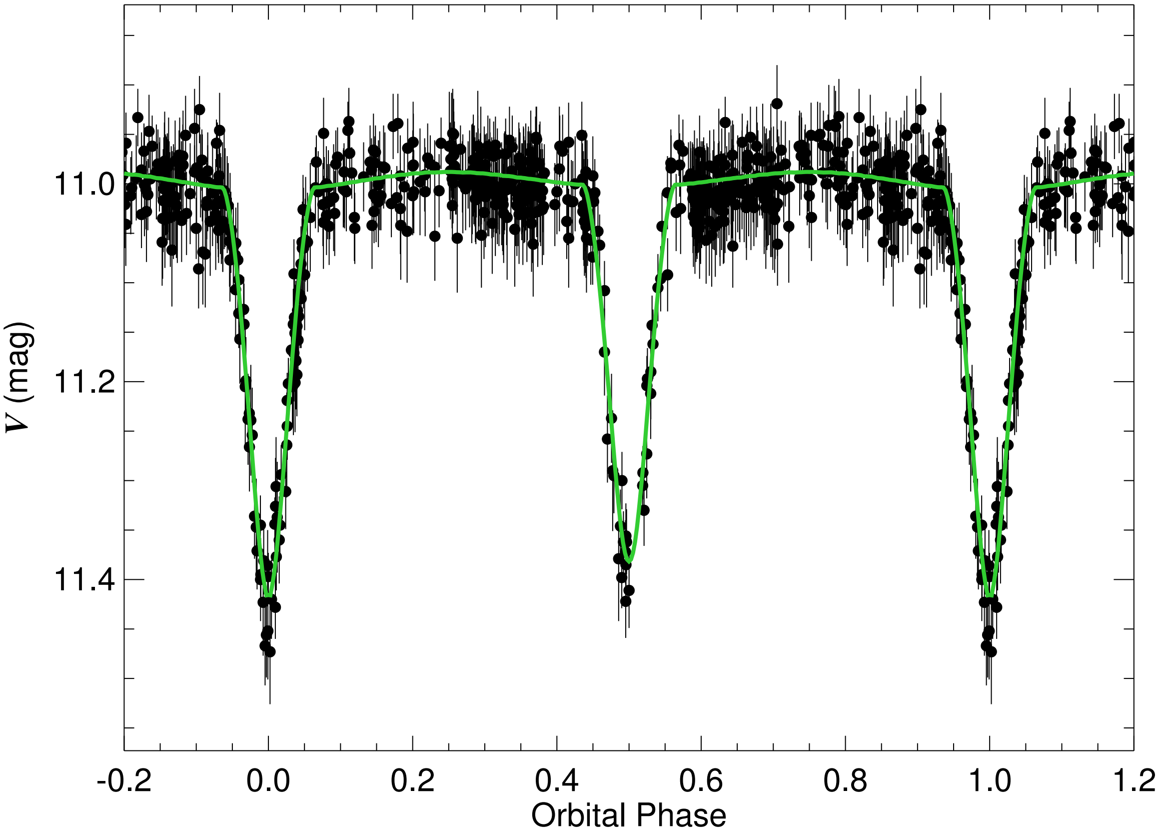

Figure A.41 The ASAS $V-$band light curve for ASAS 175659$-$2012.2 (HD 312444). Filled circles with lines represent data with associated uncertainties. The best fit orbital solution listed in Table 6.2 is shown as a solid line passing through the data.

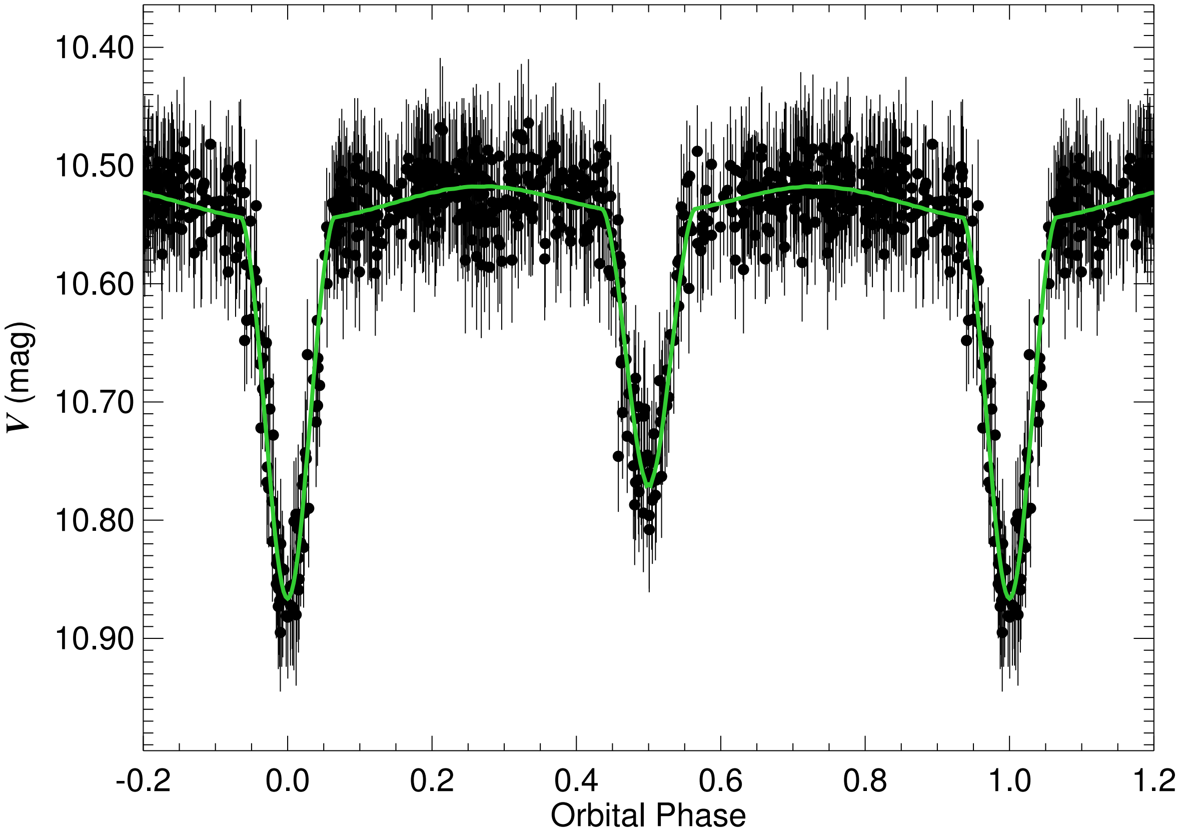

Figure A.42 The ASAS $V-$band light curve for ASAS 175859−2323.1 (HD 313508). Filled circles with lines represent data with associated uncertainties. The best fit orbital solution listed in Table 6.2 is shown as a solid line passing through the data.

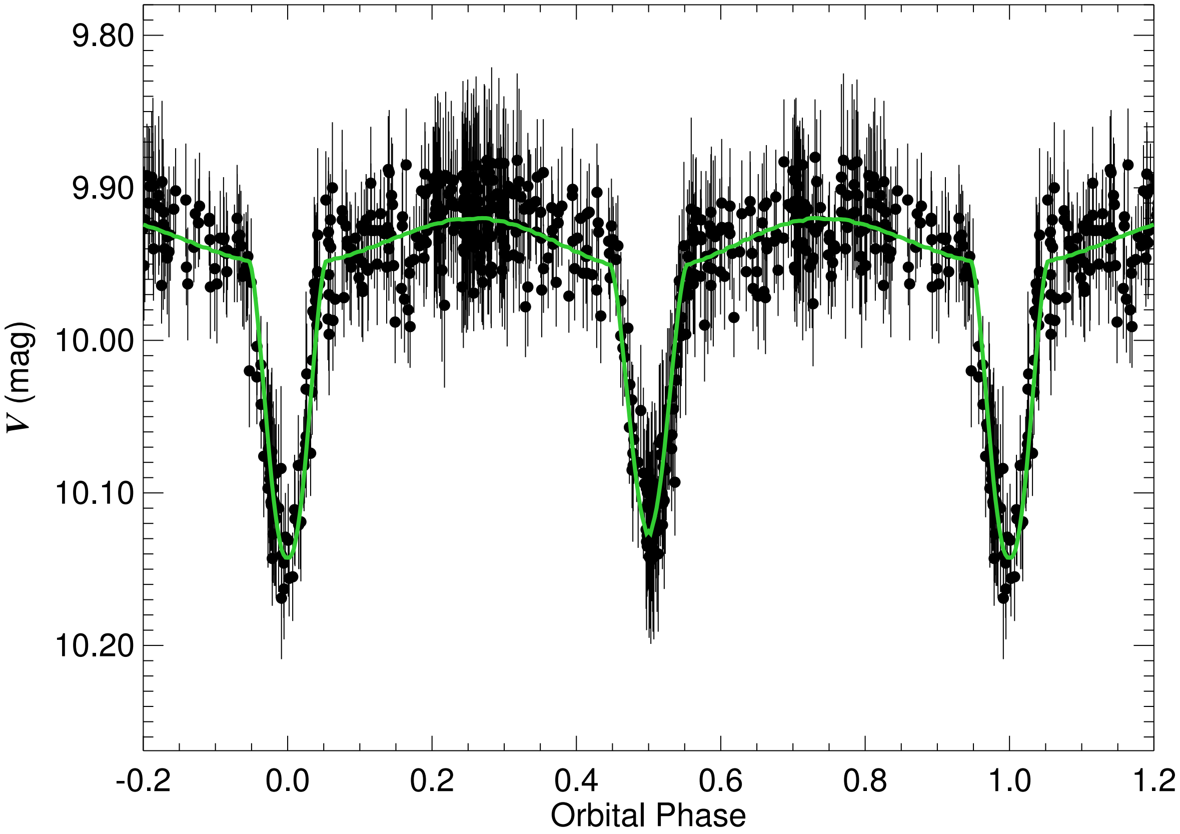

Figure A.43 The ASAS $V-$band light curve for ASAS 180903−1824.5 (HD 165890). Filled circles with lines represent data with associated uncertainties. The best fit orbital solution listed in Table 6.2 is shown as a solid line passing through the data.

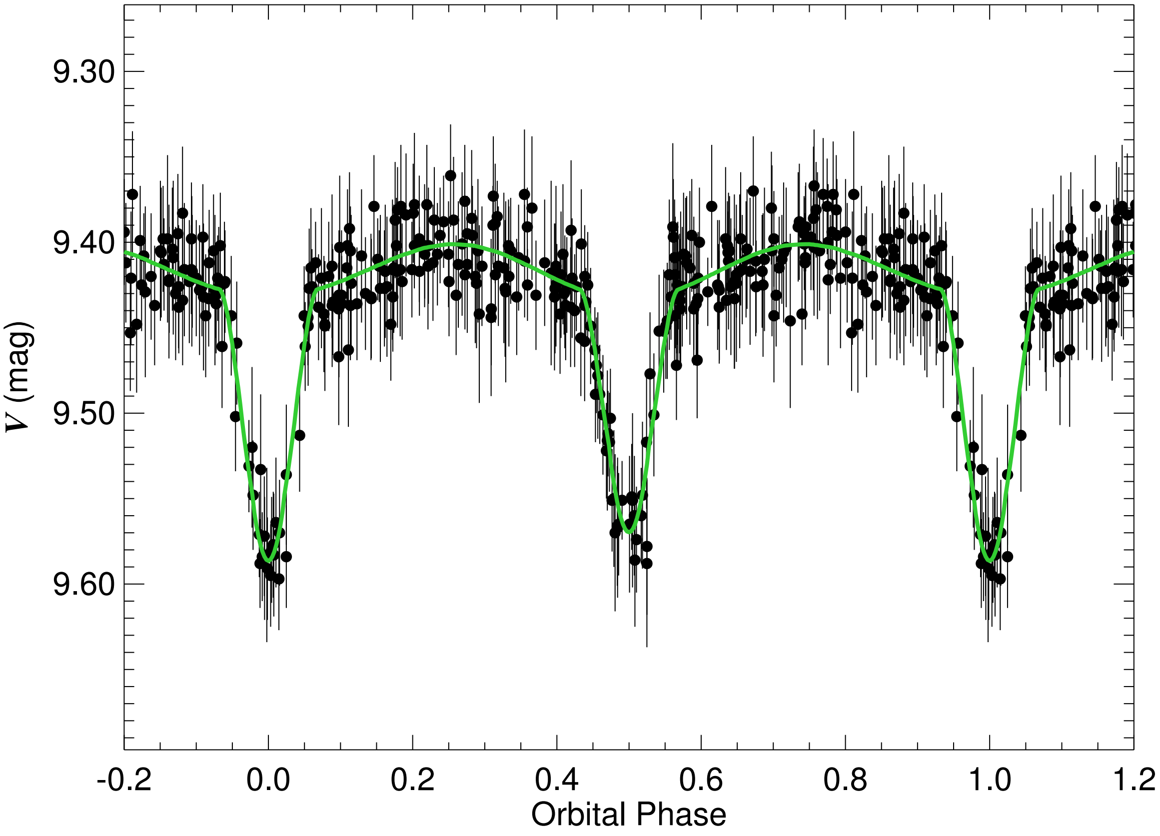

Figure A.44 The ASAS $V-$band light curve for ASAS 181025+0047.7 (HD 166383). Filled circles with lines represent data with associated uncertainties. The best fit orbital solution listed in Table 6.2 is shown as a solid line passing through the data.

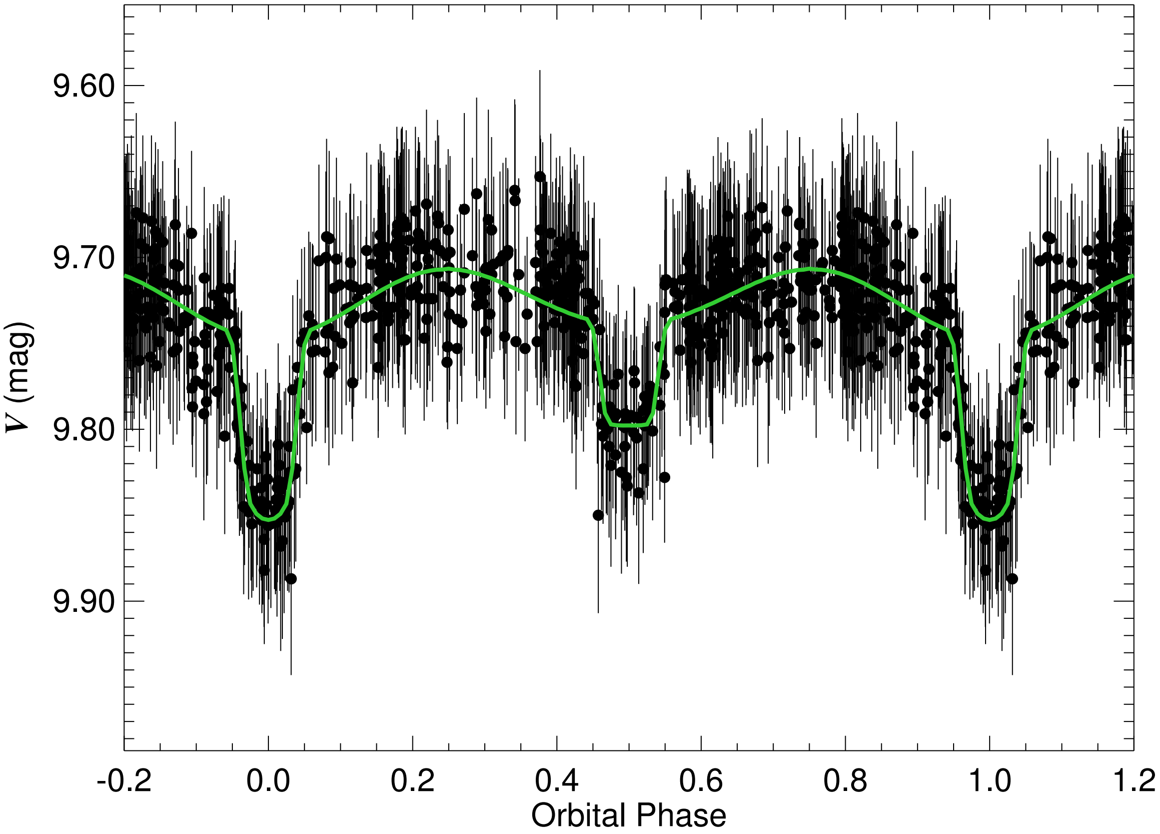

Figure A.45 The ASAS $V-$band light curve for ASAS 181328−2214.3 (HD 166851). Filled circles with lines represent data with associated uncertainties. The best fit orbital solution listed in Table 6.2 is shown as a solid line passing through the data.

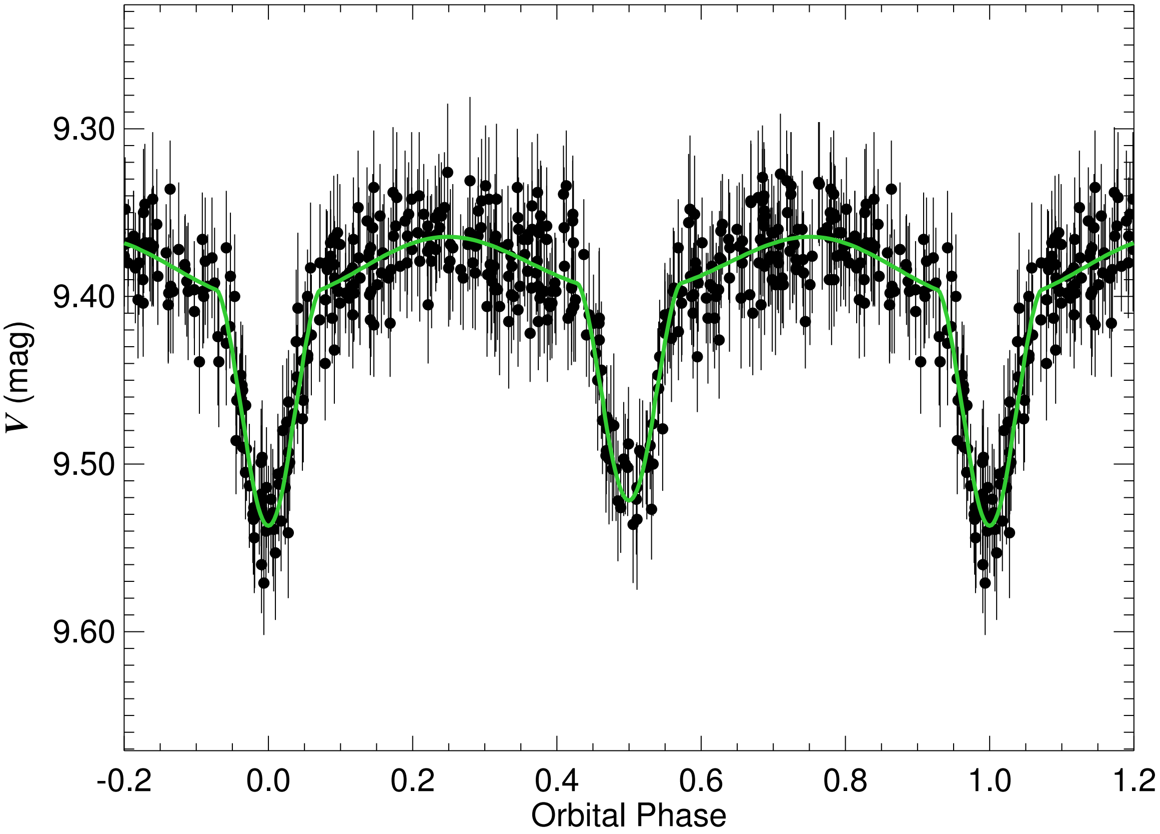

Figure A.46 The ASAS $V-$band light curve for ASAS 181909−1410.0 (HD 168207). Filled circles with lines represent data with associated uncertainties. The best fit orbital solution listed in Table 6.2 is shown as a solid line passing through the data.

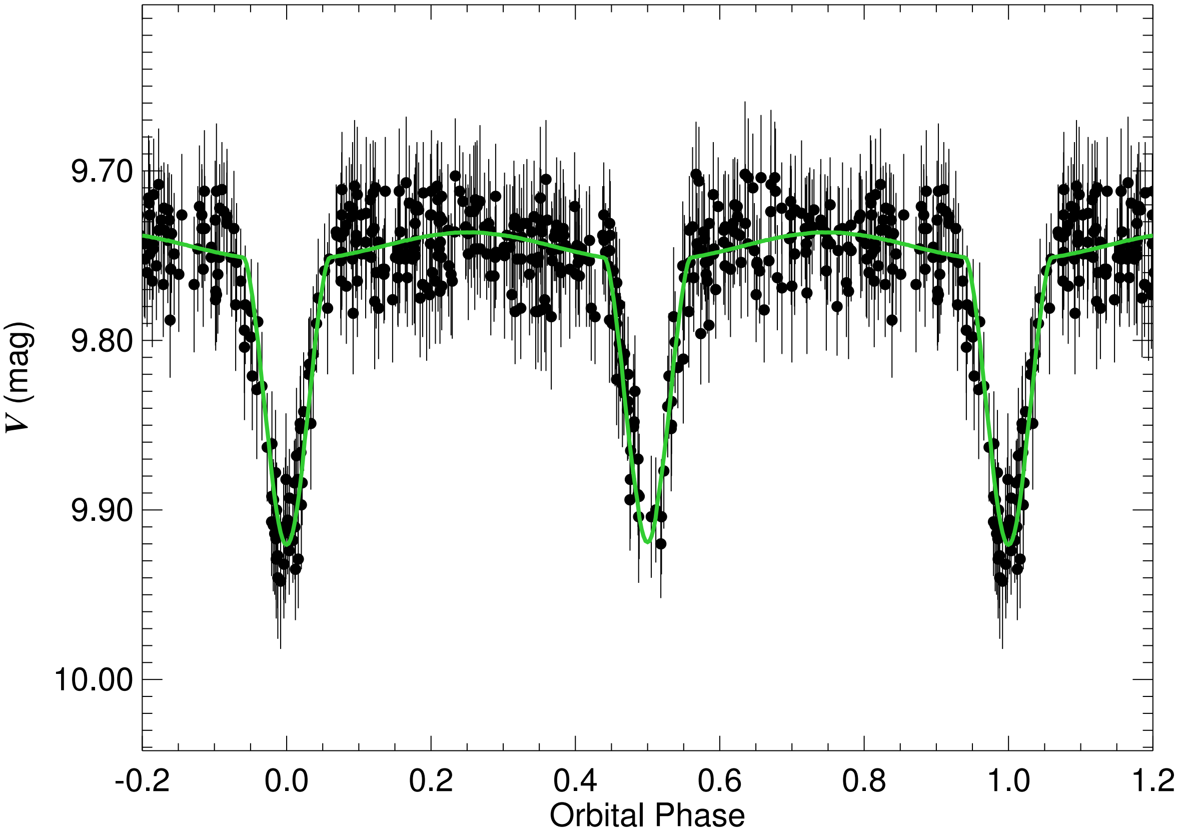

Figure A.47 The ASAS $V-$band light curve for ASAS 183129−1918.8 (BD−19°5039). Filled circles with lines represent data with associated uncertainties. The best fit orbital solution listed in Table 6.2 is shown as a solid line passing through the data.

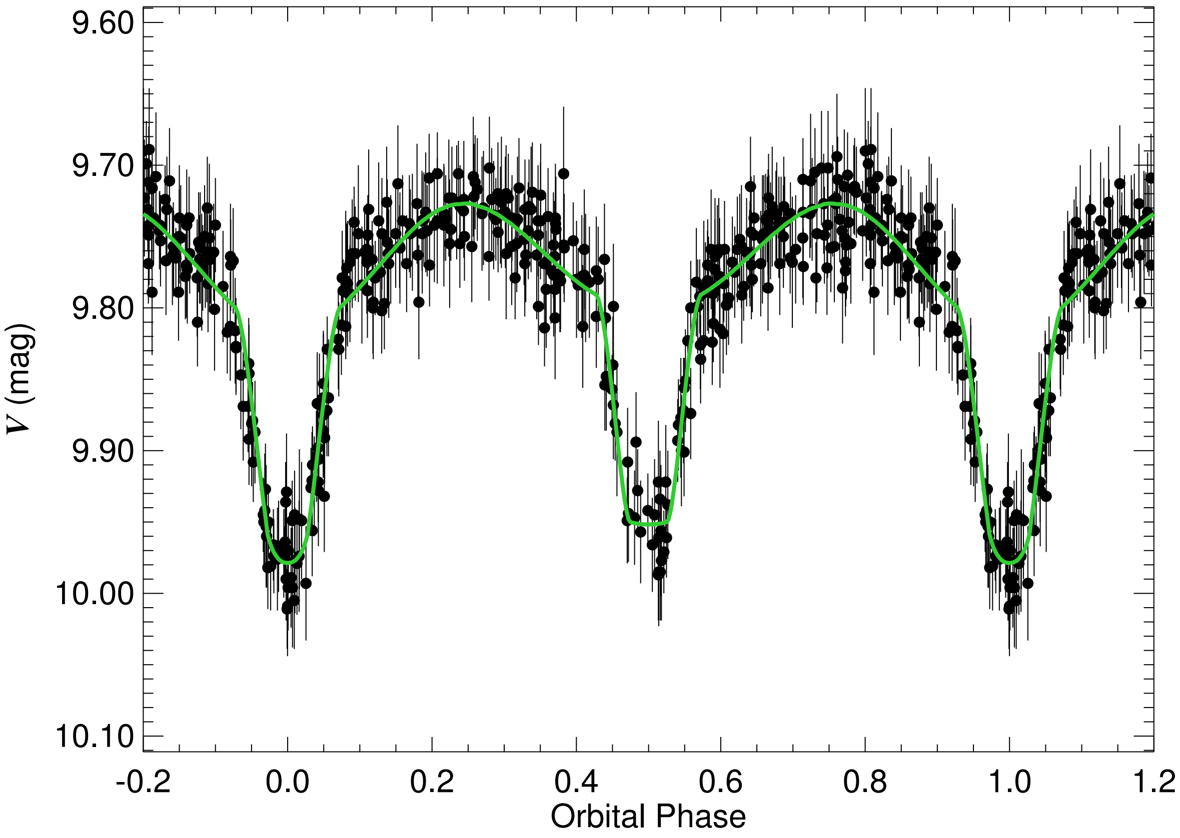

Figure A.48 The ASAS $V-$band light curve for ASAS 183219−1117.4 (BD−11∘4667). Filled circles with lines represent data with associated uncertainties. The best fit orbital solution listed in Table 6.2 is shown as a solid line passing through the data.

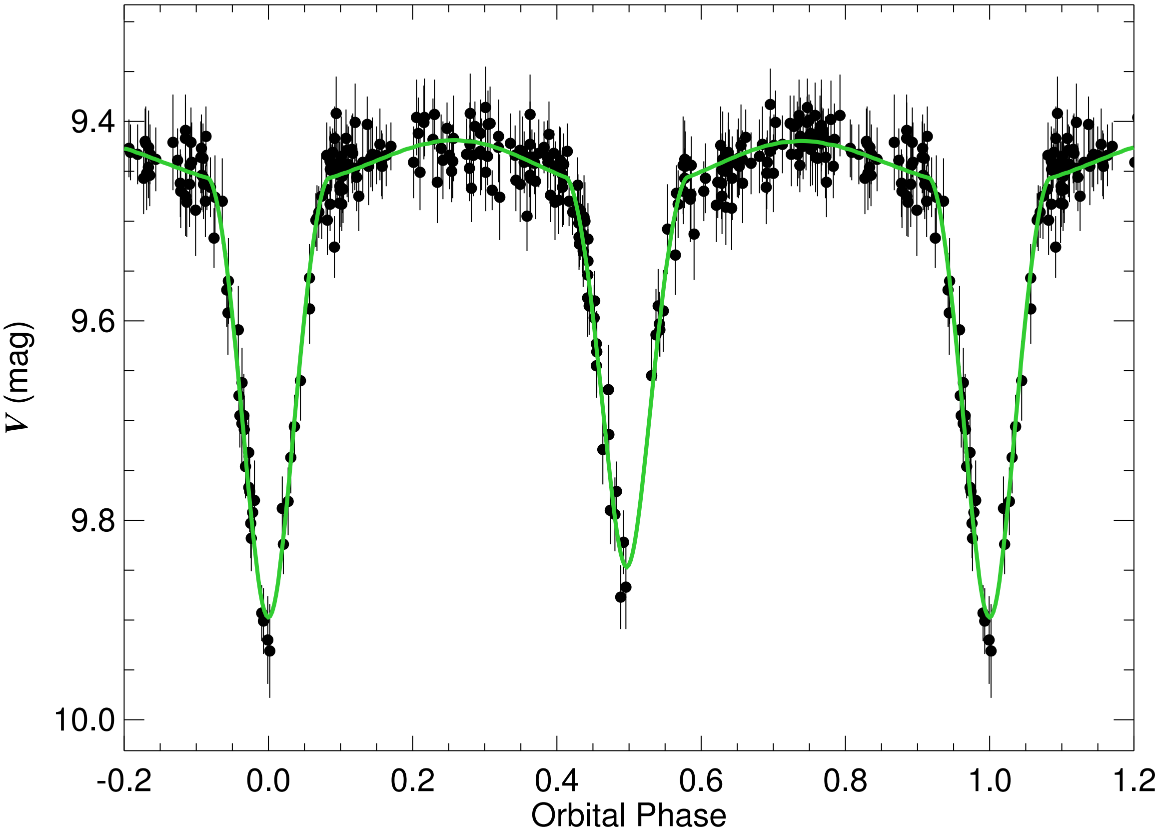

Figure A.49 The ASAS $V-$band light curve for ASAS 184223+1158.9 (BD+11°3569). Filled circles with lines represent data with associated uncertainties. The best fit orbital solution listed in Table 6.2 is shown as a solid line passing through the data.

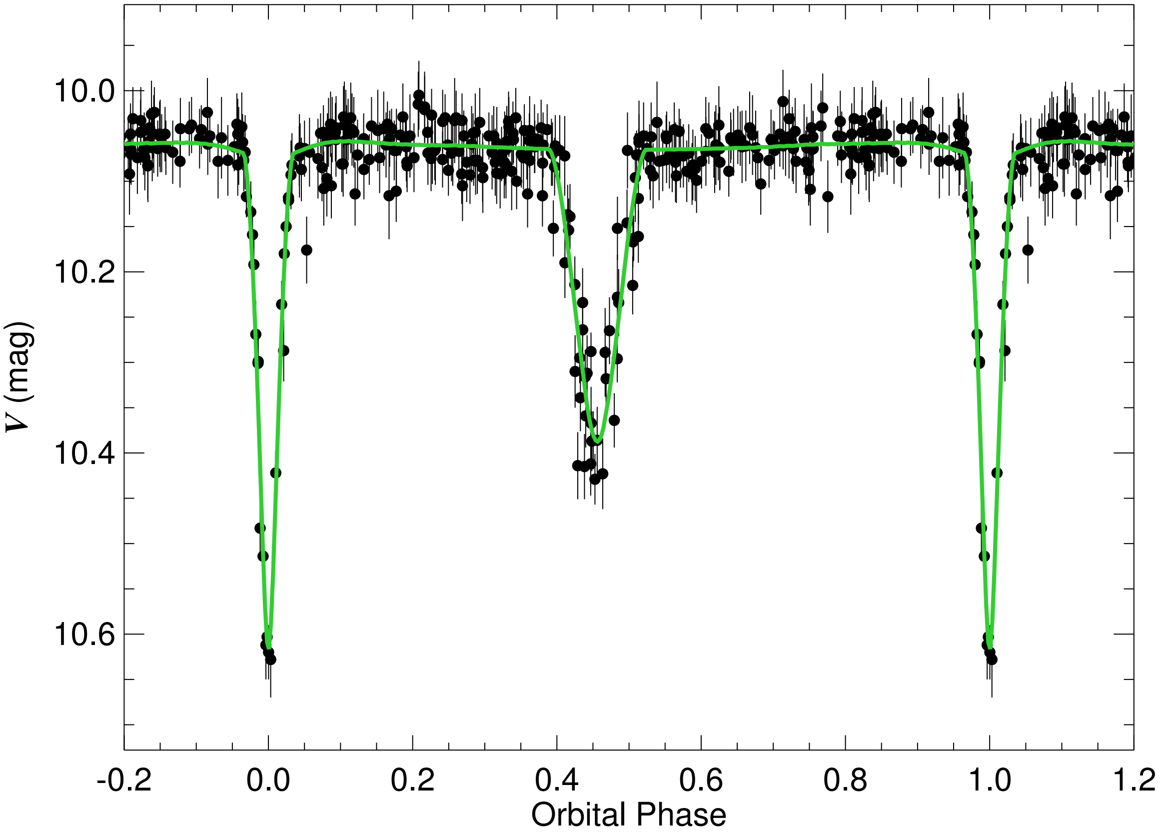

Figure A.50 The ASAS $V-$band light curve for ASAS 184327+0841.5 (TYC 1025-1524-1). Filled circles with lines represent data with associated uncertainties. The best fit orbital solution listed in Table 6.2 is shown as a solid line passing through the data.

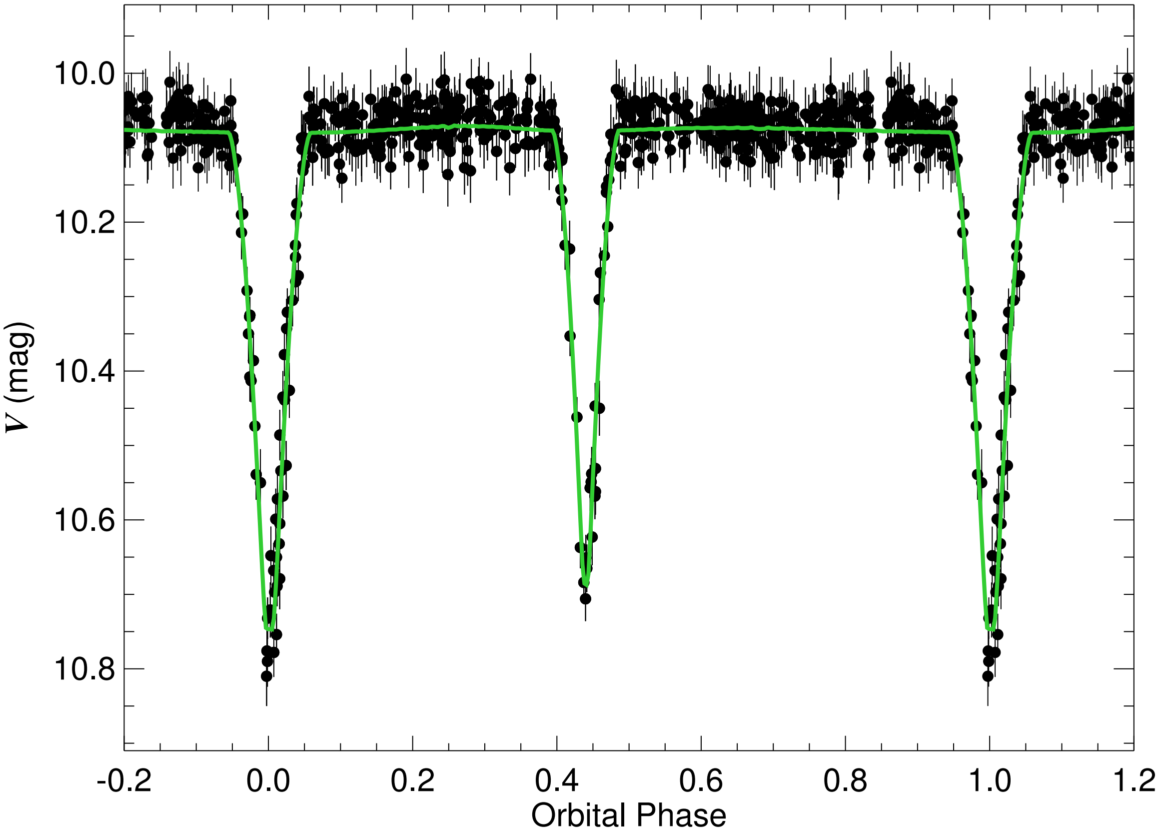

Figure A.51 The ASAS $V-$band light curve for ASAS 184436−1923.4 (YY Sgr). Filled circles with lines represent data with associated uncertainties. The best fit orbital solution listed in Table 6.2 is shown as a solid line passing through the data.

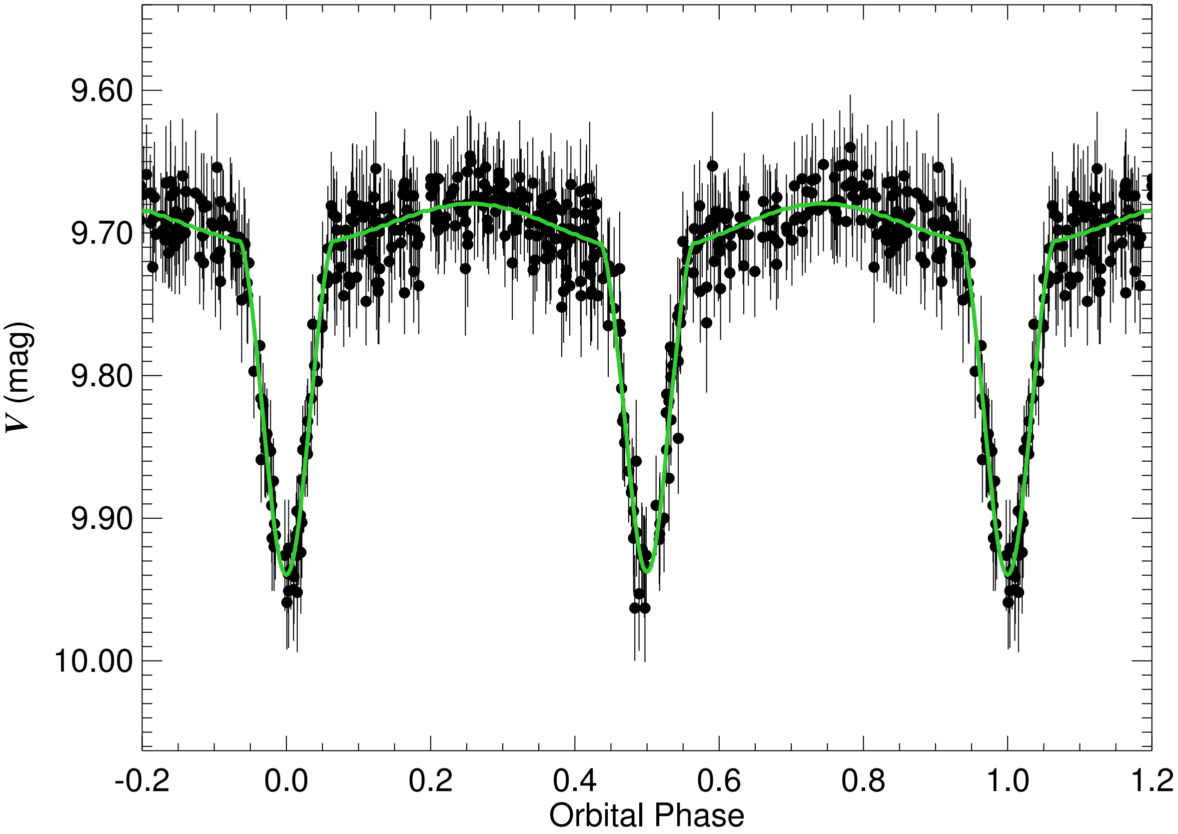

Figure A.52 The ASAS $V-$band light curve for ASAS 185051−1354.6 (HD 174397). Filled circles with lines represent data with associated uncertainties. The best fit orbital solution listed in Table 6.2 is shown as a solid line passing through the data.

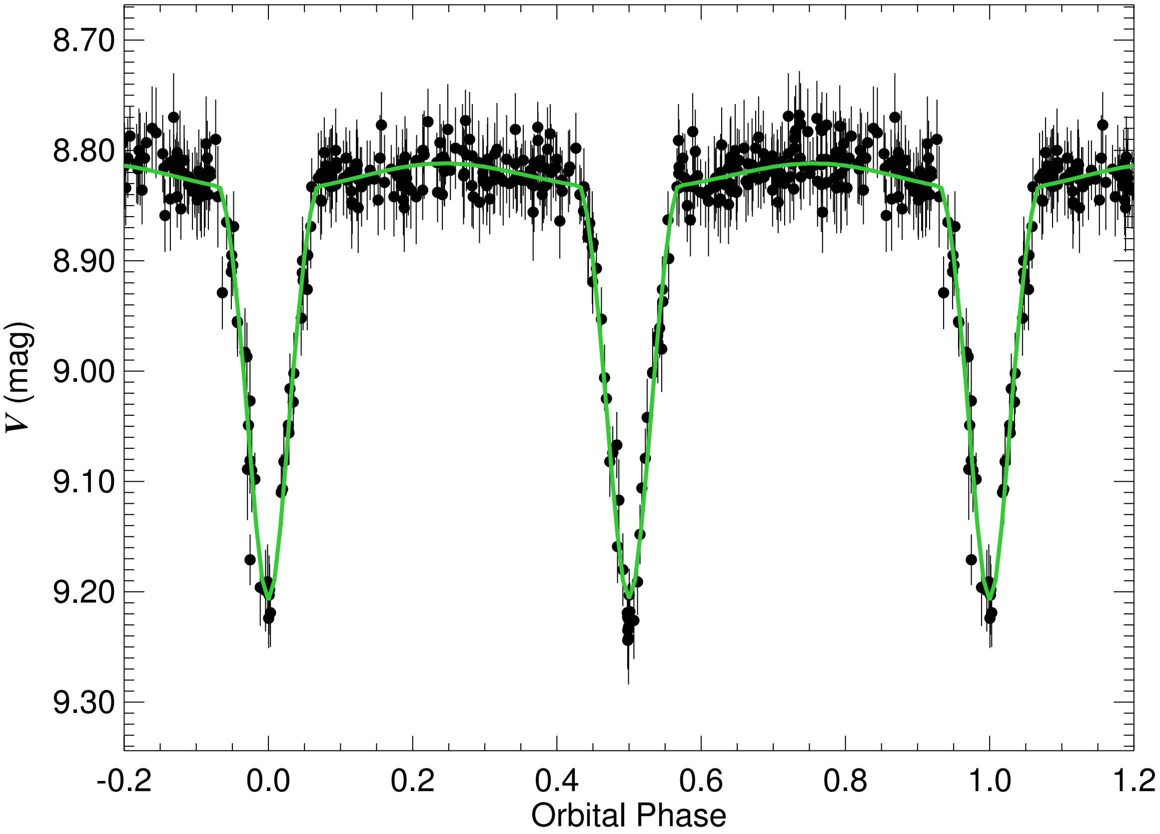

Figure A.53 The ASAS $V-$band light curve for ASAS 194334$-$0904.0 (V1461 Aql). Filled circles with lines represent data with associated uncertainties. The best fit orbital solution listed in Table 6.2 is shown as a solid line passing through the data.

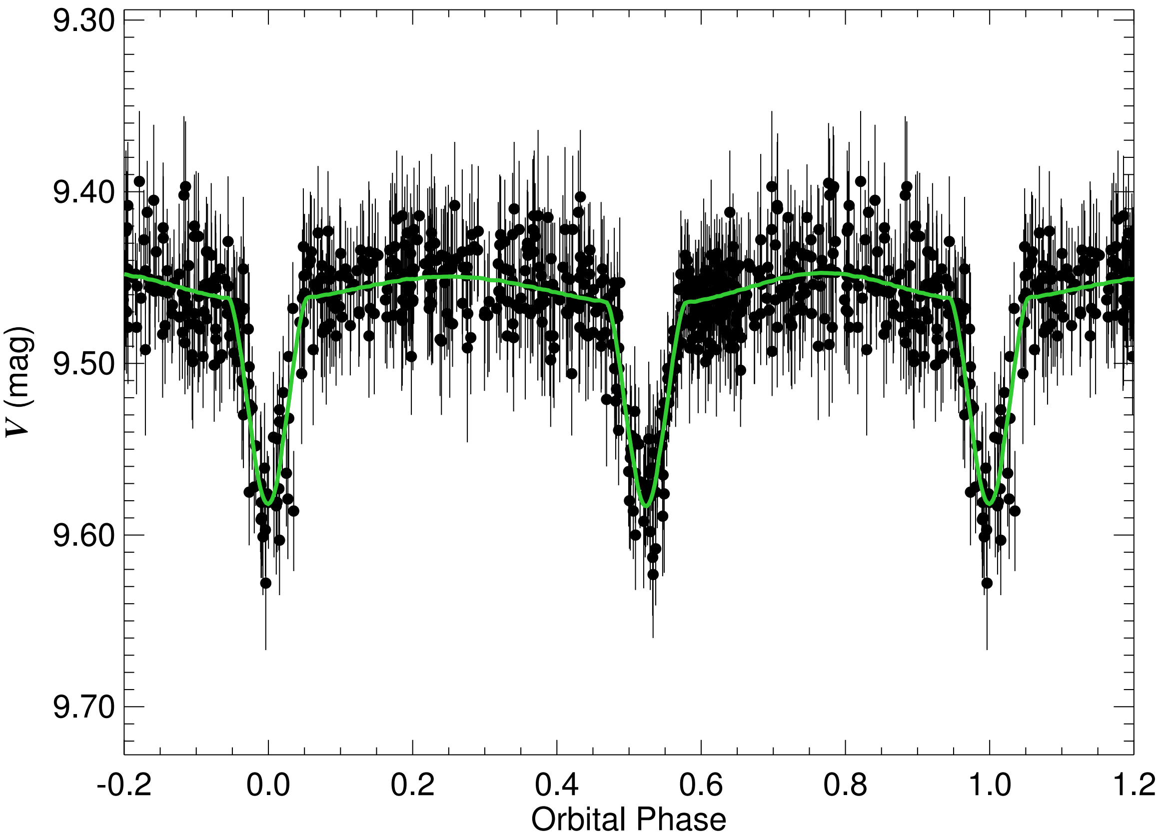

Figure A.54 The ASAS $V-$band light curve for ASAS 195342+0205.4 (HD 188153). Filled circles with lines represent data with associated uncertainties. The best fit orbital solution listed in Table 6.2 is shown as a solid line passing through the data.

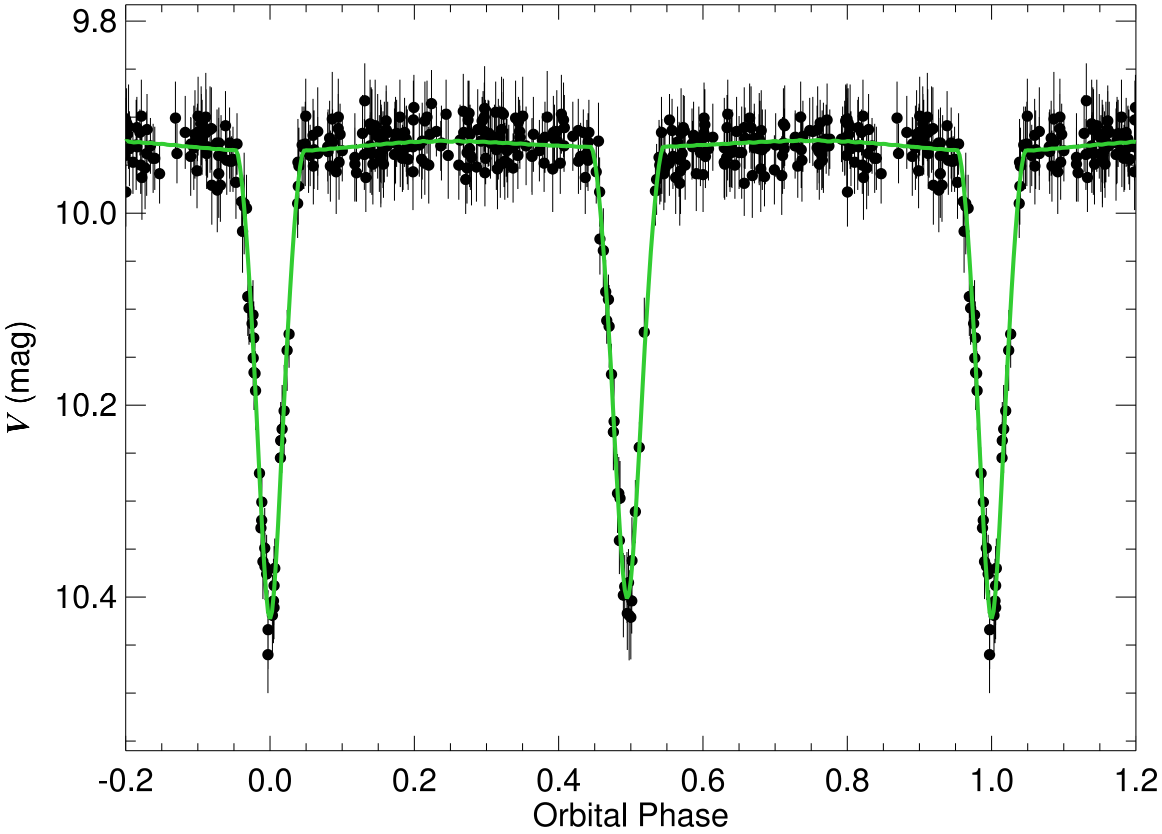

Figure A.55 The ASAS $V-$band light curve for ASAS 195613+1630.9 (HD 354110). Filled circles with lines represent data with associated uncertainties. The best fit orbital solution listed in Table 6.2 is shown as a solid line passing through the data.

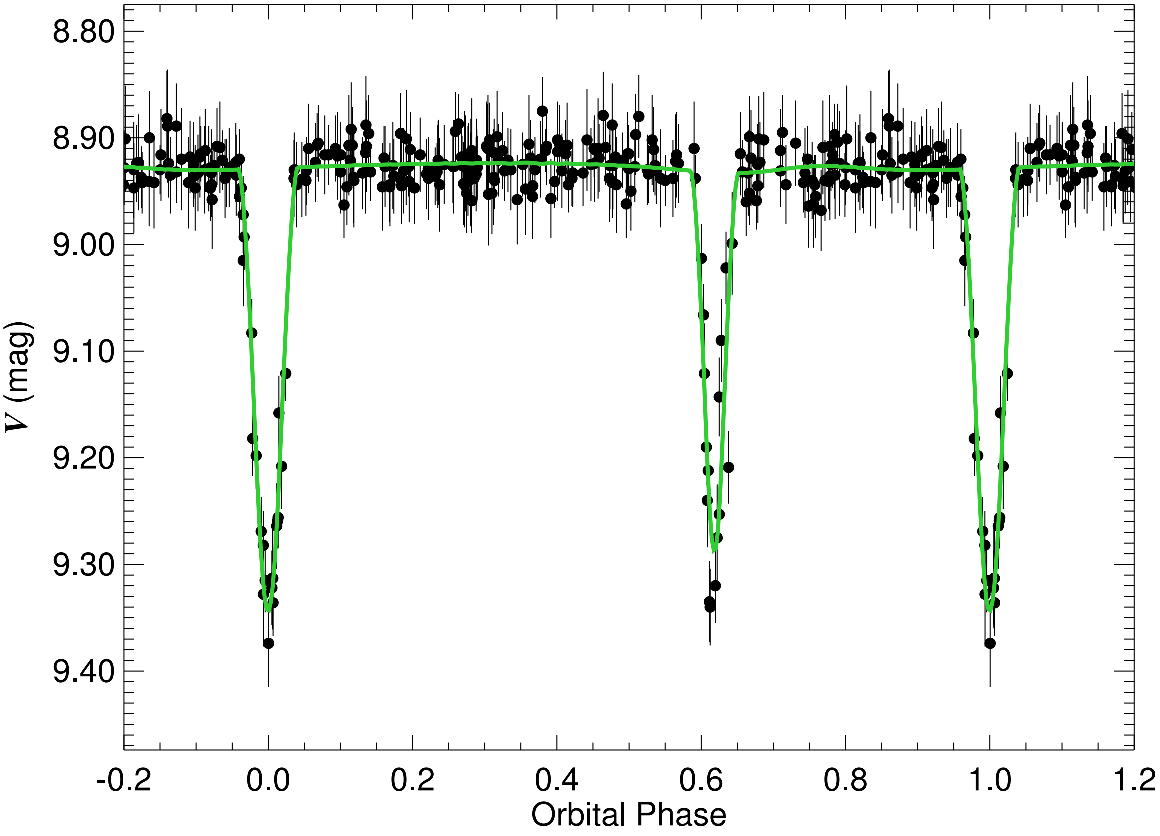

Figure A.56 The ASAS $V-$band light curve for ASAS 205642+1153.0 (HD 199428). Filled circles with lines represent data with associated uncertainties. The best fit orbital solution listed in Table 6.2 is shown as a solid line passing through the data.

– B –

Using ELC

This Appendix outlines the general approach used in this dissertation to run ELC. In this dissertation, ELC was used with systems that exhibited clear double-lined spectroscopic variation and eclipsing or ellipsoidal photometric behavior. Consequently, this meant that constraints could be used from each set of data to narrow down the parameter space searched in the simultaneous fits to data. For example, the light curve file for HI Mon (see section 5.4) contained 441 points, while only 11 radial velocities were measured and used in the combined fit. Therefore, the light curve was the most important constraint for the orbital period. Those 11 spectra, however, contain valuable information that was used to constrain the parameters fit by the light curve. Specifically, model atmosphere fits to tomographically reconstructed spectra give effective temperature and log g limits. The log g limit was used to watch ELC's estimates for the radii of each star. If ELC fit the system with one main sequence star (log $g \sim 4.0$) and one giant star (log $g \sim 3.5$), while the atmosphere model fits showed main sequence stars for each component, subsequent ELC fits were constrained via the "ratrad" (ratio of the radii) flag in "ELC.inp," one of the input files for ELC. Another constraint that can be used after analysis of the spectra is "temprat" (effective temperature ratio). A further input that was varied while using ELC was the "dphase" parameter. This value is the number of degrees the binary is turned in space while computing light curve points. A value of 3.0, will therefore compute the light curve for 120 points during one orbit. Here is a sample "ELC.inp" file for HI Mon:

```
  40                Nalph1
 15                 Nbet1
  40                Nalph2
 15                 Nbet2
0.633608726         fill1
0.617452500         fill2
  1.000000          omega1
  1.000000          omega2
  1.000000          dphase
   0.8642600000     Q
80.17625            finc
 28454.20           Teff1
 27371.00           Teff2
0.250000            Tgrav1
0.250000            Tgrav2
 2.00000            betarim
0.617453            rinner
0.750000            router
30000.0             tdisk
-0.7500             xi
 90                 Ntheta
 60                 Nradius
1.0000              alb1
1.0000              alb2
 1                  Nref
   0.00100          log10(Lx)
    1.5744300000    Period
 0.20050            fm
     -31.98013      separ
   0.000000         gamma velocity
  -5000.00          t3
  -5.00000          g3
   -0.100000        SA3
    0.000000        xecl
    0.000000        onephase
    3.450000        usepot1
    2.860000        usepot2
 54936.318800000    T0
0                   idraw
1                   iecheck
0                   idint
1                   iatm
1                   ism1
0 0 1 0 0 0 0 0     icnU,icnB,icnV,icnR,icnI,icnJ,icnH,icnK
2                   iRVfilt
0                   ionephase
0                   isquare
0                   iusepot
0                   ifixgamma (currently inactive)
 2                  ilaw  (1=linear law, 2=logarithmic law, 3=square root law, 4=quad law, >10 for power series)
 3600.0    0.6850  0.1670  0.7360  0.1580  0.4620  0.2680  0.2640  0.1800
 4500.0    0.6350  0.2420  0.6350  0.2420  0.4620  0.2680  0.4630  0.2670
 5550.0    0.6710  0.1950  0.6710  0.1950  0.4070  0.2433  0.4060  0.2400
 6700.0    0.6350  0.2420  0.6350  0.2420  0.0000  0.0000  0.0000  0.0000
 8700.0    0.6710  0.1950  0.6710  0.1950  0.4690  0.2220  0.4690  0.2220
12000.0    0.6350  0.2420  0.6350  0.2420  0.0000  0.0000  0.0000  0.0000
16200.0    0.6350  0.2420  0.6350  0.2420  0.0000  0.0000  0.0000  0.0000
22000.0    0.6350  0.2420  0.6350  0.2420  0.0000  0.0000  0.0000  0.0000
0.00000000          eccentricity
  90.00000000       argument of peristron in degrees
 0.00000000         pshift
    0.000000        asini (projected semimajor axis in seconds)
    0.000000        median fit (geneticELC only)
    0.000000        sw7 (currently inactive)
    0.000000        sw8 (currently inactive)
    0.000000        sw9 (currently inactive)
1                   ikeep (1 to put eclipse at phase 0.0)
0                   isynch (1 to keep rotation synchronous at periastron)
```

```
0                   isimp
0                   igrav
1                   itime
     0              MonteCarlo (0 for interpolation, >10 for Monte Carlo)
1                   ielite
-1.0000000          Temperature factor spot 1, star 1
 -1.0000000         Latitude of spot 1, star 1 (degrees)
 -1.0000000         Longitude of spot 1, star 1 (degrees)
 -1.0000000         Angular radius of spot 1, star 1 (degrees)
-1.0000000          Temperature factor spot 2, star 1
 -1.0000000         Latitude of spot 2, star 1 (degrees)
 -1.0000000         Longitude of spot 2, star 1 (degrees)
 -1.0000000         Angular radius of spot 2, star 1 (degrees)
-1.0000000          Temperature factor spot 1, star 2
 -1.0000000         Latitude of spot 1, star 2 (degrees)
 -1.0000000         Longitude of spot 1, star 2 (degrees)
 -1.0000000         Angular radius of spot 1, star 2 (degrees)
-1.0000000          Temperature factor spot 2, star 2
 -1.0000000         Latitude of spot 2, star 2 (degrees)
 -1.0000000         Longitude of spot 2, star 2 (degrees)
 -1.0000000         Angular radius of spot 2, star 2 (degrees)
-1.0000000          Temperature factor spot 1, disk
 -1.0000000         Azimuth of spot 1, disk (degrees)
 -1.0000000         Radial cutoff of spot 1, disk (0 <= r_cut <=1)
 -1.0000000         Angular size of spot 1, disk (degrees)
-1.0000000          Temperature factor spot 2, disk
 -1.0000000         Azimuth of spot 2, disk (degrees)
 -1.0000000         Radial cutoff of spot 2, disk (0 <= r_cut <=1)
 -1.0000000         Angular size of spot 2, disk (degrees)
  0.000000000       primmass (star 1 mass in solar masses)
 248.899000000      primK (K-velocity of star 1 in km/sec)
   0.000000000      primrad (star 1 radius in solar radii)
     0.000000000    ratrad (ratio of star 1 radius and star 2 radius)
0.00                frac1 (fractional radius star 1: R_1/a)
0.00                frac2 (fractional radius star 2: R_2/a)
 0.000000000        ecosw (phase difference between eclipses)
 0.0000000          temprat (T_2/T_1)
0                   idark1
0                   idark2
     0              Npoly (0 for numerical)
0                   ifasttrans (>0 for fast transit mode)
0                   ialign (0 for rotation aligned with orbit)
0                   ifastgen (1 for fast genetic mode)
0                   isw23 (currently inactive)
0                   isw24 (currently inactive)
 0.0000  0.0000  0.0000  0.0000  0.0000  0.0000  0.0000  0.0000  0.0000
 0.0000  0.0000  0.0000  0.0000  0.0000  0.0000  0.0000  0.0000  0.0000
 0.0000  0.0000  0.0000  0.0000  0.0000  0.0000  0.0000  0.0000  0.0000
 0.0000  0.0000  0.0000  0.0000  0.0000  0.0000  0.0000  0.0000  0.0000
 0.0000  0.0000  0.0000  0.0000  0.0000  0.0000  0.0000  0.0000  0.0000
 0.0000  0.0000  0.0000  0.0000  0.0000  0.0000  0.0000  0.0000  0.0000
 0.0000  0.0000  0.0000  0.0000  0.0000  0.0000  0.0000  0.0000  0.0000
 0.0000  0.0000  0.0000  0.0000  0.0000  0.0000  0.0000  0.0000  0.0000
80.1762500          axis_I (inclination of rotation axis if ialign=1)
 0.0000000          axis_beta (angle of rotation axis wrt to orbit if ialign=1)
0.00                sw23 (currently inactive)
0.00                sw24 (currently inactive)
```

The second input file is “gridloop.opt” where the parameters fit by ELC are set. The specific fitting program used in this dissertation was “geneticELC”. The general setup for this file is to list the input files, light curve files first, ordered by the Johnson

U, B, V, R, I, J, H, K, followed by the two radial velocity files. Next is the block of parameters to fit. First is the number of parameters, followed by the ELC specific names of those parameters. The next part is specific to the genetic version of the ELC fitting routine. The user inputs the parameters listed above in three columns, with the first two being the range of values to cover when searching for the best fit. The last column is only used for the first two entries, and tells ELC how many generations to explore for the best fit, and how many members in each generation. For the case of HI Mon, ELC used 400 generations with 100 members per generation. The input file, again from the fits to HI Mon:

```
none
none
lcV.dat
none
none
none
none
none
RV1.dat
RV2.dat
 9
t0
period
inclination
f1 (fill 1)
f2 (fill 2)
T1 (T_eff of star 1)
T2 (T_eff of star 2)
mass ratio
pk
 54930.000000000  54940.0000000000       100
     1.250000000      1.7500000000       400
    65.000000000      90.00000000          1
     0.100000000      0.9000000000         1
     0.150000000      0.9000000000         1
 27000.000000000  32000.0000000000         1
 27000.000000000  32000.0000000000         1
     0.500000000      1.0000000000         1
   225.000000000    275.0000000000         1
```

The output from ELC is extensively recorded in several output files. This allows for ease of uncertainty calculation, as the “generation.1000” through “generation.1400” (in the above setup) files contain the χ^2 statistic for each iteration along with the values of the fitted parameters with the systemic velocities, $\gamma_{1,2}$ tacked on the end. In addition, the "ELCparm.#" files list astrophysical parameters, such as mass and radius for each star, with the χ^2 statistic for each fit. Also computed are the best fit light and radial velocity curves, output in files (for HI Mon) "modelV.linear" for the light curve output, and "star1.RV" for the primary radial velocity curve, for example. The "checkfit.for" fortran program converts the ELC light curve output to match with the measured magnitudes of the light curve input (in "ELCdataV.fold"). One of the more useful outputs from ELC is "ELC.parm" where astrophysical parameters of interest are listed from the best fit.

– C –

IDL Routines

This appendix lists plainly the Interactive Data Language (IDL) routines used for analysis of spectral line fits. There are two programs, one for hydrogen Balmer series lines, where only the wings are fit. The second program fits all other lines. The two programs are identical in their function, with only a slight difference in implementation for the two cases. Each program prompts the user for starting input values of effective temperature, log g, and $v \sin i$, as well as the spectrum stack for the object, the "master" spectrum for the object, and the wavelength of the spectral feature to fit. The user is then prompted to click on the plot window for the regions to be fit by the program. For "findmodbalmer.pro" the clicked input is only the left wing of the feature to fit, while the right wing of the feature to fit is computed by the program as the reflection across the center point of the feature (also a user click). The "findmod.pro" program simply needs the user to click on the range of the spectrum plotted to fit, ideally one click on each side of a prominent absorption feature. A grid of models in temperature and log g are then computed and fit to the data via a simple squared difference calculation. This grid of values is printed to the screen after completion so the user can see how the fit varies across the parameter space. Also output to the screen are the best fit values of temperature and log g with a very rough estimation of the uncertainty. As described in Chapters 3, 4, and 5, the actual uncertainty on the final derived values is different than this computed uncertainty. With no further ado, here is "findmod.pro" for perusal:

```
pro findmod

;
; This is a program to find a model template spectrum from a grid of
; models. For now, this will use the Lanz & Hubeny Tlusty OSTAR 2002
; and BSTAR 2006 models. I hope to expand this for use with custom
; models output from David Grey's SPECTRUM for stars cooler than 15
; kK. 6-19-09 by Stephen Williams.
;

device, retain=2

;
; Declare those variables. First up is the size of the square grid in
; T_eff and log g to search. Square simply because that's easiest to
; program according to how I began this escapade. I also include here
; the size of the grid for both temperature and log g. Presumably,
; this can be changed here without much in the way of effort. PLEASE
; KEEP THE NUMBER OF GRID ELEMENTS ODD. This is currently set up to
; search the equivalent of at least one model grid point above and
; below in the OSTAR 2002 grid.
;

gridelements = 11
tstep=500.0d0
loggstep=0.05d0

c=2.99792458d5

;
; Now I need some user input for the values I will need to obtain grid
; points. I'll also need an estimate for the rotational velocity, so
; I can use that in the creation of models later.
;

usertemp=0.0d0
read,'What is your best estimate for temperature (Kelvin)? ',usertemp

userlogg=0.0d0
read,'What is your best estimate for gravity (log g in cgs)? ',userlogg

uservsini=0.0d0
read,'What is your best estimate for V sin i (km/s)? ',uservsini

;
; Now I need to use this to find the grid points I will compare to the
; co-added, high signal-to-noise spectrum for the particular star. The
; endpoints will be pretty tricky. For now, fortunately, the stars I
; wish to test right now are well within the limits of the
; models. This is now generalized to setup arrays for both T_eff and
; log g for any particular number of gridelements (odd number, of course).
;

ttemp=dblarr(gridelements)
tlogg=dblarr(gridelements)

symmet=gridelements/2
neartemp=round(usertemp/tstep)*tstep
nearlogg=round(userlogg/loggstep)*loggstep

for i=0,gridelements-1 do begin

    ttemp(i) = neartemp + (float(i-symmet)) * tstep
    tlogg(i) = nearlogg + (float(i-symmet)) * loggstep

endfor

;
```

```
; I need to read in the spectrum stack for the object in order to
; obtain the wavelength vector for later work.
;

specstack=' '
read,'Please enter the spectrum stack name for the object: ',specstack

readstk,w,ss,t,specstack

;
; Now for another calculation before we proceed. This is to give a
; reasonable value for the uncertainty involved with the later
; chi-squared type calculation.
;

sig=dblarr(n_elements(w))

for i=0,n_elements(w)-1 do begin

    sig(i) = stddev(ss(i,*))/sqrt(n_elements(t)-1.0d0)

endfor

;
; Now I need to set up a few things for the velocity shift (if needed)
; for the comparison to the model.
;

dw=deriv(w)
dvpix=mean(dw/w*c)

;
; Read in the coadded spectrum. This will be the spectrum for
; comparison.
;

coadded=' '
read,'Please enter the name of the coadded spectrum: ',coadded

flux=readfits(coadded)

;ld=1.0-flux

;
; Before going to the models, I need the linear limb darkening
; coefficient. I'll leave this out of the user input for now, and just
; remember to change this as I go along. Definitely a spot for
; improvement in the future.
;

eps=0.300d0

;
; I also need the instrumental broadening fwhm, presumably already
; known by the observer, and just needed to be input here. Note that
; this MUST BE A FLOAT, IT CANNOT BE A DOUBLE OR GSMOOTH WILL PUKE AND
; IT WILL TAKE YOU 90 MINUTES TO TRACK DOWN!!!
;

fwhm=0.0d0
read,'What is the instrumental broadening FWHM (in km/s)? ',fwhm

;
; I think I need one more input. Fitting the entire spectrum doesn't
; seem to work, so I'll request a user wavelength for a partcular
; line, plot it, and have the user click on the left and right hand
; edges of the region to fit with a model.
;
```

```
spot=0.0d0
read,'What feature would you like to fit (rest wavelength in Angstroms)? ',spot

top=spot+20.0d0
bottom=spot-20.0d0

good=where(w gt bottom and w lt top)
range=flux(good)
high=max(range)+0.1
low=min(range)-0.1
plot,w,flux,xrange=[bottom,top],yrange=[low,high],ystyle=1,xstyle=1

;
; Now get those limits for the fit.
;

print,'Click on the left side of the feature to fit '
cursor,left,empty
wait,1
print,'Click on the right side of the feature to fit '
cursor,right,empty
wait,1

;
; This is now removed with the cross-correlation technique.
;

;print,'Click on the center of the feature '
;cursor,center,empty
;wait,1

;;;;;;;;;;;;;;;;;;;;;;;;;;;;;;;;;;;;;;;;;;;;;;;;;;;;;;;;;;

;
; I need the pixel number for the cross correlation later.
;

pixels = indgen(n_elements(w))

bpix = interpol(pixels,w,[left])
epix = interpol(pixels,w,[right])

bpix = reform(fix(bpix+0.5))
epix = reform(fix(epix+0.5))

;
; This is now removed with the cross-correlation technique.
;

;vr = ((center-spot)/spot)*c
;npix = vr/dvpix

;;;;;;;;;;;;;;;;;;;;;;;;;;;;;;;;;;;;;;;;;;;;;;;;;;;;;

print,systime()

;
; Now to convert that into regions that will be fit with the loops below.
;

good2=where(w ge left and w le right)
testing=n_elements(good2)-1
ending=good2(testing)

;
; Now that I have something resembling a grid of values, I want to
; create the models from these values. This is where I will split up
```

```
; (if needed) where the models come from, based on the temperature
; cutoff for BSTAR 2006 versus OSTAR 2002. I'll do a double loop,
; first in temperature, then in log g.
;

omc=dblarr(gridelements,gridelements)

for i=0,gridelements-1 do begin

    for j=0,gridelements-1 do begin

        if(ttemp(i) le 30000.0d0) then begin

            lhtrans,'BG',ttemp(i),tlogg(j),uservsini,eps,fwhm,w,wobs,fout

        endif else begin

            lhtranso,'G',ttemp(i),tlogg(j),uservsini,eps,fwhm,w,fout

        endelse

;
; Here is where I need to account for the radial velocity of the
; star. Ok, so the star is probably shifted by some amount compared to
; the rest (and model) wavelengths. Here is a quick and hopefully not
; too dirty method to correct for this while trying to calculate the
; chi-squared fit below. It is a simple interpolation via a pixel
; shift that was calculated above. Because this is a shift and
; therefore there will be missing elements before or after the data,
; the "MISSING" merely inserts values to fill out the vector.
;

        crosscor,fout,flux,f,zero,bpix,epix,21

        fshift,fout,-zero,fnew

;
; This is now removed with the cross correlation techinique.
;

;        quest=findgen(n_elements(w))

;        quest=quest-npix

;        fnew=interpolate(fout,quest,MISSING=1.0)

;;;;;;;;;;;;;;;;;;;;;;;;;;;;;;;;;;;;;;;;;;;;;;;;;;;;

        sum=0.0d0

        for l=good2(0),ending do begin

        sum=((((flux(l)-(fnew(l))))^2.0d0) / (sig(l))) + sum

        endfor

        plot,w,flux,xrange=[bottom,top] $
               ,yrange=[low,high],ystyle=1,xstyle=1
        oplot,w,fnew,linestyle=1

;
; A trick I picked up while trying to fit Balmer line wings. An
; overplot that shows what region you are fitting. This will be easier
; than in the Balmer case, where you are fitting two separate wings.
;

        oplot,[left,left],[0.0,1.1],linestyle=2
        oplot,[right,right],[0.0,1.1],linestyle=2
```

```
        print,ttemp(i),tlogg(j),sum

        omc(i,j) = sum

    endfor

endfor

;
; Just a quick thing to print out the matrix of best fit values. For
; now, hardcoded, as I can't think of a clever way to generalize it
; inside the format statement and keep everything orderly. This helps
; if you get an error message. This will tell you if you need to alter
; your initial guess for T or log g and what direction you need to
; alter it.
;

print,'-------',tlogg,format='(1x,a7,12d8.2)'

for i=0,gridelements-1 do begin

    print,ttemp(i),omc(i,*),format='(12d8.2)'

endfor

;
; I want to find the minimum of the "omc" array. The "min" function in
; IDL seems to run through the temperature values for one log g in
; finding the element array corresponding to minimum. In other words,
; it seems to search in the j's first, then the i's according to how I
; have it set up here. Good to know for the future.
;

chimin=min(omc,bestfit)

loggbest=bestfit/gridelements
tempbest=bestfit mod gridelements

;
; Now I want to interpolate in each direction for +1.0, and use this
; as an estimate of the fit. Because this is causing so much trouble
; due to typically not having enough data points on either side (owing
; to bad normalization, among other things), I'm going to simply
; interpolate without searching each side of the chi-squared minimum.
;

chilogg=omc(tempbest,*)
chitemp=omc(*,loggbest)

;lowtindex=where(ttemp le ttemp(tempbest))
;uptindex=where(ttemp gt ttemp(tempbest))

;tlow=chitemp(lowtindex)
;tup=chitemp(uptindex)

;ttemp2low=ttemp(lowtindex)
;ttemp2up=ttemp(uptindex)

;tonesiglow=interpol(ttemp2low,tlow,chimin+1.0)
;tonesigup=interpol(ttemp2up,tup,chimin+1.0)

tonesig=interpol(ttemp,chitemp,chimin+1.0)

;print,'T(eff) = ',ttemp(tempbest),' + ',tonesigup-ttemp(tempbest),' - '$
;  ,ttemp(tempbest)-tonesiglow,' K',format='(a10,d6.0,a3,d5.0,a3,d5.0,a3)'

print,'T(eff) = ',ttemp(tempbest),' +/- ',ttemp(tempbest)-tonesig,$
  'K',format='(a10,d6.0,a5,d6.0,a3)'
```

```
;
; Now to do the similar thing for the log g's.
;

;lowgindex=where(tlogg le tlogg(loggbest))
;upgindex=where(tlogg gt tlogg(loggbest))

;glow=chilogg(lowgindex)
;gup=chilogg(upgindex)

;tlogg2low=tlogg(lowgindex)
;tlogg2up=tlogg(upgindex)

;gonesiglow=interpol(tlogg2low,glow,chimin+1.0)
;gonesigup=interpol(tlogg2up,gup,chimin+1.0)

gonesig=interpol(tlogg,chilogg,chimin+1.0)

;print,'log g = ',tlogg(loggbest),' + ',gonesigup-tlogg(loggbest),' - '$
;  ,tlogg(loggbest)-gonesiglow,' cgs',format='(a9,d5.2,a3,d5.2,a3,d5.2,a5)'

print,'log g = ',tlogg(loggbest),' +/- ',tlogg(loggbest)-gonesig,$
  ' cgs',format='(a9,d5.2,a5,d5.2,a4)'

end

@/nfs/morgan4/swilliams/research/stars/Pros/readstk.pro
@/nfs/morgan4/swilliams/research/stars/Pros/lhtrans.pro
@/nfs/morgan4/swilliams/research/stars/Pros/lhtranso.pro
@/nfs/morgan4/swilliams/research/stars/Pros/crosscor.pro
@/nfs/morgan4/swilliams/research/stars/Pros/fshift.pro
```

And “findmodbalmer.pro”:

```
pro findmodbalmer

;
; This version of the program is a quick fix to fit the line wings of
; the Balmer profiles. More specifically, to fit the H-gamma wings of
; O stars in order to break the degeneracy in log g introduced by only
; looking at He I or He II lines. I may also add some new chisquared
; calculation features as per my discussion with Doug today. 2-9-11
;

;
; This is a program to find a model template spectrum from a grid of
; models. For now, this will use the Lanz & Hubeny Tlusty OSTAR 2002
; and BSTAR 2006 models. I hope to expand this for use with custom
; models output from David Grey's SPECTRUM for stars cooler than 15
; kK. 6-19-09 by Stephen Williams.
;

device, retain=2

;
; Declare those variables. First up is the size of the square grid in
; T_eff and log g to search. Square simply because that's easiest to
; program according to how I began this escapade. I also include here
; the size of the grid for both temperature and log g. Presumably,
; this can be changed here without much in the way of effort. PLEASE
; KEEP THE NUMBER OF GRID ELEMENTS ODD. This is currently set up to
; search the equivalent of at least one model grid point above and
; below in the OSTAR 2002 grid.
```

```
;

gridelements = 11
tstep=500.0d0
loggstep=0.05d0

c=2.99792458d5

;
; Now I need some user input for the values I will need to obtain grid
; points. I'll also need an estimate for the rotational velocity, so
; I can use that in the creation of models later.
;

usertemp=0.0d0
read,'What is your best estimate for temperature (Kelvin)? ',usertemp

userlogg=0.0d0
read,'What is your best estimate for gravity (log g in cgs)? ',userlogg

uservsini=0.0d0
read,'What is your best estimate for V sin i (km/s)? ',uservsini

;
; Now I need to use this to find the grid points I will compare to the
; co-added, high signal-to-noise spectrum for the particular star. The
; endpoints will be pretty tricky. For now, fortunately, the stars I
; wish to test right now are well within the limits of the
; models. This is now generalized to setup arrays for both T_eff and
; log g for any particular number of gridelements (odd number, of course).
;

ttemp=dblarr(gridelements)
tlogg=dblarr(gridelements)

symmet=gridelements/2
neartemp=round(usertemp/tstep)*tstep
nearlogg=round(userlogg/loggstep)*loggstep

for i=0,gridelements-1 do begin

    ttemp(i) = neartemp + (float(i-symmet)) * tstep
    tlogg(i) = nearlogg + (float(i-symmet)) * loggstep

endfor

;
; I need to read in the spectrum stack for the object in order to
; obtain the wavelength vector for later work.
;

specstack=' '
read,'Please enter the spectrum stack name for the object: ',specstack

readstk,w,ss,t,specstack

;
; Now for another calculation before we proceed. This is to give a
; reasonable value for the uncertainty involved with the later
; chi-squared type calculation. This works for spectral stacks that
; are all in the same velocity frame -- but will not work for velocity
;                                        variables where a shift and
;                                        add algorithm would be more
;                                        appropriate.
;

sig=dblarr(n_elements(w))
```

```
for i=0,n_elements(w)-1 do begin

    sig(i) = stddev(ss(i,*))/sqrt(n_elements(t)-1.0d0)

endfor

;
; Now I need to set up a few things for the velocity shift (if needed)
; for the comparison to the model. I'll make use of this later, after
; prompting the user to click on the center of the feature they wish
; to fit.
;

dw=deriv(w)
dvpix=mean(dw/w*c)

;
; Read in the coadded spectrum. This will be the spectrum for
; comparison.
;

coadded=' '
read,'Please enter the name of the coadded spectrum: ',coadded

flux=readfits(coadded)

;
; Before going to the models, I need the linear limb darkening
; coefficient. This is hardcoded for now, and needs to be improved
; with future efforts.
;

eps=0.300d0

;
; I also need the instrumental broadening fwhm, presumably already
; known by the observer, and just needed to be input here. Note that
; this MUST BE A FLOAT, IT CANNOT BE A DOUBLE OR GSMOOTH WILL PUKE AND
; IT WILL TAKE YOU 90 MINUTES TO TRACK DOWN!!!
;

fwhm=0.0d0
read,'What is the instrumental broadening FWHM (in km/s)? ',fwhm

;
; I think I need one more input. Fitting the entire spectrum doesn't
; seem to work, so I'll request a user wavelength for a partcular
; line, plot it, and have the user click on the left and right hand
; edges of the region to fit with a model.
;

spot=0.0d0
read,'What feature would you like to fit (rest wavelength in Angstroms)? ',spot

top=spot+20.0d0
bottom=spot-20.0d0

good=where(w gt bottom and w lt top)
range=flux(good)
high=max(range)+0.1
low=min(range)-0.1
plot,w,flux,xrange=[bottom,top],yrange=[low,high],ystyle=1,xstyle=1

;
; Now get those limits for the fit. Two wings now.
;

print,'Click on the left side of the left wing to fit '
```

```
cursor,leftleft,empty
wait,1
print,'Click on the right side of the left wing to fit '
cursor,leftright,empty
wait,1

print,'Click on the center of the feature '
cursor,center,empty
wait,1

;
; I need the pixel number for the cross correlation later.
;

pixels = indgen(n_elements(w))

bpix = interpol(pixels,w,[leftleft])
;epix = interpol(pixels,w,[leftright])

bpix = reform(fix(bpix+0.5))
;epix = reform(fix(epix+0.5))

;
; As opposed to having the person enter the velocity shift, we'll just
; use the best shift for the line based on the user clicking in the
; center of the line.
;

vr = ((center-spot)/spot)*c
npix = vr/dvpix

print,systime()

;
; Now to convert that into regions that will be fit with the loops below.
;

goodleft=where(w ge leftleft and w le leftright)
testingleft=n_elements(goodleft)-1
endingleft=goodleft(testingleft)

;
; I want to fit the same regions around the line, thus the center of
; the line. I will mirror the wing on the left using the selected
; center of the line.
;

otherside = center - leftright
rightleft = center + otherside
rightright = rightleft + (leftright - leftleft)
goodright=where(w ge rightleft and w le rightright)
testingright=n_elements(goodright)-1
endingright = goodright(testingright)

epix = interpol(pixels,w,[leftright])
epix = reform(fix(epix+0.5))

;
; Now that I have something resembling a grid of values, I want to
; create the models from these values. This is where I will split up
; (if needed) where the models come from, based on the temperature
; cutoff for BSTAR 2006 versus OSTAR 2002. I'll do a double loop,
; first in temperature, then in log g.
;

omc=dblarr(gridelements,gridelements)

for i=0,gridelements-1 do begin
```

```
    for j=0,gridelements-1 do begin

        if(ttemp(i) le 30000.0d0) then begin

            lhtrans,'BG',ttemp(i),tlogg(j),uservsini,eps,fwhm,w,wobs,fout

        endif else begin

            lhtranso,'G',ttemp(i),tlogg(j),uservsini,eps,fwhm,w,fout

        endelse

;
; Here is where I need to account for the radial velocity of the
; star. Ok, so the star is probably shifted by some amount compared to
; the rest (and model) wavelengths. Here is a quick and hopefully not
; too dirty method to correct for this while trying to calculate the
; chi-squared fit below. It is a simple interpolation via a pixel
; shift that was calculated above. Because this is a shift and
; therefore there will be missing elements before or after the data,
; the "MISSING" merely inserts values to fill out the vector.
;

        quest=findgen(n_elements(w))

        quest=quest-npix

        fnew=interpolate(fout,quest,MISSING=1.0)

        sum=0.0d0

        for l=goodleft(0),endingleft do begin

            sum=(((flux(l)-fnew(l))^2.0d0) / sig(l)) + sum

        endfor

        for m = goodright(0),endingright do begin

            sum=(((flux(m)-fnew(m))^2.0d0) / sig(m)) + sum

        endfor

        plot,w,flux,xrange=[bottom,top] $
               ,yrange=[low,high],ystyle=1,xstyle=1
        oplot,w,fnew,linestyle=1

;
; Now a bit of code to show the regions that are being fit. Just a
; kind of check, but it should make it look even better.
;

        oplot,[leftleft,leftleft],[0.0,1.1],linestyle=2
        oplot,[leftright,leftright],[0.0,1.1],linestyle=2
        oplot,[rightleft,rightleft],[0.0,1.1],linestyle=2
        oplot,[rightright,rightright],[0.0,1.1],linestyle=2
        print,ttemp(i),tlogg(j),sum

        omc(i,j) = sum

    endfor

endfor

;
; Just a quick thing to print out the matrix of best fit values. For
; now, hardcoded, as I can't think of a clever way to generalize it
```

```
; inside the format statement and keep everything orderly. This helps
; if you get an error message. This will tell you if you need to alter
; your initial guess for T or log g and what direction you need to
; alter it.
;

print,'-------',tlogg,format='(1x,a7,12d8.2)'

for i=0,gridelements-1 do begin

    print,ttemp(i),omc(i,*),format='(12d8.2)'

endfor

;
; I want to find the minimum of the "omc" array. The "min" function in
; IDL seems to run through the temperature values for one log g in
; finding the element array corresponding to minimum. In other words,
; it seems to search in the j's first, then the i's according to how I
; have it set up here. Good to know for the future.
;

chimin=min(omc,bestfit)

loggbest=bestfit/gridelements
tempbest=bestfit mod gridelements

;
; Now I want to interpolate in each direction for +1.0, and use this
; as an estimate of the fit. Because this is causing so much trouble
; due to typically not having enough data points on either side (owing
; to bad normalization, among other things), I'm going to simply
; interpolate without searching each side of the chi-squared minimum.
;

chilogg=omc(tempbest,*)
chitemp=omc(*,loggbest)

;lowtindex=where(ttemp le ttemp(tempbest))
;uptindex=where(ttemp gt ttemp(tempbest))

;tlow=chitemp(lowtindex)
;tup=chitemp(uptindex)

;ttemp2low=ttemp(lowtindex)
;ttemp2up=ttemp(uptindex)

;tonesiglow=interpol(ttemp2low,tlow,chimin+1.0)
;tonesigup=interpol(ttemp2up,tup,chimin+1.0)

tonesig=interpol(ttemp,chitemp,chimin+1.0)

;print,'T(eff) = ',ttemp(tempbest),' + ',tonesigup-ttemp(tempbest),' - '$
;  ,ttemp(tempbest)-tonesiglow,' K',format='(a10,d6.0,a3,d5.0,a3,d5.0,a3)'

print,'T(eff) = ',ttemp(tempbest),' +/- ',ttemp(tempbest)-tonesig,$
  'K',format='(a10,d6.0,a5,d6.0,a3)'

;
; Now to do the similar thing for the log g's.
;

;lowgindex=where(tlogg le tlogg(loggbest))
;upgindex=where(tlogg gt tlogg(loggbest))

;glow=chilogg(lowgindex)
;gup=chilogg(upgindex)
```

```
;tlogg2low=tlogg(lowgindex)
;tlogg2up=tlogg(upgindex)

;gonesiglow=interpol(tlogg2low,glow,chimin+1.0)
;gonesigup=interpol(tlogg2up,gup,chimin+1.0)

gonesig=interpol(tlogg,chilogg,chimin+1.0)

;print,'log g = ',tlogg(loggbest),' + ',gonesigup-tlogg(loggbest),' - '$
;  ,tlogg(loggbest)-gonesiglow,' cgs',format='(a9,d5.2,a3,d5.2,a3,d5.2,a5)'

print,'log g = ',tlogg(loggbest),' +/- ',tlogg(loggbest)-gonesig,$
  ' cgs',format='(a9,d5.2,a5,d5.2,a4)'

end

@/nfs/morgan4/swilliams/research/stars/Pros/readstk.pro
@/nfs/morgan4/swilliams/research/stars/Pros/lhtrans.pro
@/nfs/morgan4/swilliams/research/stars/Pros/lhtranso.pro
```